The fabrication, characterization and simulation of inverted perovskite solar cells

Doctoral thesis for obtaining the academic degree Doctor of Natural Science (Dr.rer.nat.)

submitted by

Hao Hu

at the

Universität Konstanz

Faculty of Mathematics and Natural Sciences

Department of Physics

Date of the oral examination: May 8, 2019

First referee: Professor Dr. Lukas Schmidt-Mende

Second referee: Professor Dr. Peter Baum

Contents

Abstract

Halide perovskites have been attracting a lot of attentions as the absorber material in solar cells. Some of their most appreciated properties include tunable band gaps, high absorption coefficients and a unique defect tolerant nature. Within 10 years, their certificated efficiency has reached 23.3% which is close to the commercial silicon solar cells. However, to further improve the efficiency towards their Shockley Queisser limits, the current bottle neck - lower open circuit voltage (V_{OC}) needs to be increased towards its theoretical thermal limit. In this study, the inverted p-i-n type of perovskites solar cells based on the typical $CH_3NH_3PbI_3$ ($MAPbI_3$) material is studied, which provides insights into the fabrication techniques as well as the internal performance - limiting processes in the studied solar cells.

The deposition of perovskite films was a challenge due to the easily formed pin-holes during the crystallization process. A uniform and continuous perovskite layer needs to be achieved to ensure a proper functioning of the solar cell. A novel vacuum-assisted deposition technique is developed in this study to prepare voids-free perovskite films. Based on it, the inverted perovskite solar cells with an architecture of PEDOT:PSS/$MAPbI_3$/C_{60} are fabricated and optimized, yielding the best efficiency of around 16% with a high reproducibility.

The recombination processes determine the V_{OC} and subsequently the performance of the solar cells. In this study, based on the variations of the perovskite film annealing conditions, solar cells with different V_{OC}s are prepared. A clear surface potential difference is observed among the differently treated perovskite films which leads to the variation of the surface band diagram. Instead of a direct change of the recombination velocities, the change of the band structure could redistribute the charge carriers across the cell and further modify the recombination profile, which leads to a different solar cell performance. This concept is examined through the oxygen plasma treatment of the perovskite films, which increases the V_{OC} of the corresponding cell presumably by aggregating charged ions on the surface.

Based on the specific solar cell architecture employed in this study, a analytical model is established by solving the continuity equations. A large recombination velocity at the PEDOT:PSS/$MAPbI_3$ interface is extracted by fitting experimental data with the model. Considering the direction of the incoming light, a more severe recombination loss is expected due to the larger carrier population near the PEDOT:PSS/$MAPbI_3$ interface. The hysteresis feature observed in this study is well reconstructed by implementing the ion migration features to the model.

Zusammenfassung

Halogenide Perovskite haben viel Aufmerksamkeit als Material zur Lichtabsorption in Solarzellen bekommen. Einige der meist geschätzten Eigenschaften sind z.B. abstimmbare Bandlückenenergien, hohe Absorptionskoeffizienten und eine einzigartige Defekttoleranz. Innerhalb von zehn Jahren erreichte ihre bestätigte Effizienz 23,3%, was nahe der Effizienz von kommerziellen Siliziumsolarzellen herankommt. Um die Effizienz jedoch weiter Richtung Shockley-Queisser-Limit zu erhöhen, muss der derzeit limitierende Faktor, die niedrigere Leerlaufspannung (Abk.: V_{OC}, nach dem engl. open circuit voltage) erhöht werden. In dieser Arbeit wird der Typ der invertierten Perovskit Solarzellen am Beispiel des dafür typischen Materials $CH_3NH_3PbI_3$ ($MAPbI_3$) untersucht. Dabei werden Einblicke sowohl Herstellungstechniken, als auch in die internen leistungslimitierenden Prozesse der untersuchten Solarzellen gegeben.

Die Herstellung des Perovskitfilmes ist eine Herausforderung, da sich während der Kristallisation einfach Poren im Film bilden. Um eine korrekt funktionierende Solarzelle zu gewährleisten muss ein gleichmäßige Perovskitschicht erreicht werden. Hierfür wurde in dieser Arbeit ein neuartiges vakuumunterstütztes Herstellungsverfahren entwickelt und porenfreie Perovskitfilme zu erhalten. Mittels diesem Verfahren wurden invertierte Perovskit Solarzellen mit einer PEDOT:PSS/$MAPbI_3$/C_{60}-Architektur hergestellt und optimiert. Die mit diesen Zellen erreichten Effizienzen liegen bei ungefähr 16% bei einer sehr guten Reproduzierbarkeit.

Der Rekombinationsprozess bestimmt die V_{OC} und damit auch die Leistung der Solarzelle. In dieser Arbeit wurden Solarzellen mit verschiedenen V_{OC} hergestellt, indem die Bedingungen beim Glühen des Perovskitfilmes variiert wurden. Es kann ein deutlicher Unterschied des Oberflächenpotentiales zwischen den verschieden behandelten Perovskitfilmen beobachtet werden. Dies führt gleichzeitig zu einer Veränderung des Krümmungsverhaltens der Bandstruktur an den Oberflächen. Anstatt einer direkten Änderung der Rekombinationsgeschwindigkeit führt die Änderung der Bandstruktur zu einer Umverteilung der Ladungsträger über die Zelle und führt daher zu einer Modifizierung der Rekombination, woraus eine veränderte Solarzellenleistung folgt. Dieses Konzept wird mittels der Behandlung des Perovskitfilms mit Sauerstoffplasma untersucht, was die V_{OC} erhöht. Dies geschieht vermutlich durch die Ansammlung von geladenen Ionen auf der Oberfläche.

Basierend auf der in dieser Arbeit verwendeten Solarzellenarchitektur wurde ein analytisches Modell entwickelt, indem die Kontinuitätsgleichungen gelöst wurden. Durch Anfitten des Modells an experimentell erhaltene Daten kann eine hohe Rekombinationsgeschwindigkeit an der PEDOT:PSS/$MAPbI_3$-Grenzschicht erhalten werden. Berücksichtigt man die Richtung des einfallenden Lichtes erwartet man einen drastischeren Verlust durch Rekombinationsmechanismen aufgrund der hohen Ladungsträgerdichte in der Umgebung der PEDOT:PSS/$MAPbI_3$-Grenzschicht. Die in dieser Arbeit beobachtete Hysterese kann gut rekonstruiert werden, indem man Eigenschaften der Ionenmigration in das Modell integriert.

Chapter 1

An introduction - Perovskite materials and perovskite solar cells

Energy has been one of the most important terms during the development of human society. The progress of the science and technology brings a wide variety of energy sources, while the energy consumption is also continuously pushed to historic highs by the development of modern society. In 2017, according to BP Statistical Review of World Energy, primary energy consumption grows 2.2% to reach over 13500 million tonnes oil equivalent (mtoe), a new historic peak [1]. Oil, coal, natural gas, hydroelectricity, nuclear energy and renewables are the six major energy sources, sorted in descending order of magnitude (Figure 1.1).

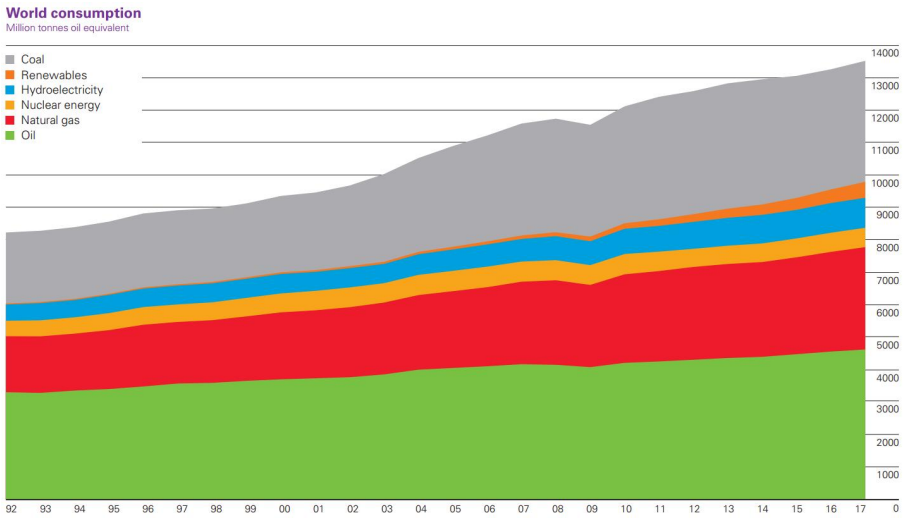

Figure 1.1: The development trend of the world energy consumption [1].

Despite the noticeable share fluctuations, oil, coal and natural gas, so called fossil fuels, have always played the major role (over 80% share) in the world energy market for the last half century [1]. This situation, however, is unsustainable and accounted for the greenhouse (global warming and climate change) effect. The fossil fuels are considered to

be non-renewable resources because their formation process takes millions of years, and the viable resources are depleted much faster than being made. Reserves-to-production (R/P) ratio is defined as the result of the remaining reserves of certain fossil fuel at the end of any year divided by its consumption in that year. If the consumption of certain fossil fuel were to continue at that rate, then its R/P ratio indicates the length of time in year that those remaining reserves would last. Accordingly, the R/P ratios of oil, coal and natural gas in 2017 are 50.2, 134, 52.6 respectively [1]. This situation underlines the necessity and urgency of replacing the fossil fuels with alternative sustainable energy sources in the energy consumption domain. On the other hand, the increasing threat of green house effect has been a major concern since the 1990s. Because GHG (greenhouse gas) is primarily emitted from the combustion of fossil fuels, the consumption and production of fossil fuels has also evoked a lot of debates [2]. The Paris agreement of the 2015 United Nations Climate Change Conference (COP21), which has become a milestone in fighting greenhouse effect, stresses the necessity of reducing GHG emission and generating energy via renewable sources.

The renewable energy sources usually include wind, geothermal, solar, biomass and so on. Among them solar energy attracts enormous interest, mainly due to solar energy is abundant, relatively low-cost and environmentally friendly. Speaking of solar energy, despite it can be utilized in many ways (transform into thermal energy, chemical energy and etc.), the electric power generation via photovoltaic (PV) effect is the most important way for large scale transformation and utilization. The global primary energy consumption in 2017 is aroud 13500 mtoe, which could be translated to 17.9 Terawatts (TW) continuous power for the whole year. Assuming using solar energy to supply this amount of electricity power, with 1.5 air mass (AM) solar intensity (1000 W/m^2) and a relatively medium energy conversion efficiency of 10%, we can calculate that a solar panel of 179000 km^2 would already suffice, which is roughly 2% the area of the Sahara desert. However, this calculation doesn't take into account the daily, seasonal and climate-dependant change of the solar energy intensity, so this 2% estimation is quite underestimated. Moreover, this plan is anyway unrealistic as it would require to transport the electric energy over long distance to where it is needed. This example merely serves to show the abundance of the solar energy. On the other hand, thanks to the financial support of government policies and reduced cost of PV modules, the levelized cost of energy (LCOE) of PV is already comparable or even lower than traditional fossil fuels in various regions across the world. And due to the reducing LCOE and enhancing commercial competitiveness, the application of PV systems is developing rapidly. In 2016, it has been reported the global cumulative solar PV capacity reached almost 300 Gigawatts (GW) and generated over 310 Terawatts hour (TWh) electricity. Also in Renewables 2017, the International Energy Agency predicted by 2022 the world PV capacity would reach around 900 GW and generate about 900 TWh electricity, which almost triples the values of 2016 [3].

Right now the working horse in commercial PV market is mainly silicon solar cells. However, after decades of research and optimization, the efficiencies of silicon-based solar cells are now close to the limitation of their theoretical maximum value. Therefore new concepts are required to further increase the efficiency, reduce the cost and promote the application of PV technology. In recent years, a new class of solar cell, perovskite solar cell (PSC), has attracted a lot of interest. Figure 1.2 presents the rapid increasing publications

on this new type of solar cells [4]. Since its first report in 2009 till 2019, according to the the web of science database, there has been almost 12000 reports. And the quantity of relevant publications increases year by year. Though it is just the beginning of the year 2019, there has been over 400 publications on this area. This unusual research enthusiasm is inspired by the rapid increase of the reported efficiencies of the solar cells. Figure 1.3 shows the rapid development of the efficiency records of PSCs [5]. The efficiency of PSC has reached 23.3% which already surpasses the efficiency record of thin film and multicrystalline silicon solar cells. In the following part of this chapter, the material properties of perovskites and device physics of the corresponding solar cells will be introduced.

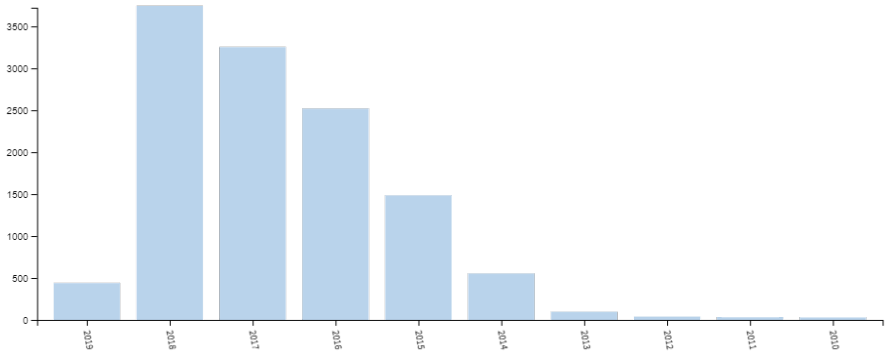

Figure 1.2: The number of publications on PSCs from 2009 to 2019, accessed on 2018-08-02 [4].

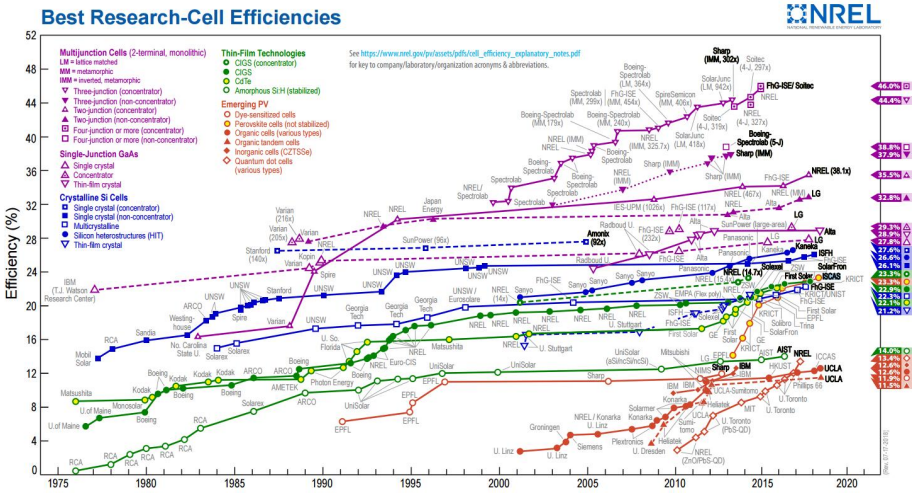

Figure 1.3: The efficiency chart of different types of solar cells, accessed on 2018-08-12 [5].

1.1 Perovskite material - properties and deposition techniques

Perovskite is technically a mineral with the chemical formula $CaTiO_3$. The mineral was firstly discovered by Gustav Rose (1798–1873) in the Ural Mountains, Russia in 1839 and then named after Russian mineralogist Lev Perovski (1792–1856). Following the term perovskite comes the term perovskite structure. Materials with a perovskite structure refer those which have the generic form ABX_3 and the same crystallographic structure as $CaTiO_3$. In practice the term perovskite and perovskite structure are often used indiscriminately. And perovskite is then usually regarded as a class of material with the perovskite structure. And in this context of recent solar cell studies, the term perovskite refer more specifically. Specifically, with the generic form ABX_3, A represents the monovalent cation $CH_3NH_3^+$ (MA), $NH_2CH{=}NH_2^+$ (FA), or Cs^+, B represents the bivalent cation Pb^{2+} or Sn^{2+}, and X represents the monovalent halogen anion Cl^-, Br^-, or I^-. In the following context, the term 'perovskite' will only refer to these materials studied in recent solar cell community.

1.1.1 Properties of halide perovskites

The cubic crystal structure of the perovskite material ABX_3 is shown in Figure 1.4. The latter can be described as A^+ and X^- ions forming a cubic closely packed lattice with B^{2+} ions occupying the octahedral centers created by the X^- ions. The perovskite structure has a three dimensional network of corner sharing BX_6 octahedra with A^+ ions in the twelve fold cavities in between the polyhedra. In the cubic ABX_3 perovskite structure (space group Pm-3m, Z = 1), the A atoms are in Wyckoff position 1b, 0.5,0.5,0.5; the B atoms in 1a, 0,0,0; and the X atoms in 3d 0.5,0,0; 0,0.5,0; 0,0,0.5 (Figure 1.4). However, the perovskite structure is known to be flexible. With certain distortion, the atom coordinates will not be at the Wyckoff positions and the crystal will form a lower symmetry structure.

These symmetry differences widely exist among the studied perovskite materials, depending on the adopted cations and anions. This phenomenon is ascribed to the influence of the size effect, namely the size of A^+ should fit into the space in between the BX_6 octahedra. The Goldschmidt's tolerance factor t allows us to estimate the degree of fitness. It is based on ionic radii (assuming pure ionic bonding), but can also be used as an indication for compounds with a high degree of ionic bonding. Its definition is given as follow[6]

$$t = \frac{r_A + r_X}{\sqrt{2}(r_B + r_X)} \tag{1.1}$$

where r_A, r_B, r_X are the ionic radii of A, B, X ion respectively. It has been suggested that the metal halide perovskite materials tend to form an orthorhombic structure when

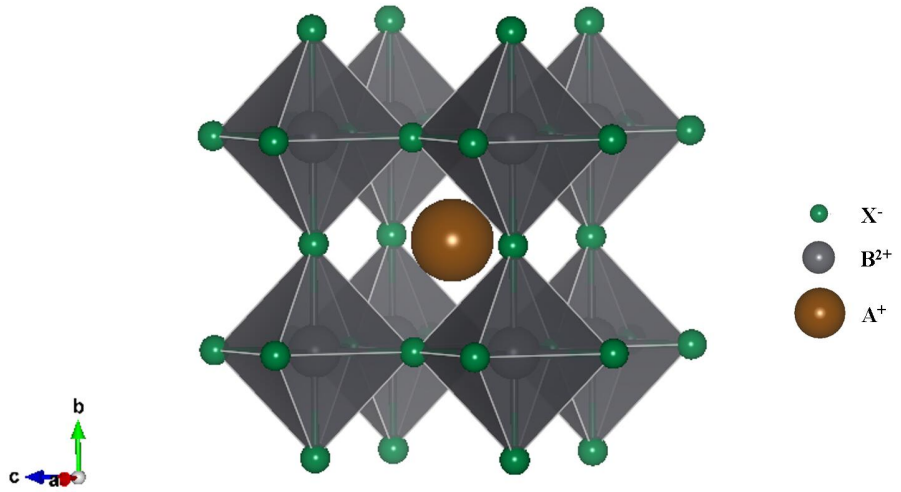

Figure 1.4: The cubic crystal structure of the perovskite material ABX_3.

$t < 0.8$, cubic structure when $0.8 < t < 1$, and hexagonal structure when $t > 1$[7][8]. Actually, a perovskite compound could posses several crystal structures of different symmetries, depending on the fabrication condition and temperature. For example, it has been reported that $MAPbI_3$ undergoes a crystal phase transition from cubic phase ($T > 330K$) to tetragonal phase ($160K < T < 330K$) to orthorhombic phase ($T < 160K$) by the tilting of the PbI_6 octahedra with the decreasing temperature[9][10][11]. As the crystal structure transition could lead to the degradation of the perovskites, stabilizing the perovskite phase at certain structure (especially the cubic structure) has been reported to lead to an improved solar cell life time and efficiency[7].

The band gap of the perovskite material is also determined by the adopted cations and anions. $MAPbI_3$ has a band gap of around 1.6 eV, while the band gap of $FAPbI_3$ is around 1.48 eV. The influence of anion is very pronounced on the band gap value. By replacing varying fractions of iodine with bromine in $MAPbI_3$, the band gap would be continuously tuned from 1.6 eV to 2.3 eV[12][13]. The similar strategy could also be applied on $FAPbI_3$, providing a controllable band gap range from 1.48 eV to 2.23 eV[14]. First principle computational approaches indicate the band gap is mainly determined by the three dimensional network of corner sharing BX_6 octahedra, while the A cation has a weaker influence on the band gap through distorting the perovskite lattice[12][15][16][17]. The band gap value of perovskites is an important property in solar cell application. The continuous band gap tuning through composition adjustment enables metal halide perovskites to be optimized for applications as either the top or bottom cell absorber in a tandem solar cell or the sole absorber in a single junction solar cell.

Another greatly appreciated property of the metal halide perovskites is its high light absorption coefficient. The light absorption coefficient of $MAPbI_3$ has been reported to be at 1.5×10^4 cm^{-1} at 550 nm, indicating a light penetration depth of 0.66 μm[18][19]. The high light absorption coefficient enables a thinner perovskite absorber layer collecting the light, which is beneficial regarding reducing both the transport length of the charge carriers and the amount of material usage. A high absorption coefficient usually requires

the oscillator strength of a direct optical transition. However, the assumption, that the metal halide perovskites have direct band gap, is being challenged. Some theoretical and experimental evidences suggest that besides the direct band gap, there is an indirect band gap which lies few tens of meV below the direct band gap[20][21][22]. Whether these perovskites are direct or indirect semiconductor, however, is still under debate[23].

Perovskites are also known for its outstanding long charge carrier diffusion length. In solar cell applications, the diffusion length is an important parameter, which indicates before the charge carriers recombine, how far they can diffuse. Its definition (L_D) is as follows[24]

$$L_D = \sqrt{\frac{k_B T}{q} \mu \tau} \tag{1.2}$$

where k_B is Boltzmann constant, T is temperature in Kelvin, q is the elementary charge, μ is the charge carrier mobility and τ is the charge carrier life time. Therefore L_D is determined by the charge carrier mobility μ and life time τ. The values of these two parameters are influenced by not only the intrinsic property of the material, but also certain external factors (for example, grain size and trap density). Here only the intrinsic factors are addressed to present the properties of the perovskite material, though the external factors are extremely important in practice.

The intrinsic factor which dominates the charge carrier life time τ is the recombination rate coefficients. Three types of recombination process exist with their respective rate coefficients as shown[25].

$$\frac{dn(t)}{t} = -k_1 n - k_2 n^2 - k_3 n^3 \tag{1.3}$$

where n is the charge carrier density, k_1 is the monomolecular recombination decay constant (which is relevant to trap-assisted recombination), k_2 is the bimolecular recombination decay constant (which is related to radiative recombination); and k_3 is the Auger recombination decay constant. Depending if the recombination type is proportional to first, second or third order of n, its significance varies with the illumination intensity. Under low-level illumination, trap-asssited recombination processes mediated by defects such as elemental vacancies, substitutions or interstitials will dominate charge-carrier recombination[26]. With increasing charge-carrier density, bimolecular recombination between free electrons and holes will start to become the leading factor, while Auger recombination which involves more charge carriers will contribute at even higher illumination intensity[27]. In the context of solar irradiation level on earth surface, the Auger recombination is reported to be inessential[28], and the life time of charge carriers depends on the rate coefficient k_1 and k_2 of the trap-assisted recombination and bimolecular recombination respectively. It has been reported that the rate coefficient of the radiative recombination can be directly derived from the the absorption spectra of halide perovskites[29]. And the rate coefficient of trap-assisted recombination k_1 depends largely on the position where

the energy states of defects are located in the band gap of perovskites. The relevant reports claim that the normal defects in perovskites mostly only lead to shallow traps, enabling a lower recombination rate coefficient k_1 and the so called defect tolerance of perovskites[30][26][31][32].

On the other hand, the charge carrier mobility μ of halide perovskites has also been investigated intensively. Multiple characterization approaches (optical-pump-THz-probe photoconductivity, space-charge limited current, Hall coefficient and resistivity measurements, etc.) have been performed on a wide variety of perovskite samples to extract the charge carrier mobility values[9][28][33][34][35][36]. And a wide range of values from around 2 to 600 $cm^2/(V\ s)$ have been reported for the most commonly studied $MAPbI_3$[37][38]. The reason for this wide variations could partly come from different samples preparation processes as well as different emphases among these measurement techniques. The theoretical studies suggest the Fröhlich interactions between charge carriers and the electric fields associated with longitudinal optical phonon modes of the ionic lattice is the dominating factor of the charge carrier mobility at room temperature[39][40][41][42]. And the electron and hole mobility values of iodine based perovskites are fundamentally limited to around 200 $cm^2/(V\ s)$ in the framework of this theory[43]. Overall, the diffusion length of single crystal $MAPbI_3$ has been measured in practice to be over 175 μm under 1 sun[36]. Even for polycrystalline $MAPbI_3$ films, the diffusion length has been reported to reach μm range which satisfies its application as a planar light absorbing layer in solar cells[44].

The above introduced excellent optoelectronic properties including adjustable band gaps, high light absorption ability and long charge carrier diffusion length make halide perovskites promising candidates in solar cell applications. However, several intrinsic disadvantageous properties need to be overcome to enable its actual application. Environmental stability is the first issue. Halide perovskites containing organic cations undergo a significant degradation process when exposed to moisture[45][46][47][48][49][50]. Different attempts have been tried to counter the stability issue, such as encapsulation with specially designed holders or top blocking layers, doping with different cations, anions or a polymer scaffold[51][52][53][54][55][56][57]. Besides, inorganic perovskites have also received a lot of attention which could achieve a long term stability[58][59][60].

Another widely notorious problematic feature in perovskite is the ionic conductivity. Experimental evidences and theoretical calculations have suggested that halide perovskites exhibit a mixed ionic-electronic conduction feature[61]. Electronic conduction of electrons and holes is expected and necessary for light absorbing materials, but ionic conduction by hopping among favorable lattice sites leads to unwanted drawbacks. Firstly, ion transport can cause a deformation of the crystal structure and then degradation of the material. The movable ions may aggregate at the interfaces between perovskites and adjacent layers launching certain electro-chemical reaction[62]. They could even penetrate into the adjacent layers causing severe degradation[63]. Secondly, the ion movements could change the electric field in halide perovskite layer leading to the so called hysteresis phenomenon[64]. This phenomenon will be introduced in details in the next section. Thirdly, this facile dissociation of ions from its lattice may introduce traps which will act as recombination centers. The exact movable species in halide perovskites are still under investigation. In $MAPbI_3$, iodine vacancy migration has been suggested as the primary

mechanism of the ionic conduction[65][66]. However, MA cations have also been reported to contribute[67][68].

1.1.2 Deposition of halide perovskites

Owning to the above-mentioned remarkable optoelectronic properties, the halide perovskites could be used as an individual absorbing layer in a planar solar cell architecture. The planar architecture spares the trouble of sintering and filling a mesoporous metal oxide layer, however, it also emphasizes the necessity and importance of controlling the morphology of halide perovskite layers. If the perovskite film surface exhibits adverse features like uncovered voids, pinholes, or large number of grain boundaries, they will lead to a suppressed charge transport and enhanced leakage current, which is detrimental to the proper functioning of solar cells. Therefore, a delicate control of the surface morphology of halide perovskites through careful deposition manipulations has been a matter of importance in the PSC research community[69].

Preliminary attempts fabricating perovskite films often introduce large noncontinuous domains with branch-like structure[70][71]. This feature comes from a quick crystallization trend due to the strong polarity of the components. A wide variety of depositing approaches has been developed ever since to settle this matter. These extensive deposition methods can be summarized into the following three catalogues based on the medium of preparation: simple solution-based techniques[72][73][74][75], mixed vapor-assisted solution method[76][77] and pure vapor deposition[78]. These different deposition techniques usually involve a simple synthetic reaction where the precursor components transform into the target perovskites. Taking $MAPbI_3$ for example

$$PbI_2 + CH_3NH_3I \longrightarrow CH_3NH_3PbI_3$$

In the pure vapor preparation method, the reaction component is usually vaporized in a thermal evaporator. Though a precise control of the evaporation rate of both components in a dual source simultaneous evaporation process, a pure and smooth perovskite film can be achieved[78]. The vapor-assisted solution method, in the other hand, uses the organic caion (MA for example) gas to re-dissolve a pre-deposited perovskite film. Through exhausting the medium gas in a defined way, a controlled recrystallization process takes place giving rise to an improved morphology of the films[77]. The solution based methods can be further divided into one-step and two-step techniques. For the one-step method, the precursor solution contains all necessary components to constitute halide perovskites. It takes only one process (spin-coating, drop-casting or doctor-blade coating) to form target perovskites by the removal of the organic solvent, while the crystallization process is artificially modulated through the usage of anti-solvents[79], vacuum chambers[80] or various additives[81][82][83][84]. Through those modulations, the perovskite crystal domains could form a continuous pin-hole free film which suits the requirements of planar solar cell devices. Comparatively, the two-step or "sequential" deposition method usually

prepares firstly a film of metal halide, one precursor component. Afterwards, the synthetic reaction is triggered by spin-coating the other precursor component solution on top of the metal halide film, or dipping the metal halide film into the other precursor component solution[85][86][87]. This technique explores the ease of the metal halide processing which enables the preparation of uniform and fully covered precursor layers. These, in turn, act as templates for the final transformation of the perovskite films and typically improve their qualities.

Single perovskite crystal growth technique has also been developed producing well defined single crystal with sizes in cm range[88][89][90]. However, the employment of perovskite single crystals into planar solar cells is very difficult due to their specific requirements of growth conditions. Very low trap densities of around 10^{11} cm^3 have been reported for $MAPbI_3$ single crystals[30][91], which increase up to around 10^{16} cm^3 for polycrystalline thin films prepared using the above mentioned deposition techniques[91][92][93]. The trap density of the polycrystalline perovskite films is relatively higher than polycrystalline silicon (10^{13}-10^{14} cm^3)[94], CdTe (10^{13}-10^{15} cm^3)[95] and CIGS (10^{13} cm^3)[96]. However, the resulting perovskite films can already be applied into highly efficient solar cells due to their unique defect chemistry.

1.2 Perovskite solar cells - an introduction

1.2.1 General working principle of solar cells

What is a solar cell?

A solar cell could be energetically described as an energy transformer which harvests solar energy and transforms it into electric energy. This description is correct but also superficial.

A solar cell could be vividly described as a current generator. It outputs electrical current under illumination. In the practical application, the solar cell works with certain load in the external circuit, where the solar cell could output power. And the current generating ability is the fundamental property of a solar cell.

A solar cell could be profoundly described as a well designed device of multiple layers which could not only generate charge carriers, but also transport them towards certain direction. The fundamental principle which makes a solar cell functional is the process in which the charge carriers move towards different electrodes with tolerable losses.

The main parameters of a solar cell (short-circuit current density (J_{SC}), open-circuit voltage (V_{OC}) and fill factor (FF) and efficiency (η)) are shown in a typical current density-voltage (J-V) curve where the current density (J) output of a solar cell is plotted against the bias (V) applied to the device (Figure 1.5).

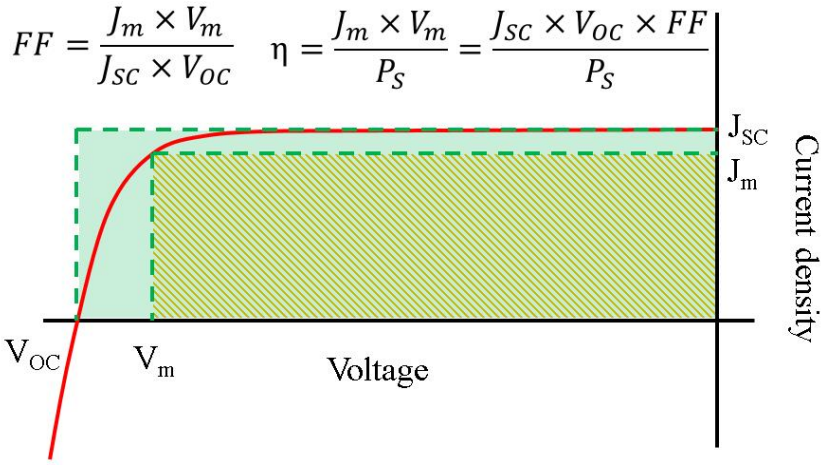

Figure 1.5: Schematic J-V curve labeled with the most important characteristic parameters.

The cell power density is given by

$$P = JV \tag{1.4}$$

P reaches the maximum at the maximum power point with an output voltage V_m and current density J_m. FF is then defined as

$$FF = \frac{J_m V_m}{J_{SC} V_{OC}} \tag{1.5}$$

The efficiency η is the ratio of the maximum power density against the incident light power density (P_S),

$$\eta = \frac{J_m V_m}{P_S} = \frac{J_{SC} V_{OC} FF}{P_S} \tag{1.6}$$

The generalized Shockley model

When measured in dark, most solar cells behave like a diode, indicating a much larger current under forward bias than under reverse bias. The reverse current is usually called the dark current in contrast to the photo current which flows through the solar cell under light. According to the Shockley diode equation, the dark current density of an ideal diode varies as

$$J_{dark}(V) = J_0(e^{\frac{qV}{k_B T}} - 1) \tag{1.7}$$

where J_0 is the reverse saturation current density.

Under illumination, the J-V curve of a solar cell can be approximated as the sum of J_{SC} and the dark current density (known as the superposition approximation[97][98][99]).

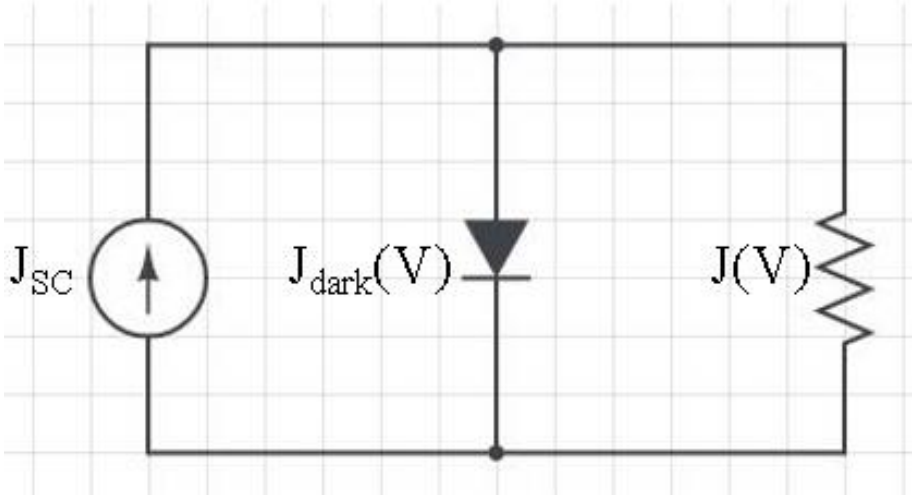

Figure 1.6: The equivalent circuit of an ideal solar cell.

Setting the photocurrent flow direction as positive, the net current density in the cell is

$$J(V) = J_{SC} - J_{dark}(V) \tag{1.8}$$

Inserting Eq. 1.7 into Eq. 1.8, we get

$$J(V) = J_{SC} - J_0(e^{\frac{qV}{k_BT}} - 1) \tag{1.9}$$

Eq. 1.9 describes the relation between the photocurrent J(V) and voltage V. The equation is electrically equivalent to a circuit where a current generator is in parallel with a diode and a resistance. This mathematical and electrical description of a solar cell is the Shockley model of solar cells.

Based on this model, the open circuit condition is when the J(V) equals zero, and J_{dark} and J_{SC} exactly cancel out. And the bias V equals V_{OC} at this point. From Eq. 1.9,

$$V_{OC} = \frac{k_BT}{q} ln(\frac{J_{SC}}{J_0} + 1) \tag{1.10}$$

Eq. 1.10 indicates that V_{OC} increases logarithmically versus J_{SC} with a slop of k_BT/q.

Considering a real solar cell also has resistances from the constituent material and leakage currents, the equivalent circuit could be further modified adding two parasitic resistances in series (R_s) and in parallel (R_{sh}) respectively (Figure 1.7).

When the parasitic resistances are included, Eq. 1.9 becomes:

$$J(V) = J_{SC} - J_0(e^{\frac{q(V+JAR_s}{k_BT}} - 1) - \frac{V + JAR_s}{R_{sh}} \tag{1.11}$$

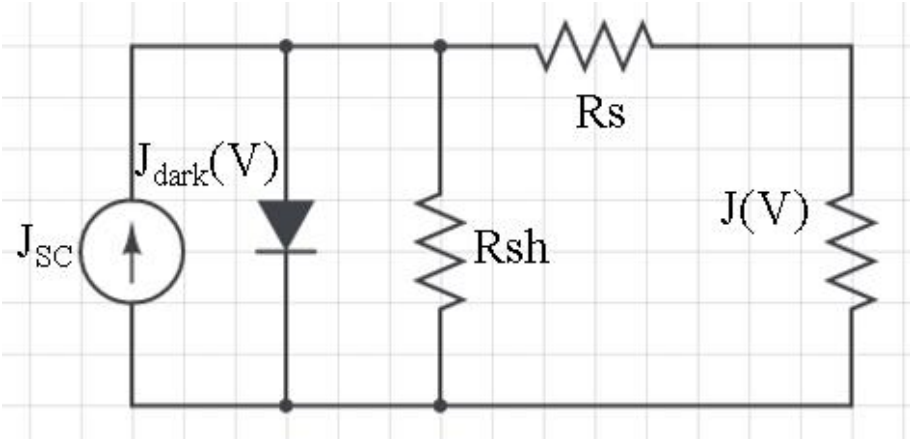

Figure 1.7: The equivalent circuit including series and shunt resistances.

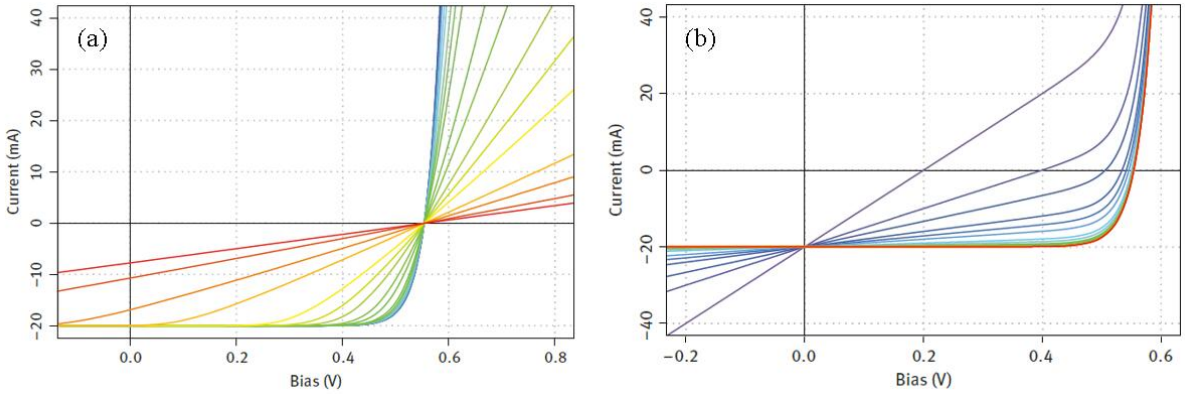

Figure 1.8: Impact of (a) series resistance (R_s) and (b) shunt resistance (R_{sh}) on the shape of the J-V curve. R_s and R_{sh} increase from blue to red curves. Adapted from [100].

The influence of R_s and R_{sh} on the shape of J-V curve could be simulated based on Eq. 1.11 (Figure 1.8)

The simulation results indicate that a higher R_s decreases the J_{SC} without impacting the V_{OC}, while a lower R_{sh} deceases the V_{OC} without influencing the J_{SC}.

The Shockley model uses equivalent circuit elements to represent a solar cell. And a ideal solar cell is represented by a current generator in parallel with a diode. This model is derived in a P-N junction silicon solar cell but not obviously applicable in other types of solar cells. And it is regarded to be largely based on an empirical hypothesis in which the real physical processes are not taken into strict consideration. For example, the origin of J_0, as well as the exponential relationship between J_{dark} and V, is not proofed in all types of solar cells. In practical application, due to the complexity of real systems, this model often needs to improvise, for example, the introduction of ideality factor or transmission line element. However, this model vividly reveals the working principle of a solar cell in an electric circuit point of view.

Absorption and emission analyze based on the detailed balance theory

In this section, the working principle of a solar cell is reviewed in the framework of absorption and thermal radiation. The detailed balance principle means that when the cell is in equilibrium, the photo absorption must match the emission, so that the concentration of charge carriers in the cell remain constant.

Considering the ambient environment as a black body, its radiation is treated as the black body radiation, at temperature T_a, the spectral photon flux density per unit solid angle of the ambiance is

$$\beta_a(E, T_a) = \frac{2}{h^3 c^2} \frac{E^2}{e^{\frac{E}{k_B T_a}} - 1} \tag{1.12}$$

where h is the Planck constant, c is the speed of light in vacuum, E is the photo energy. After integrating over the solid angle, Eq. 1.12 becomes

$$b_a(E, T_a) = \frac{2F_a}{h^3 c^2} \frac{E^2}{e^{\frac{E}{k_B T_a}} - 1} \tag{1.13}$$

where $b_a(E, T_a)$ is the normal spectral photon flux density of the ambiance and F_a is the geometrical factor of the ambiance.

Similarly, considering the solar cell as a black body of ambient temperature T_a, its normal spectral photon flux density of spontaneous emission is

$$b_e(E, T_a) = \frac{2n_s^2 F_e}{h^3 c^2} \frac{E^2}{e^{\frac{E}{k_B T_a}} - 1} \tag{1.14}$$

where n_s is the refractive index of the solar cell. And further calculation indicates that $n_s^2 F_e = F_a$, so $b_e(E, T_a) = b_a(E, T_a)$

According to Würfel's generalization of Kirchhoff's law[101], when the solar cell is under illumination, its spontaneous emission is modified by a chemical potential μ

$$b_e(E, \mu, T_a) = \frac{2n_s^2 F_e}{h^3 c^2} \frac{E^2}{e^{\frac{E-\mu}{k_B T_a}} - 1} \tag{1.15}$$

In an ideal solar cell with lossless carrier transport, μ can be assumed constant and equal to qV where V is the applied bias.

Now we consider an ideal solar cell where no carriers are lost through non-radiative recombination. The only loss process is the radiative relaxation of electrons through spontaneous emission described above. The equivalent absorption current density from ambiance is

$$J_a(T_a) = q \int_0^\infty QE_a(E) b_a(E, T_a) dE \tag{1.16}$$

Where $QE_a(E)$ is the quantum efficiency of charge generation which equals the external quantum efficiency (EQE) of the solar cell. And the equivalent emission current density from ambiance is

$$J_e(T_a) = q \int_0^\infty QE_e(E) b_e(E, T_a) dE \tag{1.17}$$

Based on the detailed balance principle, the carrier generation and recombination current should cancel out each other. And we get that

$$QE_a(E) = QE_e(E) = EQE(E) \tag{1.18}$$

It has also be shown that Eq. 1.18 holds true when the solar cell is not under equilibrium conditioning it is an ideal solar cell system.

Accordingly, for the solar cell under illumination, the normal spectral photon flux density from the sun is

$$b_s(E, T_s) = \frac{2F_s}{h^3 c^2} \frac{E^2}{e^{\frac{E}{k_B T_s}} - 1} \tag{1.19}$$

where F_s is the geometrical factor from sun to earth, T_s is the surface temperature of the sun. And the photocurrent at short circuit condition (J_{SC}) is

$$J_{SC} = q \int_0^\infty EQE(E) b_s(E, T_s) dE \tag{1.20}$$

The dark current J_{dark} is

$$J_{dark}(V) = q\int_0^\infty EQE(E)\big(b_e(E,qV,T_a) - b_e(E,T_a)\big)dE \tag{1.21}$$

Assuming the dark current and photocurrent can be superpositioned,

$$\begin{aligned} J(V) &= J_{SC} - J_{dark}(V) \\ &= q\int_0^\infty EQE(E)\Big(b_s(E,T_s) - \big(b_e(E,qV,T_a) - b_e(E,T_a)\big)\Big)dE \end{aligned} \tag{1.22}$$

As $k_BTa \approx 0.0259$ eV, the exponential term in the denominator of Eq. 1.15 is very large, Eq. 1.15 can be simplified to

$$\begin{aligned} b_e(E,qV,T_a) &= \frac{2F_a}{h^3c^2}\frac{E^2}{e^{\frac{E-qV}{k_BT_a}}} \\ &= \frac{2F_a}{h^3c^2}E^2e^{\frac{qV-E}{k_BT_a}} \end{aligned} \tag{1.23}$$

Inserting Eq. 1.23 into Eq. 1.22, J(V) turns into

$$J(V) = q\int_0^\infty EQE(E)\big(b_s(E,T_s) - b_e(E,T_a)(e^{\frac{qV}{k_BT_a}} - 1)\big)dE \tag{1.24}$$

The absorption and emission analysis leads to Eq. 1.24, which resembles Eq. 1.9 of the Shockley model. And the origin of J_{SC} (Eq. 1.20) and J_0 is revealed,

$$J_0 = q\int_0^\infty EQE(E)b_e(E,T_a)dE \tag{1.25}$$

Moreover, this model based on the detailed balance principle presents one fundamental limitations on the performance of a solar cell. Intuitively, the inevitable radiative loss leads to the dark current and limits the overall performance of the solar cell. And this radiative loss channel is an intrinsic property of the material which can not be eliminated. Assuming the EQE equals unity above the band gap (E_g) and zero below the E_g, Eq. 1.24 can be rewrited as

$$J(V) = q\int_{E_g}^\infty \big(b_s(E,T_s) - b_e(E,T_a)(e^{\frac{qV}{k_BT_a}} - 1)\big)dE \tag{1.26}$$

Setting T_s and T_a to be constants, the J-V curves of solar cells with different band gap materials can be simulated based on Eq. 1.26. And the theoretical efficiency versus the band gap values can be extracted(Figure 1.9)

The extracted efficiency is the radiative limit of the efficiency of a solar cell (known as Shockley-Queisser limit). It has a maximum value of about 33% at an E_g vaule of around 1.4 eV.

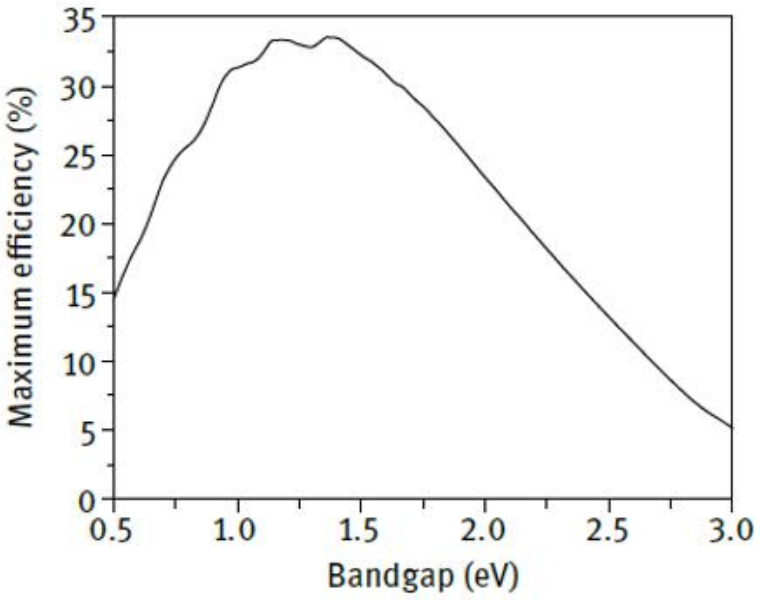

Figure 1.9: The maximum light to electric power conversion efficiency (Shockley-Queisser limit) versus the band gap of the absorber material. Adapted from [100].

Accordingly, the open circuit voltage is the bias where the photocurrent and dark current cancel out,

$$V_{OC} = \frac{k_B T_a}{q} ln\Big(\frac{\int_0^\infty EQE(E) b_s(E, T_s) dE}{\int_0^\infty EQE(E) b_e(E, T_a) dE} + 1\Big) \tag{1.27}$$

In practice, after measuring the EQE of a solar cell, its radiative V_{OC} limit can be calculated[102][103].

This model assumes that the only carrier dissipation pathway is through the radiative recombination, meaning the dark current section in Eq. 1.24 gives rise to electroluminescence (EL) behavior.

For real solar cells, the contribution of non-radiative recombination must also be considered. The EL efficiency (EQE_{EL}) could be used to quantify how much a real solar cell derives from its ideal form,

$$EQE_{EL}(V) = \frac{J_{dark}(V)}{J_{inj}(V)} \tag{1.28}$$

When biasing at V_{OC}, the injection current approximately equals the short circuit

current, $J_{inj}(V_{OC}) = J_{SC}$, Eq. 1.28 becomes

$$EQE_{EL}(V_{OC}) = \frac{q\int_0^\infty EQE(E)b_e(E,T_a)(e^{\frac{qV_{OC}}{k_BT_a}}-1)dE}{q\int_0^\infty EQE(E)b_s(E,T_s)dE} \tag{1.29}$$

$$\frac{k_BT_a}{q}lnEQE_{EL}(V_{OC}) \approx V_{OC} - \frac{k_BT_a}{q}ln\frac{\int_0^\infty EQE(E)b_s(E,T_s)dE}{\int_0^\infty EQE(E)b_e(E,T_a)dE} \tag{1.30}$$

The last section of Eq. 1.30 approximately equals the radiative V_{OC} limit $V^{rad}{}_{OC}$ (Eq. 1.27), so we get

$$V_{OC} = V_{OC}^{rad} + \frac{k_BT_a}{q}lnEQE_{EL}(V_{OC}) \tag{1.31}$$

As $EQE_{EL}(V_{OC})$ is always smaller than unity, $\frac{k_BT_a}{q}lnEQE_{EL}(V_{OC})$ is a negative term guaranteeing that the actural V_{OC} is smaller than its radiative limt $V^{rad}{}_{OC}$.

To shortly summerize, this model is based on the absorption and emission behavior analysis of an ideal solar cell by assuming the absence of non-radiative recombination. According to the detailed balance principle (kirchhoff's law as well as several generalization arguments), the J-V relationship equation is derived which agrees with the Shockley model. Moreover, it links the photovoltaic behavior of a solar cell with its electroluminescence properties (known as the reciprocity relation[104]). According to this model, a good solar cell is also a good light-emitting diode (LED) as the noncollected charge carriers must recombine radiatively and emit photons. It is worth mentioning that a good LED may not make a good solar cell. The thermal radiation of a solar cell leads finally to a limit of its theoretical efficiency.

Another interesting feature is this model enables describing a practical solar cell with non-recombination carrier losses applying Eq. 1.31. Though substituting a complicated set of various non-radiative recombination pathways with the sole term $EQE_{EL}(V)$ is sometimes oversimplified, it expands largely the practical applicable scope of this model.

However, as clearly seen, this model is mainly about the material property other than the device architectures, as no device structure details seem relevant in this model. In fact, the influences of actual physical layers are regarded to be on non-radiative recombination processes which are basically disregarded in this model. In practice, a properly functional solar cell requires a carefully designed structure, indicating this model misses some pieces of the full picture.

Charge carrier generation, transport and recombination

The Shockley model is derived by combining the Shockley diode equation and the superposition principle. The diode equation is well established through a detailed mathematical description of the voltage-current characteristics of a silicon P-N junction. However, the bottom-up deconstruction of solar cells through comprehensive mathematical expressions

of charge carrier generation, transport and recombination is neither simple nor universal. In fact, though the mathematical expressions of the voltage-current characteristics of a P-N junction are full-fledged, the Shockley model of the P-N junction based solar cell still just explores the convenience of the diode equation and disregards the detailed processes occurring in the solar cell. Nevertheless, it is still very helpful to understand the working principle of the solar cell from the perspective of the detailed processes.

A general mathematical expression of the internal process of a solar cell is the one-dimensional electron and hole continuity equation,

$$\frac{\partial n}{\partial t} = \frac{1}{q}\frac{\partial J_n}{\partial x} + G(x) - R(X) \tag{1.32}$$

$$\frac{\partial p}{\partial t} = -\frac{1}{q}\frac{\partial J_p}{\partial x} + G(x) - R(X) \tag{1.33}$$

where n and p are the electron and hole concentrations, t is time, G(x) and R(x) denote the generation and recombination flux density, and J_n and J_p are the electron and hole currents expressed as follows,

$$J_n = q\mu_n nE + qD_n\frac{\partial n}{\partial x} \tag{1.34}$$

$$J_p = q\mu_p pE - qD_p\frac{\partial p}{\partial x} \tag{1.35}$$

where μ_n and μ_p are the mobility of electrons and holes of the corresponding material, D_n and D_p are the diffusion coefficients of electrons and holes, E is the electric field.

In a steady state, the electron and hole density will stay constant, meaning the time derivative of the electron and hole concentration distribution function n and p equals zero. Inserting Eq. 1.34, 1.35 into Eq. 1.32, 1.33,

$$\mu_n(\frac{\partial n}{\partial x}E + n\frac{\partial E}{\partial x}) + D_n\frac{\partial^2 n}{\partial x^2} + G(x) - R(x) = 0 \tag{1.36}$$

$$-\mu_p(\frac{\partial p}{\partial x}E + p\frac{\partial E}{\partial x}) + D_p\frac{\partial^2 p}{\partial x^2} + G(x) - R(x) = 0 \tag{1.37}$$

To solve the equations, the electric field needs to be addressed by solving the Poisson equation, and the charge generation profile G(x) by solving the Maxwell equations. In addition, the recombination profile R(X) is also a carrier density related function which relates to the properties of the material and transporting layers.

Finally, boundary conditions which express the actual status of the solar cell need to be given to determine the specific solution.

After determining the electron and hole concentration distribution function n and p, the current function $J = J_n + J_p$ can be derived through Eq. 1.34, 1.35.

As discussed, the mathematical description of a solar cell is specific (as it depends on further modelling of the electric field, generation and recombination profiles), and the

solution is difficult to solve. However, this model also provides intuitive information which will be addressed in a lax manner to gain more insight into the working process of a solar cell.

Integrating Eq. 1.36, 1.37 over the solar cell length (L_{cell}),

$$\begin{aligned} J_n + q\int_0^{L_{cell}} G(x) - q\int_0^{L_{cell}} R(x) = 0 \\ -J_p + q\int_0^{L_{cell}} G(x) - q\int_0^{L_{cell}} R(x) = 0 \end{aligned} \tag{1.38}$$

The equation set 1.38 presents a plain rule of a solar cell: the light generated charge carriers either recombine or are transported to the external circuit. Compared with the Shockley and thermal radiation model, it is clear that the J_{dark} is representative of the recombination current.

It is certainly beneficial for the performance of a solar cell to have a higher output current and a lower recombination current. Assuming that the generation current is constant, the output and recombination of charge carriers are processes of competition. In this zero-sum game, one gets higher, the other will be lower.

The output and recombination currents are both functions of charge carrier density. However, the dependence on the carrier density is disregarded in this general discussion. And the scaling factors (or rate coefficients) of each process are addressed which make an influence on the relative amplitudes of output and recombination currents.

Based on Eq. 1.34, 1.35, the carrier mobility μ and electric field E modify the amplitudes of output current (The Einstein relation sees $D = \mu k_B T/q$). Given all other conditions are the same, a higher carrier mobility and built-in field will improve the performance of a solar cell[105].

On the other hand, the recombination profile depends on several different kinds of recombination processes. Figure 1.10 presents the existing recombination processes in a p-i-n junction solar cell (ETM is short for electron transporting material and HTM for hole transporting material)

The bimolecular recombination is the process where a light-generated electron in the conduction band recombines with a hole in the valence band and emits a photon, namely the radiative recombination included in the detailed balance principle model in the former section. The recombination rate coefficient is an intrinsic property of the material, and can be derived based on the detailed balance principle,

$$\int \alpha(E) b_a(E, T_a) dE = k_2 n_0 p_0 = k_2 n_i^2 \tag{1.39}$$

where α(E) is the absorption coefficient, b_a(E,T_a) is the normal spectral photon flux density of the ambiance, k_2 is the rate constant of the radiative transition. n_0 and p_0 are the equilibrium electron and hole concentration whose product equals the square of

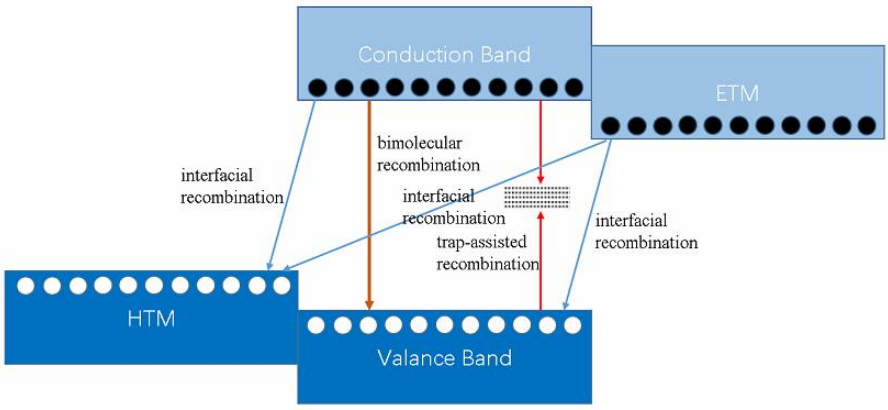

Figure 1.10: The existing recombination processes in a p-i-n structure solar cell.

the intrinsic charge carrier density (n_i). Therefore, the contribution of the bimolecular recombination is the fundamental limit factor of the performance of a solar cell as it is the nature of the absorber itself[29][106].

For the non-radiative trap-assisted recombination, the rate constant depends on the nature of the trap-states. Usually traps in middle band gap act as most effective recombination centers, possessing a higher recombination rate coefficient[107]. For a more generalized rate constant considered here, the density of traps also scales the recombination rate linearly. Note that the traps exist not only in the bulk of the absorber, but also at the interfaces.

The interfacial recombination firstly relies on the interfacial area. Moreover, the intrinsic property of the interfaces is a dominating factor of the recombination rate[108]. Generally, the band energy alignment is an important indicator of the interfacial recombination rate constant. The interfacial energy alignment is also related to the amplitude of the electric field in the absorber which influences the charge transport processes. Moreover, the direct contact of the ETM and HTM leads to a shunt path where severe interfacial recombination could occur.

In this section, a comprehensive model based on the charge generation, transport and recombination processes is introduced. A mathematical expression of this model is usually very complicated, and some descriptive arguments are presented to cover the missing pieces in the Shockley and detailed balance model. In the section, the principle of several criteria to evaluate solar cell architectures in practice is addressed.

1.2.2 The solar cell architecture of perovskite solar cells

PSCs are basically constructed as a perovskite absorber layer sandwiched between electron and hole selective layers. Various materials including not only perovskite but also ETM and HTM have been used to construct efficient cells. But the most extensively studied configuration is shown in Figure 1.11. As shown, the difference of the so called regular

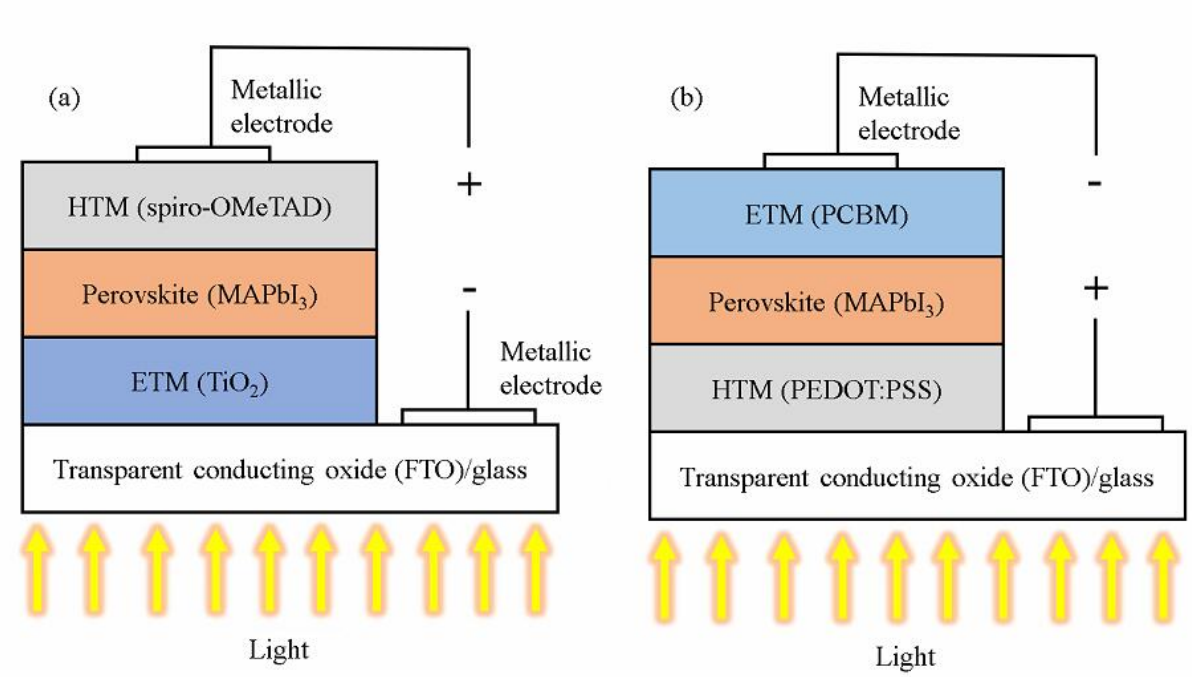

Figure 1.11: Typical architectures of PSC in (a) regular and (b) inverted configuration.

(n-i-p) and inverted (p-i-n) structure is the flow direction of the photocurrent. In the regular architecture, the photocurrent flows from the metallic electrode to the transparent conducting oxide electrode (which is often covered with an evaporated metal layer for better electrical connections). In the inverted architecture, the current direction is the other way around. Note that this definition of 'regular/inverted' is inherited from the dye sensitized solar cell which is not always valid in other types of solar cells. In other words, in the regular structure, the perovskite absorber material is deposited on ETM (n-i-p) while it is deposited on HTM (p-i-n) in the inverted structure.

In the regular architecture (Figure 1.11(a)), a planar or planar/mesoporous TiO_2 layer is deposited on fluorine doped tin oxide (FTO)/glass through spin-coating, sputtering, atomic layer deposition (ALD), or spray coating[109][110][111][112]. Other kinds of ETM adopted in this architecture include SnO_2[113][114][115], ZnO[116][117][118], Zn_2SnO_4[119][120], $BaSnO_3$[121][122], etc[123][124][125]. The ideal ETM layer for regular PSC configuration should meet the following requirements: well-matched energy levels with the perovskite and the bottom cathode for efficient electron selection and extraction, a large electron mobility to avoid the space-charge-limited effect, a high transparency to allow light passing through to be harvested in the perovskite layer, and an enough chemical and physical stability with the perovskite and necessary solvents. Afterwards, $MAPbI_3$ is deposited on top of the ETM through preparation methods as introduced above. Subsequently, the 2,2',7,7'-Tetrakis[N,N-di(4-methoxyphenyl)amino]-9,9'-spirobifluorene (spiro-OMeTAD) is spin-coated on top of the perovskite[126][127][128]. Other HTMs which can be employed in this architecture include poly(3-hexylthiophene) (P3HT)[129][130][131], poly(triarylamine) (PTAA)[132][79][133], copper(I) thiocyanate (CuSCN)[134][135][136] and so on[137][138][139]. The HTM layer of the n-i-p strucure should meet criteria such as: a good band alignment with perovskite, a high hole mobility, compatible processing

methods with other layers of the configuration, a good chemical stability against perovskite and so on. In the end, a thermally evaporated metallic electrode (usually Ag or Au) is deposited to sever as the back contact.

In the inverted architecture (Figure 1.11(b)), the most commonly used ETM and HTM are [6,6]-phenyl-C61-butyric acid methyl ester (PCBM)[140][141][142] and poly(3,4-ethylenedioxythiophene) polystyrene sulfonate (PEDOT:PSS)[143][144] respectively. Reversing the direction of HTM and ETM from the regular to inverted architecture needs to overcome several issues. Firstly, the underlying layer beneath perovskite needs to be transparent, therefore, coloured P3HT layer is not very suitable in the p-i-n configuration. Secondly, a upward compatibility is required among the subsequently processed layers. For example, the $MAPbI_3$ degrades under temperatures higher than 200 °C, so metal oxide ETM which needs high temperature sintering is unfit as a upper electron transporting layer in the p-i-n architecture. Besides processing temperatures, solubility is another matter of importance. Generally, the used ETMs in p-i-n structure include mainly the fullerene derivatives (PCBM, C_{60}, C_{70})[145][146][147], low temperature-processed metal oxide (SnO_2, ZnO)[148][149][150] and so on[151][152]. The HTMs include PEDOT:PSS[143][144], NiO_x[153][154], CuO_x[155], CoO_x[156], CuSCN[157], CuI[158], etc[159][160].

1.2.3 Sketchy device physics of perovskite solar cells

Charge carrier transport in PSCs

When PSC was firstly studied, a mesoporous metal oxide scaffold was usually introduced where the perovskite filled in the pores (Figure 1.12)[161][162][163][164]. The main consideration is that such a structure could shorten the length of charge carrier transport. If the mobility of the charge carrier is low, by reducing the carrier transport distance, the spatial derivative of the carrier density and the electric field could be improved to increase the drift and diffusion current (Eq. 1.34, 1.35). Shortly after, however, perovskite material was reported to have a quite long diffusion length[165][166][37]. As discussed above, a long diffusion length indicates relatively a higher mobility (which is beneficial increasing the output current) or a slower recombination process (which is advantageous reducing the recombination current) (Eq. 1.2), and overall the output current could have the upper hand over the recombination losses. As such, relevant studies showed that charge carriers transporting a long distance in perovskite can still construct highly efficient solar cells. And planar perovskite devices became a popular topic in the soar cell research community[78][167][168].

It is still quite unsure if the planar or mesoporous architectures will deliver the best performance of PSCs[169]. The mesoporous structure is theoretically favorable but it may also introduce side effects which will cancel the benefits of this configuration[170]. For example, a mesoporous architecture has a much larger interface area than a planar structure which can lead to stronger interfacial recombination. Also the perovskite filled inside the pores may be defect richer due to the confinement of the pore size and larger

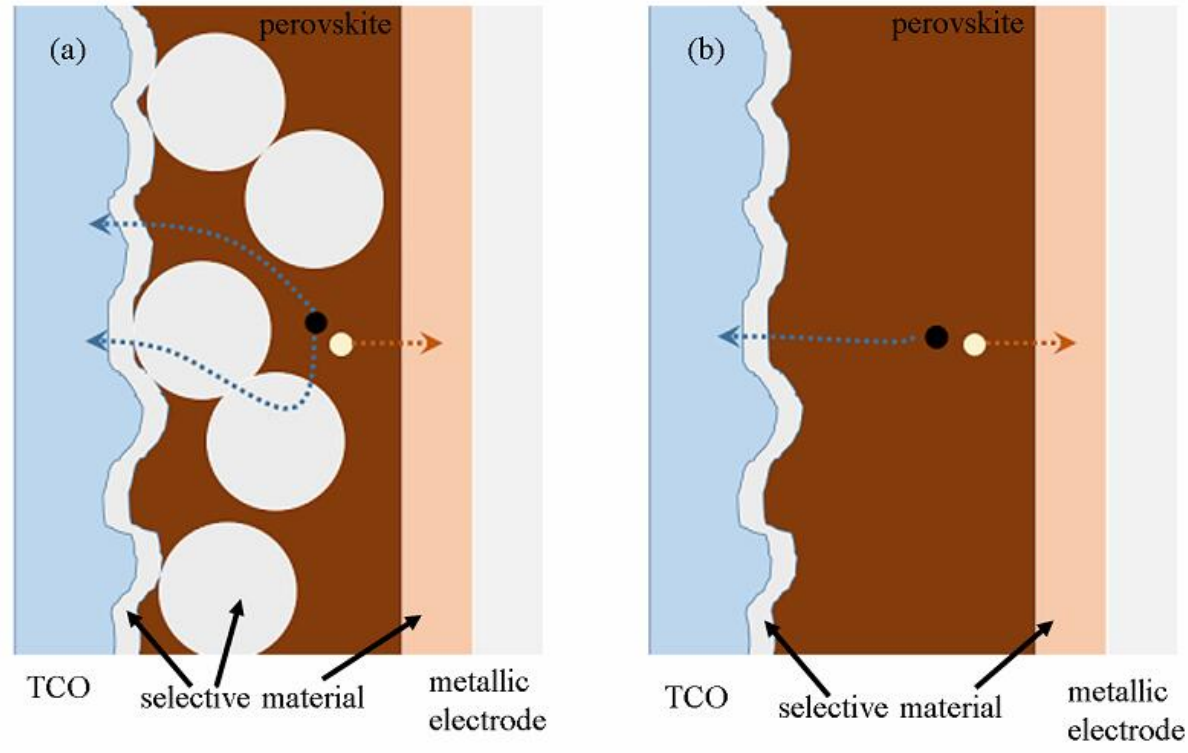

Figure 1.12: The solar cell configuration of (a) mesoporous and (b) planar structure and corresponding carrier transport pathways.

crystal surface area.

Another interesting question is whether drift or diffusion current is the dominant contribution of the output current. With the selective contacts, both parts contribute to the total current. However, ascertaining this question will help design more efficient solar devices[171]. The drift current depends on the built-in field which only exists in the depletion region whose width relies on the doping level of the semiconductor. If the drift contribution is dominant for an efficient PSC, then an intrinsic perovskite layer with larger band offsets between the selective layers is optimal for the PSCs. But if the diffusion current is already sufficient, then an efficient PSC could employ selective layers with lower energy offsets.

In several studies, PSCs with non selective contacts could function reasonably well with a built-in field induced by biasing or self-assembled dipole monolayers[172][173]. These results imply the driving force induced by the built-in field could put a PSC into operating. A cross-sectional electrical profiling study presented a depletion width of 300 nm which is consistent with the perovskite film thickness normally reported with high device efficiencies, suggesting that a properly functional PSC requires the existence of built-in fields[171]. However, in some Br-based PSC studies, the V_{OC} exceeds the band energy offsets of the ETM and HTM, which implies the contribution of diffusion current may be already quite sufficient[174][175][176].

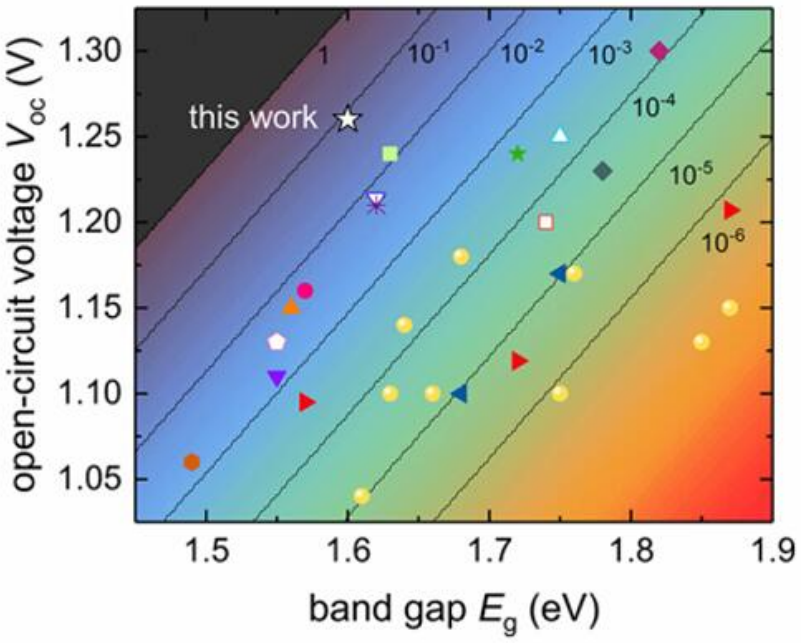

Figure 1.13: The open circuit voltage of PSC achieved in literature versus the absorber band gap. The black lines indicate the corresponding EL efficiency calculated based on Eq. 1.31. Adapted from [178]

Charge carrier recombination in PSCs

As the carrier transport and recombination are the competing processes, their 'rate coefficients' only have practical implications when comparing one to another. In this section, only the recombination processes are addressed assuming the transport profiles remain unchanged. In this context, it is reasonable to claim that V_{OC} is the adequate indicator of the severity of the recombination losses. Based on Eq. 1.31, the V_{OC} of a solar cell is given as the sum of the $V^{rad}{}_{OC}$ and a correction term related to the non-radiative recombination.

In PSCs, besides the radiative recombination, the trap-assisted recombination and interfacial recombination are the existing non-radiative recombination pathways[177]. Recent studies have significantly suppressed these non-radiative recombination processes and reduced the open circuit voltage loss to be less than 100 mV. In Figure 1.13, based on the V_{OC} of the PSC and the band gap of absorber material, the corresponding EL efficiency at V_{OC} is calculated. It presents for the state of art PSC, it has an EL efficiency close to 10% which almost keeps in step of a perovskite LED[178][179][180][181].

As perovskite has been reported to be defect tolerant, interfacial recombination seems to play the key role in non-radiative channels. For example, replacing PEDOT:PSS with PTAA layer as the hole selective layer in a p-i-n configuration cell has been reported to improve the V_{OC} by hundreds of mV[182][183]. However, it is tricky to distinguish between

suppressing interfacial recombination with reducing surface trap-assisted recombination as the modification of perovskite surfaces may lead to both effects.

Hysteresis behavior of the PSC

The hysteresis behavior of the PSC is the nonconformity of the J-V curves which strongly depend on the voltage scan rate, direction (from positive to negative bias, or the other way around), range (start and end bias) and preconditioning situation (the cell resting time, bias, illumination condition)(Figure 1.14a)[184]. This phenomenon has been firstly discovered in a n-i-p architecture cell and reported to be almost absent in PSCs of p-i-n structure[185][144][186]. The origin of such an unstable current output is obviously due to certain slow process which occurrs inside the cell. Several hypotheses have been proposed, for example, it has been suggested that the movement of ions or polarization of perovskite crystal domains contributes to the formation of the built-in field which slows down its response to the changing bias[187][188][187][189]. Another argument thinks a slow process of trap states filling/emptying is responsible for this phenomenon[190][191].

Different theoretical simulations and experimental evidences support the interpretation of the ion migration[66][192][193][194][195]. This interpretation suggests that charged ions migrate due to the existence of the built-in field, which leads to the aggregation of ions at the interface between the perovskite and selective layer. These aggregated ions create a reverse electric field which could partly or fully counteract the built-in field in the bulk of perovskite layers, creating a bulk field-free region and sharp potential drops at the interface in the dark under equilibrium (Figure 1.14b)[64]. Under changing bias, the reverse electric field is modulated by the slow movement of ions which leads to a variational electric field across the perovskite layer and then changing output current.

The hysteresis phenomenon actually reflects the 'instability' of the solar cell whose charge transport and recombination profile change during operation. And it is detrimental on evaluating the real performance of a solar cell. It has been emphasized to present the J-V curves of PSCs with all measurement parameters to facilitate evaluation and comparison. And a tracking of the solar cell behavior over longer time is regarded necessary providing a accurate evaluation of the cell[197][198]. The hysteresis behavior also complicates a lot of well-established characterization techniques. For example the impedance measurement has been reported to be influenced by the ionic conduction property of the perovskite at low frequencies[199][200][201].

The state of art PSCs seem to possess less hysteresis features. It is partially due to the chemical engineering of the perovskite material. It has been reported that enhancing the structural stability of perovskite through doping with additional cation or anion could suppress the hysteresis phenomenon, probably due to the suppression of ion movements[202][203]. Interface engineering could also eliminate the solar cell's hysteresis behavior, which could be either due to a modified ion aggregation profile or improved crystallinity of the perovskite at the interfaces[204][205].

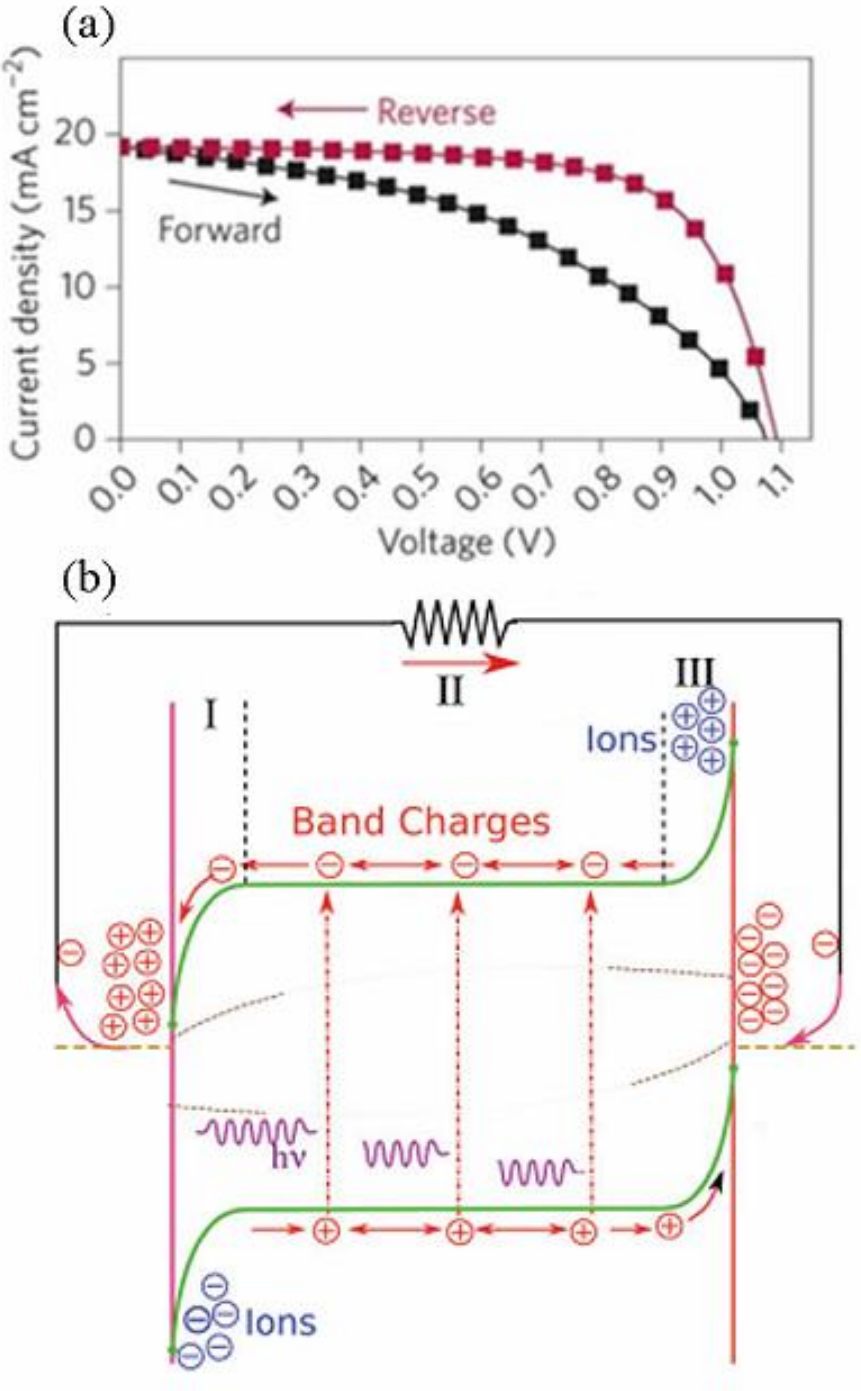

Figure 1.14: (a) a typical J-V curves of PSC with hysteresis feature; (b) the band diagram illustration of the ion aggregation interpretation of hysteresis phenomenon. Adapted from [196] and [64].

Chapter 2

The experimental details and characterization methods

In this chapter, the fabrication procedure of the PSC is described in detail. The characterization processes used in thisstudy are also clearly listed. Sketchy working principles of certain characterization techniques which are relatively mysterious or intensively utilized are summarized for reference.

2.1 The fabrication procedure of the PSCs

2.1.1 Substrates cleaning

ITO substrates (10-15 Ω $\square^{-1}$, 1.1 mm thick, purchased from Lumtech, cut to 14×14 mm^2) were cleaned in ultrasonic bath with commercial detergent, acetone and isopropanol for at least 5 min subsequently. Afterwards, a 7 min O_2 plasma cleaning was carried out in a Diener Femto plasma cleaner at 80 W with a pressure of around 1 mbar.

2.1.2 Deposition of PEDOT:PSS films

The PEDOT:PSS solution (Clevios^{TM}P VP AI 4083, purchased from Heraeus, stored in fridge) was used without further treatment. A syringe was used to extract the PEDOT:PSS solution from a refrigerated pre-distributed small-dose vial. Afterwards, a 0.2 μm PVDF fitler (ROTH) was assembled on the syringe. Before deposition, the spin-coater (WS-650, Laurell Technologies) was rewrapped with clean tissue to remove any residual solvent. The PEDOT:PSS solution was dropped from the syringe through the filter carefully on the substrate and further distributed manually with the syringe tip. Afterwards, a 60 s spin-coating process at 5000 rpm with an acceleration rate of 1000

rpm/s was performed. The substrate was then annealed at 180 °C on a hotplate (SD160, Stuart Equipment) for 5 min. The substrate was then stored in a N_2-filled glovebox for future usage.

2.1.3 The preparation of $MAPbI_3$ precursor solution

In a typical procedure to prepare around 3 mL precursor solution, the following operations were performed. In a N_2 filled golvebox (Sylatech, water content $<$ 5 ppm), 635.9 mg MAI (98%, dyenamo) was weighed in a glass vial. Then 2184 μL N,N-dimethylformamide (DMF, 99.8%, Sigma Aldrich) and 109.2 μL dimethyl sulfoxide (DMSO, 99.9%, Sigma Aldrich) were added in the vial. Afterwards, 461.0 mg PbI_2 (99%, Sigma Aldrich) and 278.1 mg $PbCl_2$ (98%, Sigma Aldrich) were weighed on weighing paper and put inside the vial. The solution was stirred at room temperature with a stir bar for at least 1 h. A clear and transparent yellow solution was then obtained.

2.1.4 The deposition of $MAPbI_3$ layer

In a typical procedure, the prepared PEDOT:PSS substrates and precursor solution were transferred inside a N_2-filled glovebox (GS GLOVEBOX Systemtechnik, water content $<$ 5 ppm) where a spin-coater (LabSpin, SÜSS MICROTEC) was installed. After dropping 40 μL precursor solution on the substrate, a 20 s spin-coating process at 3000 rpm with an acceleration rate of 1000 rpm/s was performed. Afterwards, the still colorless substrate was quickly transferred on a 60 °C hotplate (SD160, Stuart Equipment) and covered with a home-made vacuum chamber. This chamber was connected to a pump (PC 3004 VARIO, VACUUBRAND) with a monitor controller (CVC 3000, VACUUBRAND) where the vacuum pressure could be tracked. As soon as the chamber was in position, the pump was switched on to quickly reduce the pressure to around 2 mbar. The vacuum assisted annealing process lasted for 30 min. Afterwards the pump was switched off and the chamber was vented. Then the hotplate temperature was reset to 90 °C to anneal the sample for another 30 min. A shining dark film was obtained indicating the formation of $MAPbI_3$ film. Note that the above process is a typical procedure, while certain modifications could be made for specific purposes and are described when introduced.

2.1.5 The Evaporation of C_{60}, LiF and Ag layers

The $MAPbI_3$ substrates were transferred inside a thermal evaporator (UNIVEX 350 G, Leybold) in the glovebox. After pumping for 20 min, the pressure reduced to below 5 $\times$ 10^{-6} mbar. Then 20 nm C_{60} (99.99%, CreaPhys) was evaporated at around 410 °C at a rate of around 0.3 Å/s. Afterwards, 1 nm LiF (99.995%, Sigma Aldrich) was evaporated on top at a rate of around 0.05 Å/s. Then the substrates were taken out of the evaporator to anneal at 70 °C for 10 min. After scratching, 60 nm Ag (99.999%, Testbourne) was further evaporated at 1 Å/s to complete the fabrication process.

2.2 The characterization methods of films

2.2.1 Scanning electron microscopy (SEM)

The morphology of the perovskite film was characterized using a Zeiss CrossBeam 1540XB FESEM (equipped with an in-lens detector). An accelerating voltage of 5-10 kV was used for imaging. To avoid the degradation of perovskites under electron beam, a faster scanning speed was chosen to photograph. Samples were fixed on steel stubs using silver paste without any further treatment to enhance the conductivity. For cross-section images, the sample was cut with a scissor which retained most of the morphology information of the cutting shoulder.

2.2.2 X-ray diffraction (XRD)

The crystallography of the films was investigated using Bruker D8 Discover (equipped with Lynxeye XE detector, and Cu Kα is 0.15418 nm) with the help of Ms. Brigitte Bössenecker and Elana Harbalik in the Partikelanalysezentrum of Uni-Konstanz. The measurement was performed from 5° to 60°. The samples measured in air or in a N_2 filled thin plastic holder did not show any difference.

2.2.3 Ultraviolet–visible spectroscopy (UV-Vis)

The absorbance spectrum was measured by Cary5000 (Agilent technologies) from 400-850 nm in a 150 mm integrating sphere. Samples were placed in the sphere center using a center mount sample holder while the light beam illuminated on the sample under a small angle (5°) to ensure no light escaped from the sphere. Besides, all measurements were double baseline (100% and 0% transmission) corrected to determine the absorbance of a sample. The data in transmission form is corrected as

$$\frac{T - 0\%TBaseline}{100\%Tbaseline - 0\%TBaseline}$$

where T is the raw data value while 100%Tbaseline and 0%TBaseline are the baseline values of 100% and 0% transmission respectively.

2.2.4 X-ray photoelectron spectroscopy (XPS)

XPS measurements were carried out in ultra-high vacuum conditions ($< 10^{-10}$ mbar) using standard Omicron multi-probe XPS system with Al Kα 1486.7 eV monochromatic X-ray source, Argus hemispherical electron spectrometer and 128 channels MCP detector. Samples were air exposed before the XPS measurements. CASA-XPS software was used

for data analysis and curve fitting. The binding energy of the high resolution core levels was calibrated using C 1s as reference. The measurement was done by Muhammad Sultan and Azhar Fakharuddin in the National Centre for Physics, Pakistan.

2.2.5 Photoluminescence (PL) measurements

The PL spectra were recorded in a FluoTime 300 fluorescence lifetime and steady state spectrometer (PicoQuant). The illumination source was a 404 nm picosecond laser diode head. And a 575 nm filter was inserted between the sample and the detector to block scattered or reflected laser. The sample was placed in a cryostat chamber (OptistatDN-V, Oxford Instruments) which was pumped to the pressure range of 10^{-5} mbar. The set-up control and data acquisition were conducted in the customized mode of the EasyTau software. For the steady state measurement, the scan range for $MAPbI_3$ was 600 to 900 nm. While for the dynamic PL tracking, the peak position of the steady state curve was monitored. The counting rate was usually lower than 3% to ensure the reliability. The instrument response function (IRF) was measured by monitoring the laser wavelength without the filter. The life time of the perovskite sample was much longer than that of the IRF, so the IRF actually didn't influence the sample's PL decay curve. A sketchy PL measurement principle is summarized for reference.

PL and PL decay - a general introduction

Photoluminescence is a process in which a molecule or the lattice absorbs a photon, excites one of its electrons to a higher electronic excited state, and then radiates a photon as the electron returns to a lower energy state. If the system undergoes internal energy redistribution after the initial photon absorption, the radiated photon could have lower or higher energy than the absorbed photon, which is the so called Stokes or anti-Stokes shift[206].

For a semiconductor, when the incident photon energy exceeds its band gap, it could absorb the photon and generate an electron-hole pair which may further dissociate into free electron and hole. The dissipation processes of the free electron and hole could be either radiative or non-radiative. The PL measurement is monitoring the radiative fluorescence signal. The intensity of the signal depends on the carrier density in the material. For the dynamic measurement, the decay curve of the PL is indicative of the carrier density. The temporal variation of the carrier density depends on the recombination profile of the system, which, for sole perovskite films , could be described with Eq. 1.3. The Auger recombination is negligible when the carrier density is lower. As such, the trap-assisted recombination (k_1n) and radiative recombination (k_2n^2) dominate the decay trend[66].

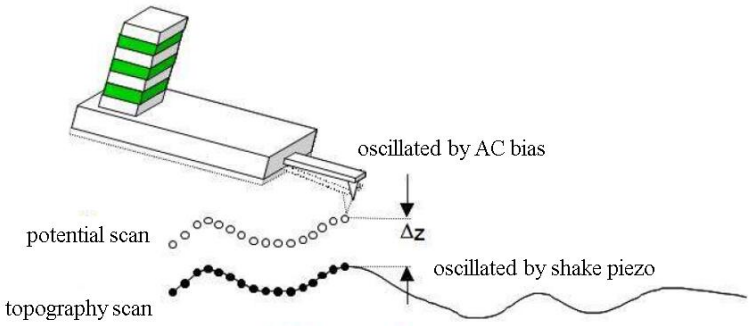

Figure 2.1: The schematic diagram of KPFM measurement by the AFM, adapted and rephrased from the user guide of asylum research.

2.2.6 Kelvin probe force microscope (KPFM)

KPFM measurment was performed on MFP-3D atomic force microscope (Asylum Research) with a Ti/Ir coated conductive tip (ASYELEC.01-R2) under dry air environment. The tip potential was measured using a mounted HOPG sample (Veeco). The measurement was performed in Prof. Dr. Giso Hahn's group with the help of Christian Derricks. A sketchy AFM/KPFM measurement principle is summarized for reference.

The working principle of the AFM/KPFM

The AFM/KPFM technique is a two-step probing method. During the first step, the topography image of the sample is obtained. Then in the second step, the topography information is used to perform another scan. The major difference of these two scans is the driving method of the oscillation of the cantilever. In a topography scan, the cantilever is typically oscillated mechanically by a small piezo electric actuator very near the cantilever chip. While for the potential scan, the oscillation is induced by an applied AC bias. A schematic diagram is shown in Figure 2.1.

As known, the topography scan is based on the distance dependence of the repulsive and attractive force between the oscillating tip and the sample surface. For the potential scan, on the other hand, it is based on the potential offset dependence of the force between the oscillating tip and the sample surface (as well as the distance which has been set the same by applying the topography information). As such, during the potential scan, besides the AC bias which oscillates the tip, a changing DC bias is also applied to the tip. When the DC bias cancels out the potential difference between the tip and the substrate, the force will be minimized. In other words, the KPFM uses a feedback loop to adjust the DC bias on the cantilever to minimize the force (amplitude). Because the tip needs to respond the the AC and DC bias, it needs to be conductive. However, the sample doesn't need to be conductive. The typical mathematical expression of the principle considers the tip and sample to be a parallel plate capacitor, which implies that the electric force is induced by charge transfer between the sample and tip through an external electric circuit. But in reality the measurement doesn't rely on the net charges of a capacitor.

2.2.7 Photo-electron Spectroscopy in Air (PESA) measurements

The valence band position of perovskite samples was measured by PESA performed by a AC-2 instrument (Riken Instruments). The measurement was conducted at 5 nW excitation light power and scanned from 4.5 eV to 6.2 eV with a step size of 0.05 eV. The 0.33 power of yields against excitation energy was plotted and a linear fit was performed to extract the takeoff energy. A sketchy PESA measurement principle is summarized for reference.

An introduction of the PESA measurement

The PESA measurement measures the work function of metal, ionization potential of a molecule, or the valence band postion of a semiconductor. In other words, the PESA measures the energy needed to remove a electron from the sample and become a free electron. The measurement is usually performed in vacuum (ultraviolet photoelectron spectroscopy) because the the emitted electron can only move several μm in air (mean free path of electron in air). However, The PESA has a specific electron counter which generates a giant electric field to detect the ionized gas molecules, so it doesn't need the vacuum environment.

2.3 The characterization methods of solar cells

2.3.1 The J-V related measurements

J-V measurements were performed using a Keithley 2400 Source Meter controlled through a self-written Matlab program (by Eugen Zimmermann) in the golvebox. Cells were illuminated via a LOT 300 W Xenon solar simulator through a shadow mask with a resulting active area of 0.133 cm^2. For light-intensity dependent measurement, a series of neutral-density filters (Thorlabs) were used to adjust the illumination intensity. And light intensities were calibrated with a certified Si reference solar cell (Fraunhofer Institute) with a KG5 filter. J-V curves were recorded at a step size of 10 mV and a sweep rate of approximately 50 mV/s.

2.3.2 Transient ionic measurements

During the transient ionic measurement, the solar cells were biased at 0 V for 60 s, 0.9 V for 60 s and 0 V for 120 s in turn under dark environment. During the fist 60 s, the solar cell was allowed to relax to an equilibrium state. Afterwards at 0.9 V, besides the injected recombination current, the ion migration hypothesis also suggests ions could redistribute in the cell. In the last 120 s, after removing the bias, there should be no free electrons

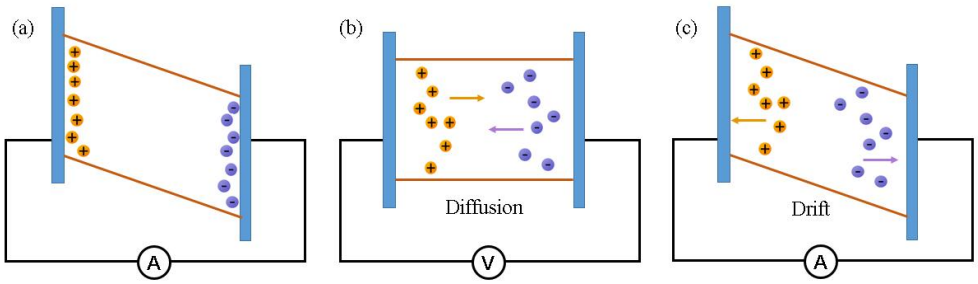

Figure 2.2: The schematic illustration of the transient ionic current measurement in which the (a), (b) and (c) presents the three subsequent stages of this measurement respectively.

and holes in the cell, and the current is ascribed to the movement and redistribution of ions (Figure 2.2)[204][207][208]. The current decay in the third period was integrated to calculate the corresponding ionic charge density.

2.3.3 The transient photo-voltage (TPV) measurement

For TPV measurements a Tekscope DPO 7254 digital oscilloscope was used, and solar cells were kept in a sample holder similar to the holder used for normal J-V measurements in a cryostat (OptistatDN-V, Oxford Instruments). The probed sample was background illuminated with a LOT Oriel LS0106 solar simulator and the intensity was adjusted using a series of neutral density filters (Thorlab). A small perturbation was generated using a pulsed Nd:YAG laser (532 nm wavelength, pulse length 2 ns, repetition rate 5-20 Hz). The laser intensity was adjusted to approximately 1-5 mW cm^2 using a filter. During TPV measurements, the device was held at a range of open-circuit conditions utilizing the 1 MΩ input resistance of the Tektronix oscilloscope and controlled by the background illumination. The intensity of the small optical excitation, which remained constant under all background illumination conditions, was set to achieve a voltage perturbation of less than 10 mV at 1-sun background illumination to operate within the small-perturbation regime.

The jungle of TPV measurements

The general principle of the TPV measurement is that, under a certain back illumination, the transient photo-voltage of a solar cell induced by a small laser pulse is tracked. The decay life time of this transient voltage could be extracted. The TPV characterization isn't a straightforward method, and its explanation in different kinds of solar cells could be different. It has been used to polymer solar cells, dye sensitized solar cells and nanocrystal sensitized solar cells to extract the carrier lifetime, calculate the carrier density in open circuit condition, probe charge transport for the rise time of the transient voltage, determine the activation energy of carrier transport and recombination and so on[209][210][211][212].

The most important assumption of this method is that the extra charge equilibrates with the device electrodes prior to any recombination, and the generation of carriers is independent of the carrier density, built-in field and so on[213]. It also needs to be aware that the induced transient photo voltage is not equivalent to an increment of V_{OC}. The V_{OC} is a steady state parameter which is related to the carrier density and recombination profile in the cell. While the transient photo voltage is induced by the injected transient carriers by a laser pulse. One major difference is that the the transient carriers are expected to not recombine before the rise of the transient voltage.

Ascertaining this difference is important to understand the connotation of the decay life time. Usually the decay life time is ascribed to the life time of charge carriers. But note that it is actually the life time of the transient photo voltage. The life time of V_{OC} can not be simply ascribed to that of charge carriers as the V_{OC} and carrier density of a cell have a complicated relation. But the transient photo voltage is directed related to the amount of extra carriers like in a parallel plate capacitor.

Typically in TPV measurements the perturbation of the short light pulse is small so that the response can always be described by a simple RC circuit. And the R (resistance) and C (capacitance) is in parallel connected[214]. So

$$\tau = R \times C$$

This relation reveals that the charge carrier recombination process is determined by both the resistance and capacitance terms in the electric circuit element point of view.

Moreover, the determined carrier life time also needs to treated with care as it has a specific physical meaning,

$$\frac{d\Delta n}{dt} = \frac{\Delta n}{\tau}$$

while assuming the actual recombination process is proportional to γ power of carrier density n,

$$\frac{dn}{dt} = \frac{n^{\gamma}}{\tau_{tot}} = \frac{n}{\frac{\tau_{tot}}{n^{\gamma-1}}}$$

where τ_{tot} is the total life time and $\frac{\tau_{tot}}{n^{\gamma-1}}$ is the pseudo-fist-order life time. Assuming the life time remains the same for the small injection condition,

$$\begin{aligned} \frac{d\Delta n}{dt} &= \frac{d(n+\Delta n)}{dt} - \frac{dn}{dt} \\ = \frac{(n+\Delta n)^{\gamma} - n^{\gamma}}{\tau_{tot}} &\approx \frac{n^{\gamma-1}\gamma\Delta n}{\tau_{tot}} \end{aligned}$$

And

$$\tau = \frac{\tau_{tot}}{n^{\gamma-1}\gamma} = \frac{\frac{\tau_{tot}}{n^{\gamma-1}}}{\gamma}$$

So the carrier life time from the TPV is $1/\gamma$ of the pseudo-first-order life time[215]. And it can not be simply applied to evaluate the recombination profiles between different devices as the carrier density n and exponential term γ also influence its value.

An important application of the TPV is to calculate the carrier density inside the cell using the so called differential charging method[216]. As the solar cell is under quasi-open circuit conditions during this measurement and the transient photo-voltage is induced by a known amount of carriers (as they are supposed to not recombine yet before the rise of the transient photo voltage), the capacitance at each different V_{OC} ($C_{V_{OC}}$) (determined by the back ground illumination) could be calculated,

$$C_{VOC} = \frac{\Delta Q}{\Delta V}$$

where ΔQ is the injected amount of carriers while ΔV is the amplitude of the transient photo voltage.

After integrating the $C_{V_{OC}}$ over the voltage, the charge carrier density at different V_{OC} can be extracted. This method has been suggested to be more accurate than the charge extraction method for the PSC. One reason is that more recombination loss occurs in the charge extraction process due to the large carrier density at higher illumination levels. More importantly, the hysteresis feature of the PSC could induce displacement currents due to the large internal field variation, which interferes with the test results[217].

2.3.4 Impedance spectroscopy (IS) measurements

A Metrohm Autolab PGSTAT 302N was used for IS measurements. The solar cell was placed in a cryostat (OptistatDN-V, Oxford Instruments) with the pressure $< 1\times10^{-5}$ mabr. The cryostat was fixed in a grounded aluminum box forming a Faraday cage to reduce electronic noises from outside and block the background illumination. Measurements were performed using the Metrohm software Nova 2.1. All measurements were performed in the dark at different biases using a perturbation voltage amplitude of 10 mV from 1 MHz to 1 Hz. As the IS data was used to perform Mott-Schottky analysis, the equivalent circuit fitting was not necessary.

A general introduction of IS measurement

During the IS measurement, the sample is probed using a low amplitude frequency-modulated AC voltage, and the output AC current signal is detected. Compared to a normal resistance measurement, additional information of the phase differences between the AC voltage and current signals can be obtained. Assuming the resistance is $|Z|$ and

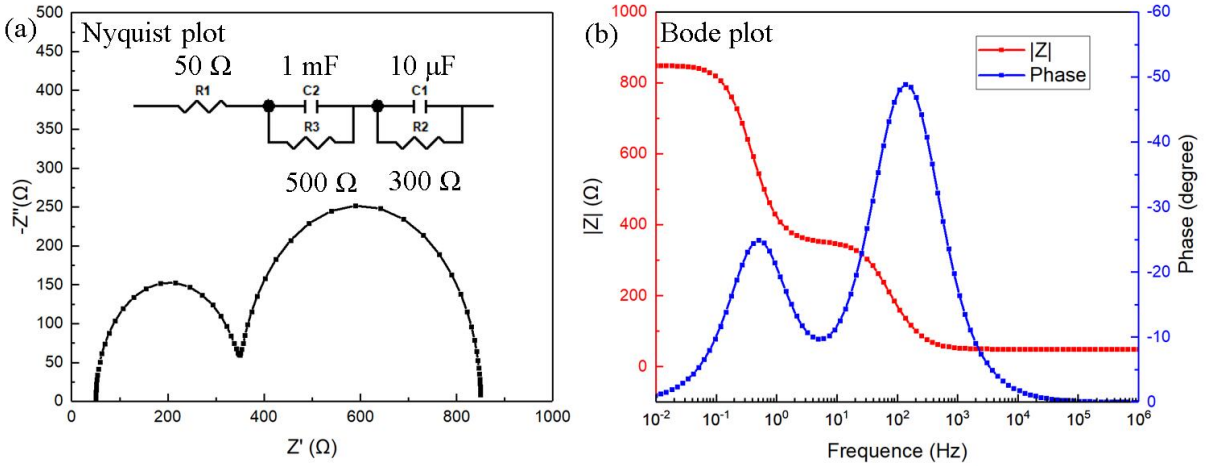

Figure 2.3: The (a) Nyquist and (b) Bode plot of the IS of the electric circuit presented in (a) simulated by ZView 3.5d.

the phase angle difference is ϕ, the impedance (Z) is usually described as

$$Z = Z^{'} + iZ^{''}$$
$$Z^{'} = |Z| \cos\phi$$
$$Z^{''} = |Z| \sin\phi$$

Z is represented by a point in the complex plane. Scanned over a wide frequency range, the obtained Z can be plotted either in the Nyquist or Bode style (Figure 2.3).

When using the IS measurement to characterize a solar cell, the main challenge is to correlate the electric feature of IS with the real physical processes in the cell[218]. In the electric circuit point of view, the IS features can all be simulated by a specific combination of electric elements (equivalent circuit). And ascertaining the representative processes behind the elements is more important. As introduced in the TPV technique, the recombination process could be represented by a parallelly connected resistance and capacitance. However, when characterizing a whole cell, the complexity of the involved processes may make it difficult to pinpoint a certain element to a specific process.

Chapter 3

The fabrication and optimization of inverted perovskite solar cells

The halide perovskites have been reported with their unique electronic properties in the 1990s[219][220][221][222]. Back then the research was focused on the dependence of the material property on its layered structure. Its application in solar cell was firstly reported in 2009 as dye in the dye sensitized solar cell. The cell gave a decent efficiency of around 3.8% but degraded fast due to the instability of the perovskite with the iodine liquid electrolyte[161]. Afterwards the utilization of the solid electrolyte successfully prolonged the life time of the perovskite sensitized solar cell and pushed the efficiency to around 10%[164]. Soon after the perovskite was reported to have excellent charge carrier transport ability and regarded more than a dye type of chemical[165][166][37]. Afterwards the unique property of halide perovskites attracts the attention of the solar cell research community. The architecture and fabrication of the PSCs have been insensitively studied pushing its efficiency to more than 23% (Figure [5]).

One major difficulty fabricating the PSC is the deposition of the perovskite film. For the solar cell application, usually a continuous film with no voids is necessary. At the initial stage, the fabrication of a pin-hole free perovskite film was unattainable and a mesoporous metal oxide scaffold seemed to be beneficial for the morphology control and cell performances[223][224]. Since then a lot of efforts have been made to develop perovskite film fabrication methods preparing the ideal morphologies.

In this chapter, a new perovskite film deposition method will be introduced. We show with the assist of vacuum and a special precursor composition, uniform perovskite films with no voids can be prepared with a thickness from 80 to 300 nm. The PSC with a PEDOT:PSS/$MAPbI_3$/C_{60} architecture was fabricated and optimized. The influences of the related parameters on the cell performances were studied. This fabrication procedure we developed can produce PSCs with the highest efficiency of around 16% and a high controllability.

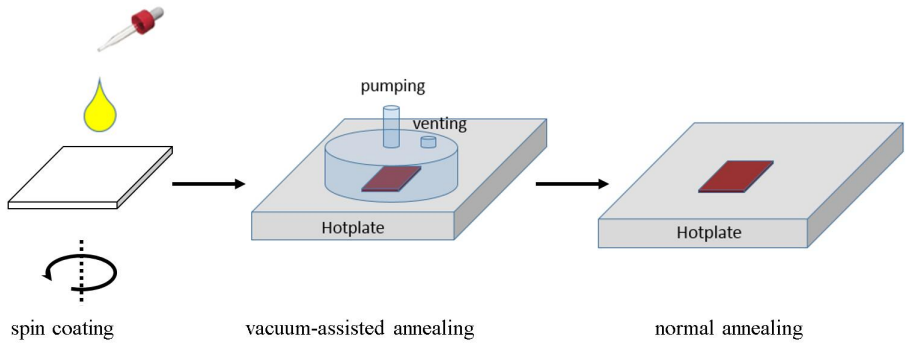

Figure 3.1: The diagram of the vacuum assisted annealing process.

3.1 The deposition of perovskite films

As introduced, halide perovskites have a strong crystallization tendency which may originate from its strong polarity. The film formation of perovskites is prone to noncontinuous large crystal domains which are not suitable for the solar cell application.

The crystallization process of perovskites could be modulated by adjusting the crystal nucleation or growth rate. Theoretically, slowing down the crystal growth rate or increasing the nucleation rate will give rise to smaller crystals and lead to a more uniform film[225][226]. As such, multiple deposition methods have been developed, for example adding MACl[227][228], NH_4Cl[229][230] or 1,8-diiodooctane (DIO) dopant [231] in the $MAPbI_3$ precursor solutions has been reported to yield films with better inter-connectivity. These additives have been suggested to participate into the crystallization processes by forming certain intermediate products which slows down the crystal growth process. Accelerating the nucleation of the precursor solution has also been proved effective. A widely known example is the so called anti-solvent method. Specifically, after spin coating, a poor solvent of perovskite (anti-solvent) is dropped on the still uncrystallized precursor sample and promotes a very fast nucleation process which smooths the forming film[79].

In this work, we developed a novel vacuum assisted deposition method which both accelerates the nucleation and slows down the crystal growth process. The corresponding process diagram is shown in Figure 3.1. In particular, after spin-coating, the precursor solution is still uncrystallized. Then it is transferred inside an isolated chamber which is connected to a pump. After starting the pump, the pressure of the chamber will quickly decrease to around 2 mbar and during this period the transparent film will turn into red brown. This step could be further modulated by adjusting the temperature, pressure and time to achieve better control over this process. Afterwards, the chamber is flushed to normal pressure and the sample is further annealed to enhance the crystalline quality.

A typical morphology of the derived perovskite film is shown in Figure 3.2 in comparison with the simple spin-coating method. The film derived through the vacuum assisted method is pin-hole free and continuous while the other one is composed of large branch-like crystal domains and a lot of voids.

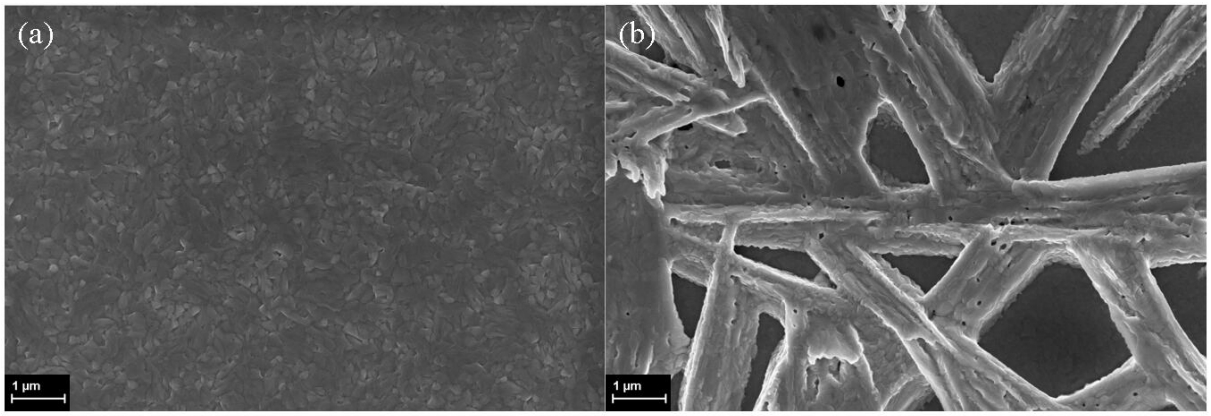

Figure 3.2: The typical morphology of $MAPbI_3$ films derived with (a) the vacuum assisted method and (b) the simple spin-coating method.

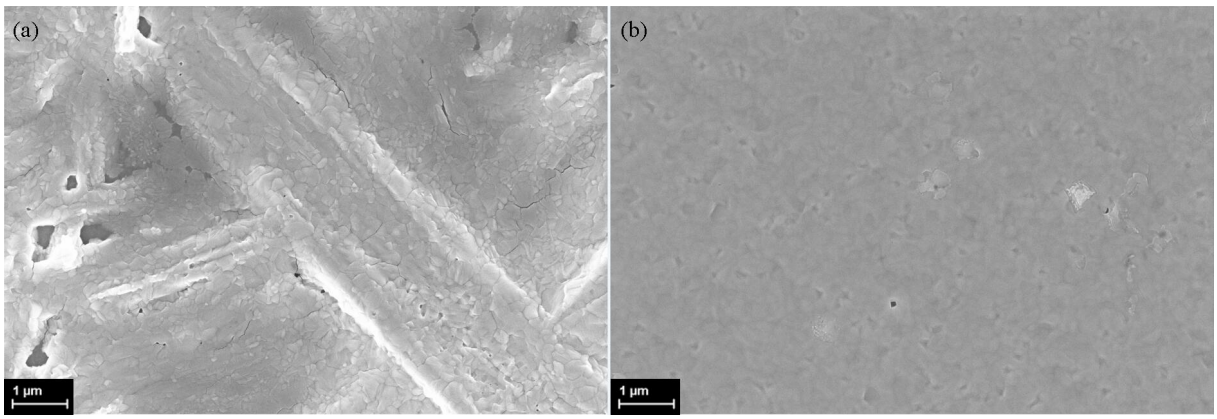

Figure 3.3: The morphology of $MAPbI_3$ films fabricated through the vacuum assisted method with (a) 20% excess MAI, (b) 100% excess MAI.

3.1.1 The influence of the precursor composition

The vacuum assisted method only works well with additional methyamine salt in the precursor solution. In Figure 3.3 the influences of different amount of additional MAI in the precursor solution on the morphology are presented. With 20% excess MAI, the branch-like structure seems suppressed compared to Figure 3.2(b), but apparently it still leads to a rough surface and uncovered voids. With 100% excess MAI, the film is much more smooth and continuous. The results suggest that the vacuum accelerated nucleation is not enough to smooth the film alone. Additional methyamine salt further helps modify the crystallization process and smooth the forming film.

However, to remove the additional methyamine salt from the film ad leave only pure perovskite, MAI is not an ideal additive as it has a high decomposition temperature. In comparison, the usage of MACl as additive has already been reported to optimize the morphology of the forming perovskite film in the simple spin-coating process[227][228]. No trace of chloride is detected after proper annealing due to the volatile nature of MACl.

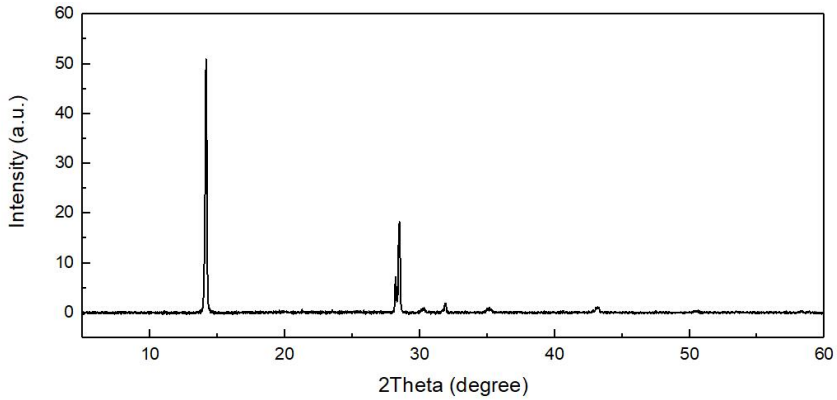

Figure 3.4: The typical XRD spectrum of the perovskite film showing pure $MAPbI_3$ phases.

Therefore, MACl is used as additive in this work. The corresponding chemical reaction is

$$PbI_2 + PbCl_2 + 4\,CH_3NH_3I + \longrightarrow 2\,CH_3NH_3PbI_3 + 2\,MACl\uparrow$$

namely the equimolar MACl is added to the $MAPbI_3$ precursor solution.

The XRD spectrum of the corresponding perovskite film is illustrated in Figure 3.4. The graph shows dominating (110) (14.1°) and (220) (28.2°) peaks which are ascribed to the $MAPbI_3$ cubic phase[9][232]. In addition, no sign of the precursor component is found indicating the resulting film is composed of pure $MAPbI_3$.

3.1.2 The parameter control during the vacuum annealing step

There are several parameters involved in the vacuum annealing step, for example the pumping speed, the vacuum degree, the temperature and the time. Of them, the pumping speed and temperature could influence the morphology at the early stage of the crystallization process while the vacuum degree may play a role at later periods.

As introduced, the nucleation and growth of the crystals are competitive processes. At the nucleation step, a higher pumping speed could already lead to lower vacuum degree promoting massive nucleation while higher temperature is more beneficial to the growth of the crystals. Figure 3.5 shows the different morphologies derived with a mild pumping speed at different temperatures. As the temperature increases, the $MAPbI_3$ also becomes noncontinuous. We think this is due to the enhanced crystal growth rate as the temperature rises.

Figure 3.5 seems to simply suggest that higher vacuum is beneficial while higher temperature is detrimental for the morphology. However, higher temperature is desired for removing the MACl impurity from the forming film. We find the application of higher temperature during the vacuum annealing process is necessary to remove the MACl while not damaging the morphology of the forming film. Figure 3.6 presents the morphology differences lead by different vacuum degrees. Through the films all seem uniform, the film

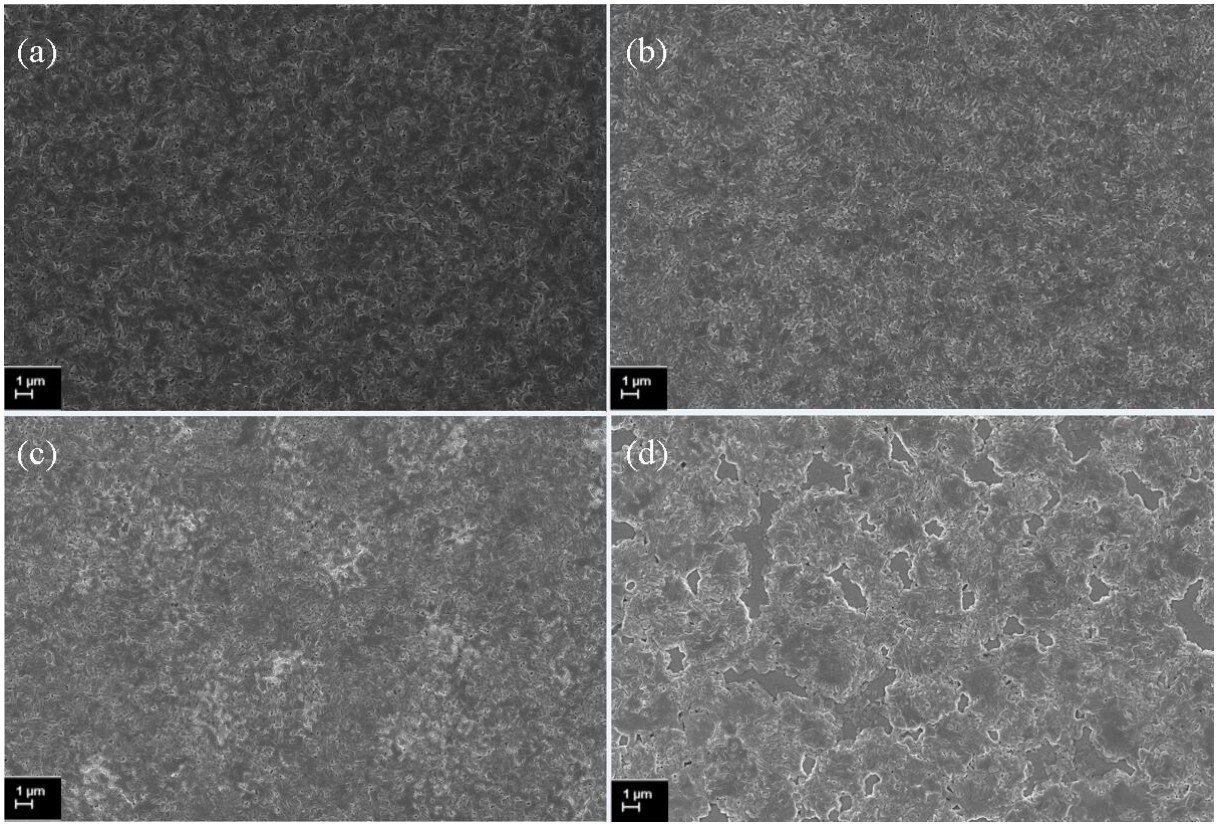

Figure 3.5: The morphology of the $MAPbI_3$ films with different vacuum annealing temperatures of (a) 40 °C, (b) 50 °C, (c) 60 °C and (d) 70 °C at a mild pumping speed.

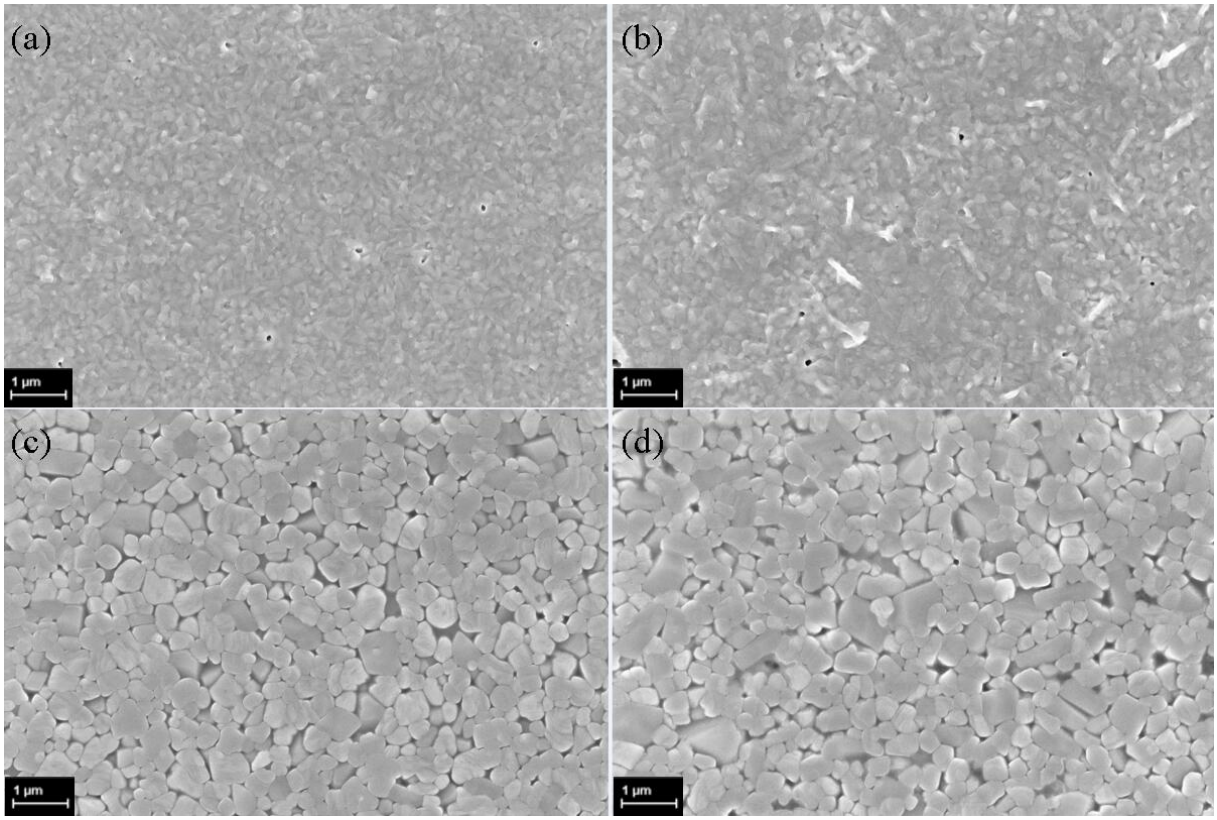

Figure 3.6: The morphology of the $MAPbI_3$ films with different vacuum degrees of (a) 2.5 mbar, (b) 5 mabr, (c) 20 mbar and (d) 100 mbar at 80°C for 10 min.

prepared through lower pressure annealing process is composed of smaller closely packed grains while the film prepared through higher pressure annealing process composed of larger grains with voids. We see these differences come from the process of removing MACl from the film.

In short summary, during the vacuum annealing step, two processes happen successively, the initial nucleation/crystallization and the removal of the MACl additive. These two steps both benefit from the a higher vacuum degree (fast pumping speed), but a higher temperature could deteriorate the formation of a better morphology at the initial stage while accelerate the removal process at the later stage. Therefore an optimized annealing parameter for our setup is found to be 60 °C for 30 min at the maximal vacuum degree our chamber could achieve (around 2 mbar). It is worth mentioning that the thermal stability of $MAPbI_3$ under vacuum environment also decreases, and higher temperature and longer time vacuum annealing may lead to unwanted defects or the decomposition of halide perovskites. The balance of temperature, time and pressure is very tricky which also depends on the thickness of the film.

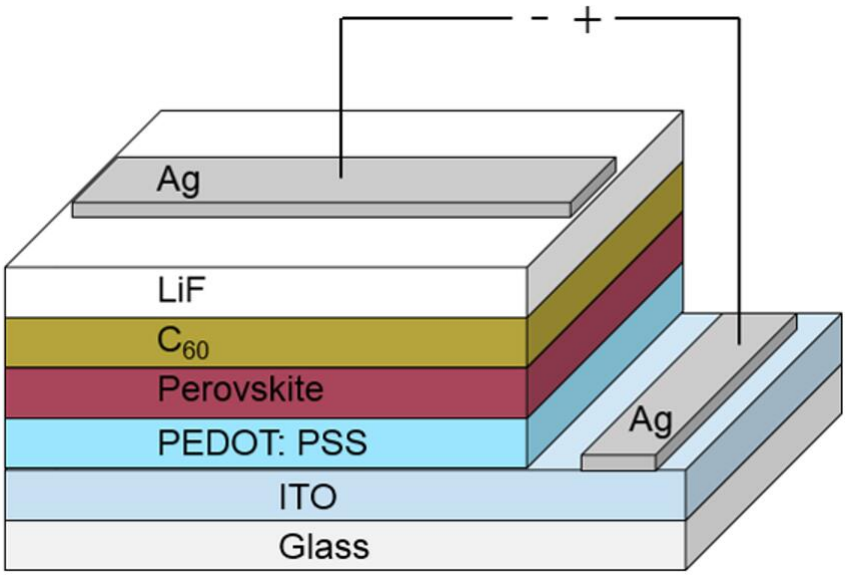

Figure 3.7: The inverted solar cell architecture employed in this work.

3.2 The fabrication of inverted perovskite solar cells

Based on the perovskite deposition techniques described above, inverted perovskite solar cells with an architecture as shown in Figure 3.7 are prepared. An detailed description of the fabrication process is given in the experimental methods section. In general, the PEDOT:PSS acts as the HTM while C_{60} as the ETM in this architecture. A thin layer of LiF is inserted to block potential diffusion of Ag particles into the C_{60}. And ITO and Ag act as the electrodes. The estimated band diagram of this architecture is illustrated in Figure 3.8.

The thickness of the PEDOT:PSS, $MAPbI_3$ and C_{60} layers are important for the performance of the solar cell. The perovskite layer has been reported to output the maximal efficiency at around 300 nm which balances the light-harvesting and carrier transport properties[78][233][234]. While for the selective layers, a thicker film could lead to higher resistance while thinner ones may have poor coverage leading to more shunt paths. We find that the performance of the solar cell is not sensitive to the thickness of the PEDOT:PSS layer. Figure 3.9 shows the cross-sectional SEM images of the PEDOT:PSS and perovskite layer. PEDOT:PSS layer has around 30 nm thickness while the $MAPbI_3$ around 300 nm. The C_{60} layer is more influential on the performance of the device which will be addresses further.

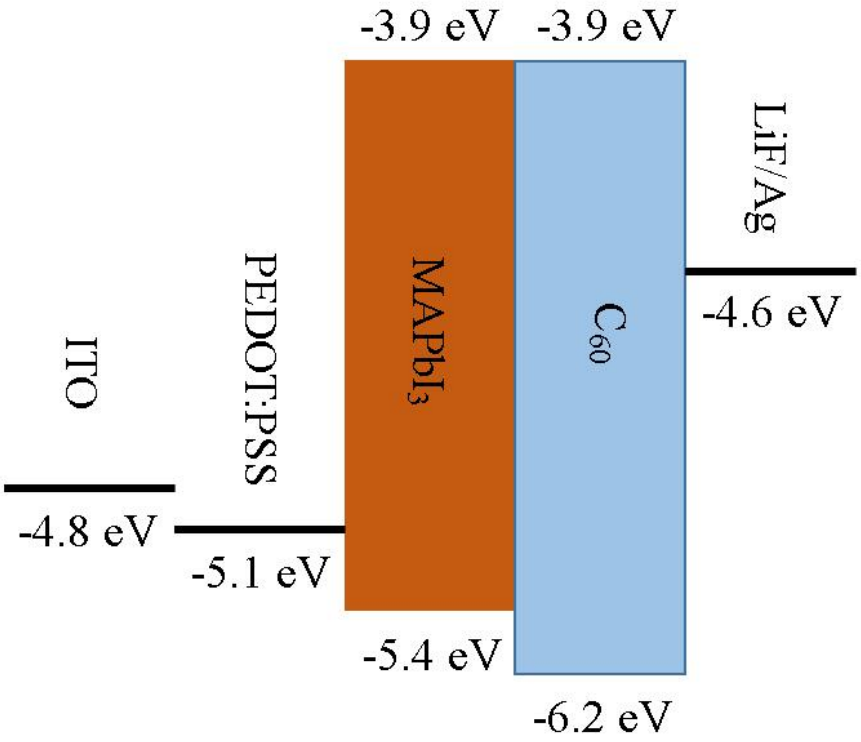

Figure 3.8: The band diagram of the employed architecture.

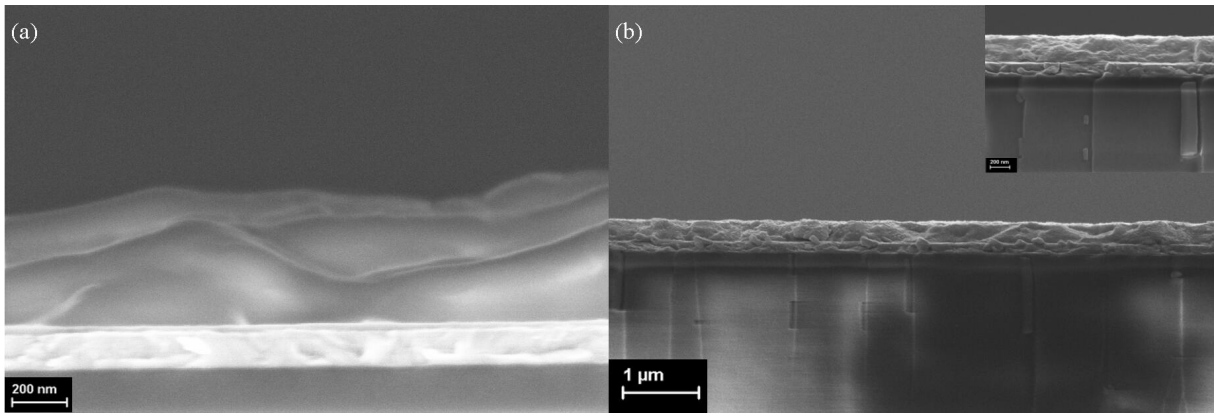

Figure 3.9: The cross sectional images of the (a) PEDOT:PSS/PEG stack and (b) PEDOT:PSS/$MAPbI_3$ stack. PEG is deposited on PEDOT:PSS for better contrast. The inset of Figure (b) is taken at a higher magnification.

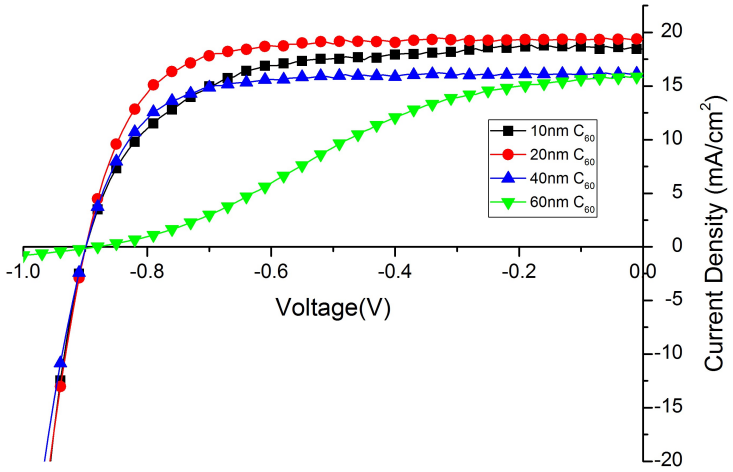

Figure 3.10: Influence of the C_{60} layer thickness on the device performance.

C_{60} layer thickness	$V_{OC}(mV)$	$J_{SC}(mA/cm^2)$	$FF(\%)$	$PCE(\%)$
$10nm$	899	18.4	63.6	10.5
$20nm$	899	19.4	72.2	12.2
$40nm$	902	16.1	65.9	9.3
$60nm$	884	15.8	35.0	4.8

Table 3.1: Effect of C_{60} layer thickness on device performance.

3.2.1 The optimization of the C_{60} layer

The C_{60} layer is used to act as the selective electron extraction layer in the solar cell. Its thickness needs to be carefully controlled, as it needs to be thick enough to fully cover the perovskite layer, but a too thick C_{60} layer will also increase the series resistance of the device. C_{60} layers with different thicknesses have been thermally evaporated on top of the perovskite film. In Figure 3.10 the influence of the C_{60} layer thickness on the device performance is shown. Detailed solar cell parameters are summarized in Table 3.1. Clearly 20 nm C_{60} is already enough as hole-blocking layer and doubling its thickness greatly impedes its ability to transfer electrons which results in a lower fill factor and also lower photo current density. If the layer too thin, the fill factor and photo current density also decreases slightly, which is ascribed to a not complete coverage of the perovskite film. Compared to PCBM, C_{60} is a more electron-conductive fullerene-based material[235]. With the flat $MAPbI_3$ film as the bottom layer, a 20 nm C_{60} could already form a compact and efficient selective layer.

It is found that the performance of solar cells will benefit from a short annealing treatment after deposition of C_{60} layer, mainly due to the increase of photo current (Figure

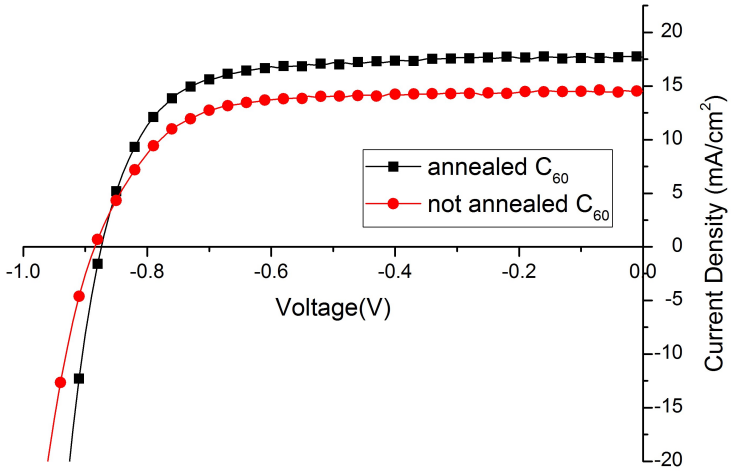

Figure 3.11: Influence of the annealing treatment of C_{60} layer on the device performance.

3.11). It has been reported the solvent annealing of PCBM layer could increase solar cell performances, implying the interface between perovskite and fullerene-based layer could be modified to promote charge transfer[236]. We see this effect leads to the increase of the performance after annealing C_{60} layer in our study. The contact between the perovskite and evaporated C_{60} layer could be strengthened by the short thermal treatment.

3.2.2 The insertion of a thin LiF blocking layer

LiF, BCP or Ca are widely used as insulating layer between ETL and metal back contact[237][238][239]. In this work we use an evaporated thin LiF layer. Amazingly, the FF of solar cell could be improved from 70-75 to around 80 just by depositing 1 nm LiF before evaporating Ag (Figure 3.12). Such an effect has been reported, suggesting the energy mismatch between the cathode and electron transporting layer is compensated by the formation of dipoles with the LiF insertion layer[142]. Another explanation is the physical blocking effect which prevents the diffusion of Ag particles into the thin C_{60} layer[240][241].

3.2.3 Optimized solar cell performance and statistical results

Based on the above mentioned optimization conclusions, 30 perovskite films are deposited to fabricate solar cells in successive three batches. The performance of the best solar cell is presented in Figure 3.13. The solar cell is measured in ambient air at 0.1 V/s. The forward and backward scanned curves are well coincident with no sign of the hysteresis behavior. The FF of the backward scan is lower(79.4 vs 81.0 in Table 3.2) mainly due to a steeper

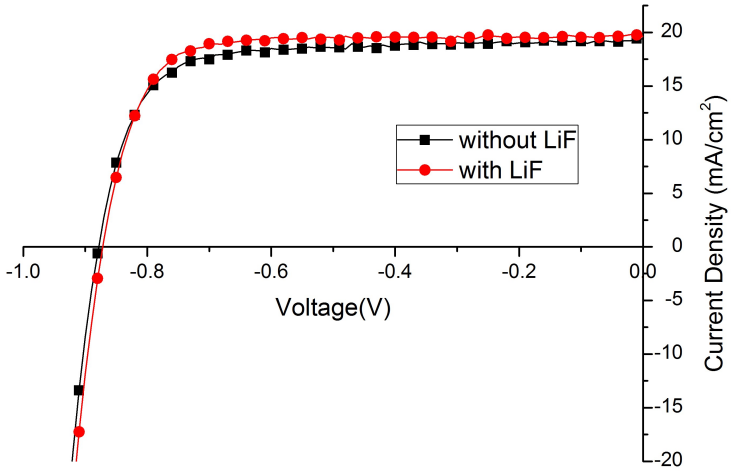

Figure 3.12: Effect of the LiF blocking layer on the J-V curve.

\	$V_{OC}(mV)$	$J_{SC}(mA/cm^2)$	$FF(\%)$	$PCE(\%)$
Forward scan	959	20.2	81	16.4
Backward scan	960	20.5	79.4	16.4

Table 3.2: The parameters of the champion solar cell.

current drop at 0 bias point which may be attributed to certain charge accumulation at the open circuit condition.

The statistical distribution of the performances of these cells is shown in Figure 3.14. As seen, our fabrication method is quite reproducible, over 80% solar cells have over 14% efficiency. The origin of the inferior cells is considered to be the perovskite spin-coating process which sometimes introduces large flaws to the film. The prepared perovskite precursor solution is colloidal and close to saturation which may contain large particles and influence the quality of the spin-coated film.

3.3 The ultra thin semi-transparent perovskite solar cell

The vacuum assisted deposition method can be easily applied to deposit ultra thin perovskite film by simply diluting the precursor solution. The ultra thin film is interesting because it enables the realization of semi-transparent solar cells. In certain circumstances (for example, building external windows), a certain light transmittance could be more desirable than higher efficiencies of the solar cells[242][243].

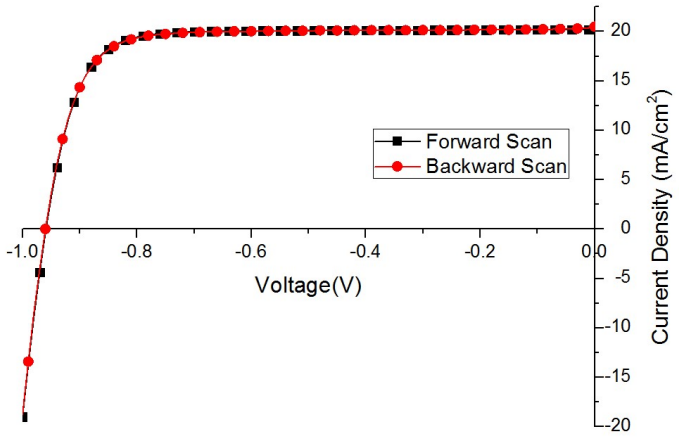

Figure 3.13: The J-V curves of the champion solar cell scanned from forward and backward directions.

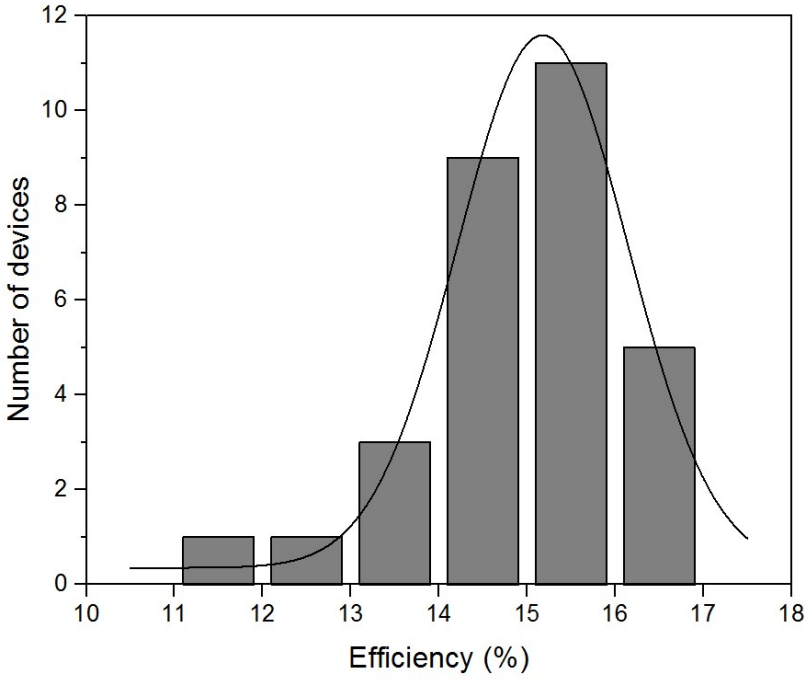

Figure 3.14: The statistical distribution of the solar cell efficiencies.

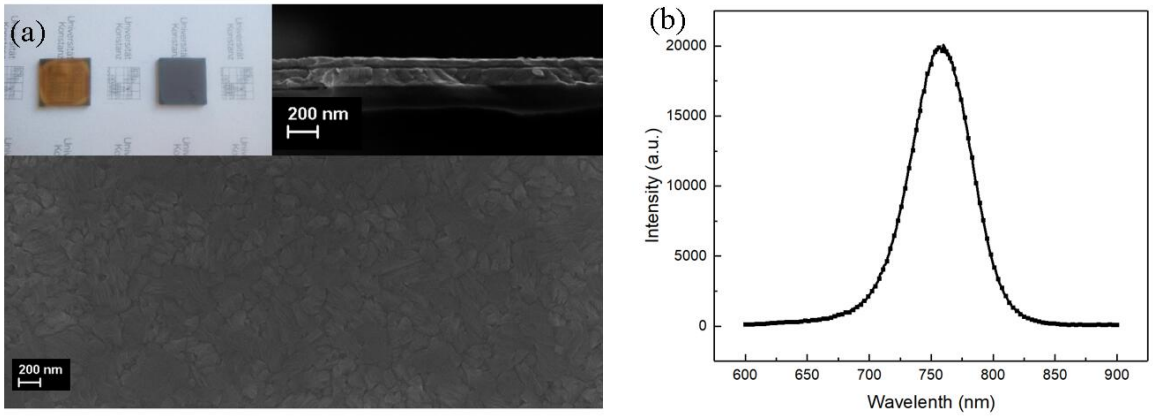

Figure 3.15: The (a) morphology and (b) static PL spectrum of the deposited ultra thin $MAPbI_3$ film. In figure (a), the optical image (in comparison with 300 nm film), the cross section picture and top view image are presented in proper order.

\	$V_{OC}(mV)$	$J_{SC}(mA/cm^2)$	$FF(\%)$	$PCE(\%)$
Forward scan	864	10.91	82.8	7.81
Backward scan	858	10.89	82.9	7.74

Table 3.3: The parameters of the ultra thin $MAPbI_3$ solar cell.

Figure 3.15 illustrates the fabricated ultra thin $MAPbI_3$ film. A thickness of around 80 nm is observed which renders this film certain transmittance. The static PL spectrum shows a peak position of around 760 nm which matches the band gap of the material in accordance with related reports[244][245]. The corresponding solar cell performance is illustrated in Figure 3.16. And the parameters are listed in Table 3.3.

Comparably, we find the J_{SC} and FF of the ultra thin $MAPbI_3$ cell is reasonably high while the V_{OC} is lower. The current density which reaches around half the theoretical value of $MAPbI_3$ suggests that most light has been absorbed in the front 80 nm film. A higher FF and lower V_{OC} is confusing. In a working solar cell with certain external load, the photo-generated charge carriers either recombine in the device or reach the external circuit. The FF qualitatively indicates the relative weight of these two pathways at the maximal power point. Higher FF implies more charge carriers could be injected into the external circuit while lower FF implies more charge carriers recombine inside the device. In the meanwhile, the V_{OC} could be understood as an indicator of the non-radiative recombination in a given system. Higher V_{OC} suggests a lower non-radiative recombination rate and vice versa. The ultra thin cell exhibits a combination of conflicting features, higher recombination rate and superior carrier output. It is worthwhile to note that the reason of this contradiction is the different viewpoint. The V_{OC} argument is valid at the open circuit condition while the FF argument at the maximal power point. Here we see the additional recombination channels don't play a main role before the maximal power point. In Chapter 5, the simulation reveals that a balanced interfacial recombination could tune the slope of the photo current drop, which supports the above

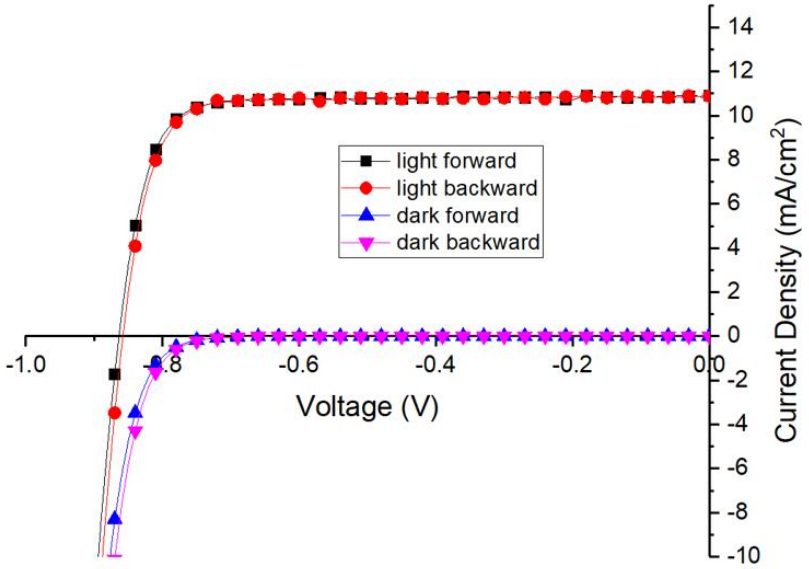

Figure 3.16: The J-V curves of the ultra thin $MAPbI_3$ solar cell scanned from forward and backward directions under illumination and dark environment.

explanation.

The ultra thin solar cell with 100% excess MAI has also been fabricated (Figure 3.3(b)). Because the excess MAI is difficult to remove, the forming film is not pure $MAPbI_3$. Actually, its PL spectrum suggests the resulting film is not a pure compound. However, the film is still very smooth and the corresponding solar cell gives an efficiency of around 3.5%. This results imply that the perovskite solar cell is very tolerant of certain 'impurities'. And the excess organic compound doesn't give rise to lots of recombination centers.

3.4 The variations of solar cell performances due to the vacuum annealing time

In the above sections several aspects regarding the fabrication processes of perovskite solar cells are introduced. The vacuum assisted annealing methods we developed can prepare very smooth and pin-hole free perovskite films with a thickness as low as 80 nm. Solar cells based on this method with the PEDOT:PSS/$MAPbI_3$/C_{60} architecture show high efficiencies of around 16%. However, this method also has its disadvantages which, as we understand, is the unfavorable surface modification of the perovskite films caused by the vacuum annealing treatment.

The organic halide perovskites have been reported to suffer from the variation of its surface chemical composition because certain components can leave the surface due to their thermal motion[246][247]. This problem is exaggerated in the vacuum assisted annealing process.

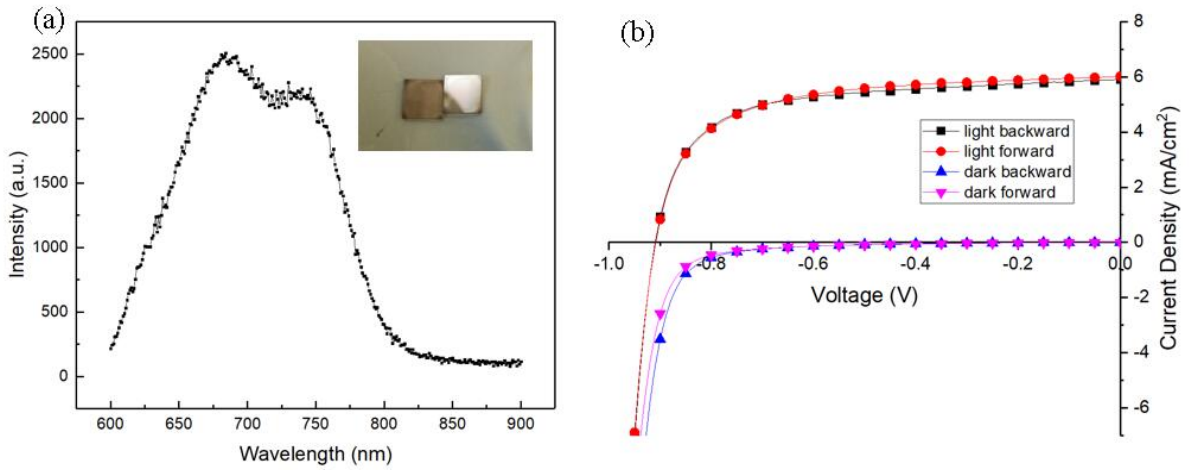

Figure 3.17: The (a) PL spectrum of the $MAPbI_3$+MAI thin film and (b) the corresponding solar cell performance. The inset of Figure (a) is the optical picture of the film showing a high reflectivity.

We monitored the in-situ PL intensity signal during the vacuum annealing step. The measurement is performed in Cryostat vacuum chamber in the PicoQuant PL setup with an additional heating accessory. A clear intensity dropping trend is observed as the annealing time increases (Figure 3.18(a)). After this measurement we further analyzed the XRD spectra of the forming films (Figure 3.18(b)). It shows that during the vacuum annealing treatments, the peak intensity (14.1°, 28.2°) of $MAPbI_3$ increases while the $MAPbCl_3$ peaks (15.7°, 31.5°) decreases[9][232][248]. During the vacuum annealing process, the MACl gas is gradually removed from the film and the $MAPbI_3$ forms. However, before the full transformation to $MAPbI_3$, the film already presents decreasing PL intensity which could be ascribed to increased defects.

In Figure 3.19 we further present the data collected through the in-situ PL measurement. As we learned during the annealing process the peak position does not shift (Figure 3.18). The peak PL intensity and decay curves are tracked. The peak PL signal firstly increases probably due to enhanced crystallinity at the initial annealing stage. Afterwards the PL signal continuously decreases. The dynamic PL results also reveal a faster recombination process since 15 min. The above measurements suggest during the vacuum annealing treatment, the surface of the film undergoes significant composition change which may form a lot of defects.

Such effect also plays a role affecting the behavior of solar cells. To investigate how the solar cells are influenced, the statistics of solar cell performances with varied vacuum annealing time are collected (Figure 3.20). In Figure 3.20(a), we see that the V_{OC} of the PSC remains stable for samples with 15 min, 20 min and 25 min vacuum annealing time, but afterwards it continuously decreases from around 0.9 V to below 0.8 V. The FF, however, increases from around 73% to 82% from 15 min to 40 min (Figure 3.20(b)). Further annealing decreases the FF slightly. This result suggests that the V_{OC} can be easily influenced by the vacuum annealing treatment. Longer annealing reduces the V_{OC}

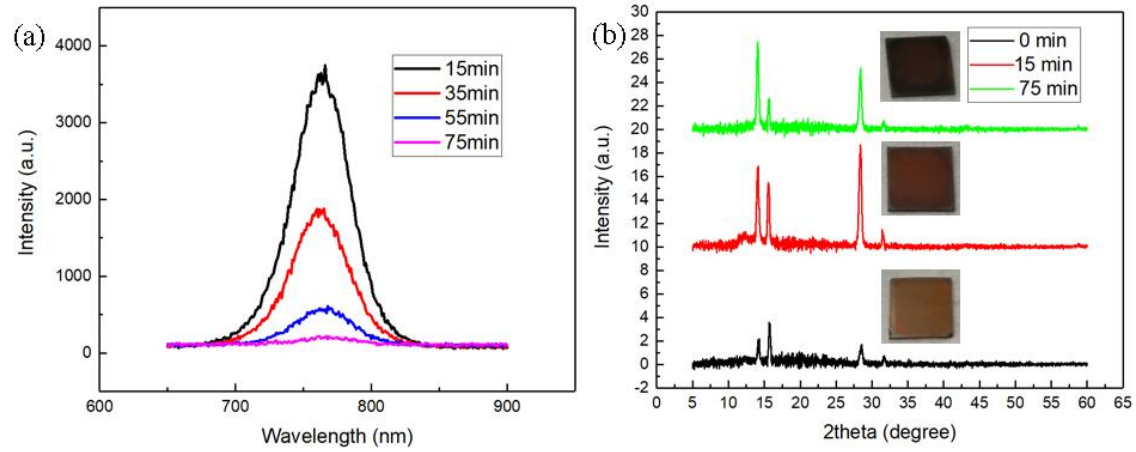

Figure 3.18: The (a) XRD and (b) static PL spectra of the perovskite films with different vacuum annealing time.

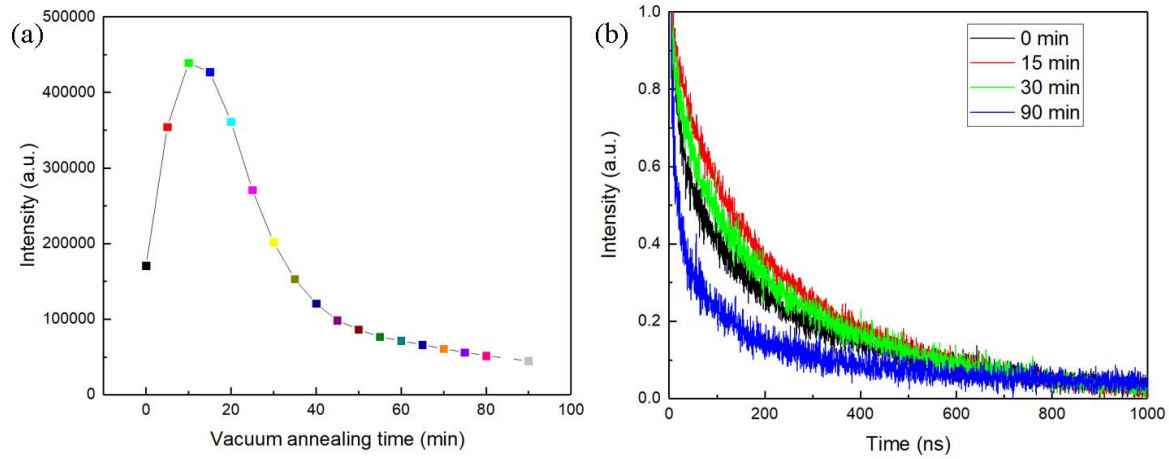

Figure 3.19: The in situ PL results of (a) peak intensity tracking and (b) the PL decay curves.

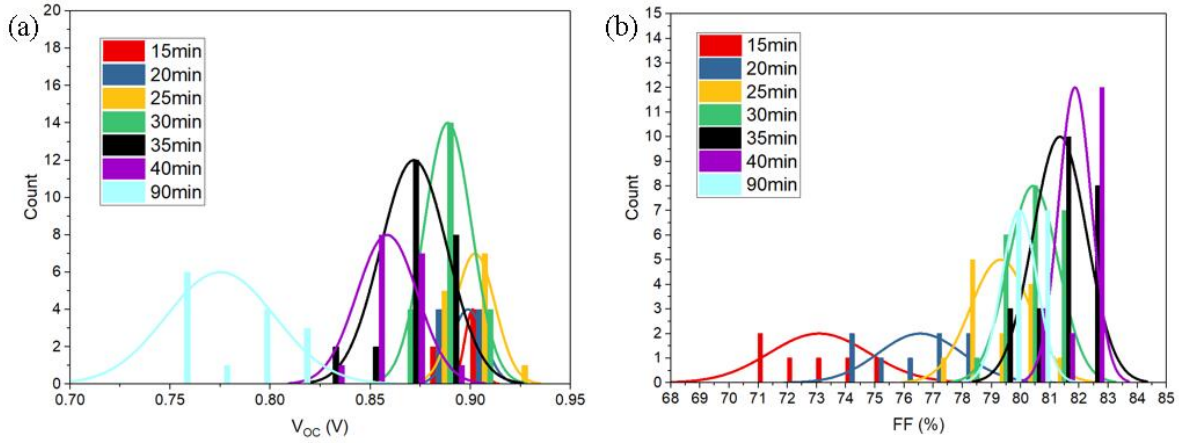

Figure 3.20: The statistic result of (a) V_{OC} and (b) FF with different vacuum annealing time.

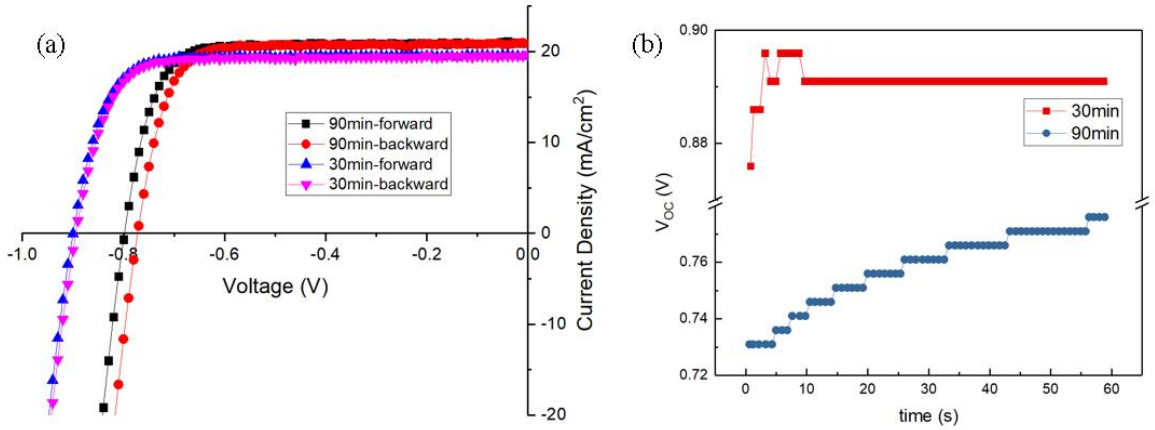

Figure 3.21: The (a) J-V curves and (b) V_{OC} track of the PSC with 30 min and 90 min vacuum annealing time.

which is ascribed to the variation of the perovskite surface. On the other hand, the FF is not showing the same trend as the V_{OC}. As a longer vacuum annealing treatment could remove the MACl more completely, we think the increasing trend of the FF may originate from a better morphology as suggested in Figure 3.6. Moreover, the loss of the V_{OC} may already contribute to the gain of the FF, as discussed above. It is worth mentioning that the V_{OC} of the PSC prepared here is lower than the front section, this is due to the change of preparation environment which, though lowers the performance, makes the whole process more controllable.

The J-V curves of the solar cells with 30 min and 90 min vacuum annealing time are shown in Figure 3.21(a). The measurement was conducted between 0 and 1 V at 0.1 V/s. Besides the V_{OC} difference, a hysteresis behavior between the forward and backward scan is observed for the 90 min sample. We further tracked the V_{OC} of the device which rested at the short circuit condition beforehand. Due to the limitation of the tracking algorithm, the curves are not smooth but still we see the V_{OC} of the 30 min sample is more stable than the 90 min sample. And the V_{OC} of the 90 min sample gradually increases from 0.73 V to 0.8 V in 60 s during tracking at the open circuit condition.

Till now the influences of the vacuum annealing time on the perovskite film and solar cells have been discussed. The vacuum annealing treatment is shown to accelerate the recombination processes due to the modification of the surface chemical composition of halide perovskite films. We show that the V_{OC} of the solar cell is significantly influenced by this effect. Moreover, the appearance of the hysteresis phenomenon also suggests that certain slow processes are also triggered by the long vacuum annealing. According to the ion migration hypothesis[192][193][194][66][195], the modification of the perovskite surface may be related to the increase of movable ions. We recorded the transient ionic current of the PSC with 30 min and 90 min vacuum annealing treatments. During this measurement, after the solar cell was biased at 0.9 V in dark, the dark short circuit current was recorded, which has been ascribed to the movement and redistribution of ions[204][207][208]. The results are illustrated in Figure 3.22.

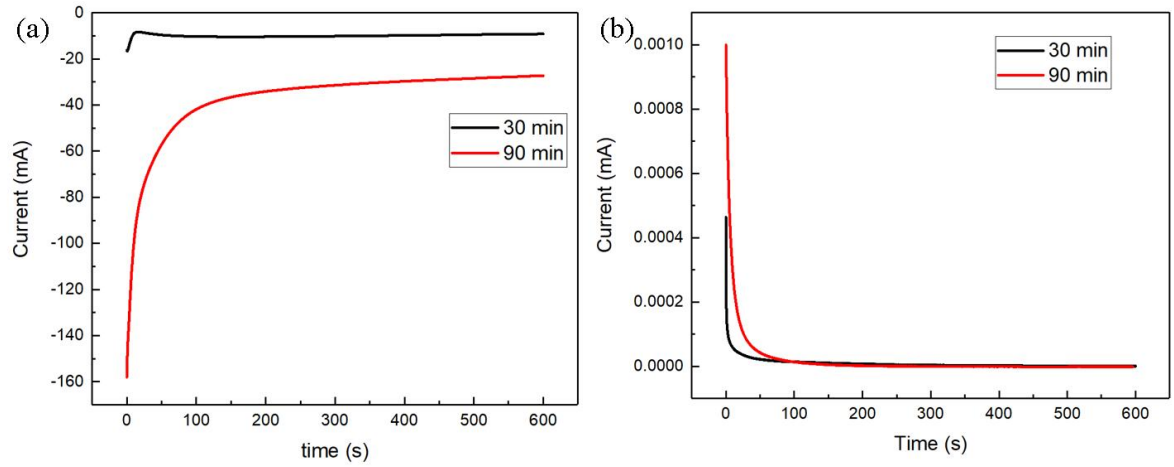

Figure 3.22: The transient ionic current measurements results. After (a) 0.9 V bias disturbance, the cell was allowed to rest at (b) 0 V.

Clearly, the responses of the 30 min and 90 min sample to the bias is very different. The 90 min sample has a stronger injection current decrease from around 180 mA to 30 mA, while the 30 min sample shows a weaker fluctuation of the injection current. The dark short circuit current in Figure 3.22(b) is ascribed to ionic current. And the 90 min sample clearly shows a higher current which suggests a larger amount of movable ions.

To further understand the influence of vacuum annealing treatment on the solar cell behavior, we performed the TPV measurements on the 30 min and 90 min samples. TPV characterization tool gives direct information on the recombination dynamics in a solar cell. With a wide range of background illumination intensities, the solar cell shows different V_{OC}s at the open circuit condition. A small amount of excess charge carriers is injected by a laser pulse and the photo voltage of the cell marginally increases. As the system returns to equilibrium, the decay trend of the transient photo voltage is recorded which shows how fast these excess charge carriers recombine. In other words, the TPV measurements reveal the recombination dynamics of a complete solar cell with a certain charge carrier density (corresponding to a certain V_{OC}) due to the background illumination.

Figure 3.23 presents the decay curves of the transient voltage with no back ground illumination for the 30 min and 90 min samples. Clearly the decay of this small transient voltage (less than 4 mV here) is much slower for the 30 min sample than the 90 min sample. The life time of the excess charge carriers is 1 ms for the 30 min sample and 0.021 ms for the 90 sample in the dark environment. Moreover, the decay curves of the 30 min sample is double exponential while the 90 min sample is single exponential.

We used a wide range of background illumination intensities and extracted the corresponding charge carrier life times. And the life time versus the V_{OC} trends are shown in Figure 3.24. As the light intensity was not calibrated, the relation between the life time and the light intensity can not be clearly established. However, as the measurements were performed under the same illumination conditions, the life time between the 30 and 90 min

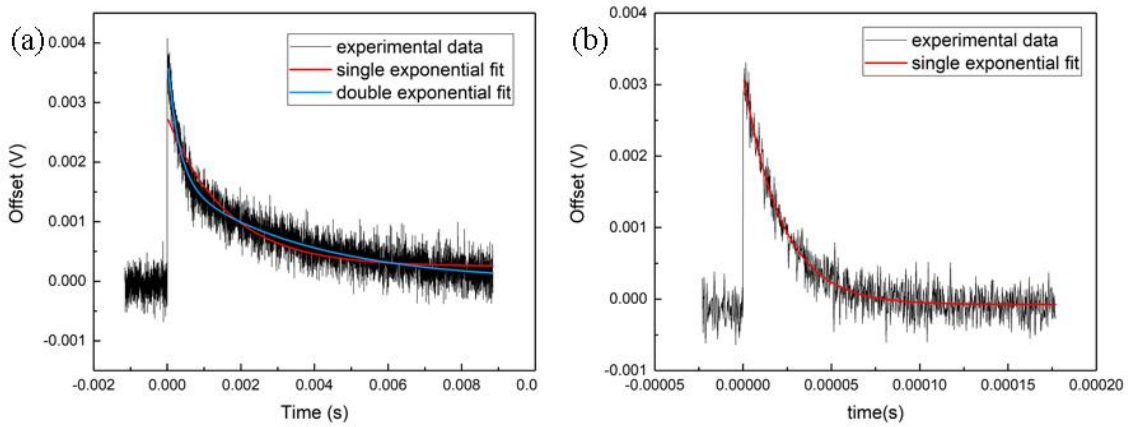

Figure 3.23: The decay curves of the transient voltage with no illumination of (a) 30 min and (b) 90 min sample.

samples can be compared under one illumination intensity. When the illumination intensity is lower, we see the 30 min sample shows a longer life time and higher V_{OC}. At a low illumination intensity, the recombination process is normally ascribed to the trap-assisted recombination. And we think that the faster recombination for the 90 min sample could result from a larger amount of defects due to the longer vacuum annealing treatment. However, as the intensity increases, the life time of the 30 min sample decreases very fast and turns shorter than 90 min sample above certain illumination intensity. This result is very surprising as it suggests that even with faster recombination rates (shorter carrier life time), the V_{OC} could still be higher under the same illumination intensity. Based on the Eq. 1.32,1.33, this behavior is possible and will be addressed further in the following chapter.

In short summary, in this chapter we present the fabrication part of the projects. A novel vacuum assisted annealing method is developed which can produce uniform and pin-hole free perovskite films. The related parameters during the deposition are studied. Based on the fine perovskite films, inverted PSCs are fabricated and optimized. Around 16% efficiencies with a high reproducibility are achieved. Moreover, semi-transparent PSCs with only around 80 nm perovskite layer are also prepared which deliver an efficiency of around 7.8%. We address the main drawback of this deposition technique is the introduction of defects which comes from the exacerbated thermal stability of $MAPbI_3$ under vacuum. Therefore, the performance of the PSC varies significantly with different vacuum annealing conditions.

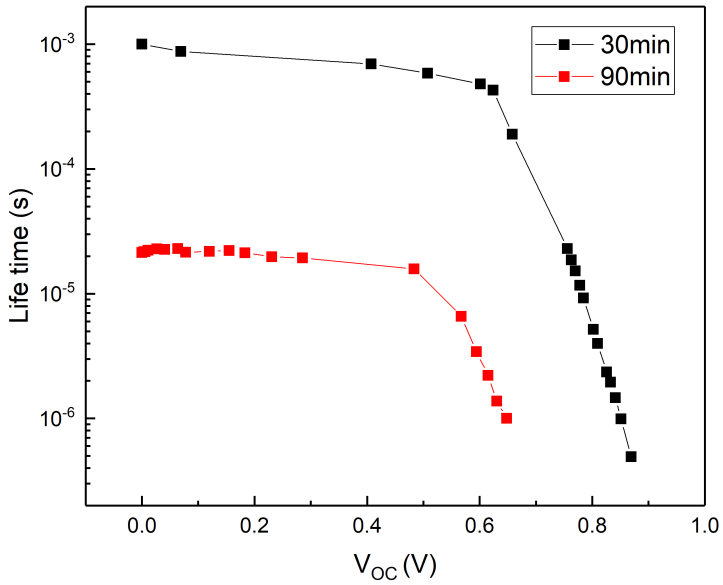

Figure 3.24: The charge carrier life time at different V_{OC} for the 30 and 90 min samples.

Chapter 4

The characterization of inverted perovskite solar cells - an investigation of V_{OC} origin

Though the efficiency of the PSC attracts the attention of the research community, ascertaining the origin of its high performance is equally important. The processes occurring in a solar cell include the generation, transport and recombination of the charge carriers[100][249]. We see the J_{SC} reflects the process of the carrier generation and transport. Harvesting a decent J_{SC} is always the first step to an efficient solar cell architecture, for example, the organic blend solar cell and the dye sensitized solar cell only work well with their specific structures which allow the carrier to be efficiently collected[250][251]. And pushing certain type of cell towards its efficiency limit also usually needs to maximize the J_{SC} by pursuing higher photon collection efficiencies[252][253]. We note that the recombination also exists in the short circuit condition, but is minimized in most efficient solar cell architectures. Of all the parameters V_{OC} is especially interesting as it also reflects the recombination processes. From short circuit to open circuit condition, the charge carrier density gradually increases in the cell and leads to higher recombination losses. How the recombination current increases with the carrier population determines the shape (FF) of the J-V curve (assuming the carrier generation is not transport limited). In the end, it also determines the point (V_{OC}) where the recombination current equals the generation current. In a given architecture, the V_{OC} is an indicator of the severity of the recombination processes. To summarize, an efficient solar cell architecture should deliver a decent J_{SC} by minimizing the recombination loss at short circuit condition, and the recombination profile determines the FF and V_{OC} of the cell.

For perovskite material, the high absorption coefficient, low exciton binding energy and long carrier diffusion length make designing suitable solar cell architectures simple. Indeed, PSCs have been reported with high photo-current densities very close to the theoretical maximal values based on the Shockley–Queisser limit[254][255]. And the FF also benefits from that and reaches around 80% in high performing solar cells[106]. Therefore, to further boost the efficiency towards higher values, additional focus on increasing the

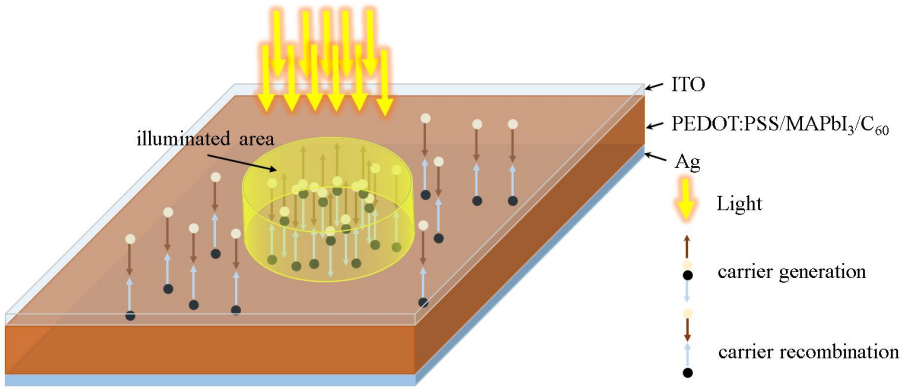

Figure 4.1: The illustration of the mismatch effect between the illuminated area and the pixel size.

V_{OC} is needed[256]. Currently, the reported V_{OC} values vary depending on the adopted solar cell architecture, but normally are still far away from the thermodynamic limit, which is reported to be 1.32 V for perovskite with a bandgap of 1.6 eV[102], indicating substantial room for efficiency enhancement. As discussed, the V_{OC} of the PSC is determined by the recombination profile in a given architecture. Specifically, according to the continuity equations (Eq. 1.32,1.33), the V_{OC} of the PSC is determined by relative amplitudes of the recombination and output current.

In this chapter, we will discuss the parameters which influence the V_{OC} of the PSC in the PEDOT:PSS/$MAPbI_{3/}$/C_{60} architecture. Different characterization methods will be referred to elaborate the involved mechanisms.

4.1 Measuring V_{OC} - an error-prone operation

The V_{OC} of our perovskite solar cell is usually determined through a normal J-V scan. Through the hysteresis behavior of the PSC makes this simple measurement not so reliable anymore, here we want to address another often-overlooked problem performing this measurement - the mask size issue.

A mask is usually used to confine the illuminated area during the J-V measurement. One reason for using it is to confine the area more accurately. The other reason is to eliminate the potential additional current contribution from the neighbouring area[257][258]. However, there are extra side effects adopting a mask to measure the cell's photovoltaic behavior. In our case, the area of a complete pixel is defined by the overlapping area of the ITO and Ag electrodes. When only the area exposed by the mask is illuminated, the measured solar cell performance is also influenced by the dark area of the pixel[259]. Figure 4.1 demonstrates the processes occurring in a only partial illuminated pixel. In the illuminated area, the charge carrier generates and recombines as in a normal cell, but in the dark area of the pixel, carrier recombination processes still occur. For the dark

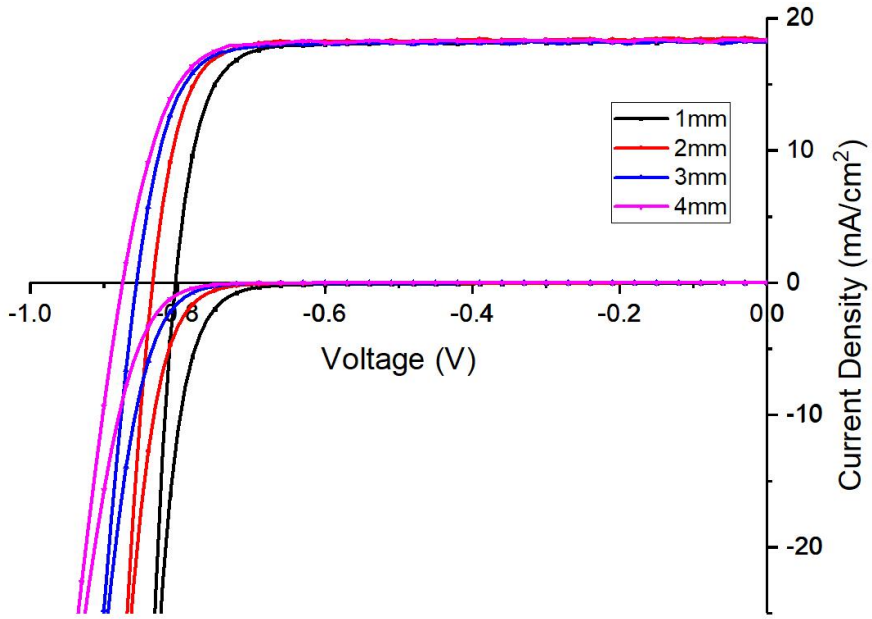

Figure 4.2: The light and dark J-V curve of our typical cell with different mask size. The measurement was scanned forward at 0.1 V/s and the window of the mask is a circle with the diameter labelled in the figure. The pixel size is 25 mm^2.

area, neglecting any carrier diffusion from the illuminated $MAPbI_3$, its behavior is the same as in the dark J-V measurement. The built-up of the potential difference between the ITO and Ag electrodes will inject carriers into the dark $MAPbI_3$ to recombine. This effect appears to enhance the recombination processes of the solar cell and decreases the measured V_{OC}.

Figure 4.2 presents the light and dark J-V curves of our typical cell with different mask sizes. The solar cell parameters and illuminated area ratios are listed in Table 4.1. We see the overall efficiency doesn't change a lot from 12.6% to 50.3% illuminated area. However, the V_{OC} and FF change quite significantly. From an illuminated area ratio of 3.1% to 50.3%, an over 70 mV V_{OC} difference is observed. This result reveals the uncertainty of the measured V_{OC} and FF of the solar cell. Moreover, it is worth mentioning that the dark current density should be calculated based of the whole pixel size. In practice, it is sometimes based on the illuminated area to compare with the light current density curve. The different mask sizes also lead to different calculated series resistances which rely on the slope of the J-V curve at the V_{OC} point.

As discussed, the recombination profile of the solar cell largely determines the V_{OC} and FF of the solar cell. When the illuminated area ratio is changing, the solar cell is in fact not the 'same' cell due to the different additional recombination pathways. The result shown here is, for practical application, exaggerated as the real illuminated ratio in practice is usually over 50%. But it points out the uncertainty of the measured parameters which depend on the illuminated area ratio. Problematically, the literatures usually do not provide the illuminated area ratio values, which makes cross-comparison of the V_{OC} or FF among different studies difficult. As the uncertainly brought by this effect may not

mask window diameter	$V_{OC}(mV)$	$J_{SC}(mA/cm^2)$	$FF(\%)$	$PCE(\%)$	illuminated area ratio (%)
$1mm$	803	18.4	83.2	12.3	3.1
$2mm$	834	18.4	83.9	12.9	12.6
$3mm$	856	18.4	83.0	13.1	28.3
$4mm$	875	18.4	81.7	13.2	50.3

Table 4.1: The influence of mask size on the performance parameters of the cell.

be larger than some other effects as spectra differences of lamps, the illumination intensity uniformity, etc.[198], it is often overlooked. However, paying attention to the illuminated area ratio is still necessary to make sure the cells are measured in a controllable and comparable manner.

4.2 Surface band bending plays a role influencing the V_{OC}

A cell reaches the V_{OC} point when the generated current equals the recombination losses. This argument is valid regarding the whole cell. It doesn't mean that there is no charge transport in the cell. No charge transport leads to a picture where the charge generation and recombination occur at the same positions and cancel out each other. That is usually not true as the charge generation and recombination profile are both position dependent. More specifically, at the V_{OC} point, for any cross section plane in a two dimensional cell model, the net current through the plane is zero (otherwise there will be net electron and holes aggregations at different sides of the plane which would further change the V_{OC}). Hence, based on the drift diffusion equation Eq. 1.34, 1.35,

$$J_n + J_p = qE(\mu_n n + \mu_p p) + qD_n \frac{\partial n}{\partial x} - qD_p \frac{\partial p}{\partial x} = 0 \tag{4.1}$$

at the open circuit condition.

The above equation is only correct at the V_{OC} point when no carriers recombine in external circuits (while the continuity equation is valid in a wider scope). It could be vividly described as the electrons and holes move synchronously to recombine in the 'target' position. The electric field E does not need to be zero or close to zero at the V_{OC} point. Sometimes the built-in field is used to estimate the V_{OC} which is not very precise (the Anderson's rule). A higher built-in field could enhance the drift current and lead to higher V_{OC} given other parameters remain unchanged. But it does not determine the V_{OC} solely. The V_{OC} is determined by both the recombination and the drift/diffusion profiles. Actually, if the recombination rate is low enough, the thermal radiation model predicts a thermal limit of the V_{OC} which does not even depend on the structure of the solar cell. Indeed, bromide-based perovskites have been reported to achieve V_{OC} larger

than the Fermi level differences of ETM and HTM[174][175][176]. Moreover, there are also reports claiming the V_{OC} does not always correlate with the HOMO levels of the HTMs[260][261].

In our primary study, we find the vacuum annealing condition could significantly influence of V_{OC} of our studied PSC with the PEDOT:PSS/$MAPbI_3$/C_{60} architecture (Figure 3.21). In general, with the same cell architecture, the major potential factor causing V_{OC} variations is the recombination profile. However, the TPV measurements show an interesting phenomenon: under the same illumination intensity, the cell with lower carrier life time delivers a higher V_{OC} at the higher illumination intensity regime (Figure 3.24). Under the same illumination intensity, lower carrier life time would mean a faster recombination process and lower carrier population in the device. This should lower the V_{OC} rather than increase it. Back to the continuity equation set (Eq. 1.36, 1.37), the origin of such unusual behavior may be, along with the variation of the recombination profile, the carrier transport process also changes.

Hereby we try to investigate the origins of the V_{OC} variations in our cells in detail. After carefully examining our deposition parameters, we use a different way to influence the V_{OC}. The methods introduced in the last chapter by directly tuning the vacuum annealing time is too sensitive to some unexpected parameters (for example the substrates amount/-material mass in the vacuum chamber during one annealing process), which makes it both time consuming and results variable. Figure 4.3 shows the different annealing processes employed here. In this method, the perovskite films after spin-coating are transferred into a vacuum chamber to promote a quick crystallization process. Afterwards, the films are annealed in three different conditions: under a Petri dish at 90 °C (referred as 90-in), or under N_2 flow (no Petri dish) at 90 °C (90-out) or 100 °C (100-out). Introducing a Petri dish cover during the perovskite annealing process has been reported to greatly influence the crystallinity properties of perovskite films due to the influence of the solvent atmosphere[262].

The SEM images of the resulting films are displayed in the Figure 4.4(a-c). All samples display similarly uniform and compact morphologies without signs of pin-holes. Independent of the annealing conditions, all three types of films are composed of closely packed grains in the range of tens to hundreds of nanometers. The XRD spectra (Figure 4.4(d)) present similar features for all samples with dominating $MAPbI_3$ (110) and (220) peaks implying a preferred orientation[263]. The ultraviolet–visible (UV-Vis) absorption measurements (Figure 4.4(e)) show similar absorbance spectra with a typical steep absorption onset for all samples suggesting a low Urbach energy[264]. The X-ray photoelectron spectroscopy (XPS) was recorded to investigate the surface composition of the three types of perovskite films (Figure 4.4(f)). After normalizing the Pb $4d_{5/2}$ signal of the 90-in, 90-out and 100-out samples, we observed that the relative intensities of the N 1_s and I $3d_{5/2}$ signals display a consistent trend, namely the 90-out sample showed the strongest intensity of N 1_s and I $3d_{5/2}$ signals while the 100-out showed the weakest intensity. This result presents a change in surface stoichiometry of the perovskite films due to the influences of the different annealing conditions. However, as the SEM, XRD and UV-Vis spectra of the different films present similar features, we conclude that these stoichiometric changes are on a small scale.

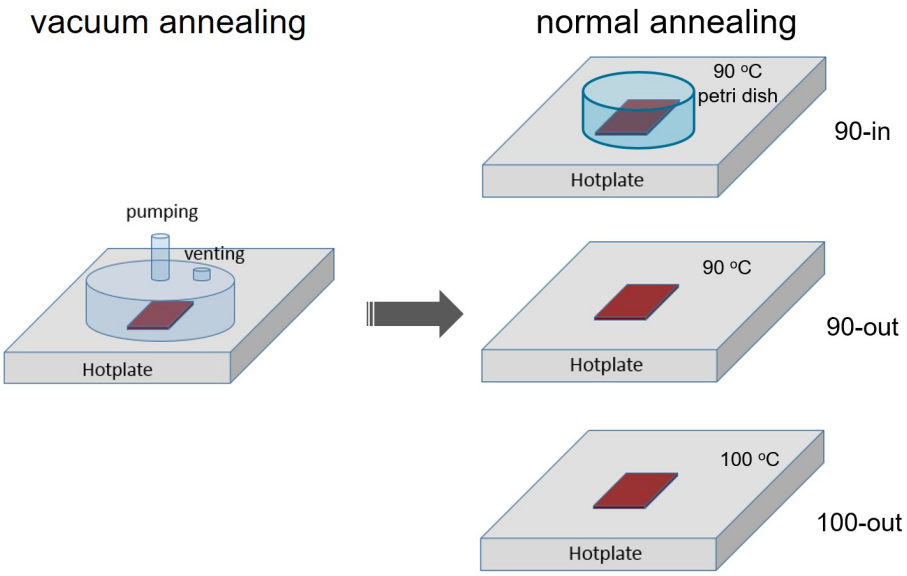

Figure 4.3: Schematic illustration of the perovskite film annealing process. A home-made chamber allows quick pumping and venting operations on a hot plate. The pressure during vacuum annealing step is around 1.5 mbar.

Figure 4.5 (a) displays the typical current density-voltage (J-V) scans for both forward and backward directions. The measurement is conducted from 0 V to 1 V with a scan speed of 0.1 V/s in a N_2 atmosphere without pre-biasing under 1 sun. In general, all devices have the characteristics of an average J_{SC} (16-18 mA/cm2), a high FF (above 70%), a V_{OC} lower than 1 V (between 0.75 V and 0.9 V) and negligible hysteresis behavior, which agree well with relevant reports on PDDOT:PSS based perovskite solar cells[143][182]. The main variations between our differently treated samples lie in the V_{OC} values as expected, with 90-in sample reaching around 0.88 V, 90-out sample 0.81 V and 100-out sample 0.78 V respectively. A statistical distribution of the V_{OC} of 90-in, 90-out and 100-out samples is given in Figure 4.6, showing a distinct trend. In Figure 4.5(b-d), the trackings of the V_{OC}, J_{SC} and power conversion efficiency are presented. It is worth mentioning that the V_{OC} tracking curves of 90-out and 100-out samples show a long stabilization process (Figure 4.5(b)) which correlates with the V_{OC} variations between the forward and backward scans in Figure 4.5(a). The V_{OC} modifying effect shown here is similar to that addressed in the last chapter by adjusting the vacuum annealing time. The reason may be the vacuum annealing and the following normal annealing have a certain combined function mechanism affecting the film quality. Moreover, the new processing method is more controllable and convenient in practice.

In the above discussions, a lot of underlying factors influencing the V_{OC} have been introduced based on the detailed balance model and continuity equations which are described earlier. These models provide a complete solution of the solar cell system to elucidate the underlying principles. On the other hand, we can use a more dynamic point of view to evaluate the cell. In this study the device architecture remains identical, including the ETM and HTM, the V_{OC} variations are ascribed to the changes of the $MAPbI_3$ layer which further influence the charge carrier populations in the transporting layers.

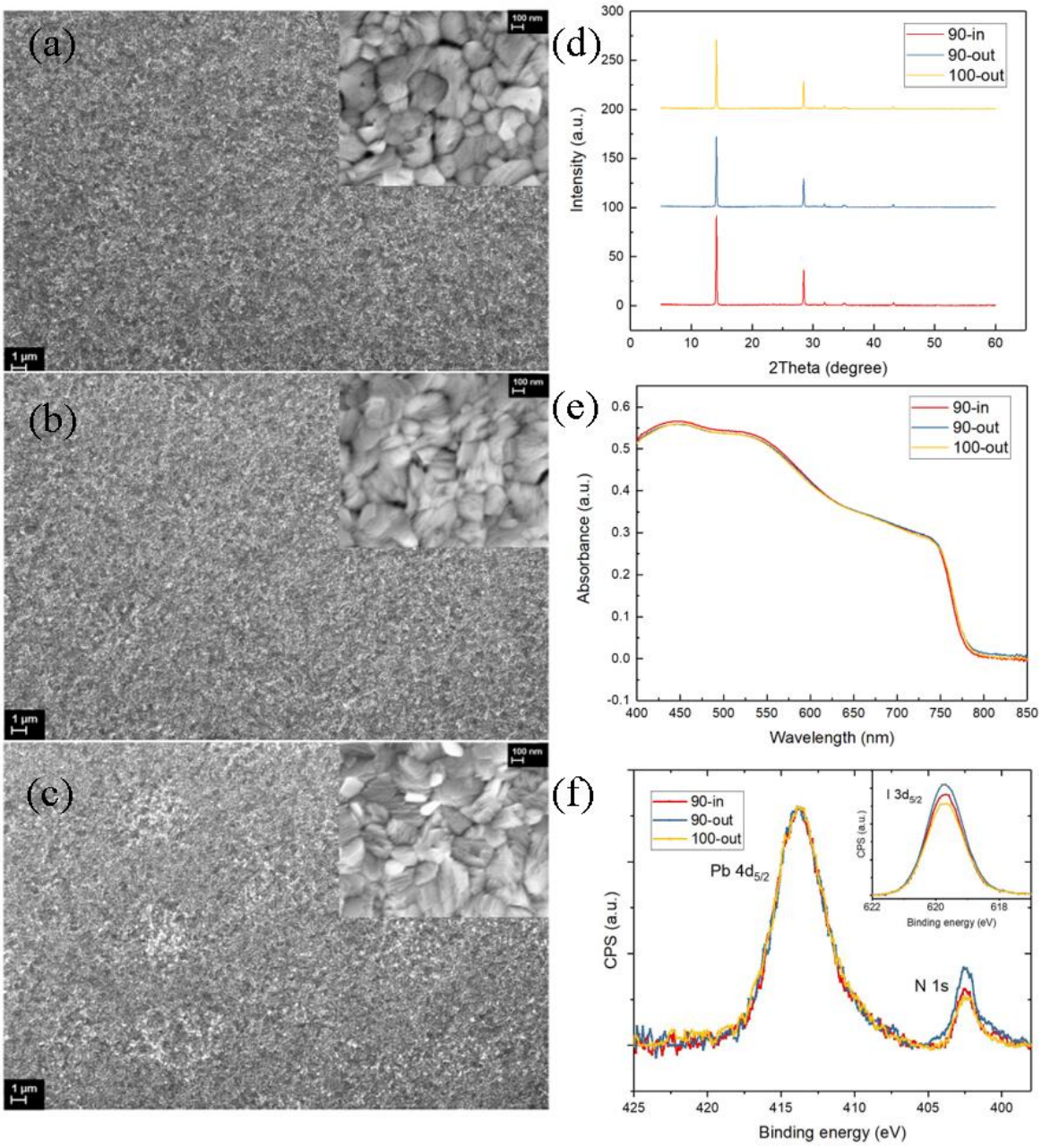

Figure 4.4: (a) 90-in, (b) 90-out and (c) 100-out samples top-view morphologies. Inset shows the zoom-in morphology at higher magnification.(d) The XRD spectra of 90-in, 90-out and 100-out samples.(e) The UV-Vis absorbance spectra of 90-in, 90-out and 100-out samples.(f) The XPS spectra of the 90-in, 90-out and 100-out samples. All spectra have been normalized based on the Pb 4d5/2 peak to remove any signal intensity deviation caused by systematic errors.

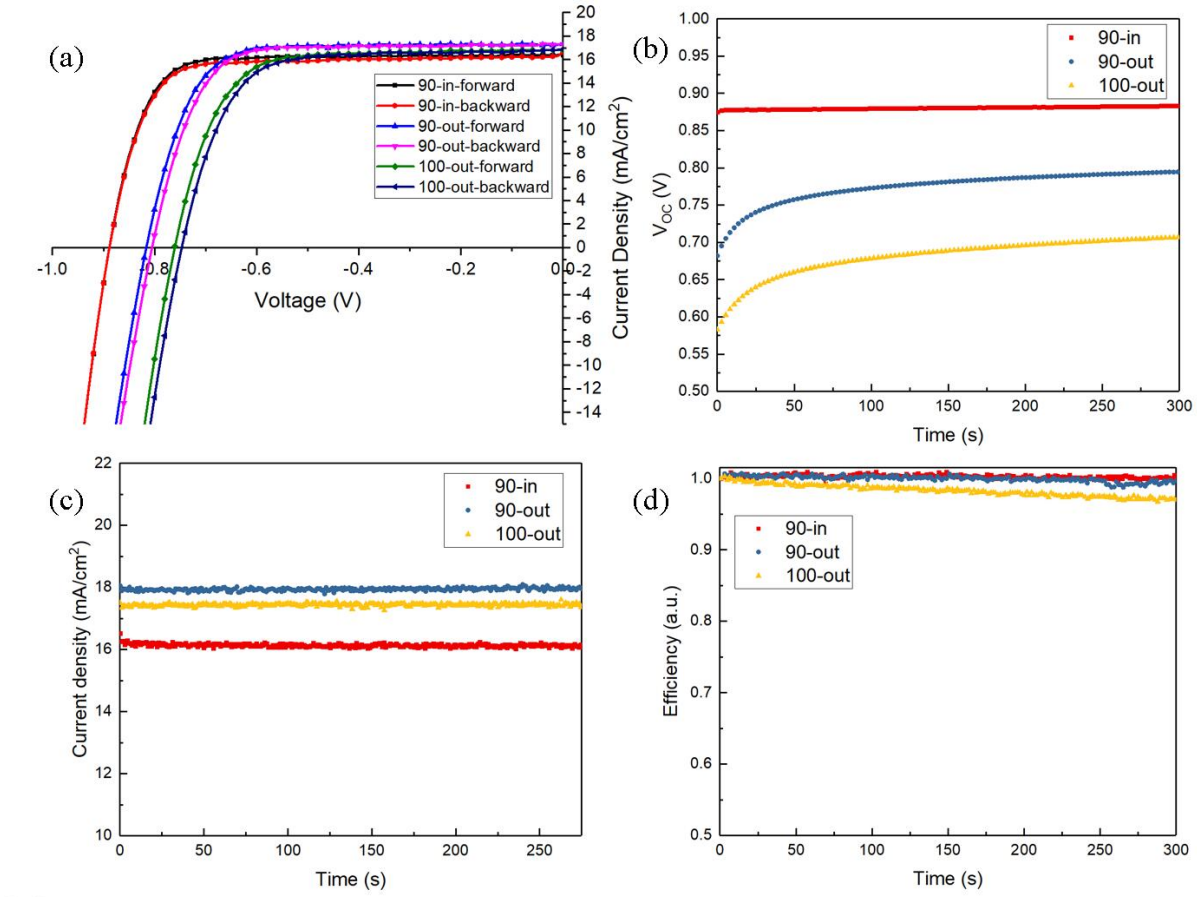

Figure 4.5: (a) Forward and backward J-V scans of 90-in, 90-out and 100-out samples.The tracking curves of 90-in, 90-out and 100-out samples, including: (b) V_{OC}, (c) J_{SC} and (d) normalized efficiency. These measurements were performed successively.

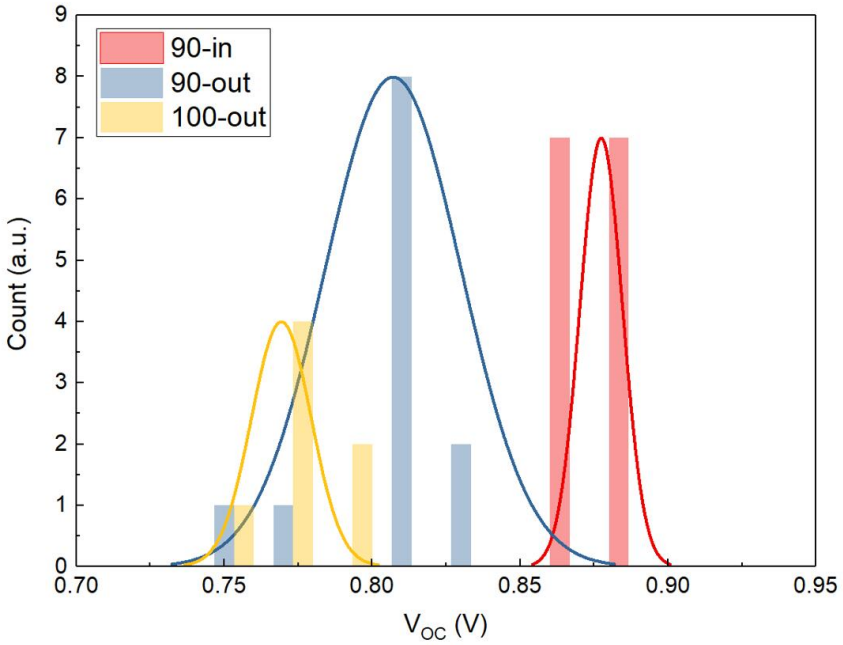

Figure 4.6: The statistical distribution of the V_{OC} of 90-in, 90-out and 100-out samples.

And the charge carrier population of the transporting layers under open circuit condition is influenced by the dynamic interfacial charge injection and recombination process. For either interface (PEDOT:PSS/ $MAPbI_3$ or C_{60}/ $MAPbI_3$), at V_{OC} condition, the recombination current at the interface (J_{rec}) is equal to the injection current from the perovskite to the transporting material (J_{inj})[212],

$$J_{rec} = J_{inj} \tag{4.2}$$

A decrease in V_{OC} is ascribed to the decrease of J_{inj} or/and increase of J_{rec}, as the density of states (DOS) together with the band structures of the ETM and HTM remain unchanged in our samples. Among others, the decrease of J_{inj} could be due to a decrease of the charge carriers generation rate, an increase of the recombination rate, or a decrease of the injection rate. The increase of J_{rec} could be due to an increased interfacial recombination rate. We suggest that the charge carrier generation profile is unlikely to vary as the absorption spectra of our samples are very similar (Figure 4.4(e)). However, as revealed by XPS measurements, the observed changes in surface stoichiometry could possibly affect the trap-assisted recombination or the charge collection process by influencing, for example, the trap state density[182][103] or the interfacial ion aggregation[64][188]. Note that in general only the recombination profiles could change the V_{OC} of a cell, however, the change of the charge collection process may change the charge carrier distribution across the cell, indirectly affect the recombination processes and influence the V_{OC}.

Light intensity dependencies of the V_{OC} and FF are investigated to gain insight into the recombination behavior in the solar cells (Figure 4.8). According to the simplified Shockley model, the V_{OC} and J_{SC} should follow the relation[265],

$$\frac{\partial V_{OC}}{\partial J_{SC}} = \frac{S k_B T}{q} \tag{4.3}$$

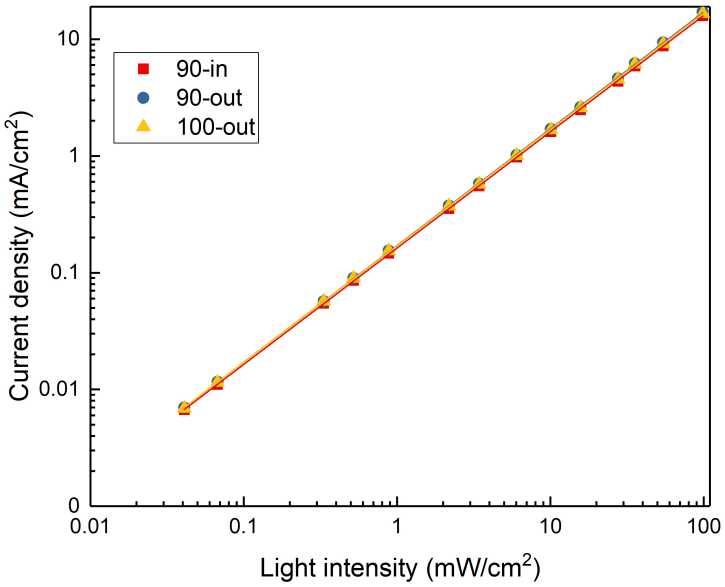

Figure 4.7: The light intensity dependent measurement of J_{SC}. The extracted α value according to $J_{SC} \propto I\alpha$ is 0.996, 0.999, 0.997 for 90-in, 90-out and 100-out sample respectively.

Where S is the ideality factor. Since J_{SC} is directly proportional to the light intensity (I) (Figure 4.7), V_{OC} will increase with increasing I, characterized by a slope (S) of "k_BT/q" when plotting against the natural logarithm of I. The value of S is typically indicative of the type of the dominant recombination mechanism in the devices: S=1 represents bimolecular recombination and S=2 represents trap-assisted recombination[266]. It is worth mentioning that the bimolecular recombination is not limited to the radiative recombination. The interfacial recombination between the minor carriers and the adjacent transporting layer may also be bimolecular as reported for the PEDOT:PSS interface[267]. In this study, the S values extracted based on Eq. 4.3 are shown in Figure 4.8(a).

The slope S gradually increases from S=1 for 90-in, S=1.03 for 90-out to S=1.21 for 100-out sample, suggesting the trap-assisted recombination is gradually enhanced in our devices. We see the reason for this enhancement of recombination in the slight stoichiometric change of the $MAPbI_3$ films (Figure 4.4(f)) due to the different annealing conditions, which leads to a different density of crystal defects and trap-states. According to the above discussion, the increase of trap-assisted recombination will lead to the decrease of the V_{OC} if other parameters remain unchanged. Another interesting feature in Figure 4.8 (a) is the decreased light intensity dependence of the V_{OC} at higher light intensities for 100-out sample. This feature has been discussed in both perovskite and organic solar devices, and the turning point is reported to locate at where the V_{OC} approaches built-in field limits[267][268]. According to this explanation, we anticipate that the built-in electric field differs among our samples.

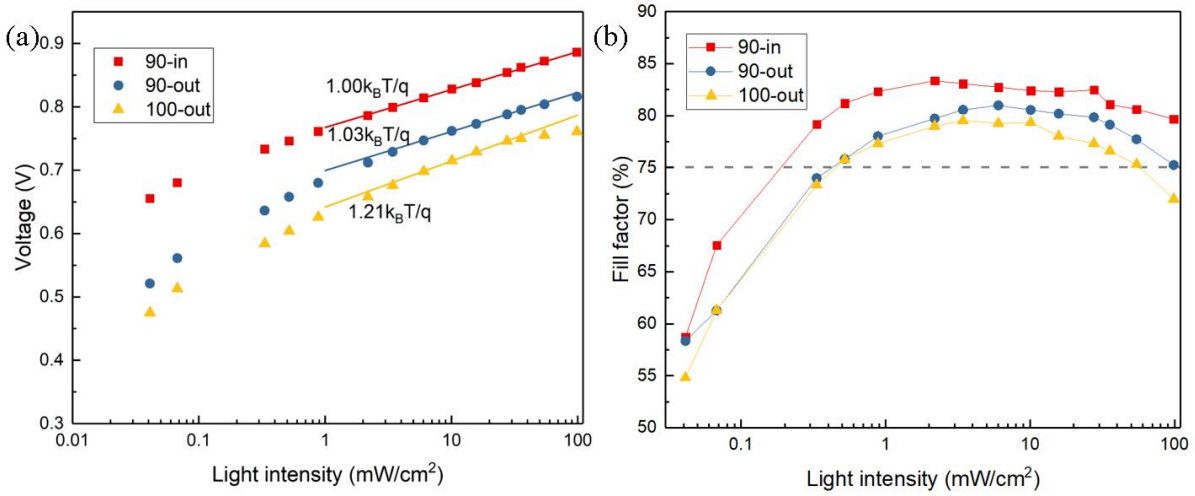

Figure 4.8: Light intensity dependent measurement of (a) $_{OC}$ and (b) FF. In Figure (a), the slope is calculated in natural logarithm scale but presented with decimal scale for clarity. The values of S are marked for each sample. In Figure (b), the dashed grey reference line at 75% is used to guide eyes.

The light intensity dependent FF measurements are displayed in Figure 4.8(b). In a working solar cell with certain external load, the photo-generated charge carriers either recombine in the device or reach the external circuit. The FF qualitatively indicates the relative weight of these two pathways at the maximal power point. Higher FF implies more charge carriers could be injected into the external circuit while lower FF implies more charge carriers recombine inside the device. We note a clear trend for the FF dependency on the light intensity. From 0.0004 sun to 0.1 sun, the FF curves of all samples show an increase till stabilization trend. At this lower light intensity region, the main recombination loss is ascribed to trap-assisted recombination pathway, and the enhancement of the FF with increasing light intensity is then attributed to the diminished influence of the trap-assisted recombination. In addition, the fact, that the 90-in sample shows the highest FF while the 100-out shows the lowest FF at lower light intensities, suggests that for 90-in sample the trap-assisted recombination loss is lower than 90-out and 100-out samples, which is in accordance with the light-intensity dependent V_{OC} trend. As the illumination intensity further increases, we observe the FF of all samples decreases, where the FF of the 90-in, 90-out and 100-out samples decreases 3.3%, 7.5% and 9.2% of their initial values from 0.1 to 1 sun respectively. At the high illumination regime, as charge carrier density further increases, the bimolecular recombination gradually becomes more dominant in the devices[269]. Therefore, the different FF behavior near 1 sun light intensity is ascribed to the influence of bimolecular recombination. We note that considering the lower illumination intensity and cell's V_{OC}, the bimolecular recombination we refer here is unlikely to be the radiative recombination. We suggest the dominating recombination pathway which limits the V_{OC} is the interfacial bimolecular recombination which may locate at the PEDOT:PSS/$MAPbI_3$ interface.

These light intensity dependent V_{OC} and FF results show that the trap-assisted recom-

bination is varied by the different annealing conditions and increases from 90-in, 90-out to 100-out samples, which is in good accordance with the observed decrease in V_{OC} among our samples. However, a detailed look indicates that the increased trap-assisted recombination is not the only influencing factor. We observe in Figure 4.8(a) that for 90-in and 90-out sample, the S values increase marginally from 1 to 1.03 while the V_{OC} drops 70 mV. On the other hand, for 90-out and 100-out sample, the S values increase from 1.03 to 1.21 along with only 30 mV V_{OC} drop. Additionally, the S value of PEDOT:PSS based perovskite solar cells has been reported to be close to 1[182]. Compared to a regular n-i-p architecture, the discrepancy of the lower V_{OC} is suggested to arise from strong surface bimolecular recombination originated from poor hole selectivity of PEDOT:PSS layer[267]. This explanation implies a weak influence of trap-assisted recombination, as the bimolecular recombination would already be significant in the devices, especially under higher illumination intensities. Moreover, these light intensity dependencies of V_{OC} and FF indicate differences in the built-in fields and bimolecular recombination behavior among the samples. The built-in field is directly related to the charge collection process, while the bimolecular recombination behavior could also be strongly affected by the charge collection dynamics. Therefore, these distinguished features suggest that the suppression of charge collection may also play a role in determining the solar cell's V_{OC}.

Several factors could lead to the variations of the built-in field, for example, doping treatment may change the width of the depletion region and thus the distribution of the built-in field. However, as the halide perovskites have been reported with the ion aggregation feature which may neutralize the built-in field[64][188], we suspect it may be also the formation of surface dipoles which influences the built-in field.

The Mott–Schottky (MS) analysis was firstly tried on the devices to gain more insight into the built-in field scenario. The Mott-Schottky equation

$$\frac{1}{C^2} = S(V - V_{FB} - \frac{k_B T}{q}) \tag{4.4}$$

is often used to determine the flat band potential (V_{FB}) of semiconductors in contact with electrolytes[270][271]. The V_{FB} is equal to the built-in potential in a solar cell and the term k_BT/q is negligible in practice. The most common method for the capacitance (C) determination is through impedance spectroscopy technique. By applying a small perturbation AC potential $\widetilde{V}$ at a given angular frequency ω, the AC current response $\widetilde{I}$ is monitored. The impedance

$$\widetilde{Z} = \frac{\widetilde{V}}{\widetilde{I}} \tag{4.5}$$

And the capacitance is the real part of the complex capacitance

$$\widetilde{C} = \frac{1}{i\omega\widetilde{Z}} \tag{4.6}$$

$$C = -\frac{Z''}{\omega|Z|^2} \tag{4.7}$$

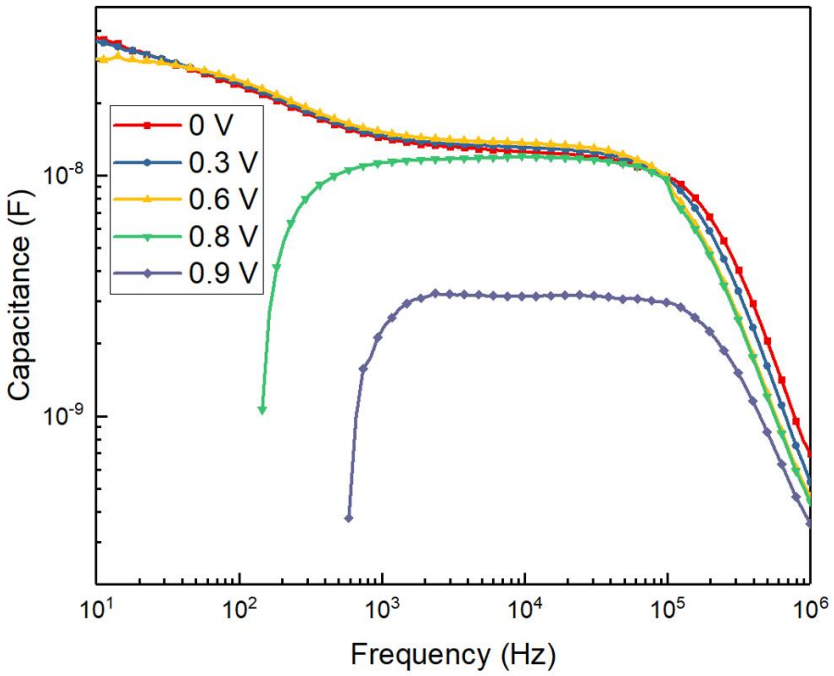

Figure 4.9: The capacitance versus frequency curves calculated from the impedance measurement at different bias in the dark.

Where Z" is the imaginary impedance and $|Z|$ is the modulus of $\widetilde{Z}$. The capacitance is typically displayed as a function of the measuring frequency f ($\omega/2\pi$). And for the MS analysis, a certain f needs to be selected.

Figure 4.9 presents the capacitance changing trend with the frequency at different biases. It has been suggested that the capacitance behavior is related to the the electrode polarization at high frequencies and ion accumulation at low frequencies. And the middle frequency range with the plateau is suggested to be related to the depletion layer capacitance[272]. So we choose a frequency of 10 kHz to perform MS analyses.

Figure 4.10 presents the Mott-Schottky curves of the 90-in and 100-out solar cells. An unexpected feature that the capacitance decreases from certain bias appears. This behavior is very strange as the theory predicts the capacitance would increase with decreasing depletion width due to the increasing bias. This feature seems to arise from the unstable internal field of the PSC. We measured the dependence of the capacitance on the solar cell pre-treatments, and we see that from certain bias, the behavior of the capacitance does depend on the pre-treatments (Figure 4.11). This result indicates the instability of the cell interferes with the MS analysis.

We checked if the interference could be suppressed with lower temperatures as it may come from internal ion movement. Indeed, at liquid nitrogen temperature, the interference is suppressed and the capacitance growth starts from a larger bias (1.15 V vs 0.8 V) (Figure 4.12). However, we still can not extract the built-in field value as the results may have be distorted before the turning point. In short summary, we tried to use the MS analysis

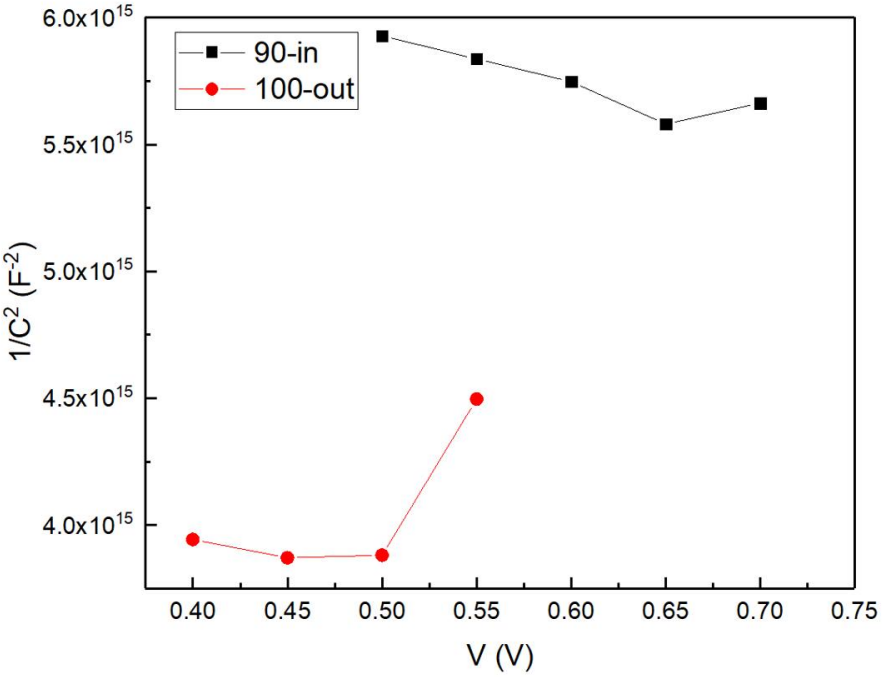

Figure 4.10: The Mott-Schottky curves of the 90-in and 100-out samples.

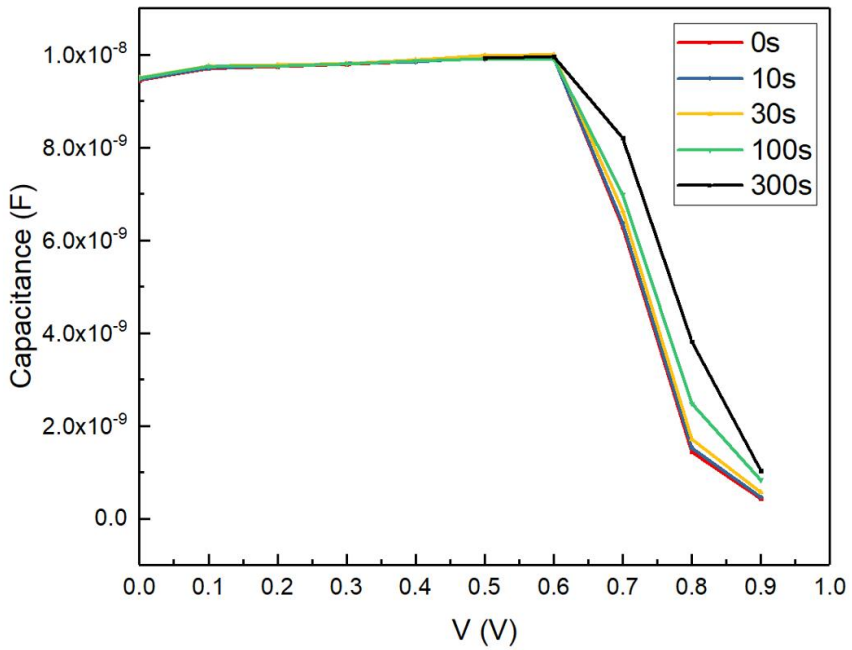

Figure 4.11: The capacitance values of the 90-in sample at 10 kHz after pre-biasing at each points for different time.

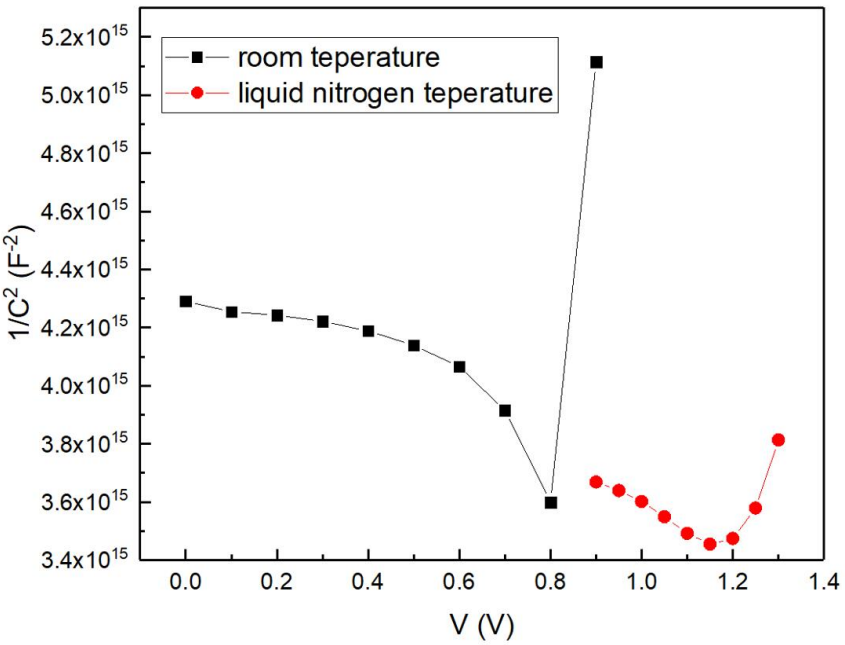

Figure 4.12: The Mott-Schottky curves of the 90-in samples at room and liquid nitrogen temperatures.

to extract the built-in field information but it didn't work out due to certain dynamic process inside the cell. We see that the 90-in sample shows a higher turning point bias than the 100-out sample which could be ascribed to a higher stability (Figure 4.10).

Besides the MS method, KPFM could also provide insights into the built-in field profile by shedding light onto the distribution of the surface potential. We firstly calibrate the potential values using freshly cleaved highly oriented pyrolytic graphite (HOPG) as reference (Figure 4.13). Afterwards the surface potential of the studied films on glass was measured and calibrated (Figure 4.14, Table 4.2). The close correlation between topography and potential profile is clearly observed, and an apparent potential drop is found across 90-in, 90-out and 100-out sample (Table 4.2). This decrease in the surface potential indicates a downward shift of the $MAPbI_3$ Fermi levels.

This downward shift could be due to an aggregation of surface charges or p-type doping of the $MAPbI_3$ film. To further clarify the built-in field profile, we also need to ascertain if the shift localizes only at the surface or extends into the bulk. To sort these doubts, we further use PESA to determine the valence band position of these $MAPbI_3$ films (Figure 4.16 and Table 4.2). The PESA characterization method is a surface sensitive technology, as only the top surface photoelectrons (several to hundreds of Å) could escape from the sample and get detected. In contrast, though the KPFM technology measures the surface potential, the result is also influenced by the properties of the bulk and the underlying layer, depending on the sample conductivity, doping level and so on. The above argument is well supported both in literature and in our experiments[274]. We measured the KPFM and PESA of $MAPbI_3$ both on glass and on PEDOT:PSS film (Figure 4.15). And the results show that the work function of PEDOT:PSS determines that of the upper $MAPbI_3$

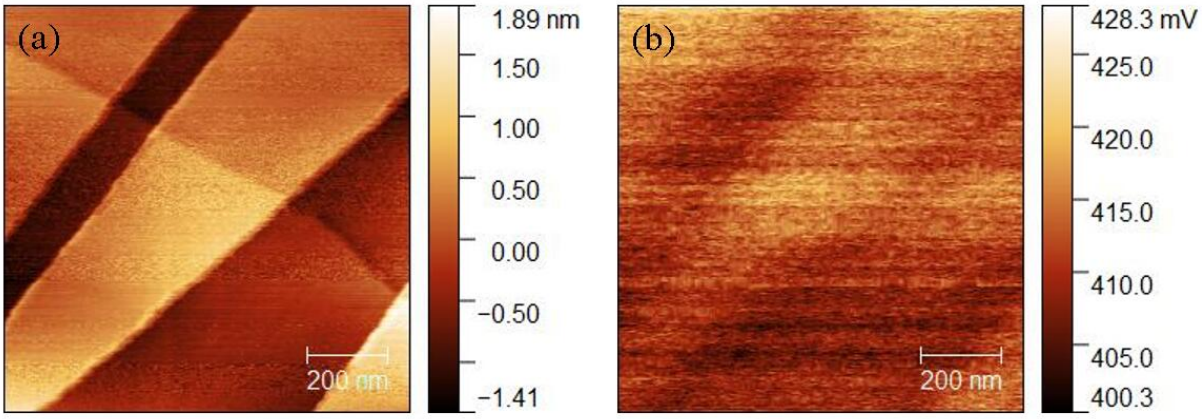

Figure 4.13: The (a) topography image and (b) potential profile of HOPG measured by KPFM. The root mean square (RMS) roughness is 0.56 nm, the mean potential is around 415 mV with 3.6 mV RMS. Based on the reported HOPG work function of -4.6 eV[273], the tip work function was calculated to be -5.015 eV.

sample	RMS roughness (nm)	average potential (Fermi level) (eV)	RMS potential (mV)	valence band position (eV)
90-in	10.6	-4.56	41.2	-5.34
90-out	7.9	-4.69	25.4	-5.46
100-out	8.1	-4.78	26.5	-5.49

Table 4.2: The surface topography root mean square (RMS) roughness, surface average and RMS potential and valence band position of the differently annealed $MAPbI_3$ films. The RMS roughness, surface average and RMS potential data are collected by the KPFM, the valence band position is determined by the PESA.

layer. The work function shifts from -4.47 eV to -5.02 eV which is close to that of the PEDOT:PSS itself[275][276]. While PEDOT:PSS has minor (if at all) influence on the PESA results.

The determined valence band positions of the PESA measurements are summarized in Table 4.2, presenting different energy levels at the sample surfaces. We observe that the valence band positions are also lowered among the samples. Hence, the p-type doping effect seems unlikely as it would not lower the valence band position, and the charge aggregation is more likely to occur. As the differences in the values of the PESA measurement among the samples are comparable to those of the KPFM measurement (especially between the 90-in and 90-out sample), we infer that the change of the potential energy only locates at the top surface of the perovskite films. This result agrees with a picture of surface band bending where both valence band position and Fermi level are synchronously influenced.

We notice that RMS potential is quite large in our samples compared to relevant

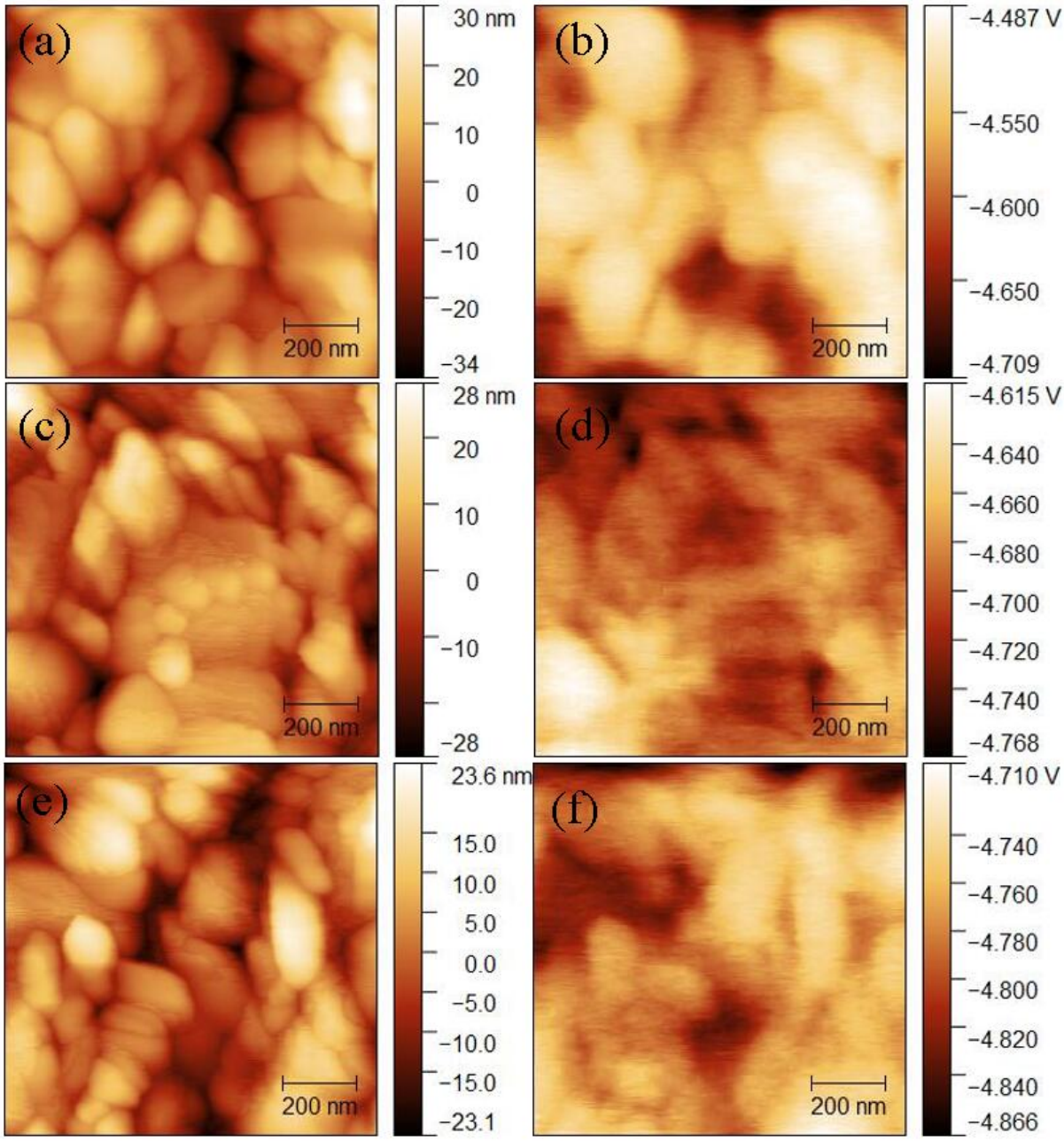

Figure 4.14: KPFM images (the left column shows topography images and right column shows surface potential profiles) of (a) (b) 90-in, (c) (d) 90-out and (e) (f) 100-out $MAPbI_3$ films.

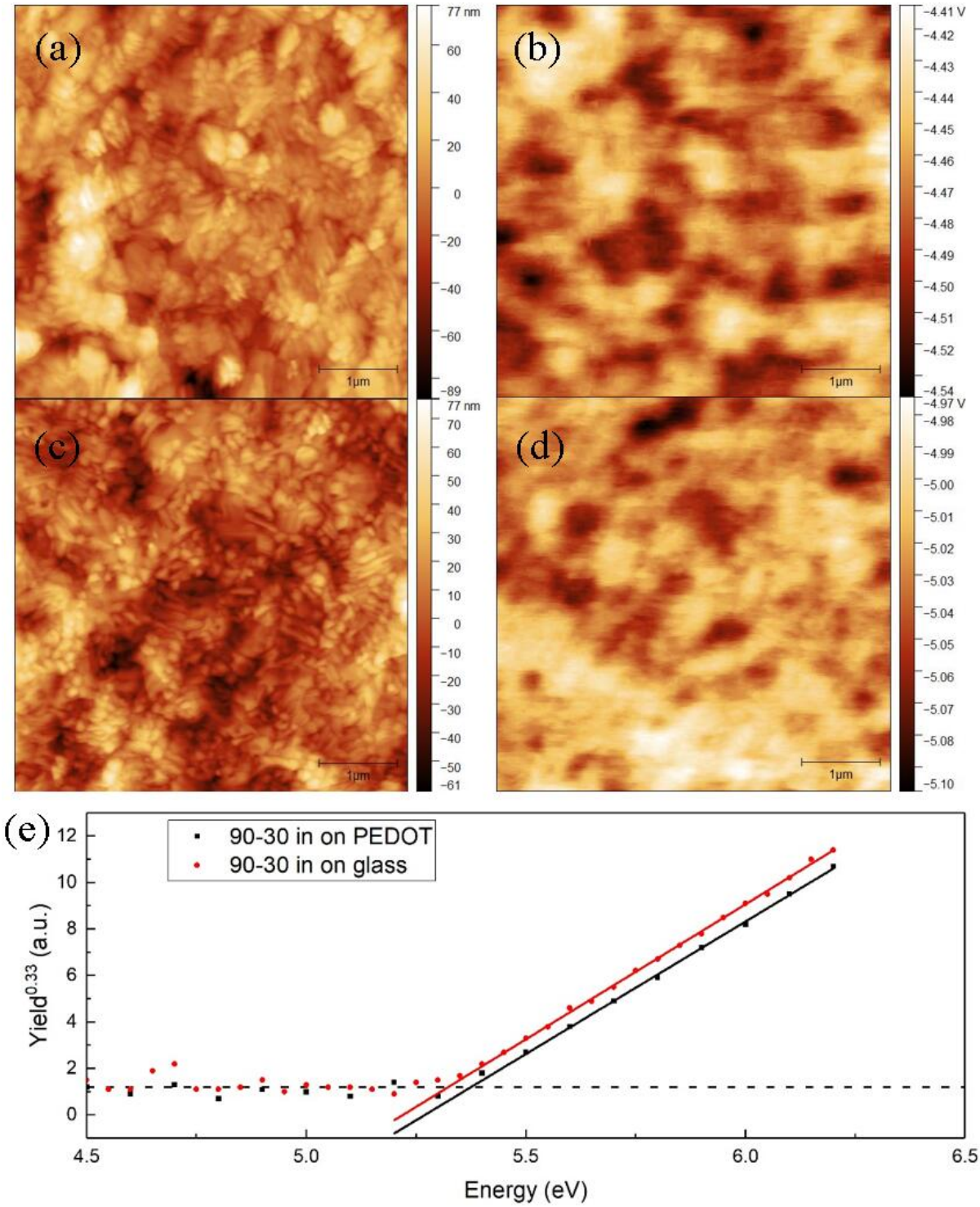

Figure 4.15: KPFM images (the left column shows topography images and right column shows surface potential profiles) of (a) (b) 90-in on glass, (c) (d) 90-in on PEDOT:PSS; (e) the PESA results of the 90-in on glass and 90-in on PEDOT:PSS samples, the minor valence band position shift may come from the different $MAPb_3$ crystalline conditions on different substrates.

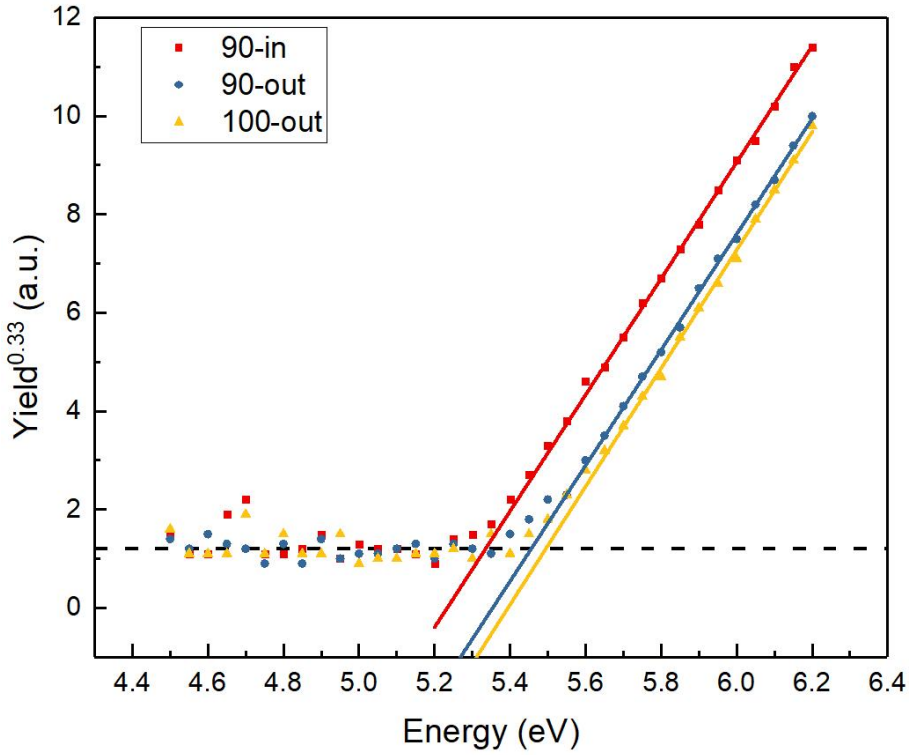

Figure 4.16: PESA measurements of 90-in, 90-out and 100-out samples on glass.

reports[277][278], and a drastic fluctuation over 100 mV is seen across a line potential profile in 90-in sample. Moreover, the RMS potential decreases from 41.2 mV to 25.4 mV between 90-in and 90-out sample, suggesting the surface potential profile undergoes a significant change because of the annealing conditions. These phenomena indicate the variability of the surface potential which could favor the formation of the surface band bending. The surface band bending model is in agreement with the hypothesis Belisle et al. proposed[260]. They found the ionization potential (IP) of HTM only had marginal influence on the V_{OC} of solar devices. They suggested that surface charge effect may be the explanation for the independence of V_{OC} on contact work functions. Surface defect, surface dipoles or ionic accumulation were suggested to be possible charge origins. As the XPS measurements in Figure 4.4 (f) indicate a stoichiometric change of surface compositions, we suggest that charged surface defects may arise from different annealing treatments.

In short summary, we used KPFM and PESA to probe the surface energetic profile of halide perovskites. We find that the $MAPbI_3$ films prepared by different annealing conditions have different surface potentials which are ascribed to charged defects at the surface. This will lead to the surface band bending and consequently influence the built-in field. We see this is another origin of the V_{OC} variations among the studied conditions.

Based on surface band bending, we propose a model to explain the correlation between the V_{OC} and surface band bending (Figure 4.17). Briefly, the surface band bending screens the built-in field in the bulk. The charge transport in the bulk is then inhibited due to the decreased built-in field, which leads to the suppressed charge injection to the transporting

layers. The model proposed here agrees well with the light intensity dependent V_{OC} and FF results. At higher illumination intensities, when the bulk built-in field approaches zero ((Figure 4.17 (f)), the surface band banding model reasonably justifies the existence of low S value and strong bimolecular recombination in Figure 4.8. The influence of perovskite band bending on V_{OC} is also supported by other studies. For example, Xiao et al. reported the giant switchable photovoltaic effect where external biasing determined the cathode/anode direction[172]. Zhang et al. reported a monotone V_{OC} variation trend with the applied electric field during annealing[279].

The influence of the built-in field modification on V_{OC} by ion aggregation has been implied in the study of hysteresis phenomena. However, the effect temporarily depends on the 'state' of the solar cell. Hereby, on the other hand, we see the variation of the V_{OC} by the annealing treatment is more permanent, though the stability of the V_{OC} is different among the samples (Figure 4.5(b)). This instability can be correlated to ion movement which is probed by the transient ionic current measurements (Figure 4.18). The calculated density of the movable ions is 1.4 x 10^{17} cm^{-3} for 90-in, 4.6 x 10^{17} cm^{-3} for 90-out and 5.5 x 10^{17} cm^{-3} for 100-out sample, respectively. We think our different annealing conditions create charged defects at the surface which are partial movable.

In conclusion, we have presented that a controlled variation in the V_{OC}s of perovskite solar cells by up to 100 mV can be achieved by slight variations in the $MAPbI_3$ film preparation process. While no significant changes in the morphology of the differently annealed perovskite films are observed, we identify the small stoichiometric changes at the film surface lead to increased trap-assisted recombination and suppressed charge collection due to the surface band bending. Considering that the reduction in FF at higher light intensities in this study is much more pronounced in comparison with reported silicon, organic and other perovskite solar cells[280][281][282][283], we suggest the suppression of charge collection to be a strongly influential effect. For the PSC, besides the recombination profiles, the built-in field seems also a susceptible parameter influencing the cell parameters.

4.3 Using plasma treatment to modify the V_{OC} of the PSC

The above results reveal an interesting point that the built-in field could be modified to change the V_{OC} with the existing cell architecture. This concept is further applied by performing plasma treatment on the perovskite films to check if we can further improve the cell's V_{OC}.

The plasma treatment is to use ionic gas atoms to bomb the sample surface. Typically it is used for surface modification such as changing the surface wetting property by ion attachments[284]. We think the plasma treatment could leave certain charged ions on the perovskite surface which may modify the V_{OC} of the resulting cell. In addition, it is meaningful to look at the effect of the plasma treatment on perovskite, as the magnetic sputtering which is often used to deposit upper layers on perovskite could introduce a

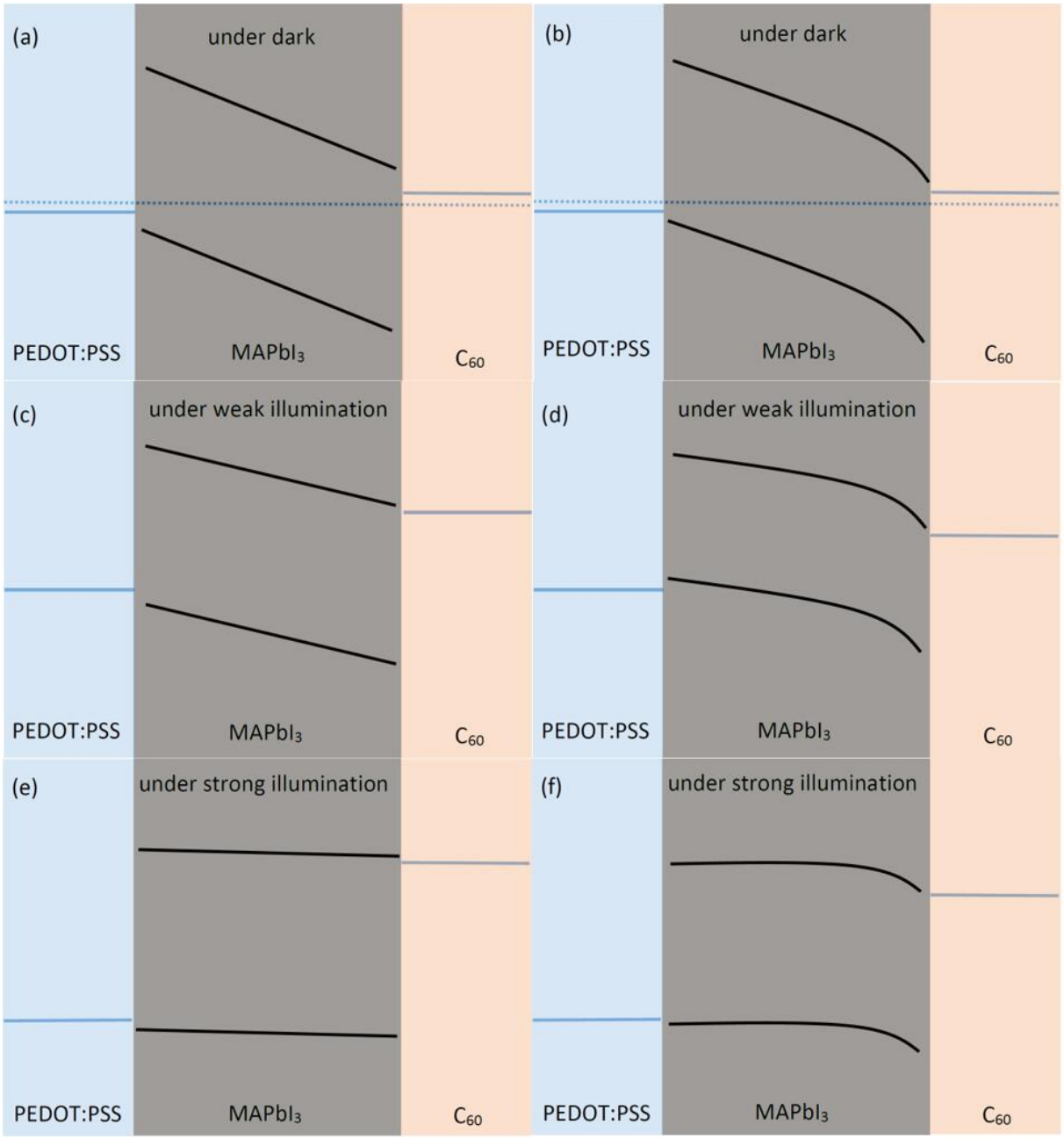

Figure 4.17: Diagram of band structure at open circuit condition without (a)(c)(e) and with (b)(d)(f) surface band bending. The downward bending diagram is given according to the KPFM and PESA characterization results. (a-b) shows the open circuit band structure in the dark, the dashed blue line indicates the Fermi level across the device; (c-d) shows the open circuit band structure under lower light intensities. With surface band bending, the reduced built-in field in bulk perovskite leads to suppressed charge transport, which results in lower V_{OC}; (e-f) shows the open circuit band structure at higher light intensities. The bulk built-in field in perovskite layers is too weak to sustain efficient charge transport and injection.

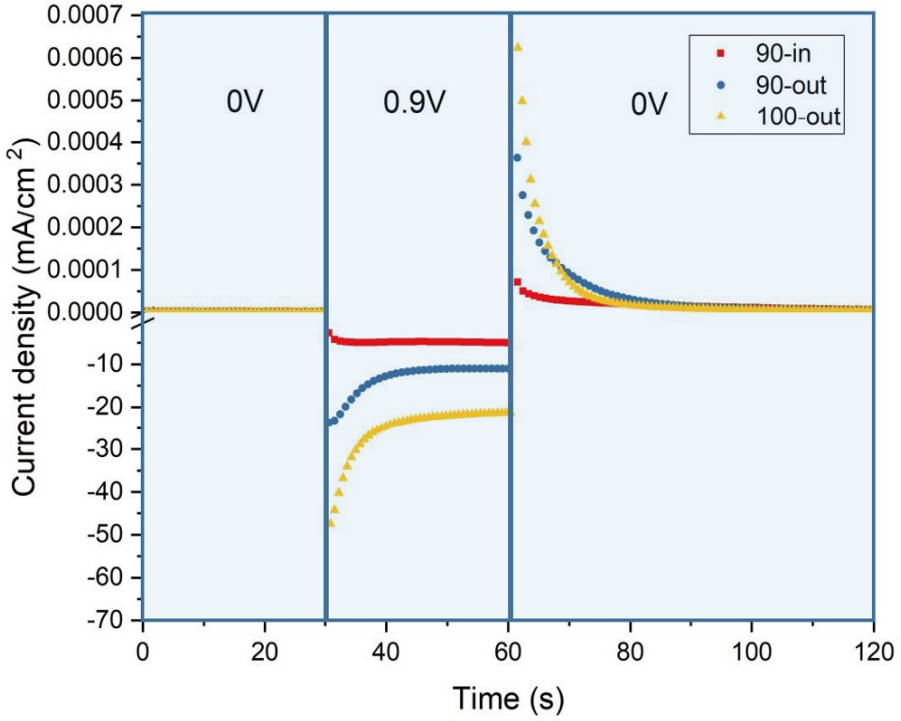

Figure 4.18: The transient ionic results of 90-in, 90-out and 100-out device samples.

plasmonic environment and lead to unknown side effect to the perovskite film. Another consideration is that the introduced ions by the plasma may shed some light on the ionic movement feature in the device. We note that the plasma treatment may be an easy and convenient way to introduce additional electric fields but the charged surface may not be very stable.

Firstly we use oxygen plasma to treat the perovskite films for different time. The J-V behaviors of the corresponding cells are shown in Figure 4.19. The V_{OC} increases from 0.88 V of 0 s to 1.04 V of 10 s. This results suggest that the plasma treatment could improve the V_{OC}, however, at the same time the J_{SC} is suppressed a lot and the overall efficiency also drops.

The light intensity dependent J_{SC} and V_{OC} were measured to analyze the carrier transport and recombination behavior (Figure 4.20). The extracted α and ideality factor values are listed in Table 4.3. We see the α and ideality factor value gradually increase from 0 to 10 s treatment time. The larger α could be explained by suppressed carrier transport at lower illumination intensity. And the larger ideality factor is due to enhanced trap-assisted recombination. We see the oxygen plasma treatment leads to suppressed charge transport and larger trap-assisted recombination loss.

The XRD spectra indicate that with the oxygen plasma treatment, the perovskite decomposes, giving rise to a small amount to PbI_2 and lower intensity of the $MAPbI_3$ peaks (Figure 4.21). We suggest the oxygen plasma treatment induces more defects on the surface and suppresses the charge collection due to the forming energy barrier, and

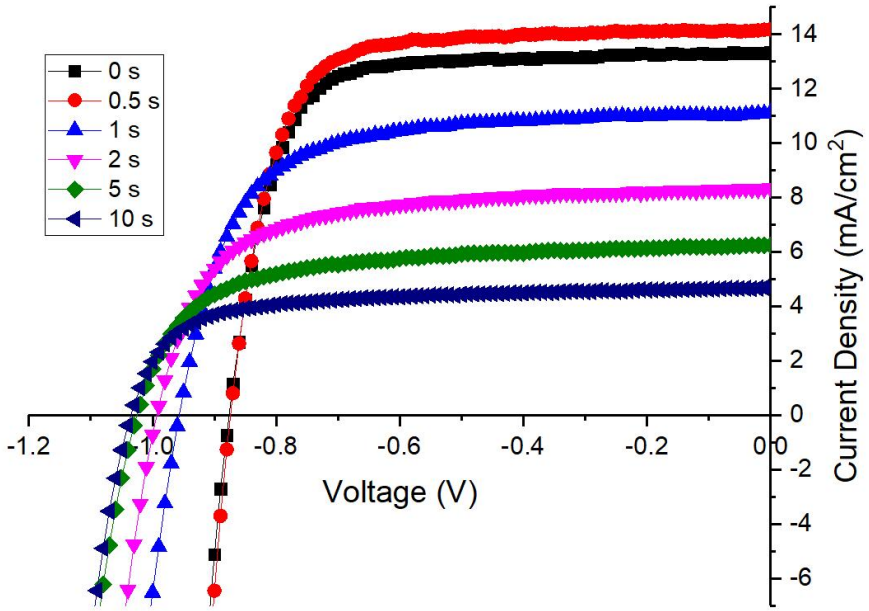

Figure 4.19: The J-V behaviors of the PSC with different oxygen plasma treatment time of 0 s, 0.5 s, 1 s, 2 s, 5 s, 10 s.

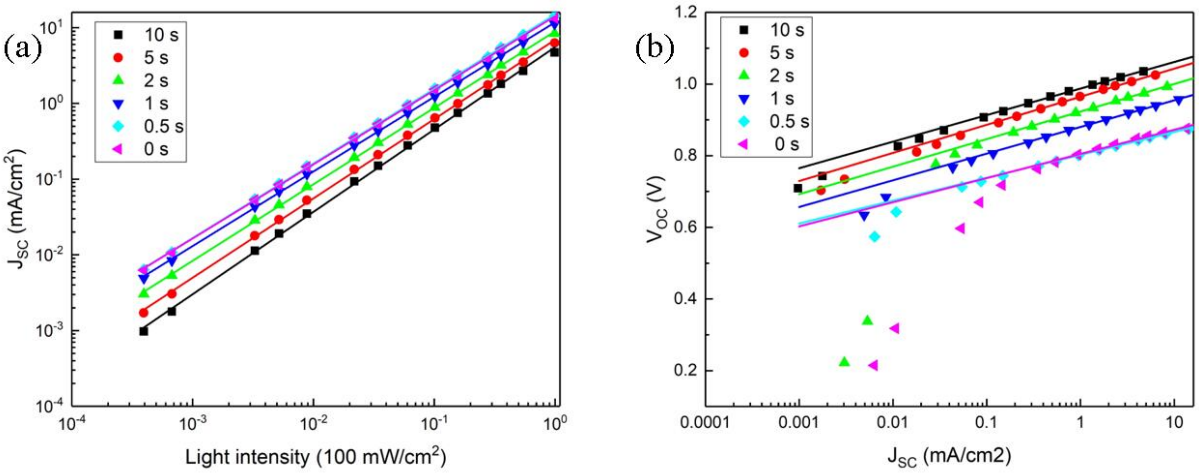

Figure 4.20: Light intensity dependent measurement of (a) J_{SC} and (b) V_{OC}. In Figure (b), the light intensity is in natural logarithm scale but labeled in decimal digits for clarity.

\	0 s	0.5 s	1 s	2 s	5 s	10 s
α	0.98	0.98	0.99	1.01	1.05	1.09
ideality factor	1.12	1.07	1.25	1.29	1.31	1.24

Table 4.3: The extracted α and ideality factor values for different oxgen plasma treatment time.

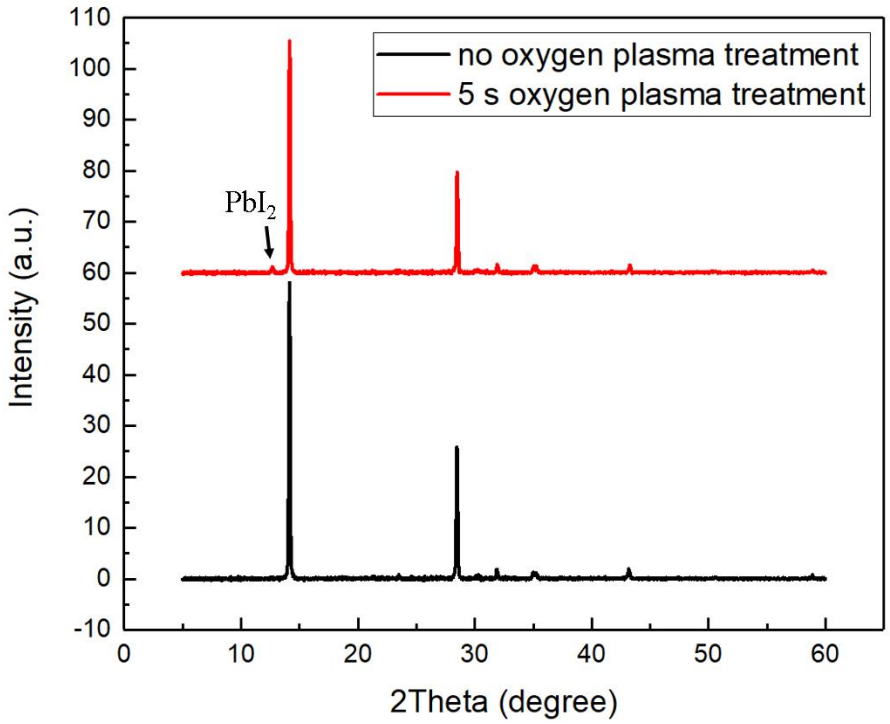

Figure 4.21: The XRD spectra of $MAPbI_3$ films without/with 5s oxygen plasma treatment. The arrows indicates the characteristic peak of PbI_2 at 12.7°.

at the same time enhances the V_{OC} due to the modified built-in field.

We checked the influence of the oxygen plasma on the surface potential by KPFM measurements (Figure 4.22). And we find the surface potential shifts around 150 mV up (-5.094 eV versus -4.947 eV). Note that the sample is with PEDOT:PSS underlayer. And without the plasma treatment, the Fermi level of the sample seems to be defined by the PEDOT:PSS layer. While with the oxygen plasma treatment, the shift-up of the surface potential is ascribed to the extra anion brought by the plasma. It is worth mentioning that the sample is not very stable under the KPFM measurement, and a holistic shift is observed during the scann from bottom to top in Figure 4.22(d). We suspect this is due to between the sample and the AFM tip, there may be an ion exchange process.

We draw a diagram to present the influence of the oxygen plasma on the band structure of the solar cell (Figure 4.23). Due the attachment of the anions, a larger built-in field is created which increase the V_{OC} of the solar cell. However, though we manage to increase the V_{OC}, the J_{SC} decreases inevitably due to the formation of the surface barrier. And also the oxygen plasma degrades perovskite and has poor long term stability, which makes it not a useful strategy pursuing better solar cells.

Besides the oxygen plasma, we also performed the argon plasma on perovskite surfaces. Interestingly, argon plasma treatment only lead to very strong hysteresis behavior of the cell. We think this reason may be the argon plasma gives rise to a lot of movable ions (either the argon ions or secondary ions from perovskite decomposition). This primary result is interesting as it suggests that the wide known hysteresis-free cell architecture

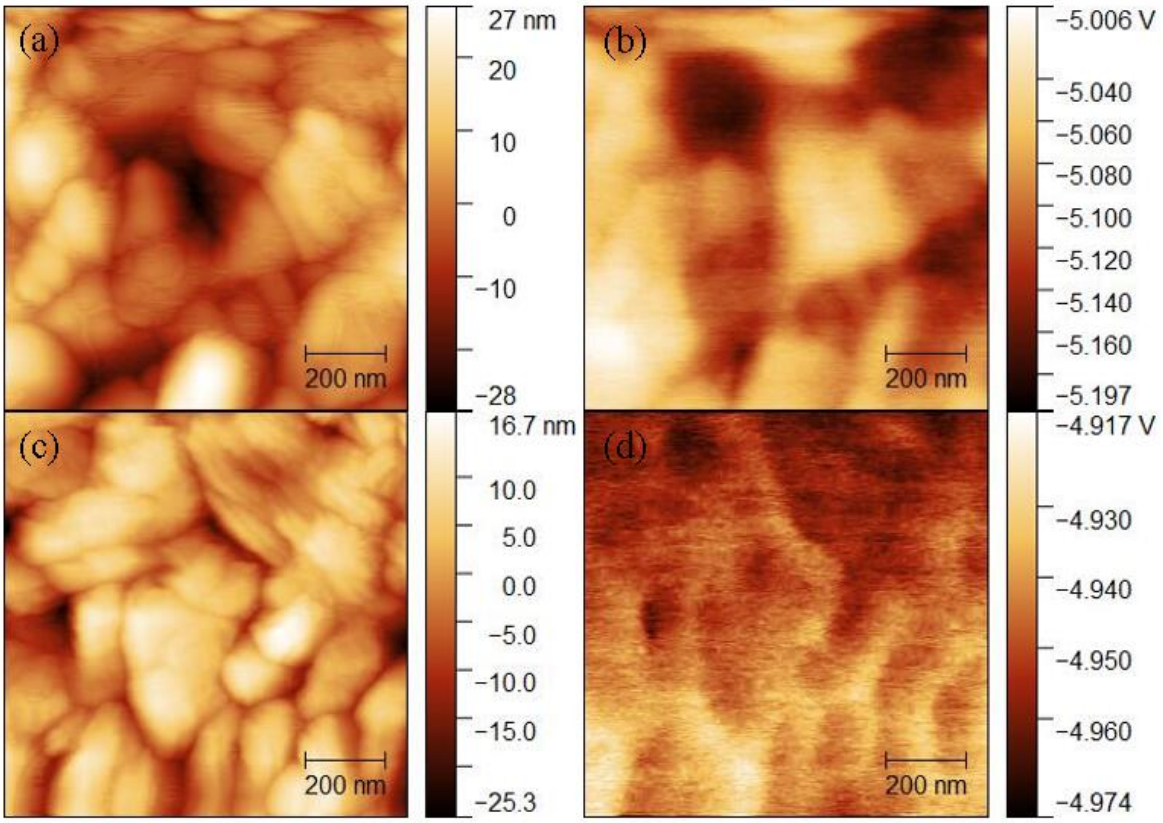

Figure 4.22: KPFM images (the left column shows topography images and right column shows surface potential profiles) of (a)(b) $MAPbI_3$/PEDOT:PSS sample and (b) $MAPbI_3$/PEDOT:PSS after oxygen plasma treatment sample.

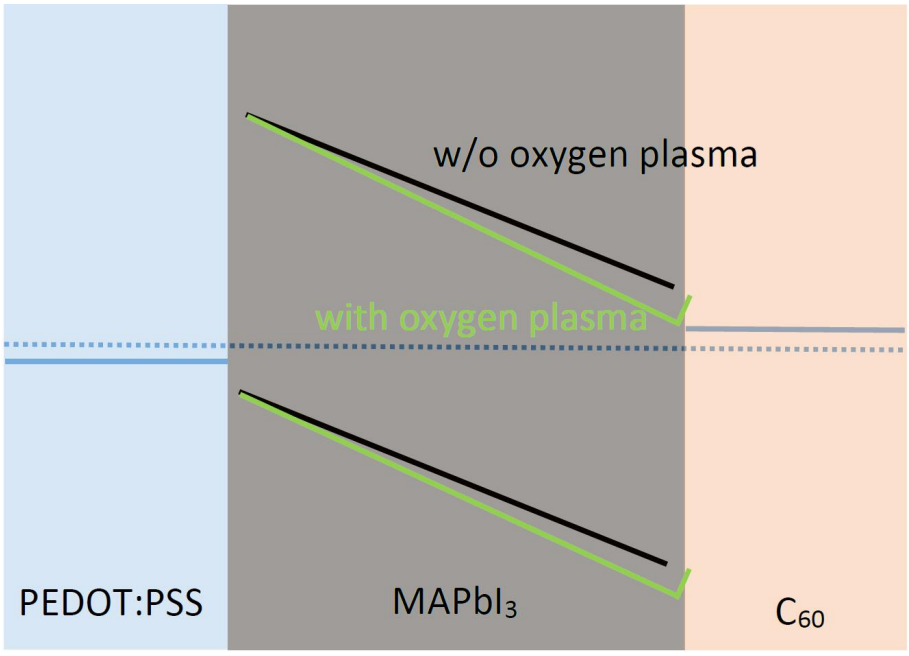

Figure 4.23: The diagram of the band structure change due to the oxygen plasma.

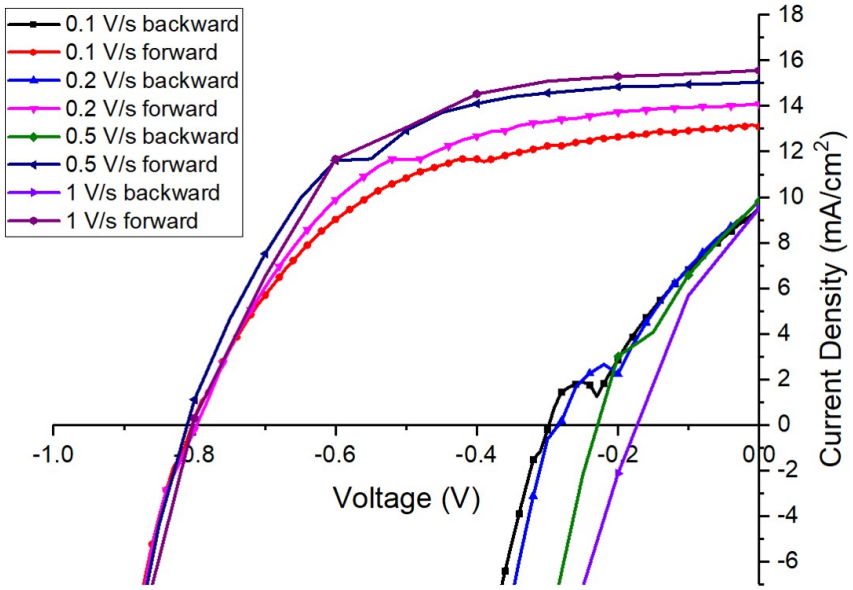

Figure 4.24: The J-V behavior of solar cells after argon plasma treatments at different scan speed.

can turns into hysteresis-rich with certain treatment. A systematic study may help us understand better what are the important factors behind the hysteresis behavior of PSCs.

To summarize, in this chapter different characterization techniques are used to clarify the underlying principles in a working cell. We see that the different illumination areas can reshape the recombination profile of the same cell, which is usually a neglected issue when measuring the V_{OC}. Next we present that a controlled variation in the V_{OC} of perovskite solar cells by up to 100 mV can be achieved by slight variations in the $MAPbI_3$ film preparation process. While no significant changes in the morphology of the differently annealed perovskite films are observed, we identify the small stoichiometric changes at the film surface lead to increased trap-assisted recombination and suppressed charge collection due to the surface band bending. Considering that the reduction in FF at higher light intensities in this study is much more pronounced in comparison with reported silicon, organic and other perovskite solar cells, we suggest the suppression of charge collection to be a strongly influential effect. Perovskite material has been known for its ionic transport and consequent dynamic band bending. However, a persistent surface band bending introduced by the usual annealing treatments is still unexpected. Finally we use the plasma treatment to deliberately change the V_{OC} of the PSC by changing the band structure of the cell. With the oxygen plasma, the V_{OC} of the cell does increase which is ascribed to the ion accumulation at the surface of the perovskite film. With the argon plasma, however, the cell shows a strong hysteresis feature which may be due to increased defect density at the $MAPbI_3$ surface.

Chapter 5

The modeling and simulation of inverted perovskite solar cells - revealing the underlying factors behind the performance and hysteresis behavior

In the former chapters, we introduced our PSC fabrication techniques as well as investigated the cell's internal processes. To further expand the understanding of the solar cell's working principles, a modeling and simulation of PSCs could be utilized. The general models of solar cells have been described in the introduction chapter, which have been applied in a lot of characterization methods as theoretical basis. Several models have been developed by various groups to simulate and explain the behavior of the PSCs (especially the hysteresis features) which, in our understanding, provide very insightful arguments[188][285][286][287]. The studied solar cell has a decent efficiency and high reproducibility, however, it also suffers from a lower V_{OC} and J_{SC} compared to the state of art PSC. Ascertaining the limitation factors from the bottom-up modeling could be a valid strategy to point out the directions for further optimization.

In this chapter based on the architecture and behavior of the studied PSC, we use a specific simplification treatment and boundary condition set to solve the continuity equations and build the cell's model. We fit our experimental data with the model to extract the corresponding physical parameters in the cell. We simulate the cell's behavior under given parameters to forecast the potential strategies improving its performance. Finally we model the hysteresis feature of the PSC based on the ion migration hypothesis and discuss the underlying factors and processes.

5.1 The model of a p-i-n junction solar cell

Here a model of a p-i-n junction PSC is presented to serve as the foundation for further hysteresis simulation. As introduced in the general working principle of solar cells, the charge carrier generation, transport and recombination processes can be mathematically expressed in Eq. 1.36, 1.37. Further elucidating the behavior of a solar cell requires specific equations to describe the charge generation, recombination and transport profiles.

Regarding the charge transport process, the Poisson equation is written as

$$\frac{\partial^2 \phi}{\partial x^2} = -\frac{\rho}{\varepsilon} \tag{5.1}$$

where ϕ is the electric potential, x is the distance, ρ is the charge density and ε is the dielectric permittivity.

Here we consider that the perovskite layer is intrinsic and $\rho = 0$, and then the electric potential changes linearly across the film,

$$|E| = \frac{\partial \phi}{\partial x} = \frac{V_{bi} - V}{L} \tag{5.2}$$

where V_{bi} is the built-in potential, V is the applied bias, and L is the thickness of the perovskite layer.

Neglecting any parasitic reflection from the back surface, the generation profile in the absorber layer is approximately described as

$$G(x) = G_{eff} e^{\frac{-x}{\lambda}} \tag{5.3}$$

where G_{eff} andλ are material specific constants.

Finally the recombination profile is simplified. In a normal picture, the carrier loss due to the recombination process is dependent on the charge carrier density and corresponding rate coefficients. And the radiative and non-radiative recombination occur at different positions across the perovskite film. To get a analytical solution, we represent the charge carrier loss with a negative current term. Specifically, a negative minority injection current is described as a boundary condition which depends on the carrier density at the interface. It represents the interfacial charge carrier recombination losses and corrects the overall current. With this simplification, the R(X) is omitted in Eq. 1.36, 1.37 with the final simple expression

$$\mu_n \frac{\partial n}{\partial x} E + D_n \frac{\partial^2 n}{\partial x^2} + G_{eff} e^{\frac{-x}{\lambda}} = 0 \tag{5.4}$$

$$-\mu_p \frac{\partial p}{\partial x} E + D_p \frac{\partial^2 p}{\partial x^2} + G_{eff} e^{\frac{-x}{\lambda}} = 0 \tag{5.5}$$

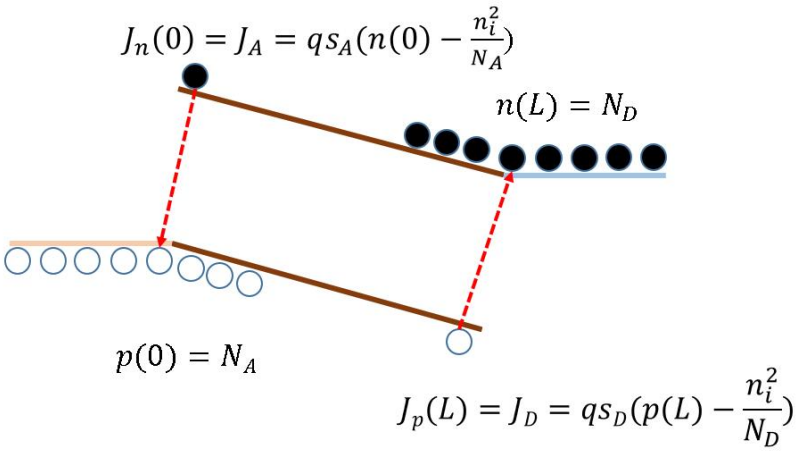

Figure 5.1: The energy diagram of a p-i-n cell with boundary conditions labeled.

Inserting the Einstein relation($D = \mu k_B T/q$), the general solutions are

$$n(x) = A_n e^{-\frac{qE}{k_B T}x} + \frac{qG_{eff}\lambda^2}{\lambda E q\mu_n - \mu_n k_B T} e^{\frac{-x}{\lambda}} + B_n \tag{5.6}$$

$$p(x) = A_p e^{\frac{qE}{k_B T}x} - \frac{qG_{eff}\lambda^2}{\lambda E q\mu_p + \mu_p k_B T} e^{\frac{-x}{\lambda}} + B_p \tag{5.7}$$

As the current flowing through the whole device is constant, the current density $J = J(0) = J_n(0) + J_p(0)$, inserting Eq. 5.6, 5.7 and the drift diffusion equations Eq. 1.34, 1.35, we get

$$J = qE(\mu_n B_n + \mu_p B_p) \tag{5.8}$$

Additional boundary conditions are needed to further solve the constant terms in Eq. 5.6, 5.7. We assume the charge carrier concentration at the surface of the intrinsic perovskite layer is determined by the interfacial formation with the selective layer, the hole density is N_A at the hole selective interface and the electron density is N_D at the electron selective interface, respectively. These classic semiconductor concepts see the relation

$$V_{bi} = \frac{k_B T}{q} ln(\frac{N_A N_D}{n_i^2}) \tag{5.9}$$

Where n_i is the intrinsic carrier density of perovskite layer.

As discussed above, the minority injection current is described as $J_{A(D)} = qs_{A(D)}\Delta p(n)$. The Δp(n) is the excess minority carrier concentration and $s_{A(D)}$ is the effective surface recombination velocity at the hole/electron selective interface. Note the minority carrier injection term is regarded as a correction of the overall current which accounts for the interfacial recombination process in the device. The band diagram of this p-i-n junction solar cell in illustrated in Figure 5.1 with the boundary conditions labeled.

The solved specific B_n and B_p are

$$B_n = \frac{-G_{eff}\lambda + \frac{qs_AG_{eff}\lambda^2}{\mu_n(qE\lambda - k_BT)}(1 - e^{\alpha - \frac{L}{\lambda}}) + s_AN_De^{\alpha} - \frac{s_An_i^2}{N_A}}{s_Ae^{\alpha} - s_A + \mu_nE} \tag{5.10}$$

$$B_p = \frac{e^{\frac{-L}{\lambda}}\left(G_{eff}\lambda - \frac{qs_DG_{eff}\lambda^2}{\mu_p(qE\lambda + k_BT)}(1 - e^{\alpha + \frac{L}{\lambda}})\right) + s_DN_Ae^{\alpha} - \frac{s_Dn_i^2}{N_D}}{s_De^{\alpha} - s_D + \mu_pE} \tag{5.11}$$

where $\alpha = \frac{qE}{k_BT}L$

The physical picture illustrated in Figure 5.1 indicates that the hole density decreases from left to right while the electron density increases from left to right. This feature sees that $\frac{\partial p}{\partial x} > 0$ and $\frac{\partial p}{\partial x} < 0$ which further define the electric field to be negative. As such, $E = \frac{V - V_{bi}}{L}$. Inserting Eq. 5.10, 5.11, 5.9 into Eq. 5.8, we get

$$\begin{aligned} J = &(\frac{\frac{n_i^2\mu_nk_BT}{N_AL}}{\frac{e^{\alpha}-1}{\alpha} + \frac{\mu_nk_BT}{s_AqL}} + \frac{\frac{n_i^2\mu_pk_BT}{N_DL}}{\frac{e^{\alpha}-1}{\alpha} + \frac{\mu_pk_BT}{s_DqL}})(e^{\frac{qV}{k_BT}} - 1) \\ &+qG_{eff}\lambda(\frac{\frac{1-e^{\alpha-\frac{L}{\lambda}}}{\alpha-\frac{L}{\lambda}} - \frac{\mu_nk_BT}{s_AqL}}{\frac{e^{\alpha}-1}{\alpha} + \frac{\mu_nk_BT}{s_AqL}} - \frac{\frac{1-e^{\alpha+\frac{L}{\lambda}}}{\alpha+\frac{L}{\lambda}} - \frac{\mu_pk_BT}{s_DqL}}{\frac{e^{\alpha}-1}{\alpha} + \frac{\mu_pk_BT}{s_DqL}}e^{\frac{-L}{\lambda}}) \end{aligned} \tag{5.12}$$

The first term with the $e^{\frac{qV}{k_BT}} - 1$ is the dark current term while the latter term with the $G_{eff}\lambda$ is the photo current term. Compared Eq. 5.12 with the Shockley model and the detailed balance model, this analytical solution derived from the continuity equation here has the similar exponential term.

As discussed, the exponential dark current term represents the process of bimolecular recombination in the detailed balance model, but here its origin is not so straightforward. A close look indicates that it comes from the constant term which is defined by the selected boundary conditions. As the injection of the minority charge carriers term represents the recombination process, we infer that the exponential increase of the dark current comes from the exponential increase of the minority carrier density with the applied bias at the interfaces.

One major simplification of this model is to assume no charge carrier losses in the perovskite layer[288]. In the classic P-N junction model, the injected charge carriers are regarded lossless in the depletion region as the native charge carriers are depleted. However, this assumption requires low injection rate (so the charge carrier density is low in the depletion region) as the prerequisite which is not true for a practical solar cell. This argument can also be rephrased as the radiative recombination can not be ignored in the solar cell. However, this model also yields a dark current term which increases exponentially with the applied bias which just happen to have the same form with the radiative recombination expression (Eq. 1.22). To clarify, it doesn't mean that this model takes the radiative recombination into consideration. It is just because the interfacial recombination has the similar mathematical expression as the radiative recombination. In other words, if all the parameters in Eq. 5.12 are known, the J-V curve could still deviate from the actual because of the neglect of the radiative recombination.

5.2 Fitting of the p-i-n cell model based on experimental J-V curves

In the above section, a p-i-n PSC model is derived by analytically solving the continuity equation (Eq. 5.12). This model neglects the contribution of radiative and trap-assisted recombination but only considers the interfacial recombination, which seems to be inadequate for the simulation of a practical solar cell. However, the applicability of this model may not be so poor. In a real solar cell with neglectable trap-assisted recombination (which can be true for the defect-tolerant PSC), the dark current should have an expression with $e^{\frac{qV}{k_BT}} - 1$ term as both the radiative and interfacial recombination share this similar form. Therefore, the fitting based on Eq. 5.12 should match the actual well. The problem is that the fitted parameter would deviate from their physical meanings, as the model only considers the interfacial recombination. To put in another way, the fitted parameter would give an overestimation of the interfacial recombination processes as the real process is a combination of both interfacial and radiative recombination. However, if the interfacial recombination is very severe, then the deviation of the fitted parameter is reduced, and the derived parameters may be more accurate.

In this context, the PEDOT:PSS based p-i-n PSC is a suitable solar cell type for this model. PEDOT:PSS has been reported to be a poor hole selective layer which causes strong interfacial bimolecular recombination[267]. This feature leads to poor V_{OC} of around 0.9 V while the typical TiO_2 n-i-p PSC has a V_{OC} of around 1.1-1.2 V[289][266]. Moreover replacing the PEDOT:PSS with PTAA could directly increase the V_{OC} to around 1.2 V which suggests the PEDOT:PSS surface provides massive interfacial recombination channels[182][183]. In addition, the light intensity-dependent V_{OC} measurements show that PEDOT:PSS based device shows an ideal factor close to 1 while the TiO_2 based device gives an higher value[267]. An higher value is indicative of a larger trap-assisted recombination proportion in the whole recombination processes. Therefore the trap-assisted recombination is neglectable due to the larger interfacial bimolecular recombination portion in the PEDOT:PSS based devices. The lower ideal factor also agrees with the model where the interfacial recombination process increases exponentially versus the bias with a prefactor of q/k_BT.

Now we need to determine the parameters which need to be fitted. The Eq. 5.12 contains the dark current and the photo current term meaning that we can use two independent series of data to run the fitting program. The photo current is the difference of the experimental light current density and dark current density. In the Shockley and thermal radiation models, this value is a constant which is only dependent on the EQE of the cell and the light radiation intensity, and independent on other parameters (namely the superposition principle). Here in this model and for real devices, the photo current also depends on the applied bias. This phenomenon is vividly shown in Figure 4.19 where the difference of the light and dark J-V curves becomes smaller as the negative bias increases. One explanation is that the recombination current is larger at the light condition than at the dark condition due to the larger charge carrier population in the cell. Several parameters are known in Eq. 5.12. The perovskite film thickness L is measured

to be around 300 nm, the carrier mobility of $MAPbI_3$ polycrystalline film is reported to be around 1 $cm^2/(V\ s)$ from long range photoluminescence quenching method for both electron and hole[37][166]. $qG_{eff}\lambda$ is estimated to be around 23 mA/cm^2. And four independent variables are found in the photo current term, including the built-in potential V_{bi} ($\alpha = q(V - V_{bi})/k_BT$), the recombination velocity at the PEDOT:PSS/perovskite interface s_A and C_{60}/perovskite interface s_D as well as the average light penetration depth λ. In the dark current term, besides V_{bi}, s_A and s_D, there are three more variables (n_i, N_A and N_D), but only two are independent.

The photo current and dark current terms are written separately with all known parameters inserted,

$$J_{dark} = \Big(\frac{1.38 * 10^{-13} n_A}{\frac{e^{(V-V_{bi})/0.0259}-1}{(V-V_{bi})/0.0259} + 863/s_A} + \frac{1.38 * 10^{-13} n_D}{\frac{e^{(V-V_{bi})/0.0259}-1}{(V-V_{bi})/0.0259} + 863/s_D}\Big)(e^{V/0.0259} - 1) \tag{5.13}$$

$$J_{photo} = 23 * \Big(\frac{\frac{1-e^{(V-V_{bi})/0.0259-300/\lambda}}{(V-V_{bi})/0.0259-300/\lambda} - 863/s_A}{\frac{e^{(V-V_{bi})/0.0259}-1}{(V-V_{bi})/0.0259} + 863/s_A} - \frac{\frac{1-e^{(V-V_{bi})/0.0259+300/\lambda}}{(V-V_{bi})/0.0259+300/\lambda} - 863/s_D}{\frac{e^{(V-V_{bi})/0.0259}-1}{(V-V_{bi})/0.0259} + 863/s_D} e^{-300/\lambda}\Big) \tag{5.14}$$

where $n_A = \frac{n_i^2}{N_A}$, $n_D = \frac{n_i^2}{N_D}$, the units of $J_{dark/photo}$, $n_{A/D}$, $s_{A/D}$, V_{bi} and λ are mA/cm^2, cm^{-3}, cm/s, V, nm, respectively.

Eq. 5.13 and Eq. 5.14 are then used in the matlab program to fit with the experimental J-V curves. As shown, Eq. 5.13 has five variables to be determined while Eq. 5.14 has four, and three of them are mutual variables. The first idea is to fit Eq. 5.13 and Eq. 5.14 separately and crosscheck if the derived parameters are self-consistent.

As shown in Figure 5.2, the derived parameters from the photo current and dark current fitting do not match. This result is not surprising as there are too many undetermined parameters which renders the fitting too many degrees of freedom. Therefore, the existing conditions do not allow for separate fitting. And then a set of conditions which satisfies both the photo current and dark current fitting is to be determined. To achieve that, we try to insert the derived parameters from one fitting (photo or dark) into the other fitting (dark or photo) process to derive the rest parameters, and check if the system's degree of freedom allows a whole self-consistent set of parameters.

In Figure 5.3, 5.4, the fitting results of the above mentioned processes are presented. It shows that the primary parameters derived from the dark current fitting don't yield self-consistent results in the photo current picture. And the primary parameters from the photo current fitting apply well in the dark current fitting process. This result highlights the issue of the degree of freedom in the fitting. If there are a series of solutions for the fitting, then the fitting result would be unreliable. If multiple-step fitting is needed, the fitting program may not be able to obtain the right solution, as shown here. Even if Figure 5.4 gives a self-consistent result, it is still unclear if the derived parameters are the only solution set. A practical method for crosschecking is to change the initial fitting parameters or the bound constraints to see if there are other solutions for the system.

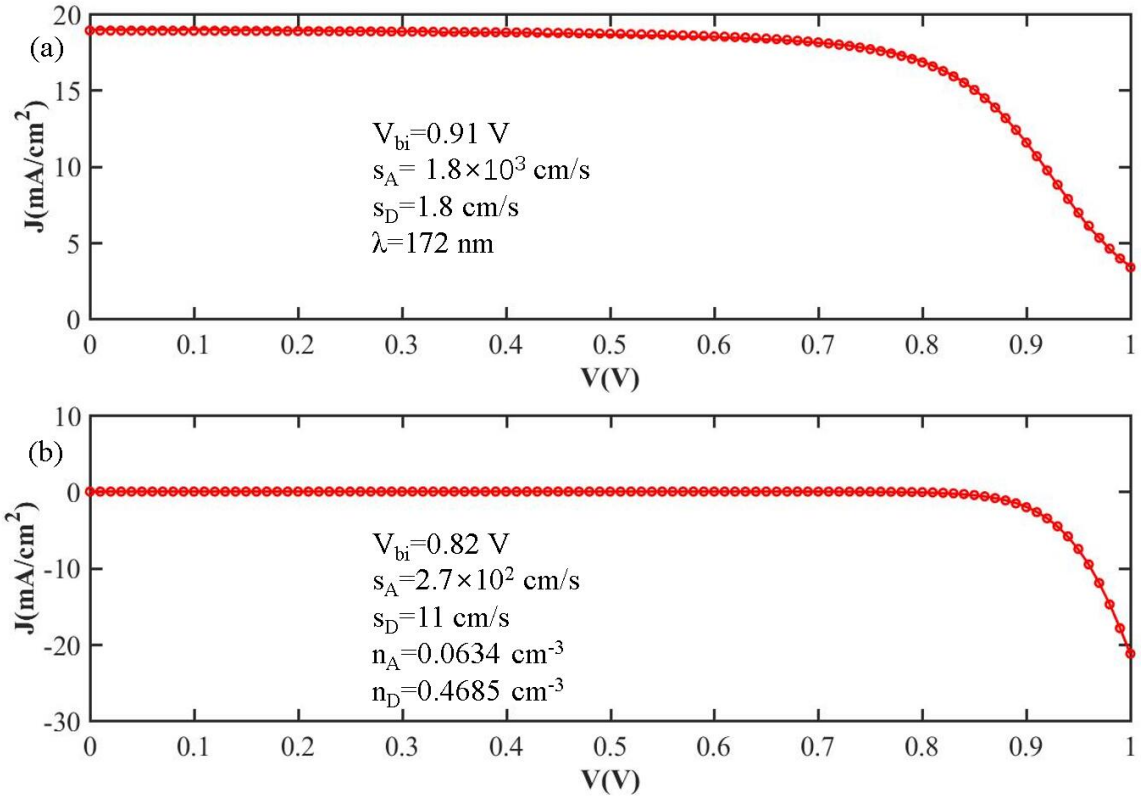

Figure 5.2: Independent fitting results of (a) photo current and (b)dark current with the derived fitting parameters labeled, the dotted line is the fitting curve and the solid line is the experimental data.

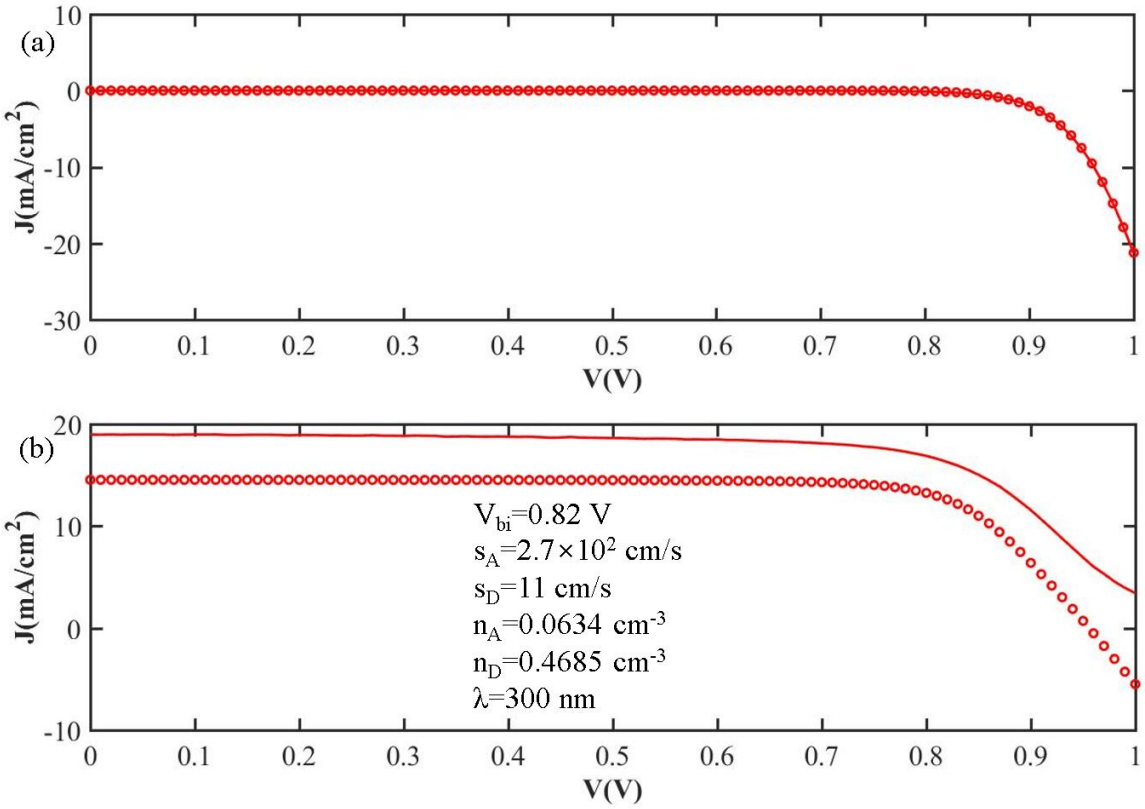

Figure 5.3: The results of inserting dark current fitting parameters into the photo current fitting process, the dotted line is the fitting curve and the solid line is the experimental data.

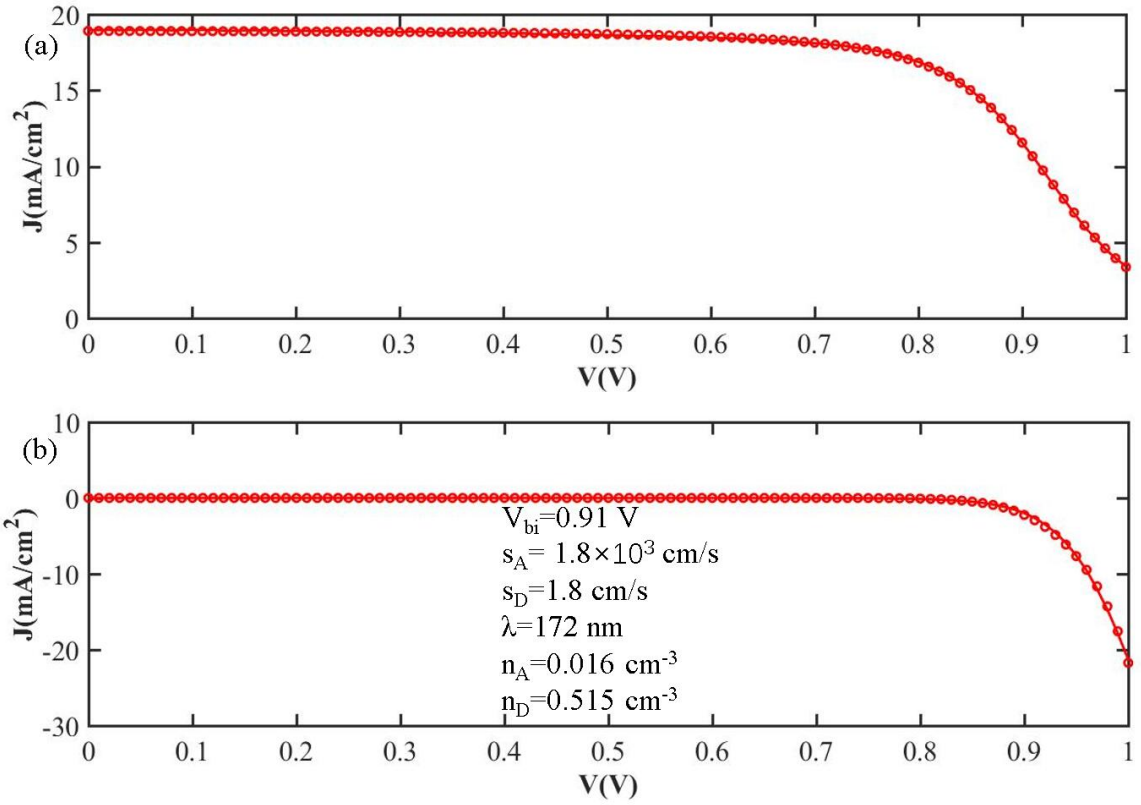

Figure 5.4: The results of inserting photo current fitting parameters into the dark current fitting process, the dotted line is the fitting curve and the solid line is the experimental data.

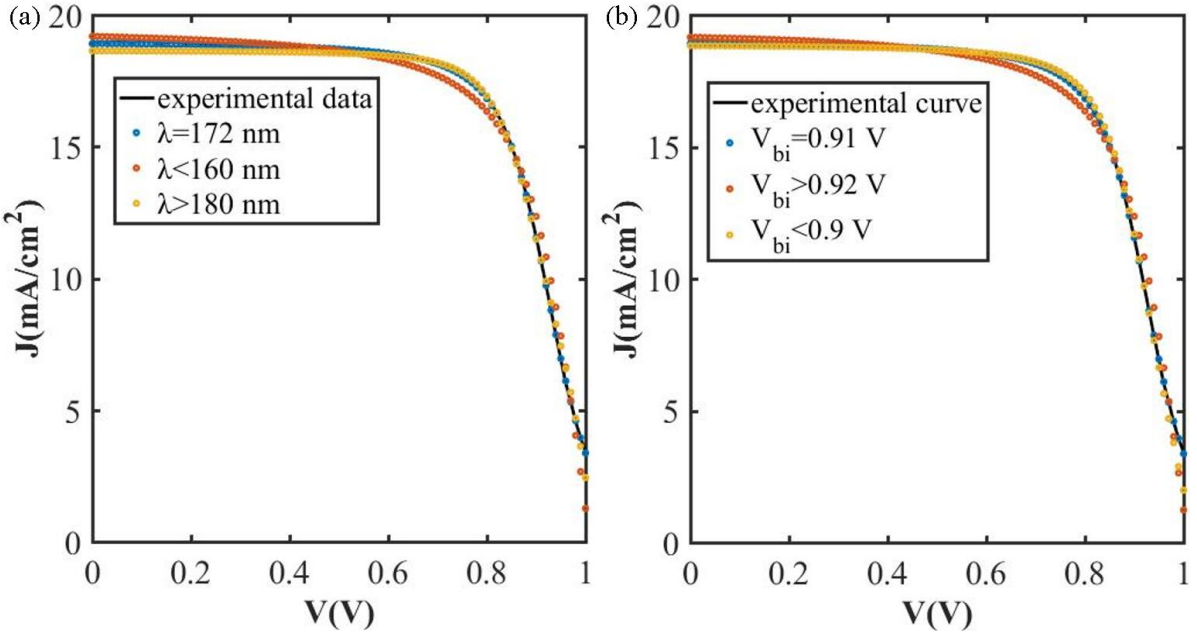

Figure 5.5: The fitting results with different bound constraints for (a) λ and (b) V_{bi}.

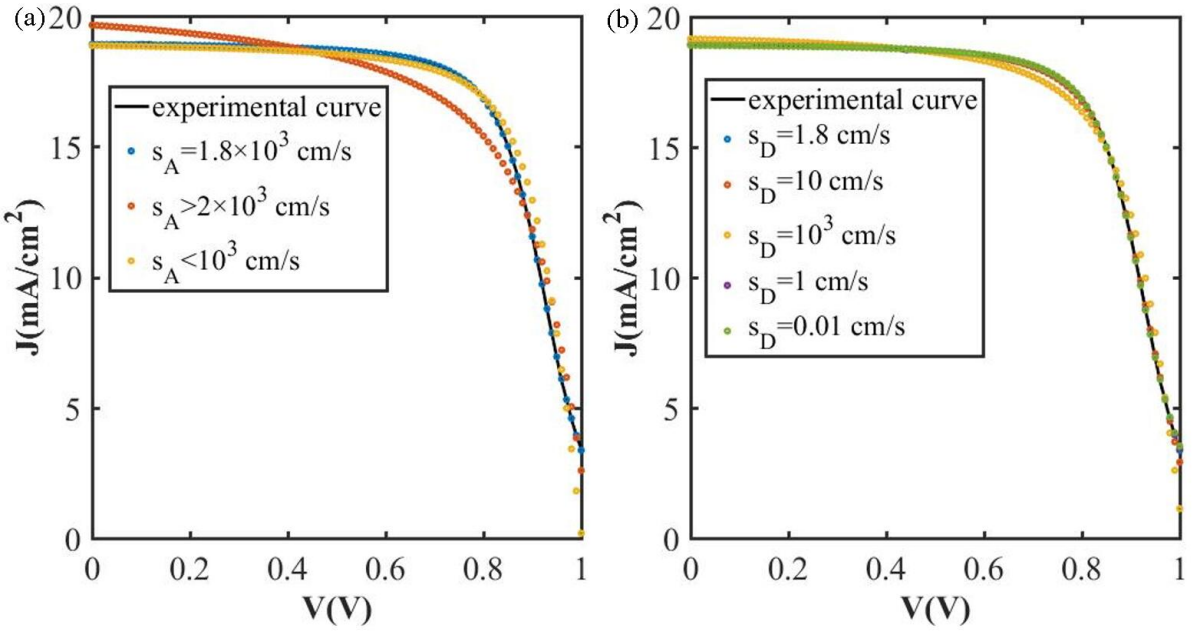

Figure 5.6: The fitting results with different bound constraints for (a) s_A and (b) s_D.

fitting constraints	$V_{bi}(V)$	$\lambda(nm)$	$s_A(cm/s)$	$s_D(cm/s)$
\	0.9088	172	1.80×10^2	1.8
$s_D < 1cm/s$	0.9079	172	1.76×10^2	1
$s_D < 0.1cm/s$	0.9069	172	1.71×10^2	0.1
$s_D < 0.01cm/s$	0.9068	172	1.71×10^2	0.01

Table 5.1: The fitting results with different bound constraints for s_D.

Figure 5.5 shows the fitting results of the photo current data with λ and V_{bi} constrained differently. It indicates that the fitting program can not find another set of parameters which matches the experimental curve. As it seems with λ or V_{bi} varying, the other parameters can not follow to compensate the change of the J-V curve, we can also see the special effect of these two parameters in the model. As shown in Figure 5.5, higher V_{bi} or lower λ increases the current at 0 V and decreases the current at 0.7 V. This is due to a lower λ or higher V_{bi} can increase the output current if other parameters are to remain unchanged. To compensate this effect, the fitted recombination velocity s_A and s_D is higher and leads to a lower FF. Similarly, a higher λ or lower V_{bi} leads to lower recombination rates and a higher FF.

Figure 5.6 presents the influence of the variations of the recombination velocity s_A and s_D. Clearly varying s_A doesn't give rise to another valid solution. But modifying s_D seems to give rise to a series of parameters sets which satisfy the experimental data. The fitting is especially well when the s_D is lower than the primary value. The fitted parameters are summarized in Table 5.1. And it shows, however, the fitted parameters are on a regression track when the restrictions are relaxed. The result only indicates that the s_D is a less sensitive parameter in this model.

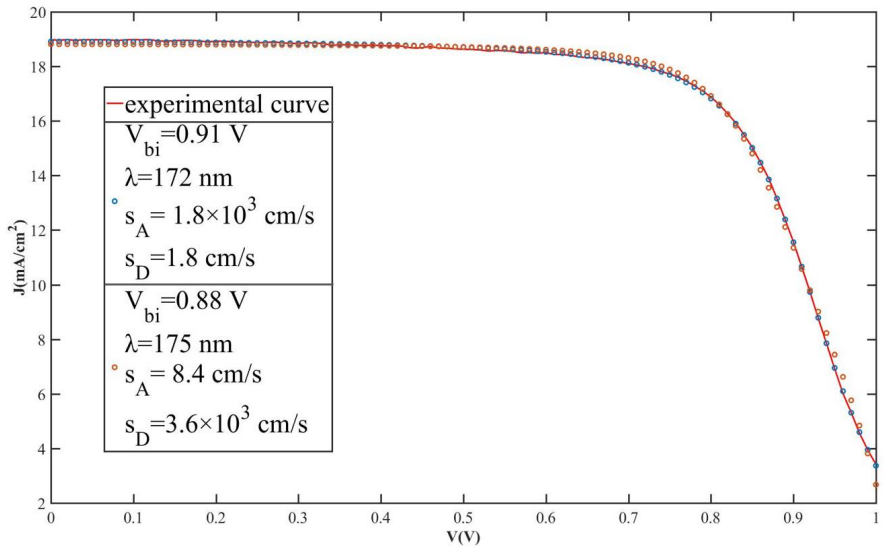

Figure 5.7: The valid solutions derived by changing the fitting initial conditions.

The above discussions address that the photo current fitting gives the only valid solution of this model if the fitting process runs the simulation over the whole range of the constraints for the parameters. However, the fitting result is usually sensitive to the initial fitting parameters. As such, different initial fitting parameters are also tested to check if there are other valid solutions. And indeed another set of parameters which fits well with the experimental curve is derived (Figure 5.7). The main difference between these two solutions is the recombination rate, where in one condition s_A is dominant and in the other s_D plays the main role. It is not surprising that these two situations could both satisfy the fitting, as s_A and s_D are introduced in the model in a similar way in the boundary conditions. The factor which differentiates them is the charge generation profile which renders larger charge generation rate near the hole selective layer (where s_A governs the recombination process).

Next we use these primary parameters to fit the dark current curve and find that n_A and n_D are independent. This result is also intuitive as Eq. 5.13 doesn't have enough degrees of freedom with the inserted V_{bi}, s_A and s_D anymore. It is worth mentioning that in this step the solution with larger s_A has a more superior fitting match with the experimental curve (Figure 5.8).

Coming back to the photo current fitting, although Figure 5.5, 5.6 suggest that there is only one eligible solution of this model. Due to the algorithm of the fitting process, there is always the possibility that other valid solutions are missed. And we find that the recombination rate s_A and s_D seem to be dependent on each other. So it is still unclear if the two sets of solutions presented in Figure 5.8 are the only two or there are more combinations of s_A and s_D. As this problem seems to be beyond the capability of the fitting function, several designed parameters sets are used to compare its degree of coincidence with the experimental data.

As shown in Figure 5.9, to check if there are other combinations of s_A and s_D which fit

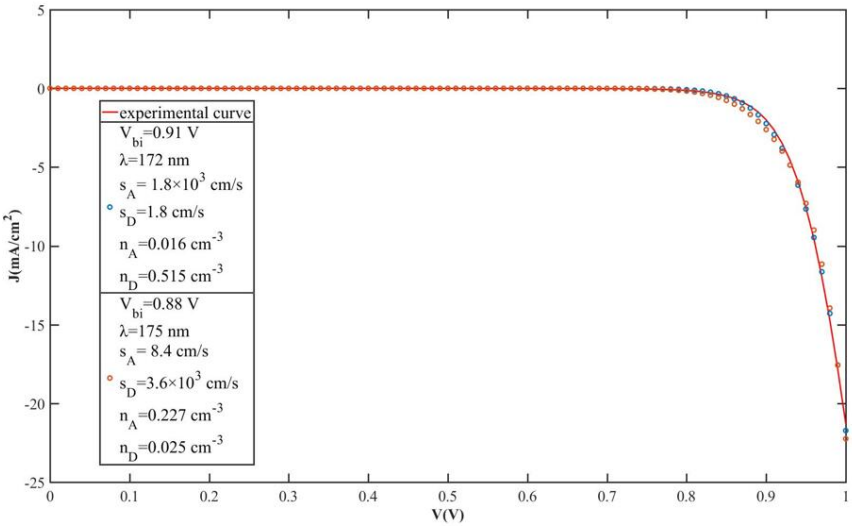

Figure 5.8: The dark current fitting results of the two primary sets of parameters.

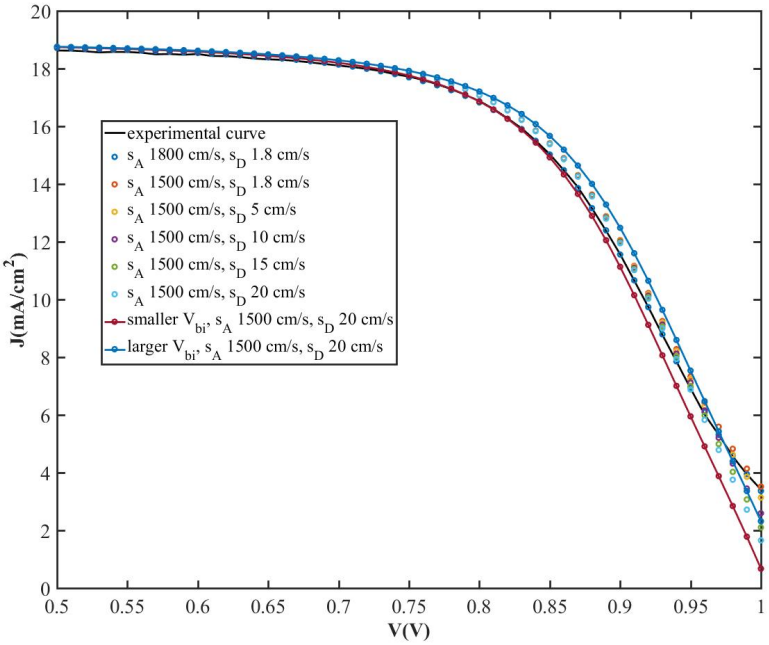

Figure 5.9: The influence of the interplay of s_A and s_D on the shape of the J-V curve.

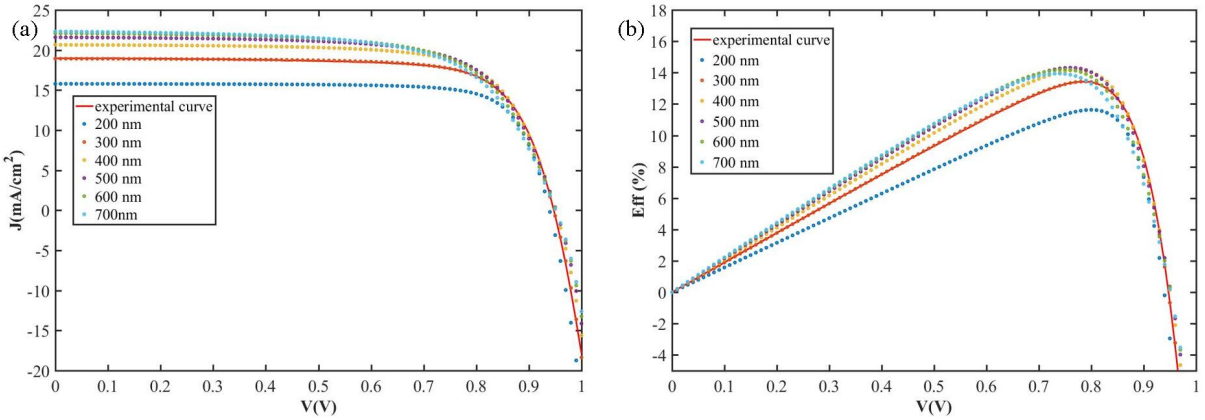

Figure 5.10: The simulation results of the (a) J-V curves and (b) efficiency voltage dependency with different thicknesses of the perovskite film.

the experimental curve, we deliberately decrease the value of s_A and increase s_D. However, there is no other combination which allows a good match. This result suggests the fitted combinations of s_A and s_D which have large value differences are necessary. This conclusion is quite interesting as it indicates the shape of the photo curve is related not only to the value of the recombination velocity but also to the 'balance' of the electron and hole recombination rates. Moreover, it shows that the inflection point of the photo curve depends more on the larger recombination velocity while the decrease slope depends more on the balance of the recombination rates. Going back to Eq. 5.12, we find the balance further expends to the ratio of carrier mobility and recombination rate (in this fitting the mobility is assumed identical for both electron and hole).

To summarize, the 'quality' of the fitting has been evaluated to check if we can derive the independent parameters and no valid solutions are neglected by the program. The results suggest that the fitting is successful yielding two sets of solutions (Figure 5.7). Further considering that PEDOT:PSS/perovskite interface should leads to a higher s_A and the degrees of coincidence of the dark current fitting (Figure 5.8), we conclude that the reasonable parameter set is: V_{bi}=0.91 V, λ=172 nm, s_A= 1.8×10^3 cm/s, s_D=1.8 cm/s, n_A=0.016 cm^{-3}, n_D=0.515 cm^{-3}.

5.3 Simulations of the J-V curves with different parameters

With the fitted parameters inserted, Eq. 5.12 allows us to simulate the corresponding current-voltage behavior when a certain parameter is altered. Here a few simulation results are shown and discussed.

Figure 5.10 presents the simulation results on the film thickness of perovskite layer. It suggests there are still some efficiency gains until the film reaches around 500 nm. The main contribution comes from the enhancement of the output current density. Further

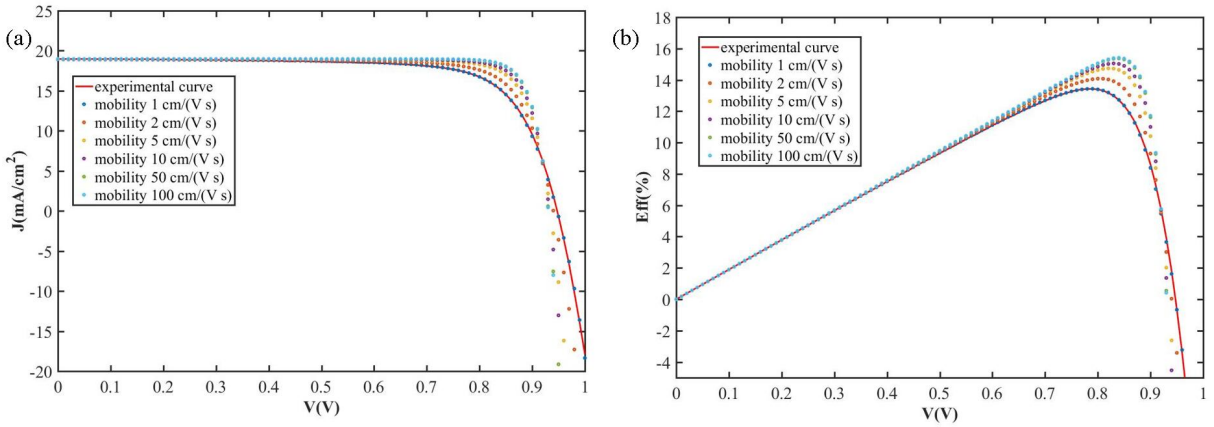

Figure 5.11: The simulation results of the (a) J-V curves and (b) efficiency voltage dependency with different mobility values of electrons and holes.

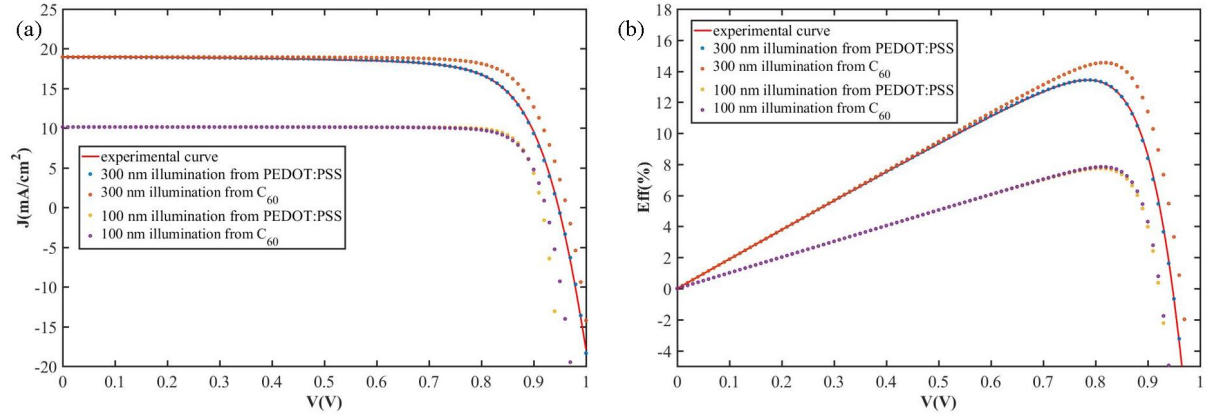

Figure 5.12: The simulation results of the (a) J-V curves and (b) efficiency voltage dependency with different illumination directions.

increasing the film thickness will decrease the performance of the solar cell. The reason could be the electric field gets weaker with increasing film thickness. And the recombination current plays a bigger role as the charge carrier transport is more suppressed.

In Figure 5.11 we simulated the impact of the mobility values of electrons and holes in perovskite on the performance of the solar cell. Here an identical value is assumed for both electrons and holes, though in this model the electron and hole mobility have different influences. As the short-range mobilities of perovskites are reported to be much higher than long-range measurement results[35][33][290], the result presented here actually forecasts the performance improvement when there are less grain boundaries in the absorption layer. Clearly more than 2 % efficiency gains are predicted when the mobility increased from 1 cm/(V s) to 50 cm/(V s) (this value has been achieved in single crystal perovskite). Further mobility enhancement only gives marginal improvements of the cell performance.

Another interesting aspect is the direction of the illumination. In practice this is un-

realistic as the upper C_{60} and silver layers will block most of the light. But the simulation could reveal if our cell will behave differently with different illumination directions, due to the giant differences between the interfacial recombination velocities. Taking advantage of the identical mobility of electrons and holes assumed in this model, s_A and s_D, n_A and n_D are simply switched in the program for this simulation. Figure 5.12 illustrates that there is indeed a quite large difference, with the incoming light from the C_{60} side leading to a higher FF. This phenomenon is due to the variations of the charge carrier distribution. Because of the limitation of the light penetration depth, more charge carrier will generate and lead to an overall higher carrier density near the incident surface. If the light incomes from the PEDOT:PSS direction, more interfacial recombination losses occur due to the larger recombination velocity and higher carrier density near the PEDOT:PSS/$MAPbI_3$ interface. With a thinner perovskite film, the charge carrier concentration will be more uniform across the film and this phenomenon is less apparent (Figure 5.12).

5.4 Modeling and simulation of the ion movement and aggregation

Hysteresis phenomenon has been widely reported to originate from ion movements in the perovskite layer[192][193][194][66][195]. The movable ions aggregate at the interface of the perovskite and selective layers forming a Debye layer. The built-in voltage will partly or largely drop across the Debye layer leaving the bulk perovskite electric field free.

The main idea of modeling the hysteresis behavior is to modify the bias in our existing model according to the ion aggregation profile. Specifically, the bias applied to the cell is corrected by the voltage drop across the Debye layer, preconditioning that the thickness of Debye layer is much thinner than the perovskite film[188].

Figure 5.13 presents the energetic diagram of perovskite film with the Debye layer. Due to the requirement of charge neutrality,

$$Q_+ = -Q_- \tag{5.15}$$

where Q_+ and Q_- are the charge amount in the opposite charged sections of the Debye layer. And

$$V_C = V - V_+ + V_- \tag{5.16}$$

in which the bias is corrected (V_C) by the voltage drop across the Debye layer (V_+ and V_-)

The relationship of the charge and voltage drop across the Debye layer could be expressed as

$$Q_{+/-} = \frac{\varepsilon k_B T}{q L_d} sign(V_{+/-}) \sqrt{2(e^{\frac{qV_{+/-}}{k_B T}} - 1 - \frac{qV_{+/-}}{k_B T})} \tag{5.17}$$

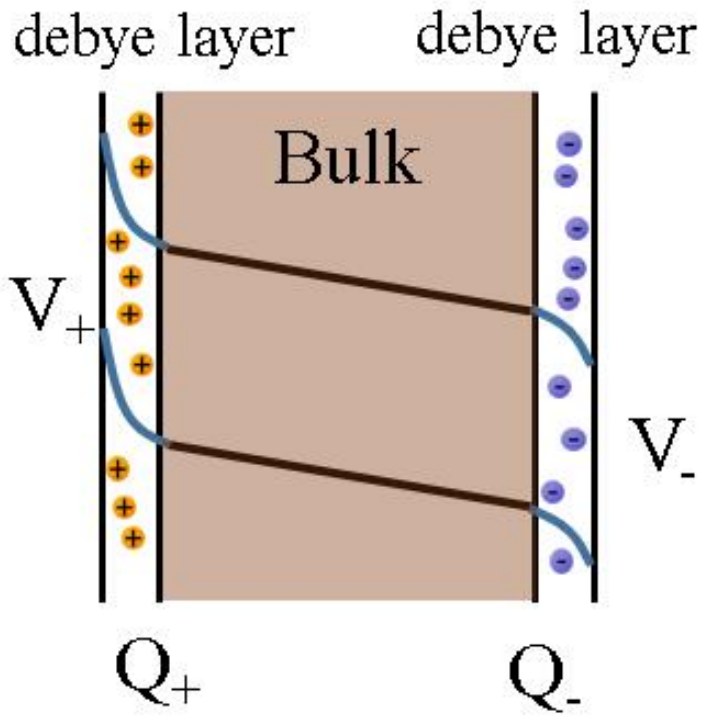

Figure 5.13: The schematic of the Debye layer and voltage drop across.

where ε is the dielectric constant of perovskite, L_d is the thickness of the Debye layer[188].

The charge amount Q is the result of ion aggregation caused by the drift process due to the bulk electric field,

$$\frac{\partial Q_{+/-}}{\partial t} = -qN_{ion}\mu_{ion}E = -qN_{ion}\mu_{ion}\frac{V - V_+ + V_- - V_{bi}}{L} \tag{5.18}$$

where the N_{ion} and μ_{ion} are the density and mobility of the movable ion in the perovskite respectively.

Eq. 5.17 and Eq. 5.18 provide a whole description of the relation between $V_{+/-}$ and time. However, the analytical solution of this time dependent differential equation is difficult to derive. Therefore, a numerical method is used to reveal the picture how V_C varies with the time.

The principle of the algorithm is very straightforward. Assuming an initial $Q_{0+/-}$, the voltage drop across the Debye layer $V_{+/-}$ could be calculated based on Eq. 5.17. The derived $V_{+/-}$ is inserted into Eq. 5.18 to compute $\frac{\partial Q_{+/-}}{\partial t}$, which is the ion accumulation rate. This numerical method regards the ion accumulation rate to be constant over a very short period dt (1 ms for example). And after dt,

$$Q = Q_0 + \frac{\partial Q}{\partial t}dt \tag{5.19}$$

And the derived Q value is used for the next iteration process. The iteration runs for the desired times (m), and the Debye layer state after m×dt is derived.

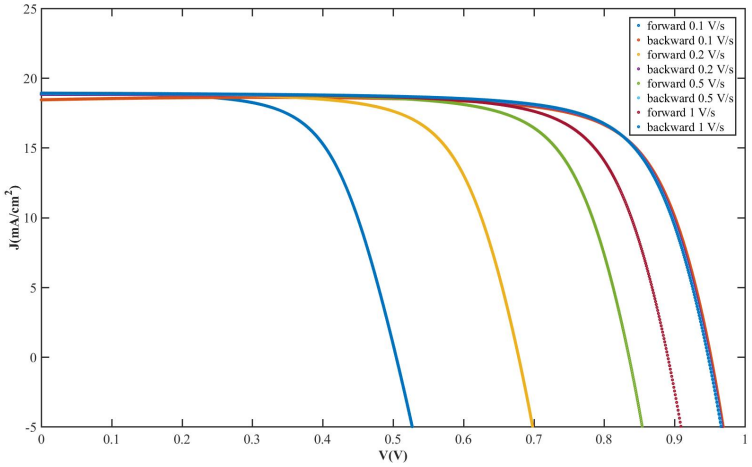

Figure 5.14: The simulation of hysteresis phenomenon with different scan speeds and directions.

The algorithm is programmed in Matlab with the help of the chebfun function, which is an external script set enabling convenient numerical calculations using conventional matlab syntax.

Assuming in Eq. 5.17, 5.18 the constants $\varepsilon = 25\varepsilon_0 = 2.2\times10^{-10}$ F/m, L_d=1.5 nm, $N_{ion} = 1.0\times10^{18}$ cm^{-3}, $\mu_{ion} = 2\times10^{-10}$ cm^2/(V s), we are able to program the scripts to model the hysteresis behavior.

Figure 5.14 presents the simulation results of the hysteresis behavior of the solar cell under different scan speeds and directions (scanned between 0 and 1 V without prebiasing, and the initial Debye layer charge is 0). The simulation indicates that the backward scan shows similar V_{OC} while the forward scan gives different V_{OC}. This result, to a certain degree, agrees with our observations though the V_{OC} differences of the forward and backward scans are much larger than the experimental results (Figure 3.21, 4.5).

The simulation results mainly originate from the fact that the voltage drop across the Debye layer weakens the electric field in the bulk perovskite, and further influences the current output processes. This principle suggests the current output and the V_{OC} of the solar cell should both be influenced. Figure 5.14 illustrates a big change of the V_{OC} while the J_{SC} remains almost the same between different scan speeds and directions. This isn't surprising considering it would require a dramatic voltage drop across the Debye layers to influence the current flow at the short circuit condition for solar cells with a such high FF. On the other hand, changing the V_{OC} would be much easier according to Eq. 5.16. However, this is not what usually the hysteresis J-V curves appear in PSC. Normally, the PSC with strong hysteresis features shows large J_{SC} variations and small V_{OC} changes with different scan parameters (Figure 1.14)[184][291][292].

In our model, considering the processes of ion movement, we see that during the backward scan, the ions gradually aggregate in the Debye layer. But at the end of the scan, the amount of the aggregated ions is too small to induce a enough decrease of the

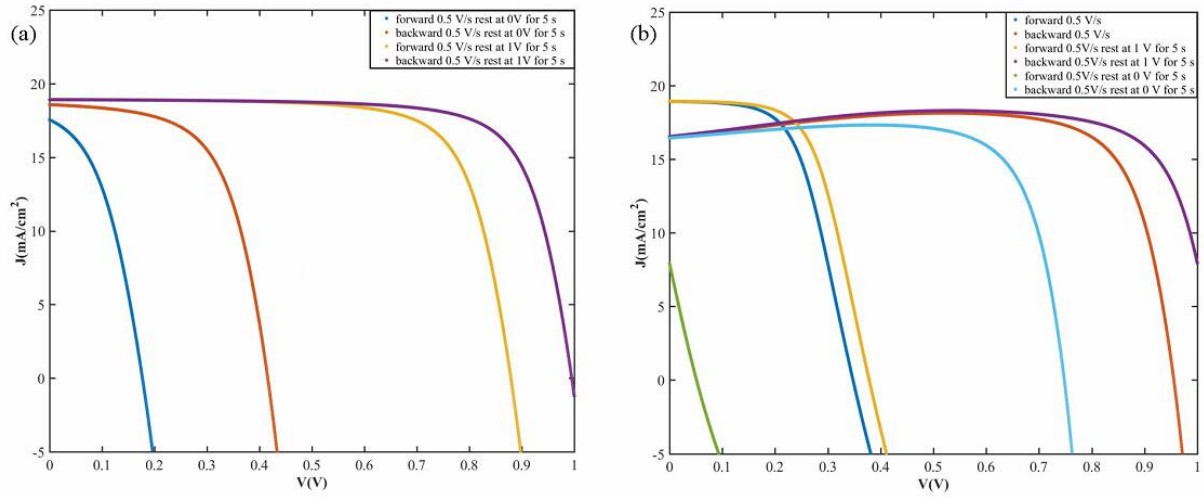

Figure 5.15: The simulation results of the forward and backward scan at 0.5 V/s with (a) different prebiasing conditions and (b) 10 times higher ion mobility/density.

bulk field to significantly reduce the current output. While during the forward scan, the aggregating ions could already significantly offset the applied bias and reduce the V_{OC}. To check if the hysteresis phenomenon could present other features, we run simulations with different prebiasing conditions and a higher ion mobility/density (Figure 5.15).

The results suggest that the prebiasing treatments could not change the overall features of the hysteresis behavior. It appears to shift the curves along the voltage axis due to the pre-aggregated ions (Figure 5.15(a)). On the other hand, assuming the ion could move faster (a higher ion mobility or density) gives rise to a new feature, during the backward scan, the current output decreases more apparently approaching 0 V. But we still see that the V_{OC}s of the forward and backward scans have a huge gap.

The above discussions present a clear conclusion, in the existing model of our solar cell, the hysteresis will behave in such a manner where the V_{OC} is more impressionable. We then check the parameters of the solar cell model to see if the hysteresis behavior could be modified. And we find that the recombination velocities have a big influence on the patterns of the hysteresis behavior (Figure 5.16).

The simulations results of Figure 5.16 is derived with a scan speed of 0.1 V/s, no prebiasing treatments and 5 times higher ion mobility/density. In simple terms, the slower scan speeds and higher ion mobility/density enable the voltage drop across the Debye layer to adjust itself quickly and largely offset the bulk electric field. In the mean time, though the drift current is suppressed due to the reduced bulk electric field, the cell can still output a decent diffusion current due to the smaller recombination rate. Here we find a combination of the internal processes which can lead to the wide-known hysteresis feature, namely fast ion movement and slow recombination.

We suggest this combination is necessary for the reported hysteresis features (Figure 1.14) in the framework of ion aggregation. On one hand, the dramatic current variations suggest a fast and giant voltage build-up across the Debye layer. On the other hand, a

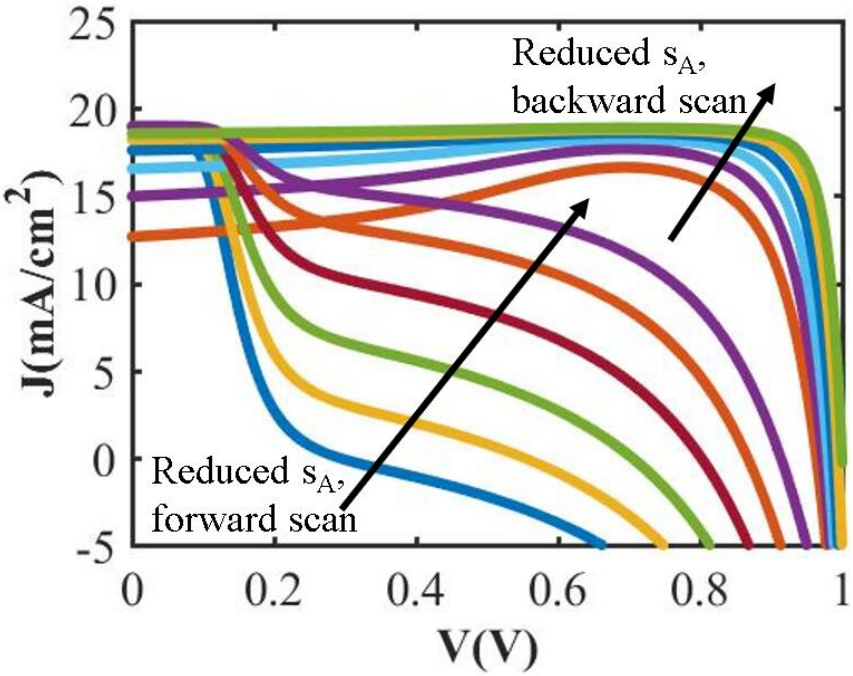

Figure 5.16: The influence of s_A on the hysteresis features of J-V curves. Following the arrows the s_A decreased from 1800 cm/s to 800, 400, 200, 100, 50 cm/s.

still decent V_{OC} requires the current flow to be not too dependent on the drift process, implying a slow recombination profile is necessary. This combination may be in reality favored. Figure 5.13 presents a steep surface band bending due to the aggregation of ions which could form a potential barrier suppressing the interfacial recombination.

In short summary, a model of our solar cell architecture is established by solving the continuity equation. Assuming the interfacial recombination is dominant in our cell, the recombination term in the equation is simplified to allow for the extraction of the analytical solution. We resort to Matlab for the fitting of the model with the experimental data. Careful examination indicates the fitting is successful with only one valid solution set. And a high recombination velocity is obtained at the PEDOT:PSS/$MAPbI_3$ interface from the solution which matches well with the reality. The simulation based on the derived model suggests 500 nm perovskite layer or a higher mobility of electrons and holes (up to 50 cm/(V s)) brings considerable efficiency gains. Also with the carriers generating and recombining close to each other, the efficiency of our PSC is notably deteriorated. The hysteresis phenomenon of the PSC is modeled and simulated based on the ion migration hypothesis. We find that our solar cell model can not present the typical hysteresis feature. And further considerations suggest that a lower recombination rate is necessary to create such J-V behavior, which may originate from the surface barrier due to the ion aggregation.

Chapter 6

Conclusion and outlook

6.1 Conclusion

Perovskites have been the 'wonder material' in recent years in the solar cell research community. Formulating in the simplest way, the magic of halide perovskites lies in the long carrier diffusion length (which is mainly ascribed to the its unique defect tolerance property)[166][36]. Besides, the tunable bandgap of perovskites enables its application in tandem solar cells either with other types of solar cell (for example, silicon cell) or with all perovskites architectures[14][12][13]. The tandem solar cell could theoretically achieve energy transform efficiencies beyond the Shockley Queisser limit (which is 30% for $MAPbI_3$) and attract lots of interest[293][294]. Another intriguing advantage is the potential application of halide perovskites on flexible solar cells thanks to the high absorption coefficient[295][296]. Moreover, the cost of perovskite solar cells in industry scale is expected to be another superiority of this technique due to the lower cost of precursor materials and solution-based deposition methods.

The efficiency of PSCs has been improved from initial 3.8% to 23.3% within 10 years[5]. This explosive improvement is partly ascribed to the intrinsic properties of perovskite materials, and also partly ascribed to the enthusiastic research community which has a solid knowledge accumulation of solar cell materials and fabrication techniques. However, it is also clear that after entering the 20% region, the efficiency gain of PSCs is much more difficult to achieve. And the main bottle neck is the V_{OC} and FF whose further improvements depend on a in-depth characterization and understanding of the cell's device physics[177]. In my understanding, the core question of the device physics of a solar cell is its recombination profile. To further improve the V_{OC} and FF of the PSCs, pinpointing the major recombination pathways and suppressing the recombination losses are, in the final analysis, the ultimate approach.

The aim of this project is to develop fabrication techniques of inverted PSCs and reveal the device physics which limits the cell's performance. In chapter 3 we presented a novel perovskite deposition technique which can produce a very uniform film. The

thickness can be easily tuned to as thin as 80 nm which can be used to produce semi-transparent solar cells. This technique delivers a high reproducibility and around 16% efficiency for the inverted PSCs. In chapter 4, focusing on the interesting phenomena introduced by the different deposition conditions, we studied the underlying principle of the V_{OC} variations of the prepared solar cells. We identified, instead of a direct change of the recombination profile, the V_{OC} variations are caused by the change of the built-in field due to the formation of the surface band bending feature. In chapter 5, the modeling and simulation based on our solar cell structure is performed. The main limitation of our solar cell is suggested to locate at the PEDOT:PSS/$MAPbI_3$ interface which has a very high interfacial recombination velocity. I also suggest that the hysteresis behavior of PSCs may accompany with a suppressed interfacial recombination.

Specifically, in the film deposition and device fabrication section (Chapter 3), firstly a detailed parameter study was performed to determine which influenced the formation quality of perovskite films in the vacuum-assisted annealing method. We conclude that this deposition technique relies on the addition of excess organic methylamine salt which slows down the crystallization process to form a more uniform morphology. And a high vacuum level is beneficial to the morphology during both the initial crystallization and latter purification processes. We showed that one main draw back of this method is the introduction of defects during the vacuum annealing which is ascribed to the exacerbated thermal stability of organic-inorganic perovskites under vacuum. Afterwards, we fabricated inverted perovskite solar cells based on the developed films deposition techniques. A normal optimization procedure was performed to maximize the efficiency of the solar cell. It shows that the thickness of C_{60} is very influential on the FF which may be due to its low conductivity. As such, a post annealing treatment is found to be beneficial probably by enhancing the electrical connection between the $MAPbI_3$ and C_{60} layers. A thin layer of LiF is also found to improve the FF. We showed that our fabrication technique is suitable to produce the semi-transparent PSCs. Interestingly we observed that PSCs with a lot of excess organic methylamine salt impurities can still deliver a decent efficiency, which suggests perovskites are very tolerant with this type of defects. In the end, we showed that the V_{OC} of our cells are strongly influenced by the vacuum annealing conditions.

In the characterization of the inverted PSCs section (Chapter 4), we firstly discussed the error-prone operation - determining the cell's V_{OC}. Besides the lamp spectra and intensity uniformity, another easily neglected parameter is the illumination area. For the current PSC structure, it is likely that an underestimation of around 10-20 mV could happen for V_{OC} while at same time FF is overestimated. This could lead to a difficult comparison of the cell parameters between different studies. Also it might be misleading regarding the determination of the limiting parameters of the efficiency. Next we studied the origin of the V_{OC} variations of the PSCs with different annealing treatments. And we find the different annealing conditions lead to a surface band bending effect which can be attributed to charged defects. This phenomenon is ascribed to be the main reason for the V_{OC} change. In general, the recombination profile should account for the amplitude of V_{OC} under a certain cell architecture. However, we suggest that the change of band structure could lead to a different distribution of the carrier populations which further influences the recombination losses. This concept is further applied by the plasma treatment on the perovskite surface. We find the oxygen plasma could significantly improve the V_{OC} which

we attribute to the change of the band structure. Although the oxygen plasma leads to the degradation of perovskites, the enhancement of the built-in field is more influential and overall improves the V_{OC} of the cell. Argon plasma, on the other hand, leads to a strong hysteresis behavior of the solar cell. We suspect this may be due to increased trap states caused by the argon plasma.

Finally we modelled the studied cell architecture and simulated its behaviors (Chapter 5). The simulation method is insightful to describe the whole dynamic processes in a cell. We get the analytical solution of the continuity equation by simplifying the recombination term. As a lot of studies suggest that the main recombination pathway in a PSC is at the interface, only the interfacial recombination between the minority carriers and the adjacent transporting layer is considered. We argue that this is especially suitable for our cell architecture with the poor hole selective PEDOT:PSS layer. We checked the reliability of the fitting algorithm and found only one valid solution set. And a very high recombination velocity at the PEDOT:PSS/$MAPbI_3$ interface is obtained which suggests our model reasonably reflects the reality. We then ran simulations based on the derived model. We find that additional efficiency gains could be obtained by increasing the thickness of the perovskite layer to 500 nm. Increasing the mobility of charge carriers by, for example, reducing grain boundaries is also an effective strategy till around 50 cm/(V s), further increasing the value only has a marginal effect on the cell's performance. We also find that the efficiency of our cell is notably deteriorated as the charge carriers generate near the PEDOT:PSS/$MAPbI_3$ interface where the recombination is more severe. Finally, we modelled and simulated the hysteresis behavior of the cell based on the ion migration hypothesis. We show that the fitting results match well with the observed hysteresis feature in the studied PSC. However, to present the features of the hysteresis behavior of relative reports[184][291][292], a lower interfacial recombination rate has to be used which may originate from the potential barrier due to ion accumulations at the interface.

6.2 Overlook

Due to the limitation of time and ability, the current project is concluded with certain unfinished and unimplemented plans which we hope to perform in the future. Firstly, the project has a loop of fabrication, characterization and re-optimization procedures. But the re-optimization part is not fully accomplished yet. We find out that the limitation of our solar cell is the low V_{OC}, which can be influenced by the built-in field and the recombination profile. We implemented oxygen plasma treatments to enhance the built-in field and increased the V_{OC} which proved to be effective. However, the instability of the plasma in air with the perovskite makes this treatment not practical regarding the long-term stability of the cell. In addition, with this treatment, the charge injection at the interface may be problematic and lead to the decrease of J_{SC} which may be overcome by a cell architecture with improved charge collection processes. To achieve an overall improved cell performance and stability, one may consider the insertion of an interfacial dipole layer with modified charge injections at the interface.

Secondly, by the simulation technique, the main recombination channel is revealed. The next step is to suppress this interfacial recombination by, for example, inserting an interfacial blocking layer to build a more efficient solar cell. Then we may use the existing model to extract the new recombination velocities and check if the model successfully simulates and guides the optimization direction of the actual device.

Moreover, we see one very intriguing question arises regarding the interaction of built-in fields and recombination processes, both of which can influence the V_{OC}. Based on the thermal radiative model, the thermal radiative limit of the V_{OC} of a PSC will not depend on the built-in field assuming no non-radiative recombination. Then the dependence of the V_{OC} on the built-in field will be a function of the recombination profiles. As achieving better energy alignments of a PSC to enhance the V_{OC} has been a popular strategy[297][174][298][299], it is interesting to probe the boundary of this concept. We predict that a higher built-in field may be more beneficial to the V_{OC}, in a PSC with a higher and uneven recombination profile.

The hysteresis feature of the PSCs is also a very interesting direction. We have built a model and simulated the hysteresis behavior of the studied cell with ion migration. And we found that argon plasma could greatly enhance the hysteresis behavior of the PSC. But the reason is still unclear. We suspect, based on the ion migration theory, the argon plasma may lead to more movable ions which may come from the damaged lattices. Though in general the hysteresis is unfavorable in the PSC, it will be very interesting to see if we can provide a solid link between the ion migration and the defect density[300][301][302].

As the efficiency of PSCs has entered the over 20% range, it will be more and more difficult to further increase it. As the perovskite is defect tolerant, pinpointing, understanding and suppressing the main interfacial recombination losses will be the most effective strategy enhancing the V_{OC} and efficiency. As employing the interfacial blocking layer seems to be an effective way to reduce the interfacial recombination rate, it might be a popular concept for PSCs in the future[177][103]. However, as the blocking layer may also impede the charge transfer at the interfaces, the mesoporous or other structures which can facilitate the charge transport maybe in the end prove valuable to achieve a higher efficiency for PSCs[170]. Right now, with not fully passivated surfaces, the reported efficiencies of mesoporous and planar perovskite solar cells are quite close to each other[303][304].

In the end, as the PSC has entered its 10th year, more and more emphases are being placed on its commercialization and application. Several tough nuts are being cracked. Regarding the stability issue, all-inorganic perovskites, 2D-3D hybrid perovskites are under intensive study and prove to provide a higher stability against moisture[305][59][306][307]. Moreover, carbon electrodes are reported to lead to greatly improved life time of the PSCs[308]. Indeed stable working PSCs over a year have been achieved. Large area PSCs (> 10 cm^2) have also be fabricated presenting the scalability of the current techniques[309][306]. Moreover, lead-free perovskites have also been studied to avoid the usage of toxic lead element[310][311]. Though the cell efficiency of tin based or double metal cation perovskites is still lower than its lead-based pioneer, they are more environmentally friendly and represent the development direction in the future. In addi-

tion, the tunable band gap of perovskites enables its potential application in a tandem cell with the commercial silicon solar cell, which is attracting a lot of interest[293][294]. With these studies continually achieving headways, the commercial PSC may be already not far away.

Appendices - the modeling and simulation codes

Code Listing A.1: Solar cell modeling functions

```
function jphoto= pero_p(coeff,V)
Vbi = coeff(1)+1e-6; %for convergence
lambda = coeff(2);
sA = coeff(3);
sD = coeff(4);
m = 300/lambda;
bA = 863/sA;
bD = 863/sD;
y = (V-Vbi)/0.0259;
alphaA = 1./((exp(y)-1)./y+bA);
alphaD = 1./((exp(y)-1)./y+bD);
A = alphaA .* ((1-exp(y-m))./(y-m)-bA);
B = alphaD .* ((1-exp(y+m))./(y+m)-bD);
jphoto = -23 * (A-B.*exp(-m));
end

function jphoto= pero_p2(coeffp,coeff,V)
Vbi = coeff(1)+1e-6; %for convergence
lambda = coeffp(2);
sA = coeff(3);
sD = coeff(4);
m = 300/lambda;
bA = 863/sA;
bD = 863/sD;
y = (V-Vbi)/0.0259;
alphaA = 1./((exp(y)-1)./y+bA);
```

```
alphaD = 1./((exp(y)-1)./y+bD);
A = alphaA .* ((1-exp(y-m))./(y-m)-bA);
B = alphaD .* ((1-exp(y+m))./(y+m)-bD);
jphoto = -23 * (A-B.*exp(-m));
end

function jdark= pero_d(coeff,V)
Vbi = coeff(1)+1e-6;
lambda = coeff(2);
sA = coeff(3);
sD = coeff(4);
nA = coeff(5);
nD = coeff(6);
m = 300/lambda;
bA = 863/sA;
bD = 863/sD;
y = (V-Vbi)./0.0259;
alphaA = 1./((exp(y)-1)./y+bA);
alphaD = 1./((exp(y)-1)./y+bD);
jdark =-(exp(V/0.0259)-1).*(alphaA*1.38e-13*nA+alphaD*1.38e-13*nD);
end

function jdark= pero_d2(coeffd,coeff,V)
Vbi = coeff(1)+1e-6; %for convergence
lambda = coeff(2);
sA = coeff(3);
sD = coeff(4);
nA = coeffd(5);
nD = coeffd(6);
m = 300/lambda;
bA = 863/sA;
bD = 863/sD;
y = (V-Vbi)./0.0259;
alphaA = 1./((exp(y)-1)./y+bA);
alphaD = 1./((exp(y)-1)./y+bD);
jdark =-(exp(V/0.0259)-1).*(alphaA*1.38e-13*nA+alphaD*1.38e-13*nD);
end
```

Code Listing A.2: Solar cell simulation function

```
function peroj= pero_simu(coeff,V)
Vbi = 0.9088; %V, for convergence
lambda = 172; %nm
L=coeff(1);
un=coeff(2);
up=coeff(3);
sA = coeff(4);%1800 cm/s
sD = coeff(5);%1.8 cm/s
nA = coeff(6);%0.016 cm-3
nD = coeff(7);%0.515 cm-3
m = L/lambda;
bA = 863*un/sA*300/L;
bD = 863*up/sD*300/L;
y = (V-Vbi)/0.0259;
alphaA = 1./((exp(y)-1)./y+bA);
alphaD = 1./((exp(y)-1)./y+bD);
A = alphaA .* ((1-exp(y-m))./(y-m)-bA);
B = alphaD .* ((1-exp(y+m))./(y+m)-bD);
jphoto = -23 * (A-B.*exp(-m));
jdark
 ↪  =-(exp(V/0.0259)-1).*(alphaA*4.14e-11*nA*un/L+alphaD*4.14e-11*nD*up/L);
peroj=jphoto+jdark;
end
```

Code Listing A.3: Debye layer modeling function

```
function
 ↪  VV=debye(Scanspeed,direction,range,startvoltage,restvoltage,resttime)
  f=chebfun({@(x) sign(x)*3.7987e-07*(2*exp((10000*x)/259) -
 ↪  (20000*x)/259 - 2)^0.5,@(x) sign(x)*3.7987e-07*(2*exp((10000*x)/259)
 ↪  - (20000*x)/259 - 2)^0.5},[-2,0,0.5]);
  g=inv(f);
  h=-f;
  j=inv(h);
  g=chebfun(g,[-5e-6,5e-6]);
```

```
  j=chebfun(j,[-5e-6,5e-6]);
  debye=g-j;
  VV=zeros(1000/Scanspeed+1,3);
  Q=0;
  for i=1:1000*resttime
          vion=5*(1.0667e-06*(0.9088-restvoltage) -
          ↪  1.0667e-06*debye(Q));
          Q=Q+vion*0.001;
  end
  VV(1,1)=startvoltage;
  VV(1,2)=debye(Q);
  VV(1,3)=Q;
  if direction==0;
      for i=1:1000*range/Scanspeed
           vion=5*(1.0667e-06*(0.9088-startvoltage) -
           ↪  1.0667e-06*Scanspeed*i/1000 -  1.0667e-06*debye(Q));
           Q=Q+vion*0.001;
           VV(i+1,1)=Scanspeed*i/1000+startvoltage;
           VV(i+1,2)=debye(Q);
           VV(i+1,3)=Q;
      end
  else

      for i=1:1000*range/Scanspeed
          vion=5*(1.0667e-06*Scanspeed*i/1000 - 1.0667e-06*debye(Q) -
          ↪  1.0667e-06*(startvoltage-0.9088));
          Q=Q+vion*0.001;
          VV(i+1,1)=startvoltage-Scanspeed*i/1000;
          VV(i+1,2)=debye(Q);
          VV(i+1,3)=Q;
      end
  end

end
```

Code Listing A.4: Solar cell fitting scripts

```
clear;
```

```
JV = xlsread('JV.xlsx', 'Sheet1', 'A:C');
JPdataH=JV(:,2)-JV(:,3);
VdataH=JV(:,1);
coeff_init = [0.8;150;100;1000;0;0];
options = optimset('Display','iter','TolFun',1e-10,'TolX',1e-25);
lb=[0; 0; 1e-3; 1e-3;-1;-1]; % lower bound constraints
ub=[1.5; 250; 1e7; 1e7;1;1]; % upper bound constraints
[coeff,resnorm,residual,exitflag] =
 ↪  lsqcurvefit(@pero_p,coeff_init,VdataH,JPdataH,lb,ub,options);
figure(1)
plot(VdataH(:,1),JPdataH,'-r','LineWidth',2);
hold on,plot(VdataH(:,1),pero_p(coeff,VdataH(:,1)),'o','LineWidth',2);
set(gca,'LineWidth',2,'FontSize',22,'FontWeight','normal','FontName','Ti
 ↪  mes')
set(get(gca,'XLabel'),'String','V(V)','FontSize',22,'FontWeight','bold',
 ↪  'FontName','Times')
set(get(gca,'YLabel'),'String','J(mA/cm^2)','FontSize',22,'FontWeight','
 ↪  bold','FontName','Times')
set(gca,'box','on');
%%
lb=[0; 0; 1e-3; 1e-3;-1;0]; % lower bound constraints
ub=[1.5; 250; 1e7; 1e7;1;1]; % upper bound constraints
pero_d3=@(coeffd,V) pero_d2(coeffd,coeff,V);% reducing the variables
coeffd = lsqcurvefit(pero_d3,coeff,VdataH,JV(:,3),lb,ub,options);
figure(2)
plot(VdataH(:,1),JV(:,3),'-r','LineWidth',2);
hold on,plot(VdataH(:,1),pero_d(coeffd,VdataH(:,1)),'o','LineWidth',2);
set(gca,'LineWidth',2,'FontSize',22,'FontWeight','normal','FontName','Ti
 ↪  mes')
set(get(gca,'XLabel'),'String','V(V)','FontSize',22,'FontWeight','bold',
 ↪  'FontName','Times')
set(get(gca,'YLabel'),'String','J(mA/cm^2)','FontSize',22,'FontWeight','
 ↪  bold','FontName','Times')
set(gca,'box','on');
```

Code Listing A.5: Solar cell simulation scripts

```
clear;
```

```
JV = xlsread('JV.xlsx', 'Sheet1', 'A:C');
JdataH=JV(:,2)
VdataH=JV(:,1);
figure(1)
plot(VdataH(:,1),JdataH,'-r','LineWidth',2);
hold all;
coeff1 = [200;1;1;1800;1.8;0.016;0.515];
plot(VdataH(:,1),pero_simu(coeff1,VdataH(:,1)),'o','LineWidth',2,'marker
    size',3);

coeff2 = [300;1;1;1800;1.8;0.016;0.515];
plot(VdataH(:,1),pero_simu(coeff2,VdataH(:,1)),'o','LineWidth',2,'marker
    size',3);

coeff3 = [400;1;1;1800;1.8;0.016;0.515];
plot(VdataH(:,1),pero_simu(coeff3,VdataH(:,1)),'o','LineWidth',2,'marker
    size',3);

coeff4 = [500;1;1;1800;1.8;0.016;0.515];
plot(VdataH(:,1),pero_simu(coeff4,VdataH(:,1)),'o','LineWidth',2,'marker
    size',3);

coeff5 = [600;1;1;1800;1.8;0.016;0.515];
plot(VdataH(:,1),pero_simu(coeff5,VdataH(:,1)),'o','LineWidth',2,'marker
    size',3);

coeff6 = [700;1;1;1800;1.8;0.016;0.515];
plot(VdataH(:,1),pero_simu(coeff6,VdataH(:,1)),'o','LineWidth',2,'marker
    size',3);

axis([0 1 -20 25])
set(gca,'LineWidth',2,'FontSize',22,'FontWeight','normal','FontName','Ti
    mes')
set(get(gca,'XLabel'),'String','V(V)','FontSize',22,'FontWeight','bold',
    'FontName','Times')
set(get(gca,'YLabel'),'String','J(mA/cm^2)','FontSize',22,'FontWeight','
    bold','FontName','Times')
set(gca,'box','on');

```

```
%%
figure(2)
plot(VdataH(:,1),VdataH(:,1).*JdataH,'-r','LineWidth',2);
hold all;
coeff1 = [200;1;1;1800;1.8;0.016;0.515];
plot(VdataH(:,1),VdataH(:,1).*pero_simu(coeff1,VdataH(:,1)),'o','LineWid
    th',2,'markersize',3);

coeff2 = [300;1;1;1800;1.8;0.016;0.515];
plot(VdataH(:,1),VdataH(:,1).*pero_simu(coeff2,VdataH(:,1)),'o','LineWid
    th',2,'markersize',3);

coeff3 = [400;1;1;1800;1.8;0.016;0.515];
plot(VdataH(:,1),VdataH(:,1).*pero_simu(coeff3,VdataH(:,1)),'o','LineWid
    th',2,'markersize',3);

coeff4 = [500;1;1;1800;1.8;0.016;0.515];
plot(VdataH(:,1),VdataH(:,1).*pero_simu(coeff4,VdataH(:,1)),'o','LineWid
    th',2,'markersize',3);

coeff5 = [600;1;1;1800;1.8;0.016;0.515];
plot(VdataH(:,1),VdataH(:,1).*pero_simu(coeff5,VdataH(:,1)),'o','LineWid
    th',2,'markersize',3);

coeff6 = [700;1;1;1800;1.8;0.016;0.515];
plot(VdataH(:,1),VdataH(:,1).*pero_simu(coeff6,VdataH(:,1)),'o','LineWid
    th',2,'markersize',3);

axis([0 1 -5 18])
set(gca,'LineWidth',2,'FontSize',22,'FontWeight','normal','FontName','Ti
    mes')
set(get(gca,'XLabel'),'String','V(V)','FontSize',22,'FontWeight','bold',
    'FontName','Times')
set(get(gca,'YLabel'),'String','Eff
    (%)','FontSize',22,'FontWeight','bold','FontName','Times')
set(gca,'box','on');
%%
figure(3)
plot(VdataH(:,1),JdataH,'-r','LineWidth',2);
```

```
hold all;
coeff1 = [300;1;1;1800;1.8;0.016;0.515];
plot(VdataH(:,1),pero_simu(coeff1,VdataH(:,1)),'o','LineWidth',2,'marker
    size',3);

coeff2 = [300;2;2;1800;1.8;0.016;0.515];
plot(VdataH(:,1),pero_simu(coeff2,VdataH(:,1)),'o','LineWidth',2,'marker
    size',3);

coeff3 = [300;5;5;1800;1.8;0.016;0.515];
plot(VdataH(:,1),pero_simu(coeff3,VdataH(:,1)),'o','LineWidth',2,'marker
    size',3);

coeff4 = [300;10;10;1800;1.8;0.016;0.515];
plot(VdataH(:,1),pero_simu(coeff4,VdataH(:,1)),'o','LineWidth',2,'marker
    size',3);

coeff5 = [300;50;50;1800;1.8;0.016;0.515];
plot(VdataH(:,1),pero_simu(coeff5,VdataH(:,1)),'o','LineWidth',2,'marker
    size',3);

coeff6 = [300;100;100;1800;1.8;0.016;0.515];
plot(VdataH(:,1),pero_simu(coeff6,VdataH(:,1)),'o','LineWidth',2,'marker
    size',3);

axis([0 1 -20 25])
set(gca,'LineWidth',2,'FontSize',22,'FontWeight','normal','FontName','Ti
    mes')
set(get(gca,'XLabel'),'String','V(V)','FontSize',22,'FontWeight','bold',
    'FontName','Times')
set(get(gca,'YLabel'),'String','J(mA/cm^2)','FontSize',22,'FontWeight','
    bold','FontName','Times')
set(gca,'box','on');
%%
figure(4)
plot(VdataH(:,1),VdataH(:,1).*JdataH,'-r','LineWidth',2);
hold all;
coeff1 = [300;1;1;1800;1.8;0.016;0.515];
```

```
91  plot(VdataH(:,1),VdataH(:,1).*pero_simu(coeff1,VdataH(:,1)),'o','LineWid
    ↪ th',2,'markersize',3);
92
93  coeff2 = [300;2;2;1800;1.8;0.016;0.515];
94  plot(VdataH(:,1),VdataH(:,1).*pero_simu(coeff2,VdataH(:,1)),'o','LineWid
    ↪ th',2,'markersize',3);
95
96  coeff3 = [300;5;5;1800;1.8;0.016;0.515];
97  plot(VdataH(:,1),VdataH(:,1).*pero_simu(coeff3,VdataH(:,1)),'o','LineWid
    ↪ th',2,'markersize',3);
98
99  coeff4 = [300;10;10;1800;1.8;0.016;0.515];
100 plot(VdataH(:,1),VdataH(:,1).*pero_simu(coeff4,VdataH(:,1)),'o','LineWid
    ↪ th',2,'markersize',3);
101
102 coeff5 = [300;50;50;1800;1.8;0.016;0.515];
103 plot(VdataH(:,1),VdataH(:,1).*pero_simu(coeff5,VdataH(:,1)),'o','LineWid
    ↪ th',2,'markersize',3);
104
105 coeff6 = [300;100;100;1800;1.8;0.016;0.515];
106 plot(VdataH(:,1),VdataH(:,1).*pero_simu(coeff6,VdataH(:,1)),'o','LineWid
    ↪ th',2,'markersize',3);
107
108 axis([0 1 -5 18])
109 set(gca,'LineWidth',2,'FontSize',22,'FontWeight','normal','FontName','Ti
    ↪ mes')
110 set(get(gca,'XLabel'),'String','V(V)','FontSize',22,'FontWeight','bold',
    ↪ 'FontName','Times')
111 set(get(gca,'YLabel'),'String','Eff(%)','FontSize',22,'FontWeight','bold
    ↪ ','FontName','Times')
112 set(gca,'box','on');
113 %%
114 figure(5)
115 plot(VdataH(:,1),JdataH,'-r','LineWidth',2);
116 hold all;
117 coeff1 = [300;1;1;1800;1.8;0.016;0.515];
118 plot(VdataH(:,1),pero_simu(coeff1,VdataH(:,1)),'o','LineWidth',2,'marker
    ↪ size',3);
119
```

```
120 coeff2 = [300;1;1;1.8;1800;0.515;0.016];
121 plot(VdataH(:,1),pero_simu(coeff2,VdataH(:,1)),'o','LineWidth',2,'marker
    ↪ size',3);
122
123 coeff3 = [100;5;5;1800;1.8;0.016;0.515];
124 plot(VdataH(:,1),pero_simu(coeff3,VdataH(:,1)),'o','LineWidth',2,'marker
    ↪ size',3);
125
126 coeff4 = [100;1;1;1.8;1800;0.515;0.016];
127 plot(VdataH(:,1),pero_simu(coeff4,VdataH(:,1)),'o','LineWidth',2,'marker
    ↪ size',3);
128
129 axis([0 1 -20 25])
130 set(gca,'LineWidth',2,'FontSize',22,'FontWeight','normal','FontName','Ti
    ↪ mes')
131 set(get(gca,'XLabel'),'String','V(V)','FontSize',22,'FontWeight','bold',
    ↪ 'FontName','Times')
132 set(get(gca,'YLabel'),'String','J(mA/cm^2)','FontSize',22,'FontWeight','
    ↪ bold','FontName','Times')
133 set(gca,'box','on');
134
135 %%
136 figure(6)
137 plot(VdataH(:,1),VdataH(:,1).*JdataH,'-r','LineWidth',2);
138 hold all;
139 coeff1 = [300;1;1;1800;1.8;0.016;0.515];
140 plot(VdataH(:,1),VdataH(:,1).*pero_simu(coeff1,VdataH(:,1)),'o','LineWid
    ↪ th',2,'markersize',3);
141
142 coeff2 = [300;1;1;1.8;1800;0.515;0.016];
143 plot(VdataH(:,1),VdataH(:,1).*pero_simu(coeff2,VdataH(:,1)),'o','LineWid
    ↪ th',2,'markersize',3);
144
145 coeff1 = [100;1;1;1800;1.8;0.016;0.515];
146 plot(VdataH(:,1),VdataH(:,1).*pero_simu(coeff1,VdataH(:,1)),'o','LineWid
    ↪ th',2,'markersize',3);
147
148 coeff2 = [100;1;1;1.8;1800;0.515;0.016];
```

```
149 plot(VdataH(:,1),VdataH(:,1).*pero_simu(coeff2,VdataH(:,1)),'o','LineWid
    ↪ th',2,'markersize',3);
150
151 axis([0 1 -5 18])
152 set(gca,'LineWidth',2,'FontSize',22,'FontWeight','normal','FontName','Ti
    ↪ mes')
153 set(get(gca,'XLabel'),'String','V(V)','FontSize',22,'FontWeight','bold',
    ↪ 'FontName','Times')
154 set(get(gca,'YLabel'),'String','Eff(%)','FontSize',22,'FontWeight','bold
    ↪ ','FontName','Times')
155 set(gca,'box','on');
```

Code Listing A.6: Hysteresis simulation scripts

```
1  clear;
2  coeff = [300;1;1;50;1.8;0.016;0.515];
3  Scanspeed=0.1;
4  direction=0;
5  range=1;
6  startvoltage=0;
7  restvoltage=0;
8  resttime=0;
9  Correction=debye(Scanspeed,direction,range,startvoltage,restvoltage,rest
   ↪ time);
10 V=Correction(:,1);
11 VC=Correction(:,1)+Correction(:,2);
12 Q=Correction(:,3);
13 figure(3);
14 hold all
15 plot(V,VC,'o','LineWidth',2,'markersize',3);
16 set(gca,'LineWidth',2,'FontSize',22,'FontWeight','normal','FontName','Ti
   ↪ mes')
17 set(get(gca,'XLabel'),'String','V(V)','FontSize',22,'FontWeight','bold',
   ↪ 'FontName','Times')
18 set(get(gca,'YLabel'),'String','V_C(V)','FontSize',22,'FontWeight','bold
   ↪ ','FontName','Times')
19 set(gca,'box','on');
20 figure(2);
```

```
hold all
plot(V,pero_simu(coeff,VC),'o','LineWidth',2,'markersize',3);
direction=1;
startvoltage=1;
restvoltage=0;
resttime=0;
Correction=debye(Scanspeed,direction,range,startvoltage,restvoltage,rest
↪ time);
V=Correction(:,1);
C=Correction(:,2);
VC=Correction(:,1)+Correction(:,2);
plot(V,pero_simu(coeff,VC),'o','LineWidth',2,'markersize',3);
xlim([0,1])
ylim([-5 25])
set(gca,'LineWidth',2,'FontSize',22,'FontWeight','normal','FontName','Ti
↪ mes')
set(get(gca,'XLabel'),'String','V(V)','FontSize',22,'FontWeight','bold',
↪ 'FontName','Times')
set(get(gca,'YLabel'),'String','J(mA/cm^2)','FontSize',22,'FontWeight','
↪ bold','FontName','Times')
set(gca,'box','on');
```

Bibliography

[1] British Petroleum Company. *BP Statistical Review of World Energy*. (accessed: 20.11.2018).

[2] Gülden Bölük and Mehmet Mert. "Fossil & renewable energy consumption, GHGs (greenhouse gases) and economic growth: Evidence from a panel of EU (European Union) countries". In: *Energy* 74 (2014), pp. 439–446.

[3] IEA-International Energy Agency. *Renewables 2017s*. Market Report Series. IEA-International Energy Agency, 2017. ISBN: 978-92-64-28185-1.

[4] Web of Science. *Publications statistics on perovskite material and solar device*. (accessed: 02.2019).

[5] The National Renewable Energy Laboratory. *Best Research-cell efficiencies*. (accessed: 12.11.2018).

[6] V. M. Goldschmidt. "Die Gesetze der Krystallochemie". In: *Naturwissenschaften* 14.21 (1926), pp. 477–485.

[7] Z. Li et al. "Stabilizing Perovskite Structures by Tuning Tolerance Factor: Formation of Formamidinium and Cesium Lead Iodide Solid-State Alloys". In: *Chemistry of Materials* 28.1 (2016), pp. 284–292.

[8] G. Kieslich, S. Sun, and A. K. Cheetham. "Solid-state principles applied to organic–inorganic perovskites: new tricks for an old dog". In: *Chemical Science*. 5 (12 2014), pp. 4712–4715.

[9] C. C. Stoumpos, C. D. Malliakas, and M. G. Kanatzidis. "Semiconducting Tin and Lead Iodide Perovskites with Organic Cations: Phase Transitions, High Mobilities, and Near-Infrared Photoluminescent Properties". In: *Inorganic Chemistry* 52.15 (2013), pp. 9019–9038.

[10] T. Baikie et al. "Synthesis and crystal chemistry of the hybrid perovskite $(CH_3NH_3)PbI_3$ for solid-state sensitised solar cell applications". In: *Journal of Materials Chemistry A* 1 (18 2013), pp. 5628–5641.

[11] M. T. Weller et al. "Complete structure and cation orientation in the perovskite photovoltaic methylammonium lead iodide between 100 and 352 K". In: *Chemical Communications* 51 (20 2015), pp. 4180–4183.

[12] J. Noh et al. "Chemical Management for Colorful, Efficient, and Stable Inorganic–Organic Hybrid Nanostructured Solar Cells". In: *Nano Letters* 13.4 (2013), pp. 1764–1769.

[13] S. A. Kulkarni et al. "Band-gap tuning of lead halide perovskites using a sequential deposition process". In: *Journal of Materials Chemistry A* 2.24 (2014), pp. 9221–9225.

[14] G. E. Eperon et al. "Formamidinium lead trihalide: a broadly tunable perovskite for efficient planar heterojunction solar cells". In: *Energy & Environmental Science* 7.3 (2014), pp. 982–988.

[15] J. Even et al. "Importance of Spin–Orbit Coupling in Hybrid Organic/Inorganic Perovskites for Photovoltaic Applications". In: *The Journal of Physical Chemistry Letters* 4.17 (2013), pp. 2999–3005.

[16] M. Bokdam et al. "Role of Polar Phonons in the Photo Excited State of Metal Halide Perovskites". In: *Scientific Reports* 6 (2016), p. 28618.

[17] R. Prasanna et al. "Band Gap Tuning via Lattice Contraction and Octahedral Tilting in Perovskite Materials for Photovoltaics". In: *Journal of the American Chemical Society* 139.32 (2017), pp. 11117–11124.

[18] N. Park. "Perovskite solar cells: an emerging photovoltaic technology". In: *Materials Today* 18.2 (2015), pp. 65–72.

[19] J. Im et al. "6.5 % efficient perovskite quantum-dot-sensitized solar cell". In: *Nanoscale* 3 (10 2011), pp. 4088–4093.

[20] E. M. Hutter et al. "Direct–indirect character of the bandgap in methylammonium lead iodide perovskite". In: *Nature Materials* 16 (2016), p. 115.

[21] T. Kirchartz and U. Rau. "Decreasing Radiative Recombination Coefficients via an Indirect Band Gap in Lead Halide Perovskites". In: *The Journal of Physical Chemistry Letters* 8.6 (2017), pp. 1265–1271.

[22] F. Zheng et al. "Rashba Spin–Orbit Coupling Enhanced Carrier Lifetime in $CH_3NH_3PbI_3$". In: *Nano Letters* 15.12 (2015), pp. 7794–7800.

[23] V. Sarritzu et al. "Direct or Indirect Bandgap in Hybrid Lead Halide Perovskites?" In: *Advanced Optical Materials* 6.10 (2018), p. 1701254.

[24] O. E. Semonin et al. "Limits of Carrier Diffusion in n-Type and p-Type $CH_3NH_3PbI_3$ Perovskite Single Crystals". In: *The Journal of Physical Chemistry Letters* 7.17 (2016), pp. 3510–3518.

[25] C. Wehrenfennig et al. "Charge-carrier dynamics in vapour-deposited films of the organolead halide perovskite $CH_3NH_3PbI_{3-x}Cl_x$". In: *Energy & Environmental Science* 7.7 (2014), pp. 2269–2275.

[26] W. Yin, T. Shi, and Y. Yan. "Unusual defect physics in $CH_3NH_3PbI_3$ perovskite solar cell absorber". In: *Applied Physics Letters* 104.6 (2014), p. 063903.

[27] M. B. Johnston and L. M. Herz. "Hybrid Perovskites for Photovoltaics: Charge-Carrier Recombination, Diffusion, and Radiative Efficiencies". In: *Accounts of Chemical Research* 49.1 (2016), pp. 146–154.

[28] R. L. Milot et al. "Temperature-Dependent Charge-Carrier Dynamics in $CH_3NH_3PbI_3$ Perovskite Thin Films". In: *Advanced Functional Materials* 25.39 (2015), pp. 6218–6227.

[29] C. L. Davies et al. “Bimolecular recombination in methylammonium lead triiodide perovskite is an inverse absorption process”. In: *Nature Communications* 9.1 (2018), p. 293.

[30] V. Adinolfi et al. “The In-Gap Electronic State Spectrum of Methylammonium Lead Iodide Single-Crystal Perovskites”. In: *Advanced Materials* 28.17 (2016), pp. 3406–3410.

[31] M. L. Agiorgousis et al. “Strong Covalency-Induced Recombination Centers in Perovskite Solar Cell Material $CH_3NH_3PbI_3$”. In: *Journal of the American Chemical Society* (2014).

[32] A. Walsh et al. “Self-Regulation Mechanism for Charged Point Defects in Hybrid Halide Perovskites”. In: *Angewandte Chemie* 127.6 (2015), pp. 1811–1814.

[33] C. S. Ponseca et al. “Organometal Halide Perovskite Solar Cell Materials Rationalized: Ultrafast Charge Generation, High and Microsecond-Long Balanced Mobilities, and Slow Recombination”. In: *Journal of the American Chemical Society* 136.14 (2014), pp. 5189–5192.

[34] E. M. Hutter et al. “Charge Carriers in Planar and Meso-Structured Organic–Inorganic Perovskites: Mobilities, Lifetimes, and Concentrations of Trap States”. In: *The Journal of Physical Chemistry Letters* 6.15 (2015), pp. 3082–3090.

[35] O. G. Reid et al. “Grain-Size-Limited Mobility in Methylammonium Lead Iodide Perovskite Thin Films”. In: *ACS Energy Letters* 1.3 (2016), pp. 561–565.

[36] Q. Dong et al. “Electron-hole diffusion lengths ¿ 175 μm in solution-grown $CH_3NH_3PbI_3$ single crystals”. In: *Science* 347.6225 (2015), pp. 967–970.

[37] G. Xing et al. “Long-Range Balanced Electron- and Hole-Transport Lengths in Organic-Inorganic $CH_3NH_3PbI_3$”. In: *Science* 342.6156 (2013), pp. 344–347.

[38] D. A. Valverde-Chávez et al. “Intrinsic femtosecond charge generation dynamics in single crystal $CH_3NH_3PbI_3$”. In: *Energy & Environmental Science* 8.12 (2015), pp. 3700–3707.

[39] Z. Yu. “Rashba Effect and Carrier Mobility in Hybrid Organic–Inorganic Perovskites”. In: *The Journal of Physical Chemistry Letters* 7.16 (2016), pp. 3078–3083.

[40] A. D. Wright et al. “Electron–phonon coupling in hybrid lead halide perovskites”. In: *Nature Communications* 7 (2016), p. 11755.

[41] A. Filippetti et al. “Low electron-polar optical phonon scattering as a fundamental aspect of carrier mobility in methylammonium lead halide $CH_3NH_3PbI_3$ perovskites”. In: *Physical Chemistry Chemical Physics* 18.22 (2016), pp. 15352–15362.

[42] M. A. Pérez-Osorio et al. “Vibrational Properties of the Organic–Inorganic Halide Perovskite $CH_3NH_3PbI_3$ from Theory and Experiment: Factor Group Analysis, First-Principles Calculations, and Low-Temperature Infrared Spectra”. In: *The Journal of Physical Chemistry C* 119.46 (2015), pp. 25703–25718.

[43] L. M. Herz. “Charge-Carrier Mobilities in Metal Halide Perovskites: Fundamental Mechanisms and Limits”. In: *ACS Energy Letters* 2.7 (2017), pp. 1539–1548.

[44] R. Brenes et al. “Metal Halide Perovskite Polycrystalline Films Exhibiting Properties of Single Crystals”. In: *Joule* 1.1 (2017), pp. 155–167.

[45] J. Yang et al. “Investigation of $CH_3NH_3PbI_3$ Degradation Rates and Mechanisms in Controlled Humidity Environments Using in Situ Techniques”. In: *ACS Nano* 9.2 (2015), pp. 1955–1963.

[46] T. A. Berhe et al. “Organometal halide perovskite solar cells: degradation and stability”. In: *Energy & Environmental Science* 9.2 (2016), pp. 323–356.

[47] Q. Wang et al. “Scaling behavior of moisture-induced grain degradation in polycrystalline hybrid perovskite thin films”. In: *Energy & Environmental Science* 10.2 (2017), pp. 516–522.

[48] J. Schlipf et al. “In Situ Monitoring the Uptake of Moisture into Hybrid Perovskite Thin Films”. In: *The Journal of Physical Chemistry Letters* 9.8 (2018), pp. 2015–2021.

[49] Y. Kye et al. “Critical Role of Water in Defect Aggregation and Chemical Degradation of Perovskite Solar Cells”. In: *The Journal of Physical Chemistry Letters* 9.9 (2018), pp. 2196–2201.

[50] A. M. A. Leguy et al. “Reversible Hydration of $CH_3NH_3PbI_3$ in Films, Single Crystals, and Solar Cells”. In: *Chemistry of Materials* 27.9 (2015), pp. 3397–3407.

[51] L. Wagner et al. “High Photovoltage of 1 V on a Steady-State Certified Hole Transport Layer-Free Perovskite Solar Cell by a Molten-Salt Approach”. In: *ACS Energy Letters* 3.5 (2018), pp. 1122–1127.

[52] T. Liu et al. “Perovskite Solar Cells: Stable Formamidinium-Based Perovskite Solar Cells via In Situ Grain Encapsulation”. In: *Advanced Energy Materials* 8.22 (2018), p. 1870101.

[53] L. Zuo et al. “Polymer-modified halide perovskite films for efficient and stable planar heterojunction solar cells”. In: *Science Advances* 3.8 (2017), e1700106.

[54] Y. Zhao et al. “A polymer scaffold for self-healing perovskite solar cells”. In: *Nature Communications* 7 (2016), p. 10228.

[55] Q. Jiang et al. “Pseudohalide-Induced Moisture Tolerance in Perovskite $CH_3NH_3Pb(SCN)_2I$ Thin Films”. In: *Angewandte Chemie International Edition* 54.26 (2015), pp. 7617–7620.

[56] J. Gong et al. “Divalent Anionic Doping in Perovskite Solar Cells for Enhanced Chemical Stability”. In: *Advanced Materials* 30.34 (2018), p. 1800973.

[57] F. Xu et al. “Mixed cation hybrid lead halide perovskites with enhanced performance and stability”. In: *Journal of Materials Chemistry A* 5.23 (2017), pp. 11450–11461.

[58] P. Wang et al. “Solvent-controlled growth of inorganic perovskite films in dry environment for efficient and stable solar cells”. In: *Nature Communications* 9.1 (2018), p. 2225.

[59] C. Liu et al. “All-Inorganic $CsPbI_2Br$ Perovskite Solar Cells with High Efficiency Exceeding 13%”. In: *Journal of the American Chemical Society* 140.11 (2018), pp. 3825–3828.

[60] W. Xiang et al. "Europium-Doped $CsPbI_2Br$ for Stable and Highly Efficient Inorganic Perovskite Solar Cells". In: *Joule* (2018).

[61] C. Eames et al. "Ionic transport in hybrid lead iodide perovskite solar cells". In: *Nature Communications* 6 (2015), p. 7497.

[62] R. Gottesman et al. "Dynamic Phenomena at Perovskite/Electron-Selective Contact Interface as Interpreted from Photovoltage Decays". In: *Chem* 1.5 (2016), pp. 776–789.

[63] A. Guerrero et al. "Interfacial Degradation of Planar Lead Halide Perovskite Solar Cells". In: *ACS Nano* 10.1 (2016), pp. 218–224.

[64] R. A. Belisle et al. "Interpretation of inverted photocurrent transients in organic lead halide perovskite solar cells: proof of the field screening by mobile ions and determination of the space charge layer widths". In: *Energy & Environmental Science* 10.1 (2017), pp. 192–204.

[65] A. Senocrate et al. "The Nature of Ion Conduction in Methylammonium Lead Iodide: A Multimethod Approach". In: *Angewandte Chemie International Edition* 56.27 (2017), pp. 7755–7759.

[66] C. Li et al. "Real-Time Observation of Iodide Ion Migration in Methylammonium Lead Halide Perovskites". In: *Small* 13.42 (2017), p. 1701711.

[67] Y. Yuan et al. "Photovoltaic Switching Mechanism in Lateral Structure Hybrid Perovskite Solar Cells". In: *Advanced Energy Materials* (2015), n/a–n/a.

[68] K. Domanski et al. "Migration of cations induces reversible performance losses over day/night cycling in perovskite solar cells". In: *Energy & Environmental Science* 10.2 (2017), pp. 604–613.

[69] G. Li et al. "Identifying the Optimum Morphology in High-Performance Perovskite Solar Cells". In: *Advanced Energy Materials* 5.9 (2015), p. 1401775.

[70] L. Zheng et al. "Morphology control of the perovskite films for efficient solar cells". In: *Dalton Trans* 44.23 (2015), pp. 10582–93.

[71] M. Xiao et al. "A Fast Deposition-Crystallization Procedure for Highly Efficient Lead Iodide Perovskite Thin-Film Solar Cells". In: *Angewandte Chemie International Edition* 53.37 (2014), pp. 9898–9903.

[72] G. E. Eperon et al. "Morphological Control for High Performance, Solution-Processed Planar Heterojunction Perovskite Solar Cells". In: *Advanced Functional Materials* 24.1 (2014), pp. 151–157.

[73] K. Liang, D. B. Mitzi, and M. T. Prikas. "Synthesis and Characterization of Organic-Inorganic Perovskite Thin Films Prepared Using a Versatile Two-Step Dipping Technique". In: *Chemistry of Materials* 10.1 (1998), pp. 403–411.

[74] J. Burschka et al. "Sequential deposition as a route to high-performance perovskite-sensitized solar cells". In: *Nature* 499.7458 (2013), pp. 316–9.

[75] D. Liu and T. L. Kelly. "Perovskite solar cells with a planar heterojunction structure prepared using room-temperature solution processing techniques". In: *Nature Photonics* 8 (2013), p. 133.

[76] Q. Chen et al. "Planar heterojunction perovskite solar cells via vapor assisted solution process". In: *Journal of the American Chemical Society* 136.2 (2013), pp. 622–625.

[77] Z. Zhou et al. "Methylamine-Gas-Induced Defect-Healing Behavior of $CH_3NH_3PbI_3$ Thin Films for Perovskite Solar Cells". In: *Angewandte Chemie International Edition* 54.33 (2015), pp. 9705–9709.

[78] M. Liu, M. B. Johnston, and H. J. Snaith. "Efficient planar heterojunction perovskite solar cells by vapour deposition". In: *Nature* 501.7467 (2013), pp. 395–8.

[79] N. J. Jeon et al. "Solvent engineering for high-performance inorganic–organic hybrid perovskite solar cells". In: *Nature Materials* 13 (2014), p. 897.

[80] X. Li et al. "A vacuum flash–assisted solution process for high-efficiency large-area perovskite solar cells". In: *Science* 353.6294 (2016), pp. 58–62.

[81] C. C. Chueh et al. "The roles of alkyl halide additives in enhancing perovskite solar cell performance". In: *Journal of Materials Chemistry A* 3.17 (2015), pp. 9058–9062.

[82] C. Chang et al. "Tuning Perovskite Morphology by Polymer Additive for High Efficiency Solar Cell". In: *ACS Applied Materials & Interfaces* 7.8 (2015), pp. 4955–4961.

[83] P. W. Liang et al. "Additive enhanced crystallization of solution-processed perovskite for highly efficient planar-heterojunction solar cells". In: *Advanced Materials* 26.22 (2014), pp. 3748–54.

[84] Y. Chen, Y. Zhao, and Z. Liang. "Nonvolatile chlorinated additives adversely influence $CH_3NH_3PbI_3$ based planar solar cells". In: *Journal of Materials Chemistry A* 3.17 (2015), pp. 9137–9140.

[85] Y. Wu et al. "Retarding the crystallization of PbI_2 for highly reproducible planar-structured perovskite solar cells via sequential deposition". In: *Energy & Environmental Science* 7.9 (2014), pp. 2934–2938.

[86] T. Zhang et al. "Controllable Sequential Deposition of Planar $CH_3NH_3PbI_3$ Perovskite Films via Adjustable Volume Expansion". In: *Nano Letters* 15.6 (2015), pp. 3959–3963.

[87] L. Hu et al. "Sequential Deposition of $CH_3NH_3PbI_3$ on Planar NiO Film for Efficient Planar Perovskite Solar Cells". In: *Acs Photonics* 1.7 (2014), pp. 547–553.

[88] Y. Y. Dang et al. "Bulk crystal growth of hybrid perovskite material $CH_3NH_3PbI_3$". In: *Crystengcomm* 17.3 (2015), pp. 665–670.

[89] D. Shi et al. "Low trap-state density and long carrier diffusion in organolead trihalide perovskite single crystals". In: *Science* 347.6221 (2015), pp. 519–522.

[90] Y. Liu et al. "Two-Inch-Sized Perovskite $CH_3NH_3PbX_3$ (X = Cl, Br, I) Crystals: Growth and Characterization". In: *Advanced Materials* 27.35 (2015), pp. 5176–5183.

[91] Y. Chen et al. "Extended carrier lifetimes and diffusion in hybrid perovskites revealed by Hall effect and photoconductivity measurements". In: *Nature Communications* 7 (2016), p. 12253.

[92] T. Leijtens et al. "Carrier trapping and recombination: the role of defect physics in enhancing the open circuit voltage of metal halide perovskite solar cells". In: *Energy & Environmental Science* 9.11 (2016), pp. 3472–3481.

[93] D. W. de Quilettes et al. "Impact of microstructure on local carrier lifetime in perovskite solar cells". In: *Science* 348.6235 (2015), pp. 683–686.

[94] J. R. Ayres. "Characterization of trapping states in polycrystalline-silicon thin film transistors by deep level transient spectroscopy". In: *Journal of Applied Physics* 74.3 (1993), pp. 1787–1792.

[95] A. Balcioglu, R. K. Ahrenkiel, and F. Hasoon. "Deep-level impurities in CdTe/CdS thin-film solar cells". In: *Journal of Applied Physics* 88.12 (2000), pp. 7175–7178.

[96] L. L. Kerr et al. "Investigation of defect properties in Cu(In,Ga)Se_2 solar cells by deep-level transient spectroscopy". In: *Solid-State Electronics* 48.9 (2004), pp. 1579–1586.

[97] F. A. Lindholm, J. G. Fossum, and E. L. Burgess. "Application of the superposition principle to solar-cell analysis". In: *IEEE Transactions on Electron Devices* 26.3 (1979), pp. 165–171.

[98] S. J. Robinson, A. G. Aberle, and M. A. Green. "Departures from the principle of superposition in silicon solar cells". In: *Journal of Applied Physics* 76.12 (1994), pp. 7920–7930.

[99] F. E. Guibaly and K. Colbow. "The superposition principle for semiconductor-electrolyte junction solar cells". In: *Journal of Applied Physics* 52.8 (1981), pp. 5247–5249.

[100] L. Schmidt-Mende and J. Weickert. *Organic and hybrid solar cells*. Walter de Gruyter GmbH, 2016. ISBN: 978-3-11-028318-1.

[101] P. Wurfel. "The chemical potential of radiation". In: *Journal of Physics C: Solid State Physics* 15.18 (1982), pp. 3967–3985.

[102] W. Tress et al. "Predicting the Open-Circuit Voltage of $CH_3NH_3PbI_3$ Perovskite Solar Cells Using Electroluminescence and Photovoltaic Quantum Efficiency Spectra: the Role of Radiative and Non-Radiative Recombination". In: *Advanced Energy Materials* 5.3 (2015), p. 1400812.

[103] C. M. Wolff et al. "Reduced Interface-Mediated Recombination for High Open-Circuit Voltages in $CH_3NH_3PbI_3$ Solar Cells". In: *Advanced Materials* 29.28 (2017), p. 1700159.

[104] U. Rau. "Reciprocity relation between photovoltaic quantum efficiency and electroluminescent emission of solar cells". In: *Physical Review B* 76.8 (2007), p. 085303.

[105] H. Oga et al. "Improved Understanding of the Electronic and Energetic Landscapes of Perovskite Solar Cells: High Local Charge Carrier Mobility, Reduced Recombination, and Extremely Shallow Traps". In: *Journal of the American Chemical Society* 136.39 (2014), pp. 13818–13825.

[106] W. Tress. "Perovskite Solar Cells on the Way to Their Radiative Efficiency Limit – Insights Into a Success Story of High Open-Circuit Voltage and Low Recombination". In: *Advanced Energy Materials* 7.14 (2017), p. 1602358.

[107] D. Meggiolaro et al. "Iodine chemistry determines the defect tolerance of lead-halide perovskites". In: *Energy & Environmental Science* 11.3 (2018), pp. 702–713.

[108] E. T. Roe, K. E. Egelhofer, and M. C. Lonergan. "Limits of Contact Selectivity/Recombination on the Open-Circuit Voltage of a Photovoltaic". In: *ACS Applied Energy Materials* 1.3 (2018), pp. 1037–1046.

[109] J. Qin et al. "The optimum titanium precursor of fabricating TiO_2 compact layer for perovskite solar cells". In: *Nanoscale Research Letters* 12.1 (2017), p. 640.

[110] J. Lee et al. "Rutile TiO_2-based perovskite solar cells". In: *Journal of Materials Chemistry A* 2.24 (2014), pp. 9251–9259.

[111] H. Hu et al. "Atomic Layer Deposition of TiO_2 for a High-Efficiency Hole-Blocking Layer in Hole-Conductor-Free Perovskite Solar Cells Processed in Ambient Air". In: *ACS Applied Materials & Interfaces* 8.28 (2016), pp. 17999–18007.

[112] A. Huang et al. "One step spray-coated TiO_2 electron-transport layers for decent perovskite solar cells on large and flexible substrates". In: *Nanotechnology* 28.1 (2016), 01LT02.

[113] B. Roose et al. "Mesoporous SnO_2 electron selective contact enables UV-stable perovskite solar cells". In: *Nano Energy* 30 (2016), pp. 517–522.

[114] J. Song et al. "Low-temperature SnO_2-based electron selective contact for efficient and stable perovskite solar cells". In: *Journal of Materials Chemistry A* 3.20 (2015), pp. 10837–10844.

[115] Y. Li et al. "Mesoporous SnO_2 nanoparticle films as electron-transporting material in perovskite solar cells". In: *RSC Advances* 5.36 (2015), pp. 28424–28429.

[116] D. Bi et al. "Efficient and stable $CH_3NH_3PbI_3$-sensitized ZnO nanorod array solid-state solar cells". In: *Nanoscale* 5.23 (2013), pp. 11686–11691.

[117] M. H. Kumar et al. "Flexible, low-temperature, solution processed ZnO-based perovskite solid state solar cells". In: *Chemical Communications* 49.94 (2013), pp. 11089–11091.

[118] K. Mahmood, B. S. Swain, and A. Amassian. "16.1% Efficient Hysteresis-Free Mesostructured Perovskite Solar Cells Based on Synergistically Improved ZnO Nanorod Arrays". In: *Advanced Energy Materials* 5.17 (2015), p. 1500568.

[119] A. Bera et al. "Fast Crystallization and Improved Stability of Perovskite Solar Cells with Zn_2SnO_4 Electron Transporting Layer: Interface Matters". In: *ACS Applied Materials & Interfaces* 7.51 (2015), pp. 28404–28411.

[120] S. S. Mali et al. "Reduced graphene oxide (rGO) grafted zinc stannate (Zn_2SnO_4) nanofiber scaffolds for highly efficient mixed-halide perovskite solar cells". In: *Journal of Materials Chemistry A* 4.31 (2016), pp. 12158–12169.

[121] L. Zhu et al. "Mesoporous $BaSnO_3$ layer based perovskite solar cells". In: *Chemical Communications* 52.5 (2016), pp. 970–973.

[122] S. S. Shin et al. "Colloidally prepared La-doped $BaSnO_3$ electrodes for efficient, photostable perovskite solar cells". In: *Science* 356.6334 (2017), pp. 167–171.

[123] L. Wang et al. "Low temperature solution processed planar heterojunction perovskite solar cells with a CdSe nanocrystal as an electron transport/extraction layer". In: *Journal of Materials Chemistry C* 2.43 (2014), pp. 9087–9090.

[124] W. A. Dunlap-Shohl et al. "Effects of Cd Diffusion and Doping in High-Performance Perovskite Solar Cells Using CdS as Electron Transport Layer". In: *The Journal of Physical Chemistry C* 120.30 (2016), pp. 16437–16445.

[125] A. Bera et al. "Perovskite Oxide $SrTiO_3$ as an Efficient Electron Transporter for Hybrid Perovskite Solar Cells". In: *The Journal of Physical Chemistry C* 118.49 (2014), pp. 28494–28501.

[126] N. Ahn et al. "Highly Reproducible Perovskite Solar Cells with Average Efficiency of 18.3% and Best Efficiency of 19.7% Fabricated via Lewis Base Adduct of Lead(II) Iodide". In: *Journal of the American Chemical Society* 137.27 (2015), pp. 8696–8699.

[127] W. H. Nguyen et al. "Enhancing the Hole-Conductivity of Spiro-OMeTAD without Oxygen or Lithium Salts by Using $Spiro(TFSI)_2$ in Perovskite and Dye-Sensitized Solar Cells". In: *Journal of the American Chemical Society* 136.31 (2014), pp. 10996–11001.

[128] J. H. Noh et al. "Nanostructured $TiO_2/CH_3NH_3PbI_3$ heterojunction solar cells employing spiro-OMeTAD/Co-complex as hole-transporting material". In: *Journal of Materials Chemistry A* 1.38 (2013), p. 11842.

[129] J. Xiao et al. "Efficient $CH_3NH_3PbI_3$ Perovskite Solar Cells Based on Graphdiyne (GD)-Modified P3HT Hole-Transporting Material". In: *Advanced Energy Materials* 5.8 (2015), p. 1401943.

[130] Y. Zhang et al. "Enhanced performance of perovskite solar cells with P3HT hole-transporting materials via molecular p-type doping". In: *RSC Advances* 6.110 (2016), pp. 108888–108895.

[131] N. Y. Nia et al. "High-Efficiency Perovskite Solar Cell Based on Poly(3-Hexylthiophene): Influence of Molecular Weight and Mesoscopic Scaffold Layer". In: *ChemSusChem* 10.19 (2017), pp. 3854–3860.

[132] Y. Kim et al. "Sequentially Fluorinated PTAA Polymers for Enhancing V_{OC} of High-Performance Perovskite Solar Cells". In: *Advanced Energy Materials* 8.29 (2018), p. 1801668.

[133] D. Luo et al. "Enhanced photovoltage for inverted planar heterojunction perovskite solar cells". In: *Science* 360.6396 (2018), pp. 1442–1446.

[134] M. Jung et al. "Thermal Stability of CuSCN Hole Conductor-Based Perovskite Solar Cells". In: *ChemSusChem* 9.18 (2016), pp. 2592–2596.

[135] V. E. Madhavan et al. "Copper Thiocyanate Inorganic Hole-Transporting Material for High-Efficiency Perovskite Solar Cells". In: *ACS Energy Letters* 1.6 (2016), pp. 1112–1117.

[136] N. Arora et al. “Perovskite solar cells with CuSCN hole extraction layers yield stabilized efficiencies greater than 20%”. In: *Science* 358.6364 (2017), pp. 768–771.

[137] P. Ganesan et al. “A simple spiro-type hole transporting material for efficient perovskite solar cells”. In: *Energy & Environmental Science* 8.7 (2015), pp. 1986–1991.

[138] T. Malinauskas et al. “Branched methoxydiphenylamine-substituted fluorene derivatives as hole transporting materials for high-performance perovskite solar cells”. In: *Energy & Environmental Science* 9.5 (2016), pp. 1681–1686.

[139] Y. S. Kwon et al. “A diketopyrrolopyrrole-containing hole transporting conjugated polymer for use in efficient stable organic–inorganic hybrid solar cells based on a perovskite”. In: *Energy & Environmental Science* 7.4 (2014), pp. 1454–1460.

[140] C. Chiang and C. Wu. “Bulk heterojunction perovskite–PCBM solar cells with high fill factor”. In: *Nature Photonics* 10.3 (2016), pp. 196–200.

[141] J. Jeng et al. “Nickel Oxide Electrode Interlayer in $CH_3NH_3PbI_3$ Perovskite/PCBM Planar-Heterojunction Hybrid Solar Cells”. In: *Advanced Materials* 26.24 (2014), pp. 4107–4113.

[142] J. Seo et al. “Benefits of very thin PCBM and LiF layers for solution-processed p-i-n perovskite solar cells”. In: *Energy & Environmental Science* 7.8 (2014), pp. 2642–2646.

[143] H. Xu et al. “Efficient Perovskite Hybrid Solar Cells by Highly Electrical Conductive PEDOT:PSS Hole Transport Layer”. In: *Advanced Energy Materials* 6.3 (2016), p. 1501773.

[144] J. H. Heo et al. “Hysteresis-less inverted $CH_3NH_3PbI_3$ planar perovskite hybrid solar cells with 18.1% power conversion efficiency”. In: *Energy & Environmental Science* 8.5 (2015), pp. 1602–1608.

[145] S. Dai et al. “Pristine fullerenes mixed by vacuum-free solution process: Efficient electron transport layer for planar perovskite solar cells”. In: *Journal of Power Sources* 339 (2017), pp. 27–32.

[146] C. Tian et al. “Improved Performance and Stability of Inverted Planar Perovskite Solar Cells Using Fulleropyrrolidine Layers”. In: *ACS Applied Materials & Interfaces* 8.45 (2016), pp. 31426–31432.

[147] J. Jeng et al. “$CH_3NH_3PbI_3$ Perovskite/Fullerene Planar-Heterojunction Hybrid Solar Cells”. In: *Advanced Materials* 25.27 (2013), pp. 3727–3732.

[148] Z. Zhu et al. “Enhanced Efficiency and Stability of Inverted Perovskite Solar Cells Using Highly Crystalline SnO_2 Nanocrystals as the Robust Electron-Transporting Layer”. In: *Advanced Materials* 28.30 (2016), pp. 6478–6484.

[149] J. You et al. “Improved air stability of perovskite solar cells via solution-processed metal oxide transport layers”. In: *Nature Nanotechnology* 11 (2015), p. 75.

[150] K. O. Brinkmann et al. “Suppressed decomposition of organometal halide perovskites by impermeable electron-extraction layers in inverted solar cells”. In: *Nature Communications* 8 (2017), p. 13938.

[151] D. Zhao et al. “Hexaazatrinaphthylene Derivatives: Efficient Electron-Transporting Materials with Tunable Energy Levels for Inverted Perovskite Solar Cells”. In: *Angewandte Chemie International Edition* 55.31 (2016), pp. 8999–9003.

[152] P. Gu et al. “Pushing up the efficiency of planar perovskite solar cells to 18.2% with organic small molecules as the electron transport layer”. In: *Journal of Materials Chemistry A* 5.16 (2017), pp. 7339–7344.

[153] J. Park et al. “Efficient $CH_3NH_3PbI_3$ Perovskite Solar Cells Employing Nanostructured p-Type NiO Electrode Formed by a Pulsed Laser Deposition”. In: *Advanced Materials* 27.27 (2015), pp. 4013–4019.

[154] S. Seo et al. “An ultra-thin, un-doped NiO hole transporting layer of highly efficient (16.4%) organic–inorganic hybrid perovskite solar cells”. In: *Nanoscale* 8.22 (2016), pp. 11403–11412.

[155] H. Rao et al. “A 19.0% efficiency achieved in CuO_x-based inverted $CH_3NH_3PbI_{3-x}Cl_x$ solar cells by an effective Cl doping method”. In: *Nano Energy* 27 (2016), pp. 51–57.

[156] A. E. Shalan et al. “Cobalt Oxide (CoO_x) as an Efficient Hole-Extracting Layer for High-Performance Inverted Planar Perovskite Solar Cells”. In: *ACS Applied Materials & Interfaces* 8.49 (2016), pp. 33592–33600.

[157] N. Wijeyasinghe et al. “Copper(I) Thiocyanate (CuSCN) Hole-Transport Layers Processed from Aqueous Precursor Solutions and Their Application in Thin-Film Transistors and Highly Efficient Organic and Organometal Halide Perovskite Solar Cells”. In: *Advanced Functional Materials* 27.35 (2017), p. 1701818.

[158] W. Chen et al. “Low-cost solution-processed copper iodide as an alternative to PEDOT:PSS hole transport layer for efficient and stable inverted planar heterojunction perovskite solar cells”. In: *Journal of Materials Chemistry A* 3.38 (2015), pp. 19353–19359.

[159] H. Rao et al. “Solution-Processed CuS NPs as an Inorganic Hole-Selective Contact Material for Inverted Planar Perovskite Solar Cells”. In: *ACS Applied Materials & Interfaces* 8.12 (2016), pp. 7800–7805.

[160] X. Yao et al. “Solution-processed vanadium oxide thin film as the hole extraction layer for efficient hysteresis-free perovskite hybrid solar cells”. In: *Organic Electronics* 47 (2017), pp. 85–93.

[161] A. Kojima et al. “Organometal Halide Perovskites as Visible-Light Sensitizers for Photovoltaic Cells”. In: *Journal of the American Chemical Society* 131.17 (2009), pp. 6050–6051.

[162] J. Im et al. “6.5% efficient perovskite quantum-dot-sensitized solar cell”. In: *Nanoscale* 3.10 (2011), pp. 4088–4093.

[163] L. Etgar et al. “Mesoscopic $CH_3NH_3PbI_3/TiO_2$ Heterojunction Solar Cells”. In: *Journal of the American Chemical Society* 134.42 (2012), pp. 17396–17399.

[164] H. Kim et al. “Lead Iodide Perovskite Sensitized All-Solid-State Submicron Thin Film Mesoscopic Solar Cell with Efficiency Exceeding 9%”. In: *Scientific Reports* 2 (2012), p. 591.

[165] M. M. Lee et al. “Efficient Hybrid Solar Cells Based on Meso-Superstructured Organometal Halide Perovskites”. In: *Science* 338.6107 (2012), pp. 643–647.

[166] S. D. Stranks et al. “Electron-Hole Diffusion Lengths Exceeding 1 Micrometer in an Organometal Trihalide Perovskite Absorber”. In: *Science* 342.6156 (2013), pp. 341–344.

[167] A. T. Barrows et al. “Efficient planar heterojunction mixed-halide perovskite solar cells deposited via spray-deposition”. In: *Energy & Environmental Science* 7.9 (2014), pp. 2944–2950.

[168] C. Chen et al. “Efficient and Uniform Planar-Type Perovskite Solar Cells by Simple Sequential Vacuum Deposition”. In: *Advanced Materials* 26.38 (2014), pp. 6647–52.

[169] W. Chen et al. “A comparative study of planar and mesoporous perovskite solar cells with printable carbon electrodes”. In: *Journal of Power Sources* 412 (2019), pp. 118–124.

[170] M. Liu et al. “Identifying an Optimum Perovskite Solar Cell Structure by Kinetic Analysis: Planar, Mesoporous Based, or Extremely Thin Absorber Structure”. In: *ACS Applied Energy Materials* 1.8 (2018), pp. 3722–3732.

[171] C. Jiang et al. “Carrier separation and transport in perovskite solar cells studied by nanometre-scale profiling of electrical potential”. In: *Nature Communications* 6 (2015), p. 8397.

[172] Z. Xiao et al. “Giant switchable photovoltaic effect in organometal trihalide perovskite devices”. In: *Nature Materials* 14 (2014), p. 193.

[173] X. Lin et al. “Dipole-field-assisted charge extraction in metal-perovskite-metal back-contact solar cells”. In: *Nature Communications* 8.1 (2017), p. 613.

[174] C. Wu, C. Chiang, and S. Chang. “A perovskite cell with a record-high-Voc of 1.61 V based on solvent annealed $CH_3NH_3PbBr_3$/ICBA active layer”. In: *Nanoscale* 8.7 (2016), pp. 4077–4085.

[175] N. Arora et al. “High Open-Circuit Voltage: Fabrication of Formamidinium Lead Bromide Perovskite Solar Cells Using Fluorene–Dithiophene Derivatives as Hole-Transporting Materials”. In: *ACS Energy Letters* 1.1 (2016), pp. 107–112.

[176] Y. Zhang et al. “Planar FAPbBr3 Solar Cells with Power Conversion Efficiency above 10%”. In: *ACS Energy Letters* 3 (2018), pp. 1808–1814.

[177] M. Stolterfoht et al. “Visualization and suppression of interfacial recombination for high-efficiency large-area pin perovskite solar cells”. In: *Nature Energy* 3.10 (2018), pp. 847–854.

[178] Z. Liu et al. “Open-Circuit Voltages Exceeding 1.26 V in Planar Methylammonium Lead Iodide Perovskite Solar Cells”. In: *ACS Energy Letters* 4.1 (2019), pp. 110–117.

[179] D. Bi et al. “Efficient luminescent solar cells based on tailored mixed-cation perovskites”. In: *Science Advances* 2.1 (2016), e1501170.

[180] M. Ban et al. "Solution-processed perovskite light emitting diodes with efficiency exceeding 15% through additive-controlled nanostructure tailoring". In: *Nature Communications* 9.1 (2018), p. 3892.

[181] X. Yang et al. "Efficient green light-emitting diodes based on quasi-two-dimensional composition and phase engineered perovskite with surface passivation". In: *Nature Communications* 9.1 (2018), p. 570.

[182] D. B. Khadka et al. "Exploring the effects of interfacial carrier transport layers on device performance and optoelectronic properties of planar perovskite solar cells". In: *Journal of Materials Chemistry C* 5.34 (2017), pp. 8819–8827.

[183] E. Serpetzoglou et al. "Improved Carrier Transport in Perovskite Solar Cells Probed by Femtosecond Transient Absorption Spectroscopy". In: *ACS Applied Materials & Interfaces* 9.50 (2017), pp. 43910–43919.

[184] H. J. Snaith et al. "Anomalous Hysteresis in Perovskite Solar Cells". In: *The Journal of Physical Chemistry Letters* 5.9 (2014), pp. 1511–5.

[185] E. L. Unger et al. "Hysteresis and transient behavior in current–voltage measurements of hybrid-perovskite absorber solar cells". In: *Energy & Environmental Science* 7.11 (2014), pp. 3690–3698.

[186] C. Wu et al. "High efficiency stable inverted perovskite solar cells without current hysteresis". In: *Energy & Environmental Science* 8.9 (2015), pp. 2725–2733.

[187] J. Wei et al. "Hysteresis Analysis Based on Ferroelectric Effect in Hybrid Perovskite Solar Cells". In: *The Journal of Physical Chemistry Letters* 5.21 (2014), pp. 3937–45.

[188] G. Richardson et al. "Can slow-moving ions explain hysteresis in the current-voltage curves of perovskite solar cells?" In: *Energy & Environmental Science* 9.4 (2016), pp. 1476–1485.

[189] H. Chen et al. "Emergence of Hysteresis and Transient Ferroelectric Response in Organo-Lead Halide Perovskite Solar Cells". In: *The Journal of Physical Chemistry Letters* 6.1 (2014), pp. 164–169.

[190] J. Lee et al. "The Interplay between Trap Density and Hysteresis in Planar Heterojunction Perovskite Solar Cells". In: *Nano Letters* 17.7 (2017), pp. 4270–4276.

[191] H. Uratani and K. Yamashita. "Charge Carrier Trapping at Surface Defects of Perovskite Solar Cell Absorbers: A First-Principles Study". In: *The Journal of Physical Chemistry Letters* 8.4 (2017), pp. 742–746.

[192] P. Calado et al. "Evidence for ion migration in hybrid perovskite solar cells with minimal hysteresis". In: *Nature Communications* 7 (2016), p. 13831.

[193] D. W. deQuilettes et al. "Photo-induced halide redistribution in organic–inorganic perovskite films". In: *Nature Communications* 7 (2016), p. 11683.

[194] B. Wu et al. "Charge Accumulation and Hysteresis in Perovskite-Based Solar Cells: An Electro-Optical Analysis". In: *Advanced Energy Materials* 5.19 (2015), p. 1500829.

[195] S. A. L. Weber et al. "How the formation of interfacial charge causes hysteresis in perovskite solar cells". In: *Energy & Environmental Science* 11.9 (2018), pp. 2404–2413.

[196] A. M. A. Leguy et al. "The dynamics of methylammonium ions in hybrid organic–inorganic perovskite solar cells". In: *Nature Communications* 6 (2015), p. 7124.

[197] E. Zimmermann et al. "Characterization of perovskite solar cells: Towards a reliable measurement protocol". In: *APL Materials* 4.9 (2016), p. 091901.

[198] R. B. Dunbar et al. "How reliable are efficiency measurements of perovskite solar cells? The first inter-comparison, between two accredited and eight non-accredited laboratories". In: *Journal of Materials Chemistry A* 5.43 (2017), pp. 22542–22558.

[199] P. Wang, M. Ulfa, and T. Pauporté. "Effects of Perovskite Monovalent Cation Composition on the High and Low Frequency Impedance Response of Efficient Solar Cells". In: *The Journal of Physical Chemistry C* 122.4 (2018), pp. 1973–1981.

[200] D. A. Jacobs et al. "The two faces of capacitance: New interpretations for electrical impedance measurements of perovskite solar cells and their relation to hysteresis". In: *Journal of Applied Physics* 124.22 (2018), p. 225702.

[201] A. Dualeh et al. "Impedance Spectroscopic Analysis of Lead Iodide Perovskite-Sensitized Solid-State Solar Cells". In: *ACS Nano* 8.1 (2014), pp. 362–373.

[202] D. Wei et al. "Ion-Migration Inhibition by the Cation–π Interaction in Perovskite Materials for Efficient and Stable Perovskite Solar Cells". In: *Advanced Materials* 30.31 (2018), p. 1707583.

[203] D. Son et al. "Universal Approach toward Hysteresis-Free Perovskite Solar Cell via Defect Engineering". In: *Journal of the American Chemical Society* 140.4 (2018), pp. 1358–1364.

[204] Y. Shao et al. "Origin and elimination of photocurrent hysteresis by fullerene passivation in $CH_3NH_3PbI_3$ planar heterojunction solar cells". In: *Nature Communications* 5 (2014), p. 5784.

[205] J. K. Kim et al. "Resolving Hysteresis in Perovskite Solar Cells with Rapid Flame-Processed Cobalt-Doped TiO_2". In: *Advanced Energy Materials* 8.29 (2018), p. 1801717.

[206] Y. Kanemitsu. "Luminescence spectroscopy of lead-halide perovskites: materials properties and application as photovoltaic devices". In: *Journal of Materials Chemistry C* 5.14 (2017), pp. 3427–3437.

[207] Y. Cheng et al. "The detrimental effect of excess mobile ions in planar $CH_3NH_3PbI_3$ perovskite solar cells". In: *Journal of Materials Chemistry A* 4.33 (2016), pp. 12748–12755.

[208] H. Zhang et al. "Dynamic interface charge governing the current-voltage hysteresis in perovskite solar cells". In: *Physical Chemistry Chemical Physics* 17.15 (2015), pp. 9613–9618.

[209] C. G. Shuttle et al. "Experimental determination of the rate law for charge carrier decay in a polythiophene: Fullerene solar cell". In: *Applied Physics Letters* 92.9 (2008), p. 093311.

[210] B. C. O'Regan and J. R. Durrant. "Calculation of Activation Energies for Transport and Recombination in Mesoporous TiO_2/Dye/Electrolyte FilmsTaking into Account Surface Charge Shifts with Temperature". In: *The Journal of Physical Chemistry B* 110.17 (2006), pp. 8544–8547.

[211] B. C. O'Regan et al. "Measuring Charge Transport from Transient Photovoltage Rise Times. A New Tool To Investigate Electron Transport in Nanoparticle Films". In: *The Journal of Physical Chemistry B* 110.34 (2006), pp. 17155–17160.

[212] B. C. O'Regan et al. "The Effect of Al_2O_3 Barrier Layers in TiO_2/Dye/CuSCN Photovoltaic Cells Explored by Recombination and DOS Characterization Using Transient Photovoltage Measurements". In: *The Journal of Physical Chemistry B* 109.10 (2005), pp. 4616–4623.

[213] S. Wheeler et al. "Transient Optoelectronic Analysis of the Impact of Material Energetics and Recombination Kinetics on the Open-Circuit Voltage of Hybrid Perovskite Solar Cells". In: *The Journal of Physical Chemistry C* 121.25 (2017), pp. 13496–13506.

[214] W. M. M. Lin et al. "Transient Photovoltage Measurements in Nanocrystal-Based Solar Cells". In: *The Journal of Physical Chemistry C* 120.23 (2016), pp. 12900–12908.

[215] B. C. O'Regan et al. "Influence of the $TiCl_4$ Treatment on Nanocrystalline TiO_2 Films in Dye-Sensitized Solar Cells. 2. Charge Density, Band Edge Shifts, and Quantification of Recombination Losses at Short Circuit". In: *The Journal of Physical Chemistry C* 111.37 (2007), pp. 14001–14010.

[216] D. Credgington et al. "In Situ Measurement of Energy Level Shifts and Recombination Rates in Subphthalocyanine/C_{60} Bilayer Solar Cells". In: *The Journal of Physical Chemistry C* 118.40 (2014), pp. 22858–22864.

[217] B. C. O'Regan et al. "Optoelectronic Studies of Methylammonium Lead Iodide Perovskite Solar Cells with Mesoporous TiO_2: Separation of Electronic and Chemical Charge Storage, Understanding Two Recombination Lifetimes, and the Evolution of Band Offsets during J–V Hysteresis". In: *Journal of the American Chemical Society* 137.15 (2015), pp. 5087–5099.

[218] J. Bisquert et al. "Theory of Impedance and Capacitance Spectroscopy of Solar Cells with Dielectric Relaxation, Drift-Diffusion Transport, and Recombination". In: *The Journal of Physical Chemistry C* 118.33 (2014), pp. 18983–18991.

[219] D. B. Mitzi et al. "Conducting tin halides with a layered organic-based perovskite structure". In: *Nature* 369.6480 (1994), pp. 467–469.

[220] D. B. Mitzi et al. "Transport, Optical, and Magnetic Properties of the Conducting Halide Perovskite $CH_3NH_3SnI_3$". In: *Journal of Solid State Chemistry* 114.1 (1995), pp. 159–163.

[221] D. B. Mitzi et al. "Conducting Layered Organic-inorganic Halides Containing 110-Oriented Perovskite Sheets". In: *Science* 267.5203 (1995), pp. 1473–1476.

[222] D. B. Mitzi and K. Liang. "Synthesis, resistivity, and thermal properties of the cubic perovskite $NH_2CH = NH_2SnI_3$ and related systems". In: *Journal of Solid State Chemistry* 134.2 (1997), pp. 376–381.

[223] G. E. Eperon et al. "Morphological Control for High Performance, Solution-Processed Planar Heterojunction Perovskite Solar Cells". In: *Advanced Functional Materials* 24.1 (2014), pp. 151–157.

[224] A. Dualeh et al. "Effect of Annealing Temperature on Film Morphology of Organic–Inorganic Hybrid Pervoskite Solid-State Solar Cells". In: *Advanced Functional Materials* 24.21 (2014), pp. 3250–3258.

[225] H. Gao et al. "Nucleation and Crystal Growth of Organic–Inorganic Lead Halide Perovskites under Different Relative Humidity". In: *ACS Applied Materials & Interfaces* 7.17 (2015), pp. 9110–9117.

[226] Y. Tidhar et al. "Crystallization of Methyl Ammonium Lead Halide Perovskites: Implications for Photovoltaic Applications". In: *Journal of the American Chemical Society* 136.38 (2014), pp. 13249–13256.

[227] Y. Zhao and K. Zhu. "CH_3NH_3Cl-Assisted One-Step Solution Growth of $CH_3NH_3PbI_3$: Structure, Charge-Carrier Dynamics, and Photovoltaic Properties of Perovskite Solar Cells". In: *The Journal of Physical Chemistry C* 118.18 (2014), pp. 9412–9418.

[228] Y. Zhao and K. Zhu. "Efficient Planar Perovskite Solar Cells Based on 1.8 eV Band Gap $CH_3NH_3PbI_2Br$ Nanosheets via Thermal Decomposition". In: *Journal of the American Chemical Society* 136.35 (2014), pp. 12241–12244.

[229] Y. Chen, Y. Zhao, and Z. Liang. "Non-Thermal Annealing Fabrication of Efficient Planar Perovskite Solar Cells with Inclusion of NH_4Cl". In: *Chemistry of Materials* 27.5 (2015), pp. 1448–1451.

[230] J. He and T. Chen. "Additive regulated crystallization and film formation of $CH_3NH_3PbI_{3-x}Br_x$ for highly efficient planar-heterojunction solar cells". In: *Journal of Materials Chemistry A* 3.36 (2015), pp. 18514–18520.

[231] P. Liang et al. "Additive Enhanced Crystallization of Solution-Processed Perovskite for Highly Efficient Planar-Heterojunction Solar Cells". In: *Advanced Materials* 26.22 (2014), pp. 3748–3754.

[232] Q. Wang et al. "Transition from the Tetragonal to Cubic Phase of Organohalide Perovskite: The Role of Chlorine in Crystal Formation of $CH_3NH_3PbI_3$ on TiO_2 Substrates". In: *The Journal of Physical Chemistry Letters* 6.21 (2015), pp. 4379–4384.

[233] D. Liu, M. K. Gangishetty, and T. L. Kelly. "Effect of $CH_3NH_3PbI_3$ thickness on device efficiency in planar heterojunction perovskite solar cells". In: *Journal of Materials Chemistry A* 2.46 (2014), pp. 19873–19881.

[234] J. Xi et al. "Controlled thickness and morphology for highly efficient inverted planar heterojunction perovskite solar cells". In: *Nanoscale* 7.24 (2015), pp. 10699–10707.

[235] P. W. Liang et al. "Roles of Fullerene-Based Interlayers in Enhancing the Performance of Organometal Perovskite Thin-Film Solar Cells". In: *Advanced Energy Materials* 5.10 (2015), pp. 1402321–1402327.

[236] C. Chiang, Z. Tseng, and C. Wu. "Planar heterojunction perovskite/$PC_{71}BM$ solar cells with enhanced open-circuit voltage via a (2/1)-step spin-coating process". In: *Journal of Materials Chemistry A* 2.38 (2014), pp. 15897–15903.

[237] P. Zhao et al. "Insulated Interlayer for Efficient and Photostable Electron-Transport-Layer-Free Perovskite Solar Cells". In: *ACS Applied Materials & Interfaces* 10.12 (2018), pp. 10132–10140.

[238] C. Chen et al. "Effect of BCP buffer layer on eliminating charge accumulation for high performance of inverted perovskite solar cells". In: *RSC Advances* 7.57 (2017), pp. 35819–35826.

[239] B. Qi, Z. Zhang, and J. Wang. "Uncovering the role of cathode buffer layer in organic solar cells". In: *Scientific Reports* 5 (2015), p. 7803.

[240] X. Liu et al. "Triple Cathode Buffer Layers Composed of PCBM, C_{60}, and LiF for High-Performance Planar Perovskite Solar Cells". In: *ACS Applied Materials & Interfaces* 7.11 (2015), pp. 6230–6237.

[241] K. Sun et al. "Efficiency enhancement of planar perovskite solar cells by adding zwitterion/LiF double interlayers for electron collection". In: *Nanoscale* 7.3 (2015), pp. 896–900.

[242] L. Yuan et al. "Semi-transparent perovskite solar cells: unveiling the trade-off between transparency and efficiency". In: *Journal of Materials Chemistry A* 6.40 (2018), pp. 19696–19702.

[243] C. Roldan-Carmona et al. "High efficiency single-junction semitransparent perovskite solar cells". In: *Energy & Environmental Science* 7.9 (2014), pp. 2968–2973.

[244] M. De Bastiani et al. "Role of the crystallization substrate on the photoluminescence properties of organo-lead mixed halides perovskites". In: *APL Materials* 2.8 (2014), p. 081509.

[245] Ke. Wu et al. "Temperature-dependent excitonic photoluminescence of hybrid organometal halide perovskite films". In: *Physical Chemistry Chemical Physics* 16.41 (2014), pp. 22476–22481.

[246] E. J. Juarez-Perez et al. "Photodecomposition and thermal decomposition in methylammonium halide lead perovskites and inferred design principles to increase photovoltaic device stability". In: *Journal of Materials Chemistry A* 6.20 (2018), pp. 9604–9612.

[247] E. J. Juarez-Perez et al. "Thermal degradation of $CH_3NH_3PbI_3$ perovskite into NH_3 and CH_3I gases observed by coupled thermogravimetry–mass spectrometry analysis". In: *Energy & Environmental Science* 9.11 (2016), pp. 3406–3410.

[248] G. Maculan et al. "$CH_3NH_3PbCl_3$ Single Crystals: Inverse Temperature Crystallization and Visible-Blind UV-Photodetector". In: *The Journal of Physical Chemistry Letters* 6.19 (2015), pp. 3781–3786.

[249] Jenny N. *The physics of solar cells*. Imperial College Press, 2003. ISBN: 1-86094-340-3.

[250] G. Yu et al. "Polymer Photovoltaic Cells: Enhanced Efficiencies via a Network of Internal Donor-Acceptor Heterojunctions". In: *Science* 270.5243 (1995), pp. 1789–1791.

[251] B. O'Regan and M. Grätzel. "A low-cost, high-efficiency solar cell based on dye-sensitized colloidal TiO_2 films". In: *Nature* 353.6346 (1991), pp. 737–740.

[252] R. Brendel. "Coupling of light into mechanically textured silicon solar cells: A ray tracing study". In: *Progress in Photovoltaics: Research and Applications* 3.1 (1995), pp. 25–38.

[253] C. van Lare et al. "Light Coupling and Trapping in Ultrathin Cu(In,Ga)Se_2 Solar Cells Using Dielectric Scattering Patterns". In: *ACS Nano* 9.10 (2015), pp. 9603–9613.

[254] J. Correa-Baena et al. "Unbroken Perovskite: Interplay of Morphology, Electro-optical Properties, and Ionic Movement". In: *Advanced Materials* 28.25 (2016), pp. 5031–5037.

[255] J. M. Ball et al. "Optical properties and limiting photocurrent of thin-film perovskite solar cells". In: *Energy & Environmental Science* 8.2 (2015), pp. 602–609.

[256] J. Correa-Baena et al. "Identifying and suppressing interfacial recombination to achieve high open-circuit voltage in perovskite solar cells". In: *Energy & Environmental Science* 10.5 (2017), pp. 1207–1212.

[257] H. Zhou et al. "Interface engineering of highly efficient perovskite solar cells". In: *Science* 345.6196 (2014), pp. 542–546.

[258] H. J. Snaith. "How should you measure your excitonic solar cells?" In: *Energy & Environmental Science* 5.4 (2012), pp. 6513–6520.

[259] X. Xu et al. "The influence of different mask aperture on the open-circuit voltage measurement of perovskite solar cells". In: *Journal of Renewable and Sustainable Energy* 7.4 (2015), p. 043104.

[260] R. A. Belisle et al. "Minimal Effect of the Hole-Transport Material Ionization Potential on the Open-Circuit Voltage of Perovskite Solar Cells". In: *ACS Energy Letters* 1.3 (2016), pp. 556–560.

[261] A. Abate et al. "Hole-transport materials with greatly-differing redox potentials give efficient TiO_2-$[CH_3NH_3][PbX_3]$ perovskite solar cells". In: *Physical Chemistry Chemical Physics* 17.4 (2015), pp. 2335–2338.

[262] Y. Numata et al. "Controlled Crystal Grain Growth in Mixed Cation–Halide Perovskite by Evaporated Solvent Vapor Recycling Method for High Efficiency Solar Cells". In: *ACS Applied Materials & Interfaces* 9.22 (2017), pp. 18739–18747.

[263] C. Quarti et al. "Structural and optical properties of methylammonium lead iodide across the tetragonal to cubic phase transition: implications for perovskite solar cells". In: *Energy & Environmental Science* 9.1 (2016), pp. 155–163.

[264] S. De Wolf et al. "Organometallic Halide Perovskites: Sharp Optical Absorption Edge and its Relation to Photovoltaic Performance". In: *The Journal of Physical Chemistry Letters* 5.6 (2014), pp. 1035–1039.

[265] L. J. A. Koster et al. "Light intensity dependence of open-circuit voltage of polymer:fullerene solar cells". In: *Applied Physics Letters* 86.12 (2005), p. 123509.

[266] D. Yang et al. "Surface optimization to eliminate hysteresis for record efficiency planar perovskite solar cells". In: *Energy & Environmental Science* 9.10 (2016), pp. 3071–3078.

[267] W. Tress et al. "Interpretation and evolution of open-circuit voltage, recombination, ideality factor and subgap defect states during reversible light-soaking and irreversible degradation of perovskite solar cells". In: *Energy & Environmental Science* 11.1 (2018), pp. 151–165.

[268] S. Solak, P. W. M. Blom, and G. A. H. Wetzelaer. "Effect of non-ohmic contacts on the light-intensity dependence of the open-circuit voltage in organic solar cells". In: *Applied Physics Letters* 109.5 (2016), p. 053302.

[269] T. S. Sherkar et al. "Recombination in Perovskite Solar Cells: Significance of Grain Boundaries, Interface Traps, and Defect Ions". In: *ACS Energy Letters* 2.5 (2017), pp. 1214–1222.

[270] T. Kirchartz et al. "Sensitivity of the Mott–Schottky Analysis in Organic Solar Cells". In: *The Journal of Physical Chemistry C* 116.14 (2012), pp. 7672–7680.

[271] Z. Li et al. "Electrochemical impedance analysis of perovskite–electrolyte interfaces". In: *Chemical Communications* 53.16 (2017), pp. 2467–2470.

[272] O. Almora et al. "On Mott-Schottky analysis interpretation of capacitance measurements in organometal perovskite solar cells". In: *Applied Physics Letters* 109.17 (2016), p. 173903.

[273] P. A. F. Garrillo et al. "Calibrated work function mapping by Kelvin probe force microscopy". In: *Review of Scientific Instruments* 89.4 (2018), p. 043702.

[274] A. Zohar et al. "What Limits the Open-Circuit Voltage of Bromide Perovskite-Based Solar Cells?" In: *ACS Energy Letters* 4.1 (2019), pp. 1–7.

[275] H. Dong et al. "Modified deposition process of electron transport layer for efficient inverted planar perovskite solar cells". In: *Chemical Communications* 51.43 (2015), pp. 8986–8989.

[276] G. Chen et al. "Fabrication of high-performance and low-hysteresis lead halide perovskite solar cells by utilizing a versatile alcohol-soluble bispyridinium salt as an efficient cathode modifier". In: *Journal of Materials Chemistry A* 5.34 (2017), pp. 17943–17953.

[277] J. S. Yun et al. "Benefit of Grain Boundaries in Organic–Inorganic Halide Planar Perovskite Solar Cells". In: *The Journal of Physical Chemistry Letters* 6.5 (2015), pp. 875–880.

[278] D. Kim et al. "Effects of Postsynthesis Thermal Conditions on Methylammonium Lead Halide Perovskite: Band Bending at Grain Boundaries and Its Impacts on Solar Cell Performance". In: *The Journal of Physical Chemistry C* 120.38 (2016), pp. 21330–21335.

[279] C. Zhang et al. "Electric-field assisted perovskite crystallization for high-performance solar cells". In: *Journal of Materials Chemistry A* 6.3 (2018), pp. 1161–1170.

[280] K. Rühle et al. "Evaluating Crystalline Silicon Solar Cells at Low Light Intensities Using Intensity-Dependent Analysis of I–V Parameters". In: *IEEE Journal of Photovoltaics* 5.3 (2015), pp. 926–931.

[281] C. M. Proctor and T. Nguyen. "Effect of leakage current and shunt resistance on the light intensity dependence of organic solar cells". In: *Applied Physics Letters* 106.8 (2015), p. 083301.

[282] C. G. Shuttle et al. "Charge-density-based analysis of the current–voltage response of polythiophene/fullerene photovoltaic devices". In: *Proceedings of the National Academy of Sciences* 107.38 (2010), pp. 16448–16452.

[283] M. Liu et al. "Light Intensity Dependence of Performance of Lead Halide Perovskite Solar Cells". In: *Journal of Photopolymer Science and Technology* 30.5 (2017), pp. 577–582.

[284] M. Lejeune et al. "Plasma-Based Processes for Surface Wettability Modification". In: *Langmuir* 22.7 (2006), pp. 3057–3061.

[285] S. E. J. O'Kane et al. "Measurement and modelling of dark current decay transients in perovskite solar cells". In: *Journal of Materials Chemistry C* 5.2 (2017), pp. 452–462.

[286] N. E. Courtier et al. "How transport layer properties affect perovskite solar cell performance: insights from a coupled charge transport/ion migration model". In: *Energy & Environmental Science* 12.1 (2019), pp. 396–409.

[287] N. E. Courtier, G. Richardson, and J. M. Foster. "A fast and robust numerical scheme for solving models of charge carrier transport and ion vacancy motion in perovskite solar cells". In: *Applied Mathematical Modelling* 63 (2018), pp. 329–348.

[288] X. Sun et al. "A Physics-Based Analytical Model for Perovskite Solar Cells". In: *IEEE Journal of Photovoltaics* 5.5 (2015), pp. 1389–1394.

[289] J. H. Heo et al. "Planar $CH_3NH_3PbI_3$ Perovskite Solar Cells with Constant 17.2% Average Power Conversion Efficiency Irrespective of the Scan Rate". In: *Advanced Materials* 27.22 (2015), pp. 3424–3430.

[290] D. H. Kim et al. "300% Enhancement of Carrier Mobility in Uniaxial-Oriented Perovskite Films Formed by Topotactic-Oriented Attachment". In: *Advanced Materials* 29.23 (2017), p. 1606831.

[291] L. K. Ono et al. "Temperature-dependent hysteresis effects in perovskite-based solar cells". In: *Journal of Materials Chemistry A* 3.17 (2015), pp. 9074–9080.

[292] W. Tress et al. "Understanding the rate-dependent J-V hysteresis, slow time component, and aging in $CH_3NH_3PbI_3$ perovskite solar cells: the role of a compensated electric field". In: *Energy & Environmental Science* 8.3 (2015), pp. 995–1004.

[293] T. Leijtens et al. "Opportunities and challenges for tandem solar cells using metal halide perovskite semiconductors". In: *Nature Energy* 3.10 (2018), pp. 828–838.

[294] M. Jošt et al. "Textured interfaces in monolithic perovskite/silicon tandem solar cells: advanced light management for improved efficiency and energy yield". In: *Energy & Environmental Science* 11.12 (2018), pp. 3511–3523.

[295] D. Yang et al. "High efficiency flexible perovskite solar cells using superior low temperature TiO_2". In: *Energy & Environmental Science* 8.11 (2015), pp. 3208–3214.

[296] J. Yoon et al. "Superflexible, high-efficiency perovskite solar cells utilizing graphene electrodes: towards future foldable power sources". In: *Energy & Environmental Science* 10.1 (2017), pp. 337–345.

[297] Q. Wang et al. "Large fill-factor bilayer iodine perovskite solar cells fabricated by a low-temperature solution-process". In: *Energy & Environmental Science* 7.7 (2014), pp. 2359–2365.

[298] L. E. Polander et al. "Hole-transport material variation in fully vacuum deposited perovskite solar cells". In: *APL Materials* 2.8 (2014), p. 081503.

[299] W. Yan et al. "Increasing open circuit voltage by adjusting work function of hole-transporting materials in perovskite solar cells". In: *Nano Research* 9.6 (2016), pp. 1600–1608.

[300] T. Zhang et al. "Crystallinity Preservation and Ion Migration Suppression through Dual Ion Exchange Strategy for Stable Mixed Perovskite Solar Cells". In: *Advanced Energy Materials* 7.15 (2017), p. 1700118.

[301] Y. Shao et al. "Grain boundary dominated ion migration in polycrystalline organic–inorganic halide perovskite films". In: *Energy & Environmental Science* 9.5 (2016), pp. 1752–1759.

[302] D. Meggiolaro, E. Mosconi, and F. De Angelis. "Formation of Surface Defects Dominates Ion Migration in Lead-Halide Perovskites". In: *ACS Energy Letters* (Publication Date (Web): February 20, 2019).

[303] D. Yang et al. "High efficiency planar-type perovskite solar cells with negligible hysteresis using EDTA-complexed SnO_2". In: *Nature Communications* 9.1 (2018), p. 3239.

[304] W. S. Yang et al. "Iodide management in formamidinium-lead-halide–based perovskite layers for efficient solar cells". In: *Science* 356.6345 (2017), pp. 1376–1379.

[305] K. Wang et al. "All-inorganic cesium lead iodide perovskite solar cells with stabilized efficiency beyond 15%". In: *Nature Communications* 9.1 (2018), p. 4544.

[306] G. Grancini et al. "One-Year stable perovskite solar cells by 2D/3D interface engineering". In: *Nature Communications* 8 (2017), p. 15684.

[307] M. Li et al. "Highly Efficient 2D/3D Hybrid Perovskite Solar Cells via Low-Pressure Vapor-Assisted Solution Process". In: *Advanced Materials* 30.30 (2018), p. 1801401.

[308] A. Mei et al. "A hole-conductor–free, fully printable mesoscopic perovskite solar cell with high stability". In: *Science* 345.6194 (2014), pp. 295–298.

[309] H. Chen et al. "A solvent- and vacuum-free route to large-area perovskite films for efficient solar modules". In: *Nature* 550 (2017), p. 92.

[310] M. Chen et al. "Highly stable and efficient all-inorganic lead-free perovskite solar cells with native-oxide passivation". In: *Nature Communications* 10.1 (2019), p. 16.

[311] S. Shao et al. “Highly Reproducible Sn-Based Hybrid Perovskite Solar Cells with 9% Efficiency”. In: *Advanced Energy Materials* 8.4 (2018), p. 1702019.

List of Figures

List of Tables

Publications

1. **H. Hu**, K. K. Wong, T. Kollek, F. Hanusch, S. Polarz, P. Docampo, L. Schmidt-Mende, Highly Efficient Reproducible Perovskite Solar Cells Prepared by Low-Temperature Processing, *Molecules* **2016**, *4*, 542.

2. **H. Hu**, S. Birkhold, M. Sultan, A. Fakharuddin, S. Koch, and L. Schmidt-Mende, Surface Band Bending Influences the Open-Circuit Voltage of Perovskite Solar Cells, *ACS Applied Energy Materials*, **under review**.

3. S. T. Birkhold, **H. Hu**, P. Hoeger, K. K. Wong, P. Rieder, A. Baumann, L. Schmidt-Mende, Mechanism and Impact of Cation Polarization in Methylammonium Lead Iodide, *The Journal of Physical Chemistry C* **2018**, *122*, 12140-12147.

4. P. Ehrenreich, S. T. Birkhold, E. Zimmermann, **H. Hu**, K.-D. Kim, J. Weickert, T. Pfadler, L. Schmidt-Mende, H-Aggregate Analysis of P3HT Thin Films-Capability and Limitation of Photoluminescence and UV/Vis Spectroscopy, *Scientific Reports* **2016**, *6*, 32434.

5. A. Fakharuddin, M. Seybold, A. Agresti, S. Pescetelli, F. Matteoci, S. T. Birkhold, **H. Hu**, R. Giridharagopal, D. S. Ginger, I. M. Sero, A. D. Carlo, L. Schmidt-Mende, Perovskite-Polymer Blends In uencing Microstructure, Non-Radiative Recombination Pathways and Photovoltaic Performance of Perovskite Solar Cells, *ACS Applied Materials & Interfaces* **2018**, *10*, 42542–42551.

Acknowledgments

It has been really a pleasant and memorable journey to have the opportunity to do my Ph.D. study in the Hybrid Nanostructures group, university of Konstanz.

Firstly I want to thank Prof. Lukas Schmidt-Mende for his great supervision during the past years. Without your patient guidance and kind support, I won't be able to finish this thesis. I have learned a lot from the helpful discussions with you. Besides the scientific suggestions, you also kindly give me assistance in my life. I won't forget your help during the birth of my baby. You are always friendly when I turn to you. It has always been relaxing and fruitful talking with you. It has been a real fortune to have you as my Ph.D. supervisor.

Then I want to thank all the teammates in the group who I had the opportunity to work with. Eugen Zimmermann is the first colleague I met in the group. You kindly helped me with all the technical issues and I sincerely appreciated it. You showed me the initial lab work and fabricated the first batch of decent perovskite solar cells. You are always reliable and happy to offer help. Kevin has been in the same study area with me. You are always friendly and humble. I thank you for all your suggestions and support during the past years. I want to express my thanks to Susanne Birkhold. Thank you for your patient review and constructive suggestions to my projects! I would like to thank Sajad Hussain, Azhar Fakharuddin, Michael Seybold and Susanne Koch for their help. You have all kindly helped me and I miss those days working with you.

I am also very thankful to my office mates from the beginning to now. Kwang-Dae Kim and Chaw Loon Thu were great office mates. You were all so experienced and gave me so much help in my beginning days in the group. It was really happy time with you talking about the different cultures in our home countries. Paul and Pius only stayed short time. But you are both cheerful and friendly. It is really enjoyable to chat with you with the updates when meeting you in the campus. Timo Raab, the current mate. Thank you a lot for your help on the German language. You are a valuable asset in this international office.

I would like to express my thanks to all the group members I had the honor to know. Jonas Weickert, James Dorman, Philipp Ehrenreich, Julian Kalb, Julian Reindl, Karl-Philipp Strunk, Thomas Pfadler, William Wang, Carola Ebenhoch, Stefan Schupp, Tobias Seewald, Sohaila Zaghloul Nabi Mohammed, Patrick Pfeiffer, Matthias Noebels, Martin

Putnik, Alexander Graf, Sara Sand. I miss those days with you around. I want to express my special thanks to Hamidreza Riazi-Nejad. You have been very helpful and always try to cheer me up.

I also want to thank my Chinese friends I met in the university. Feng Yuyi, Zheng Hong, Yang Fan, Yu Guilan, Zeng Zhaoke, it is very fortunate to have you around. It has been very comforting and relaxing to meet and cook with you from time to time.

At last I want to thank my parents for their selfless sacrifice. I love you. Your support has been the most reassuring harbour for my heart. I also want to thank my beloved wife, Xiaoman. Your company is the most luxurious thing I ever have. At last I want to thank my baby boy, Hu Zhiheng. You have been 5 month old and changing every day. It is really amazing to play with and take care of you. You are my life changer.

Thank you all for this amazing journey!